

Design, Synthesis and Application of Light-activated Tools for Chemical and Biological Research



Joanna Louise Donnelly

Institute of Chemistry
University College London

This thesis is submitted for the degree of
Doctor of Philosophy

Declaration

I, Joanna Louise Donnelly, confirm that the work presented in this thesis is my own. Where information or data has been derived from other sources, I confirm that this has been indicated in the thesis.

Abstract

Chromophores are fundamental tools for chemical and biological research and are readily applied in many aspects of life and material science. Their applications are broad and illustrate the diversity and importance of light-activated tools in a variety of scientific fields. The applications of fluorophores include diagnostics, biological discovery, biomedical research and as sensitizing dyes for photovoltaic devices.

There is increasing demand for chromophores with highly specific optical properties. Meeting these demands can improve the performance of chromophores for a variety of applications. A classic example of this is long wavelength photon absorption and emission. This is predominantly due to the strong compatibility of infra-red light with biological tissue. The intricacies of biological events can be monitored safely and accurately using target specific fluorophores that are activate within the biological optical window; this is typically above 600 nm. Other highly desirable characteristics of long wavelength fluorophores include solvatochromism, environmentally dependent fluorescence emission, target specificity and non-cytotoxicity. In addition, sensitizing dyes active at longer wavelengths promote faster electronic recombination, thus improving the power conversion efficiency of photovoltaic devices. There is a consequential impetus to design chromophores with finely and reliably tuneable photophysical properties that can be applied as specialized light-activated tools. Designing chromophores with these desirable properties requires a detailed understanding of the structure activity relationships (SAR) between chromophore design and photophysical properties.

A series of 17 organic chromophores built around the BODIPY molecule have been designed and synthesised to address these demands. Functionalisation has been

carried out at three different positions of the BODIPY molecule, with substituents ranging in steric bulk, polarity and electronic effect. Photophysical profiles have been determined including absorption and emission spectra, alongside computational modelling to establish molecular orbital stabilities. From these data, correlation between substituents and loci on the BODIPY construct, and resultant photophysical properties and application potential has been established. Establishment of structural activity relationships enables fine-tuning of spectral properties to facilitate the development of specialised chromophores able to meet specific application demands.

Long wavelength chromophores with environmental sensitivity can be applied in several applications. The designed BODIPY analogues have been successfully applied for target-specific bio-imaging of lipophilic membranes. The “switch-on” fluorescence enables visualization of lipid membranes with good signal-to-noise ratio, with biocompatibility and low cytotoxicity. A fluorophore integrating all desirable properties is expected to drive bio-imaging of cells, tissues and organisms to facilitate detection, observation and control of biological systems, and promote research and diagnostics. The photophysical profiles of some of the analogues also allows them to perform as sensitizing dyes in dye sensitized solar cells (DSSCs). This has been undertaken successfully using two of the generated analogues.

Impact statement

The research described in this thesis explores the potential of multifunctional fluorophores for a range of applications in chemical and biological research. These extend from fluorescence imaging and probing of biological environments to sensitizing dyes for photovoltaic devices.

Designing chromophores for biological applications requires a fundamental understanding of the relationship between chromophore structure and spectroscopic properties. The insight from developing structure activity relationships will enable the development of novel fluorophores with rationally designed photochemical properties, including absorption towards the near infra-red. The impact of long wavelength absorption facilitates *in vivo* application due to its inherent lower toxicity and deeper reach into biological tissue. Further, implementing photocaging for accurately controlled photorelease of drug molecules could reduce side effects during applications such as disease treatment. In combination with other favourable properties such as good target specificity and intense fluorescence emission, these attributes could broaden applicability to encompass a wide range of biological targets with excellent spatial and temporal control. Subsequent increased understanding of biological structures using deep tissue imaging could lead to superior diagnostic techniques, facilitate the development of novel drugs and improve public health.

Acknowledgements

I would like to thank Prof. Stefan Howorka and Dr. Jon Wilden for the opportunity to work on this project and for their guidance throughout. I would also like to thank the members of the Howorka and Wilden research groups.

I would like to extend my gratitude to Loris Rizello and the rest of the Battaglia group for their guidance during my cell biological studies. I also thank Dr José Marin Beloqui, Dr Tom MacDonald and Filip Ambroz for their help and support in collaboration work with photophysical studies and DSSC experiments. Also, a thank you to Abil Aliev and Kersti Karu for the assistance with NMR and mass spectrometry, as well as to Tony Field for his help in stores.

Finally, I would like to say a huge thank you to all my friends and family for their help and support throughout this process. I would not have been able to do this without you.

Table of contents

Declaration.....	1
Abstract.....	2
Impact statement.....	4
Acknowledgements	5
List of Figures.....	9
List of Schemes.....	13
List of Tables.....	14
Abbreviations	15
Publications and presentations.....	18
1 Introduction.....	19
1.1 Long wavelength chromophores	20
1.2 Principles of fluorescence	25
1.3 Fluorophores.....	27
1.3.1 Fluorescent proteins.....	27
1.3.2 Quantum dots.....	29

1.3.3	Organic fluorophores	30
1.4	Environmental sensitivity	38
1.5	Organic fluorophores for near infra-red bio-imaging	40
1.6	Boron dipyrromethene	45
1.6.1	Use of BODIPY as a fluorophore	46
1.7	Aims and objectives	54
2	Synthesis and characterisation of BODIPY analogues	56
2.1	Introduction	56
2.2	<i>Meso</i> – substitution of BODIPY analogues	67
2.3	Substitution at the 2,6 – position of BODIPY	73
2.4	Substitution at the 3,5 – position of BODIPY	80
2.5	Summary and discussion	88
3	Photophysical analyses	102
3.1	Density functional theory	102
3.2	Transient absorption spectroscopy	119
3.3	Time correlated single photon counting and photoluminescence quantum yield	121
4	Lipid membrane interactions	126
4.1	Introduction	126
4.2	Insertion of BODIPY fluorophores into synthetic lipid membranes	127
4.2.1	Confocal microscopy with GUVs	128
4.2.2	Insertion of fluorophore into cytoplasmic membranes	129
4.3	Visualization of cytoplasmic membranes with BODIPY compound 24	136
4.3.1	Staining of live cells	136
4.3.2	Cell viability studies using MTT assays	138
4.3.3	Interaction of compound 24 with FaDu cells pre and post fixation	139
4.3.4	Permeabilization studies	142

4.3.5	Cell membrane trafficking with immunofluorescence microscopy	
	145
4.4	Discussion	148
5	Conclusions and further work.....	151
5.1	Summary	151
5.2	Future outlook.....	153
6	Bibliography	156
7	Appendix.....	167
7.1	General experimental.....	167
7.2	Synthetic experimental methods.....	173
7.3	Density functional theory	186
7.4	Confocal fluorescence microscopy	193
7.5	Publications.....	199

List of Figures

1. *Graph to show the relative absorption spectra of the main chromophores in biological tissue.....*
2. *BODIPY analogues indicating the effects of chemical modification on maximum absorption wavelengths.....*
3. *Coumarin analogues indicating the effects of chemical modification on maximum absorption wavelengths.....*
4. *Jablonski diagram demonstrating the different decay pathways electrons may take from the excited singlet and triplet states back to the ground state.....*
5. *Example of a cyanine fluorophore, Cy5.....*
6. *Example of a squaraine fluorophore.....*
7. *Examples of naphthalene, anthracene and pyrene fluorophores.....*
8. *Examples of fluorescein, acridine and rhodamine fluorophores.....*
9. *Example of a coumarin fluorophore.....*
10. *Example of an oxazine fluorophore.....*
11. *The dipyrin (left), BODIPY (centre) and dipyrromethene (right) cores.....*
12. *Structure of the aza-BODIPY with a nitrogen at the meso position.....*
13. *The structures of compounds as alternatives to the traditional BODIPY.....*
14. *Diagram to show the planned substituents with which to modify the BODIPY core to establish photophysical profile SAR.....*
15. *Planned synthetic targets with modifications at the meso position of the BODIPY core.....*
16. *Planned synthetic targets with modifications at the 2 and 6 positions of the BODIPY core. R = CH₂Br, CH₂OAc or CH₂COEt.....*
17. *Planned synthetic targets with modifications at the 3 and 5 positions of the BODIPY core.....*

18. Planned synthetic targets with alternative structural modifications	
19. UV/Vis spectra of compounds 27-37	
20. Fluorescence emission spectra of compounds 27-37	
21. a) UV/Vis spectra of compounds 38-44 in polar (left) and apolar (right) solvent ...	
22. a) UV/Vis spectra of compounds 46-48 in polar (left) and apolar (right) solvent; b) fluorescence emission spectra of compounds 46-48 in polar (left) and apolar (right) solvent	
23. Summary of modifications to the BODIPY core that were unsuccessful	
24. Visual representation of the photophysical trends established based on modification of the BODIPY scaffold	
25. Representation to show the relative energies of HOMOs and LUMOs for compounds 27-48	
26. Molecular orbital diagrams and energies for compound 47 without solvent	
27. Orbital transition energies of compound 47 without solvent	
28. Molecular orbital diagrams and energies for compound 47 in ether	
29. Molecular orbital transitions energies of compound 47 in ether with assignment of transitions to absorption spectrum	
30. Molecular orbital diagrams and energies for compound 47 in MeCN	
31. Molecular orbital transitions energies of compound 47 in MeCN with assignment of transitions to absorption spectrum	
32. Molecular orbital diagrams and energies for compound 47 in MeOH	
33. Molecular orbital transitions energies of compound 47 in MeOH with assignment of transitions to absorption spectrum	
34. Transient absorption spectra for compound 47 in MeCN (a) and DMSO (b) indicating that little intersystem crossing to the triplet excited state is occurring	
35. a) Time correlated single photon counting decays of compound 47 in three different solvents, excited at 443 nm and measured at various wavelengths (see Figure legend); b)-d) Photoluminescence spectra of compound 47 with excitation wavelengths from 550-700 nm in ether (b), MeCN (c) and MeOH (d) with corresponding absorption spectra and transition energies	
36. Confocal microscopy image of POPC GUV after incubation with Nile Red showing insertion into the membrane	

37. *BODIPY analogues chosen for lipid membrane insertions, selected based on their environmentally dependent fluorescence emission profiles.....*
38. *Confocal microscopy images of POPC GUVs incubated with 100 μ M solutions of each compound.....*
39. *Relative fluorescence emission intensity produced by BODIPY analogues upon incubation with POPC GUVs using 100 μ M solutions of dyes for five minutes. a) Compounds **28-44** all excited at 532 nm; b) Compounds **46-48** all excited at 635 nm*
40. *Confocal microscopy images of live FaDu cells after incubation with 10 μ M solution of compound **47** for 5 (a), 7 (b), 30 (c) and 60 (d) min. Excitation using 633 nm laser beam for red channel and 405 nm laser beam for blue channel. Single channel images available in the appendix. Scale bar 10 μ M. for all except 60 min, 8 μ M*
41. *MTT assay readout for the treatment of FaDu cells with compound **47** over 24 hours.*
42. *Confocal microscopy images of FaDu cells after incubation with 10 μ M solution of compound **47** for 5 (a), 30 (b) and 60 (c) min followed by immediate fixation with paraformaldehyde (3.75%)*
43. *Confocal microscopy images of FaDu cells after fixation with paraformaldehyde (3.75%) followed by incubation with 10 μ M solution of compound **47** for 5 (a), 30 (b) and 60 (c) min.....*
44. *Effect of incubation time on fluorescence intensity in live cells, cells fixed post-staining (staining + fixation) and cells fixed pre-staining (fixation + staining)*
45. *Confocal microscopy images of FaDu cells before treatment (a) and after treatment with 0.2% Triton X for 5 (b) and 10 min (c), after staining with compound **47** for 30 min. A concentration of 0.2% Triton-X is higher than 0.1% usually used for permeabilization. Scale bar 50 μ m; d) effect of permeabilization on fluorescence intensity over time.....*
46. *Confocal microscopy images of cells fixed with para-formaldehyde (3.75%), incubated for 60 min with compound **47** and treated with 0.1% Triton X. Imaging carried out after 10 minutes. The images show a) DAPI (blue channel) and compound **47** (red channel); b) compound **47** (red channel) only.....*
47. *Immunofluorescence microscopy. Confocal microscopy images of FaDu cells fixed with paraformaldehyde (3.75%) before 60 min incubation with compound **47**,*

treatment with 0.1% Triton X, blocking with BSA (5% in PBS) and incubation with LAMP1-H483 antibody followed by Donkey A488 anti-rabbit secondary antibody

48. Comparison of the fluorophore profiles of CellBrite 640 (pictured) and compound **47**

.....

A1. Confocal microscopy images; top to bottom: compounds **28**, **29**, **43a**, and **44a**

A2. Confocal microscopy images for compounds **47** and **48a**

A3. Confocal microscopy images for compounds **31** and **46**

A4. Confocal microscopy images of live FaDu cells after incubation with 10 μ M solution of compound **47** for 5, 7, 30 and 60 min

A5. Confocal microscopy images of FaDu cells after incubation with 10 μ M solution of compound **47** for 5, 7, 30 and 60 min followed by immediate fixation with paraformaldehyde

A6. Confocal microscopy images of FaDu cells after fixation with paraformaldehyde followed by incubation with 10 μ M solution of compound **47** for 5, 7, 30 and 60 min.

List of Schemes

1. *Tautomerization between the lactone and quinoid forms of xanthene fluorophore, fluorescein*
2. *Synthetic routes towards compounds **27** and **28***
3. *Synthetic routes towards compounds **29**, **30** and **31***
4. *Synthetic routes towards compounds **32**, **33**, and **34***
5. *Synthetic routes towards compounds **36** and **37***
6. *Synthesis of compound **38***
7. *Synthetic routes towards compounds **39**, **43a** and **44a***
8. *Proposed mechanism for the reduction of the meso substituent during the synthesis of compounds **43** and **44***
9. *Synthesis of compound **46***
10. *Synthetic routes towards compounds **47** and **48a***
11. *Summary of BODIPY analogues achieved with varied meso substituents*
12. *Summary of BODIPY analogues achieved with varied substitution and the 2, 3, 5 and 6 positions of the BODIPY core*

List of tables

1. *Reaction conditions for compound **35** that was not successfully synthesised*
2. *Reaction conditions for compounds **40**, **41** and **42** that were not successfully synthesised.....*
3. *Reaction conditions for compound **45** that was not successfully synthesised*
4. *Reaction conditions for compounds **49-55** that were not successfully synthesised*
5. *Summary of the photophysical parameters for compounds **27-38***
6. *HOMO and LUMO energies for compound **47** in different solvents with varying associated polarities*
7. *Energies of quantum mechanical transitions to singlet excited states with corresponding oscillator strengths and molecular orbital transitions for compound **47**.....*
8. *Fluorescence lifetime measurements for compound **47** in three solvents with different detection wavelengths*
9. *Photoluminescence quantum yield (PLQY) for compound **47** in three solvents: ether, MeCN and MeOH using detection probes of varying wavelengths*
10. *Comparison of fluorescence intensities for compounds **28-48a** and normalized to allow more accurate comparison.....*
- A1. *HOMO and LUMO energies for compounds **1-25***

Abbreviations

AcOH	Acetic acid
Abs	Absorption
ATR	Attenuated total reflectance
BODIPY	Boron dipyrromethene
BOIMPY	Boron complexes of iminopyrrolide liganes
BSA	Bovine serum albumin
ChR2	Channel-rhodopsin-2
CT	Charge transfer
CuTC	Copper(I) thiophene-2-carboxylate
Cy	Cyanine
DABCO	1,4-diazabicyclo[2.2.2]octane
DAPI	4',6-diamidino-2-phenylindole
DBa	Dibenzylideneacetone
DBN	1,5-Diazabicyclo[4.3.0]non-5-ene
DCM	Dichloromethane
DFT	Density functional theory
DIPEA	Diisopropylethylamine
DMAP	4-dimethylaminopyridine
DMBA	Dimethylbenzamide
DMF	Dimethylformaldehyde
(<i>d</i> ₆ -) DMSO	Dimethyl sulphoxide (deuterated)
<i>E</i>	Entgegen
EDG	Electron donation group
EEA1	Early endosomal antigen one
ELISA	Enzyme linked immunosorbent assay

eq.	Equivalents
ES	Excited state
EtOAc	Ethyl acetate
EWG	Electron withdrawing group
FaDu	Human hypopharyngeal squamous carcinoma cells
Flu	Fluorescence
GFP	Green fluorescent protein
GS	Ground state
GUV	Giant uni-lamellar vesicles
h	Hours
Hb	haemoglobin
HeLa	Henrietta Lacks
HOMO	High occupied molecular orbital
HPLC	High performance liquid chromatography
ICT	Intramolecular charge transfer
IR	Infra-red
ISC	Intersystem crossing
IUPAC	International union of pure and applied chemistry
LAMP1	Lysosomal associated membrane protein one
LCMS	Liquid chromatography mass spectrometry
LUMO	Lowest unoccupied molecular orbital
mg	Milligrams
mL	Millilitres
mmol	Millimoles
MHz	Megahertz
mins	Minutes
MTT	3-(4,5- dimethylthiazol -2-yl)-2,5-di phenyl tetrazolium bromide
<i>m/z</i>	Mass to charge ratio
NIS	<i>N</i> -iodosuccinimide
NMR	Nuclear magnetic resonance
OmpG	Outer membrane protein G
PBS	Phosphate buffered saline

PDT	Photodynamic therapy
PEG	Polyethylene glycol
PL	Photoluminescence
PLQY	Photoluminescence quantum yield
POPC	Phosphatidylcholine
PPD	<i>p</i> -Phenylenediamine
ppm	Parts per million
PTAA	Poly[bis(4-phenyl)(2,4,6-trimethylphenyl)amine]
Py	Pyridine
RAB7	Recombinant antibody seven
RFP	Red fluorescent protein
RNA	Ribonucleic acid
SAR	Structural activity relationship
ssDNA	single stranded DNA
SUV	Small unilamellar vesicles
TAS	Transient absorption spectroscopy
TEA	Triethylamine
TCSPC	Time correlated single photon counting
TES	Triethylsilane
THF	Tetrahydrofuran
TICT	Twisted intramolecular charge transfer
TLC	Thin layer chromatography
TMS	Tetramethylsilane
TPSA	Topological polar surface area
TRITC	Tetramethylrhodamine
TTA	Triple triplet annihilation
TTET	Triplet triplet energy transfer
UM	<i>n</i> -undecyl- β -D-maltopyranoside
UV	Ultra-violet
Z	Zusammen

Publications and presentations

The work has been presented in the following forms:

Publications:

1. **A switchable fluorophore for specific and high-contrast imaging of cellular membranes in the near-infrared.** Donnelly *et al.* *Chem. Eur. J.* 2020, 26, 863-72
2. **Carboxylic Acid Functionalization of the *meso*-position of the BODIPY Core and its Influence on Photovoltaic Performance.** Ambroz *et al.* *Nanomaterials*, 2019, 9, 1346

Presentations:

1. Design and synthesis of light-activated compounds as tools for chemical and biological research. **Poster presented at the Institute of Structural and Molecular Biology Retreat, Cambridge, 2017**
2. Design and synthesis of light-activated compounds as tools for chemical and biological research. **Oral presentation at the GSK Travel Award Finals, University College London, 2017**
3. Design and synthesis of light-activated compounds as tools for chemical and biological research. **Poster presented at the IUPAC International Symposium on Photochemistry, University College Dublin, 2018**

Chapter 1

Introduction

Light is a highly attractive candidate for chemical and biological research, primarily because it can be applied both globally and locally with predictable orthogonality.¹ With easily controlled direction, amplitude and time of exposure, light can be readily manipulated to rapidly reach a target.¹

Chromophores are regularly used as targets for a broad range of applications. To achieve application specificity, fine-tuning of physical and chemical properties is required. To understand this, correlation between photophysical profiles and structural design must be established. By determining structure activity relationships (SAR) between chemical structures and resultant properties, chromophores with exact and accurately predictable properties can be developed. With this, light responsive tools designed to address highly specific targets and functions can be prepared for applications ranging from biological imaging and diagnostics to photovoltaic devices.

Selective targeting in biomedicine becomes challenging when addressing disorders not localised to a unique receptor. Diseases such as cancer require targeting of cells that despite being oncogenic, often present as a biologically analogous to healthy cells. The clear requirements for this involve selective targeting of cancerous cells within the relevant areas of the body without damage to non-cancerous cells. With

increasing development of DNA/RNA targeting treatments for cancer, the importance of drug selectivity cannot be overstated, particularly given that a large majority of the genome is not yet understood.^{2,3} The development of chromophores with highly specific photophysical properties, such as activity at wavelengths towards the near infra-red and solvatochromism, can be used to address these demands. As such, establishing SAR for chromophores is vital for the successful design of highly effective tools.

1.1 Long wavelength chromophores

There is increasing desire for chromophores that are active at long wavelengths, particularly towards the near infra-red. Meeting these demands enables the use of multiple chromophores in a singular system, each with unique photophysical triggers. Without this it is difficult to selectively target individual chromophores, in part due to spectral overlap. This does not only improve the variety of chromophores available, but also facilitates biological compatibility.

The optical requirements for biological studies using light as an endogenous trigger can be best understood by examining the paths of radiation upon interaction with human skin.⁴ The least problematic factor is reflection, which can occur directly at the boundary between skin and the air, and also between the layers below the surface of the skin. This has only a minor effect on the biological efficiency of light penetration.

Both the scattering and absorption of photons pose a threat to efficacy. Scattering occurs as a result of collagen fibres, which in turn limit the depth to which photons can penetrate biological tissue. This effect is minimised when wavelengths of light within an optical window of 600-1300 nm are used. Here, maximum penetration of tissues with minimal scattering is achieved, which ensures specific and efficient targeting.⁵ Use of these longer wavelengths also minimises damage to surrounding healthy tissue, as short wavelengths of light can destroy biological material.^{6,7}

Absorption of photons by cellular components also affects the availability of light *in vivo*. The key chromophores present in biological systems are haemoglobin (Hb) and melanin, which easily absorb light below ~600 nm. To improve the efficiency of photon delivery, light of wavelengths above 600 nm should therefore be applied to minimise absorption by melanin, Hb and oxygenated Hb (Figure 1). This absorption impedes both the penetration depth and quantum yield of photon delivery for wavelengths below 600 nm. Similarly, water significantly absorbs wavelengths of light above 1300 nm. This therefore limits desirable wavelengths to the optical window indicated in Figure 1.⁸ Thus, there are increasing efforts to design and synthesise chromophores that absorb light within this window.

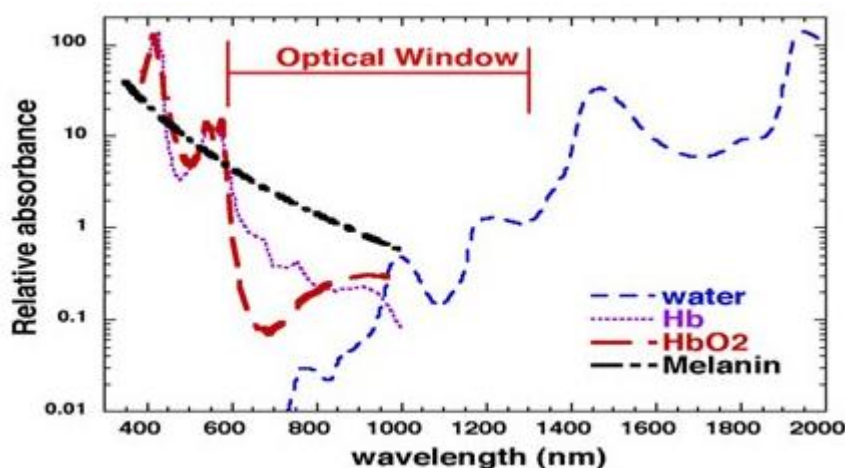


Figure 1: Graph to show the relative absorption spectra of the main chromophores in biological tissue⁸

The design and development of novel chromophores is challenging. Accurate prediction of absorption wavelengths mostly relies on Woodward-Fieser rules; this set of empirically derived rules can guide predictions for maximum absorption wavelengths for organic compounds. Briefly, this methodology correlates numerical changes in maximum absorption wavelength with the addition of functional groups, such as a diene. However, these can be unreliable, given the complexity of electron-electron and electron-hole interactions within a chemical system. Moreover, chromophores should be biocompatible which, beyond estimating lipophilicity based

on molecular mass and the presence of hydrogen donors and acceptors using Lipinski's rules of 5, is difficult to accurately forecast.

One of the most regularly applied techniques to increase absorption wavelengths is therefore the modification of existing chromophores, such as porphyrins, coumarins or boron dipyrromethenes (BODIPYs). There are four key methods utilised to increase maximum absorption wavelengths for chromophores: 1) extension of the conjugated system; 2) addition of auxochromes; 3) inclusion of sulphur or heavy atoms; 4) introducing strong electron withdrawing groups.⁹

Extension of the conjugated system increases maximum absorption wavelengths by narrowing the gap between the HOMO and LUMO. Hence the energy required for electron promotion is decreased, and the associated absorption wavelength increases proportionally.

Auxochromes induce a similar effect on HOMO-LUMO gaps, changing the energy difference and resultant wavelength of absorption for the chromophore. These are normally small organic functional groups that can facilitate this effect due to their non-bonding electrons. They are typically situated at the terminus of an unsaturated carbon chain. Delocalisation of these non-bonding electrons within the conjugated system of the chromophores simulates extension of the π system, typically inducing a bathochromic shift. Auxochromes can be either acidic or basic, and include amines, carboxylic acids and alcohols. The efficacy of these tools is therefore pH dependent; for example, acidic environments will restrict the availability of the lone pair of an amine, reducing the magnitude of the bathochromic shift. Sufficiently low pH could therefore completely suppress any changes in absorption wavelength that would otherwise have been caused by auxochromes.

Figure 2 shows the effectiveness of increasing the size of conjugated systems and including auxochromes, on the maximum wavelength of absorption. Here, extension of the conjugated system of a BODIPY chromophore leads to a bathochromic shift of 125 nm between compounds **1** and **2**. In addition, the addition of auxochromes, such as methoxy groups, causes a further increase in the absorption maximum of 21 nm

for compound **3**. As expected, the effectiveness of the auxochromes is less than conjugation size, given that the addition of the methoxy group is approximately analogous to increasing the size of the conjugated system by one π bond. These examples demonstrate the potency of these strategies to achieve longer wavelength chromophores.

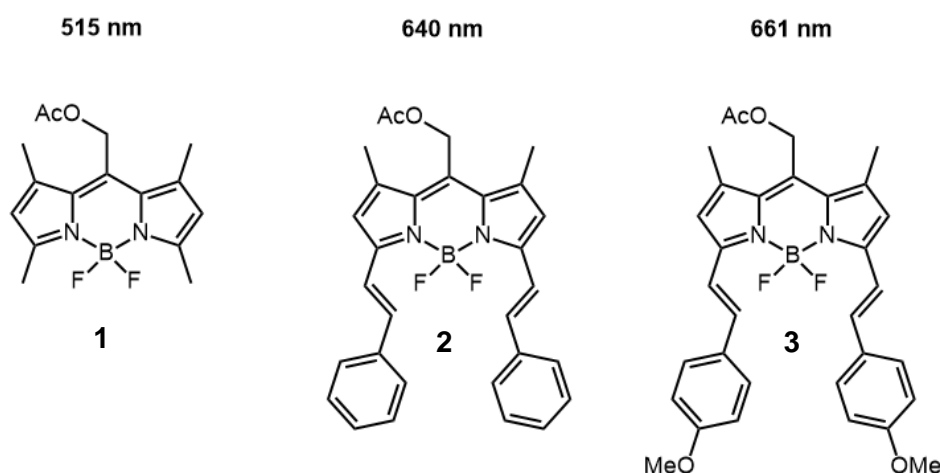


Figure 2: BODIPY analogues indicating the effects of chemical modification on maximum absorption wavelengths¹⁰

The inclusion of sulphur or heavy atoms, often in place of oxygen atoms, have been shown to increase absorption wavelengths. In the case of thiocarbonyls for example, longer absorption wavelengths are caused by the energy mismatch between carbon and sulphur orbitals in comparison to the overlap between carbon and oxygen orbitals. This results in a longer and weaker C-S bond compared with a C-O bond, narrowing the gap between the HOMO and LUMO and increasing the wavelength of photons required for excitation between these two orbitals. This effect is magnified with larger elements such as selenium or tellurium.¹¹

Electron withdrawing groups provide a useful strategy for increasing absorption wavelengths for chromophores. Their incorporation into conjugated systems can induce large dipole moments which increase photoinduced intramolecular charge transfer. The resultant shift in absorption is bathochromic, the extent of which is limited by the size and design of the conjugated system. Larger linear systems typically cause greater bathochromic shifts.¹²

Figure 3 shows three coumarin moieties, compounds **4**, **5** and **6**, that demonstrate the efficacy of these modifications on the photophysical properties of coumarin chromophores. Here, the simple substitution of a lactam for a thiolactam increases the maximum absorption wavelength by 75 nm. In addition, introduction of a cyano substituent within the conjugated system causes a further shift in absorption wavelength of 45 nm in the bathochromic direction.⁹

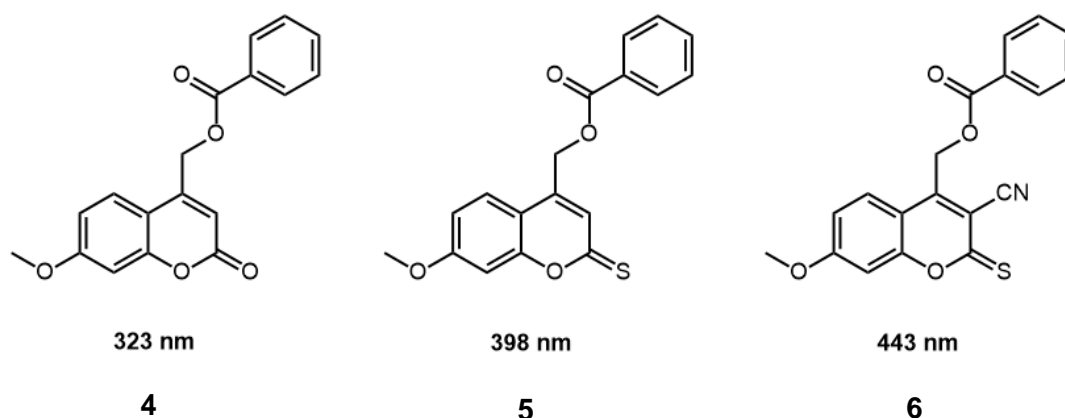


Figure 3: Coumarin analogues that show the effects of chemical modification on maximum absorption wavelengths⁹

Typically, efforts to modify existing analogues combine multiple strategies to achieve precisely designed chromophores with a range of wavelengths within the desirable optical window of 600-1300 nm. The fine-tuning of molecules to achieve photophysically unique profiles is fundamental to the use of chromophores as specialised tools for chemical and biological research. This would allow multiple chromophores to be used distinctly in a single system, without overlapping of absorption wavelengths.

1.2 Principles of fluorescence

Fluorescence was first observed, although most likely not fully understood, in the sixteenth century.¹³ This phenomenon describes the process by which light is emitted from a substance, referred to as a lumophore, which has absorbed either light or electromagnetic radiation. Conceptually this is fairly simple; photons are absorbed from an external source and the energy is subsequently released as light, normally of lower energy.¹⁴ This process is depicted in Figure 4.

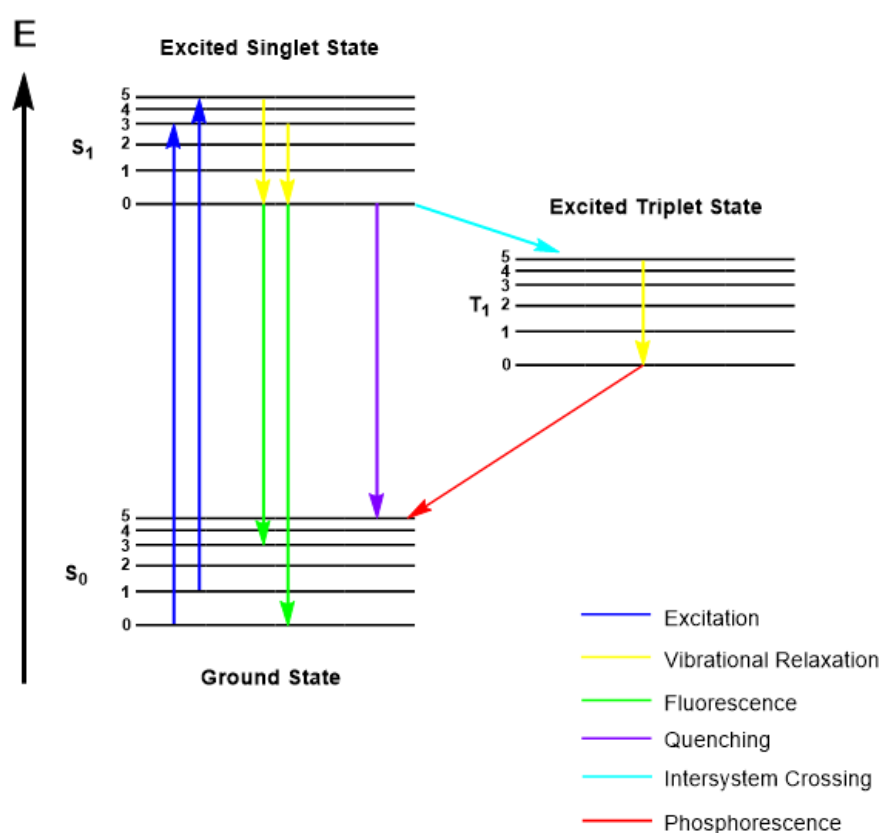


Figure 4: Jablonski diagram demonstrating the different decay pathways electrons may take from the excited singlet and triplet states back to the ground state

The Jablonski diagram (Figure 4) shows the electronic transitions that occur during excitation from an external source. Excitation occurs from various vibrational energy levels as electrons within the ground state (S_0) are excited to the higher energy singlet state (S_1) upon absorption of light. Vibrational relaxation to the lowest vibrational

energy level of the excited singlet state enables emission of fluorescence as electrons subsequently relax and return to the lower energy ground state.

Other than fluorescence, there are two major alternative pathways for the transfer of energy from the excited singlet state. The first of these occurs when light is absorbed in the presence of quenching groups. Fluorescence quenching can be partial or complete, taking place as a result of heavy metals,¹⁵ other fluorescence acceptor molecules,¹⁶ or changes in the environment, including pH,¹⁶ temperature¹⁷ and oxygen concentration.¹⁸ When this quenching takes place, photons are forced to undergo non-radiative decay, during which the excited fluorophore transfers its energy to the quenching species. This occurs because fluorescence quenchers, in particular heavy atoms, can strengthen spin-orbital coupling; this increases the rate of intersystem crossing to the excited triplet state. The resultant emission takes place by phosphorescence instead, decreasing the yield of fluorescence emission.¹⁹

Non-radiative decay may also occur from both the singlet and triplet excited states. This is shown in purple in Figure 4. Major processes by which this can occur include bond rotation and vibration, molecular collision or photoinduced electron transfer. Consequently, it is unusual for fluorescence quantum yields to be quantitative, as loss of energy via non-radiative decay is inevitable in most cases.

Fluorescence emission from a material is theoretically continuous unless processes such as photo-bleaching occur. This occurs during irreversible photolytically induced molecular decay, often as a consequence of overexposure to a light source. This is typically caused by an overproduction of reactive oxygen species, predominantly singlet oxygen. It is possible to minimise this effect by reducing exposure to excitation sources maximising emission detection efficiency or adding antifade reagents. Although often unnecessary, antifade reagents are reactive oxygen species scavengers and thus can mediate photo-bleaching. Examples of these reagents include DABCO and PPD.

1.3 Fluorophores

A number of different strategies are used to design fluorophores. There are three key categories of fluorophores: fluorescent proteins, quantum dots, and synthetic organic fluorophores.

1.3.1 Fluorescent proteins

Fluorescent proteins were first discovered during the 1960s when Shimomura *et al.* observed the emission of blue light from bioluminescent protein Aequorin in Jellyfish.²⁰ This was discovered to work in tandem with another protein, later named green fluorescent protein (GFP), to trigger a fluorescent response from the conversion of Ca^{2+} induced luminescence into green fluorescence emission upon illumination with UV light. In 1992, Prasher *et al.* presented the full mechanism for this emission, demonstrating how GFP could be used for a number of functions outside its native Jellyfish host.²¹ The structure of fluorescent proteins consists of an intrinsic chromophore that forms a central helix and is surrounded by an 11-stranded β -barrel. The nature of this structure shields the chromophore from biological metabolism, maintaining its integrity and stabilising the structure.²² This insight opened the door to the engineering of modified GFP analogues that are capable of emitting different wavelengths of light, including blue, yellow and orange.²³ These mutant proteins have been employed for a variety of functions, for example, as a reporter gene,²⁴ to monitor environmental changes such as pH²⁵ and for selective bio-imaging.²⁶ Of particular interest is the development of red fluorescent proteins (RFP). The significance of these cannot be overstated, as the increase in fluorescence emission wavelength broadens the application potential to *in vivo* studies where longer wavelengths of light are required to maximise tissue penetration with minimal scattering of light. These were not described until 2008, when Miyawaki *et al.* discussed the first successful design of a fluorescent protein with fluorescence emission maxima above 529 nm.^{22,27} Here an emission maximum of 585 nm was achieved. Despite the marginal increase in emission, this was significant, given that no progress had been made in the 15

years since the structure of GFP was presented. More recently, efforts have moved to alternative sources, the most consequential of which was extracted from reef-building corals, *Anthozoa Scleractinia*. This protein has a fluorescence emission maximum of over 600 nm and is currently paving the way for the use of fluorescent proteins at wavelengths towards the infra-red.^{22,26,28,29}

Fluorescent proteins are particularly advantageous as their structural complexity permits targeting of a broad range of stimuli. These range from whole biological systems to subcellular components, often targeted non-invasively with good spacial and temporal precision. Their intrinsic biocompatibility enables facile use in a biological setting with little chance of undesired toxicity.³⁰ They are also much smaller than traditionally used fluorescently tagged antibodies, making them easier to work with in a biological environment. Despite this there are some drawbacks to fluorescent proteins. Expression of mutant proteins often requires an artificial increase in protein expression which can be expensive and disrupts cellular physiology. In addition, more extreme modifications to the protein can result in fragility and a decrease in target compatibility.

1.3.2 Quantum dots

Quantum dots comprise the second class of fluorophores and were first documented in 1981 by Ekimov *et al.*³¹ They are built from as few as 100 to as many as 100,000 atoms to form nanoscopic semiconductor particles normally ranging from 2 to 10 nm in diameter.³¹ Exposing these particles to photons enables an excitation/emission response comparable with that of a single molecule, despite the presence of multiple particles.³² The region of activity within the electromagnetic spectrum is predominantly dependent on the size of the quantum dot, with wavelength increasing proportionally with size. Hence, controlling the spectroscopic profile is facile, with minimal modification required to achieve tuneable emission within a range of a few hundred nanometers.³² It is also possible to moderate these photophysical properties by changing particle size and dispersity, or by chemically modifying the surface of the material. Emission wavelengths of over 1000 nm have been achieved using quantum dots, far superior to GFP or RFP. This has been realised using a combination of cadmium, lead and tellurium to build the semiconductor surface.³³ Therefore, this nanotechnology provides a highly credible alternative to fluorescent proteins. In comparison, quantum dots also tend to exhibit greater intensity fluorescence emission that is easily detectable.³⁴ In addition, they are highly photostable, have a long fluorescence lifetime, provide a good signal-to-noise ratio and are mostly resistant to photo-bleaching.³⁵

The main challenge for the application of quantum dots is their poor biocompatibility, due to mostly being constructed from toxic heavy metals.^{36,37} However, steps have been taken to generate biocompatible quantum dots.³³ These range from using living organisms as bioreactors,^{38,39} taking biomimetic approaches such as artificial cellular structures or biomolecules,^{40–42} and chemically modifying the surface material.⁴³ It is projected that these advances will facilitate a broader range of applications to an otherwise ideally designed fluorescent system.

1.3.3 Organic fluorophores

The final class of fluorescent tools are organic fluorophores. Organic fluorophores with spectroscopic activity in the near infra-red are regularly used in chemical and biological research. Control of molecular structures at an atomic level enables highly specific design of optical properties for specialised applications. For example, aromatic hydrocarbons with high π electron densities inherently have high a molar absorptivity and fluorescence emission that varies with polarity. This can be attributed to narrowing of the gap between the π and π^* orbitals. Electron withdrawing groups can also be used to increase quantum yields of fluorescence. Control of spectral properties helps with molecular design to meet specific applications. Furthermore, organic fluorophores tend to have sharp absorption bands, making them ideal for use in conjunction with other fluorophores that are active in different regions of the electromagnetic spectrum.

The earliest well established example of a small molecule organic fluorophore was the natural product quinine.⁴⁴ Although often overlooked due to its potent antimalarial properties, quinine played a crucial role in our understanding of fluorescent molecules.⁴⁵ Since then a number of other endogenous fluorophores have been utilised, including aromatic amino acids such as tryptophan, for applications ranging from fluorescence quenching to ligand binding.⁴⁵ In a number of these cases, environmentally dependent fluorescence emission proved extremely useful. Since, there have been numerous synthetic organic fluorophores active towards the near infra-red region that were designed to meet a variety of functions. The most commonly used can be categorized into different classes: cyanines, squaraines, naphthalenes, anthracenes, pyrenes, xanthenes, acridines, coumarins, oxazines, tetrapyrroles and BODIPYs. The latter of these classes, BODIPY, are discussed in greater detail in Section 1.6.

Cyanine dyes are organic molecules typically constructed from two nitrogen bearing heteroaromatic rings conjoined via a polymethine bridge.⁴⁶ This connecting bridge varies in length, with longer absorption and emission wavelengths normally measured

for longer bridges. Typically, most derivatives have spectroscopic profiles in the visible region, however modification of the scaffold has enabled to significant bathochromic shifts.⁴⁷ A number of cyanines have achieved emission wavelengths above 700 nm and have been applied commercially, with success, as fluorescent tags and biomarkers. An example of this, Cy7 (compound **7**, Figure 5) contains 7 methine groups; it absorbs light at 755 nm and emits fluorescence at 788 nm.⁴⁷

Cyanine fluorophores are highly desirable not only due to their variety of absorption wavelengths, but also because of their large molar extinction coefficients, tending towards $10^5 \text{ M}^{-1}\text{cm}^{-1}$. Their structural diversity also lends itself to conjugation to other molecules, such as semiconductors and biological structures.⁴⁸ They are cationic and hence they have also been employed as fluorophores in biological probes, semiconducting materials and even for monitoring blood flow. Cyanine fluorophores were among the first to be approved by the FDA for use in medicine.⁴⁶ Nevertheless, many analogues suffer from poor fluorescence emission yields in aqueous environments, aggregation, poor photostability and small stokes shifts. The latter of these is particularly problematic as reabsorption of fluorescence emission due to overlapping spectra, compromises the yield of detectable response. Typically, the R group consists of a hydroxyl group or an NHS-ester to permit coupling to other structures.

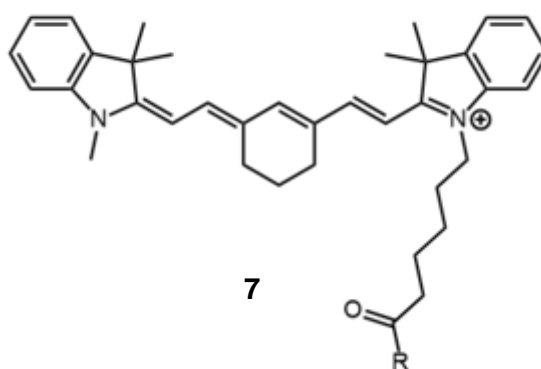


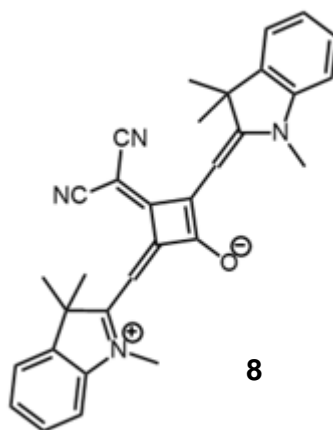
Figure 5: Example of a cyanine fluorophore, Cy5⁴⁷

Recent developments have sought to overcome these insufficiencies, with particular focus on instability. This was proposed by Nani *et al.* in 2015; they demonstrated that increasing the rigidity of the polymethine linker not only improves photostability, but also the quantum yield of fluorescence emission.⁴⁹ Hence, this class of organic fluorophores has great scope for a range of applications, which are showing increasing development and improvement.

Squaraine fluorophores are notable for their zwitterionic structure. Their design focuses around an oxycyclobutenolate core with aromatic or heterocyclic components at either ends of the molecule.⁵⁰ A variety of structural designs are possible for these dyes, resulting in a broad range of physical and chemical properties. It is hence possible to construct fluorophores with high sensitivity and specificity with photophysical properties that are heavily dependent on the external environment. An example of this style of fluorophore (compound **8**, Figure 6) demonstrates the highly conjugated nature of these compounds.⁵¹ This particular fluorophore has absorption and emission wavelengths close to 700 nm, with significant environmentally dependent fluorescence emission and solvatochromism. This dependency was demonstrated using organic solvent MeOH, aqueous buffer and BSA. This study shows the value of a fluorophore with a photophysical profile dependent on external factors. This could be exploited to examine the hydrophobicity of biological systems, for example. Hence, squaraines are ideally designed as responsive probes.⁴⁶ Further, squaraines possess high molar extinction coefficients in the same region as cyanine dyes, towards $10^5 \text{ M}^{-1}\text{cm}^{-1}$. They rarely show photolytic instability and generally have good fluorescence quantum yields.^{46,50}

Despite this, the aqueous solubility of squaraines is poor, hindered by their large planar conjugated π systems; therefore, biocompatibility is low. Of those that are soluble in water, few emit fluorescence at wavelengths towards the near infra-red in an aqueous environment. In light of this, synthetic modifications have been undertaken to introduce substituents designed to increase surface polarity and reduce aggregation.⁵² This has been carried out successfully, by drastically increasing the size of the structure and incorporating charged substituents. The application potential of squaraines has improved with this development.⁴⁶ However,

the chemical composition of squaraines makes them reasonably reactive. This proves increasingly problematic when these fluorophores are used in complex environments, such as a biological system. This can result in aggregation and changes to the expected fluorescence emission, potentially rendering the fluorophores useless. Combined with the relatively small Stokes shifts, accurately recording fluorescence emission from these highly reactive fluorophores can be challenging.



towards fluorophores that are biologically compatible, with respect to solubility and long absorption maxima.

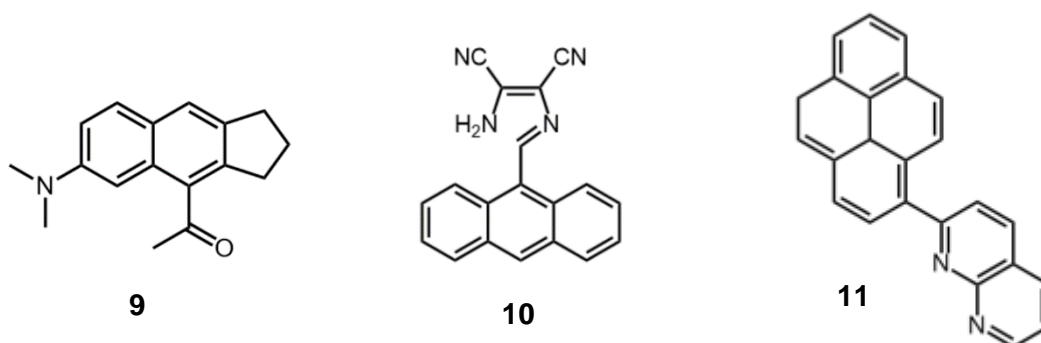


Figure 7: Examples of naphthalene, anthracene and pyrene fluorophores^{54–56}

To combat this, efforts have been undertaken recently to develop naphthalenes, anthracenes and pyrenes with better water solubility. Techniques have ranged from incorporating biologically relevant groups such as amino acid mimics⁵⁷ to the design of amphiphilic structures.⁵⁸ With these advances, it has been possible to use these fluorophores for applications including the imaging of biological structures such as proteins⁵⁹, detection of inorganic ions^{54,57,58} pH responsivity⁵⁶ and even to probe macrocycles.⁶⁰

Two other classes of fluorophores are based on derivatives of the anthracene structure. Xanthene and acridine are heterocyclic analogues with either an oxygen or nitrogen atom in place of one of the central carbons, respectively (Figure 8). The most well-known and widely used xanthene is Fluorescein (compound **12**), a fluorophore which has shown great longevity, having been first synthesised in 1871.⁴⁵ Since then, the core structure of Fluorescein has been extensively modified to yield fluorophores active in unique photophysical niches of the electromagnetic spectrum. Fluorescein derivatives were also the first fluorophores to be successfully utilised in immunofluorescence microscopy and are still regularly used in medicine today, most commonly in optometric diagnostics.⁶¹

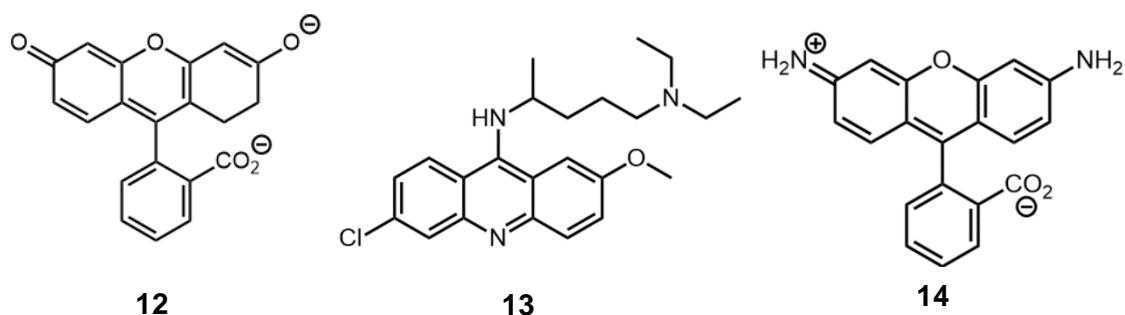
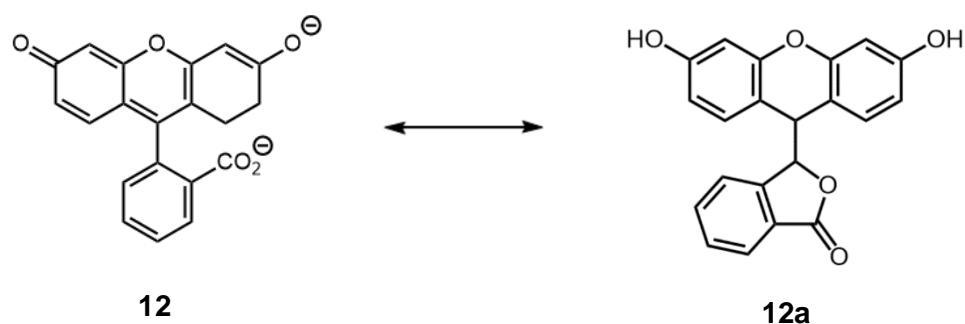


Figure 8: Examples of xanthene, acridine and rhodamine fluorophores^{62–64}

Analogues of these fluorophores, referred to as Rhodamines (compound **14**), also have similar photophysical properties and are regularly used in similar applications, depending on the photophysical requirements. The biological applications of these fluorophore derivatives are extensive: ophthalmic imaging, analyte detection⁶⁵ and even oncologic surgery.⁶⁶

These fluorophores are generally photostable, produce intense fluorescence emission and have easily fine-tuned photophysical properties, which can afford a broad range of fluorescent tools.⁶¹ Furthermore, as they are normally zwitterionic, aqueous solubility is rarely a challenge.⁴⁵ Despite this, tautomerisation between the lactone and quinoid forms of the structures of xanthene and rhodamine restricts their use in less polar environments (Scheme 1). With the closed form favoured in a non-aqueous environment, fluorescence emission is completely inhibited. As a result, they are unsuitable for probing complex lipophilic environments.



Scheme 1: Tautomerization between the lactone and quinoid forms of xanthene fluorophore, fluorescein

Coumarin dyes are based around a benzopyrone core; this structure lends itself to photostability, low toxicity and intense fluorescence emission.⁶⁷ These fluorophores have fairly large stokes shifts⁶⁸ (~30-60 nm), making them suitable for imaging with other photophysically distinct fluorophores without the concern of optical overlap.⁶⁹ The applications of coumarins are very broad and they are widely used in cosmetics and perfumes, as well as for biological imaging, fluorescent labelling and dye sensitized solar cells.^{67,69} The coumarin scaffold even forms the basis of fundamental medicine, Warfarin.⁷⁰ Analyte detection with these compounds can encompass a broad range of anions and metal ions, often with multiple substrates detected using the same analogue.^{71,72} Despite these advantages, coumarins typically absorb below 500 nm, which limits their use in a biological setting. They are therefore unsuitable for *in vivo* applications.⁶⁷

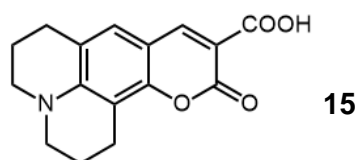


Figure 9: Example of a coumarin fluorophore⁷³

A less commonly used group of fluorophores are constructed from oxazine heterocycles, each consisting of a doubly unsaturated six membered ring with an oxygen and a nitrogen atom. Several isomers can be synthesised by changing the relative positions of these heteroatoms and unsaturated carbons. Oxazine fluorophores active towards the near infra-red often consist of multiple oxazine rings. These compounds show good molar absorptivities and fluorescence emission quantum yields. Although absorption wavelengths are typically not as long as for some fluorophores, oxazines can be used in a biological setting for techniques such as cell viability studies and ELISA assays^{45,68}, the staining of biological tissues including specificity to nervous systems^{74,75}, super-resolution microscopy⁷⁶ and the probing of biological targets such as esterases.⁷⁷ Widely used fluorophores such as Nile Red and Nile Blue (compound **16**, Figure 10) are classed as oxazine dyes and

are used often in biology and histology as lipophilic stains, and even as sensitizers in photodynamic therapy (PDT).⁷⁸

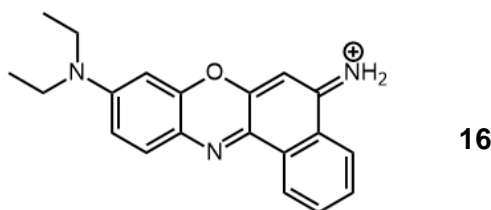


Figure 10: Example of an oxazine fluorophore, Nile Blue⁷⁸

Tetrapyrroles are built from four pyrrole moieties that are interconnected to form a macromolecule with high electron density. An example of a tetrapyrrole fluorophore, naphthalocyanine, is presented in Figure 11, compound **17**.⁷⁹ These fluorophores are normally intensely coloured and absorb light at long wavelengths, often above 600 nm.⁷⁹ However, the bulky aromaticity of many porphyrin analogues is incompatible with aqueous solubility; this issue has been addressed by extensive structural modification using, for example, PEG groups to form charged micelles and ensure aqueous solubility.⁸⁰ These fluorophores are photostable and therefore regularly employed in medical applications, such as photodynamic therapy. They have narrow optical windows, normally less than 20 nm, which makes for an efficient fluorophore, compatible with other fluorescence techniques without issues such as absorption and emission spectral overlap.⁸¹ Increasing structural complexity, including the introduction of coordinated metal ions, enables their use in diagnostics, permitting visualisation of biological structures in the visible and near infra-red spectrum, of malignant and other abnormal tissues.⁸²

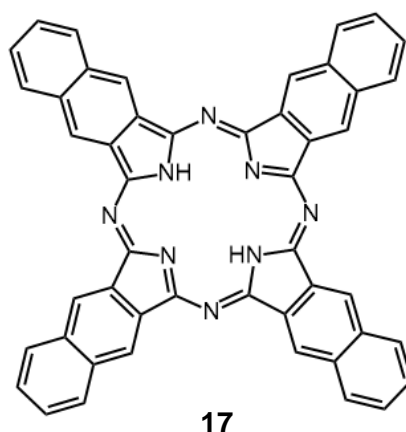


Figure 11: Example of a porphyrin fluorophore⁷⁹

All these fluorophores have photophysical profiles that are promising for a range of applications. However, each class of fluorophore presents some problems, limiting its full application. These range from poor biocompatibility and photostability, to narrow optical windows. Yet, with the great potential of these fluorophores, alongside the need for their optimisation, it is expected that their development will remain an area of intense focus in the near future.

1.4 Environmental sensitivity

Fluorophores with photophysical properties that are dependent on the surrounding environment are valuable for probing biological systems. These sensitive probes normally respond to environmental changes including, but not limited to, viscosity, pH and polarity. Their environmental sensitivity is reflected in distinct detectable variation in absorption and emission wavelengths (including solvatochromism) and/or fluorescence emission intensity.⁸³ In the most efficient environmentally dependent fluorophores, environmental changes can result in complete quenching of fluorescence emission, leading to “on/off” fluorescence. These probes are particularly valuable in the investigation of biological systems. The conjugation of environmentally sensitive fluorophores to relevant biomolecules such as nucleic acids or proteins can facilitate drug delivery^{84,85}, bio-sensing⁸⁶, diagnostics⁸⁷ and many other applications.

Molecular sensitivity towards a specific biological target can thus enable a “light switch” effect, by which fluorescence emission is only detectable upon the fluorophore reaching the target.

Sensitivity to changes in pH is common, particularly for small organic fluorophores.⁸⁸ A classic example of this is Fluorescein, which is highly sensitive to changes in pH due to its structural rearrangement to a non-fluorescent state.⁴⁵ This effect has also been observed in oxazine fluorophores, such as resorufin, which can be used as fluorescent labels.⁴⁵ These techniques have been refined to improve sensitivity, during which changes in pH across a range of only 1.28 have been successfully monitored.^{56,89} This is vital for biological applications as variation in pH tends to be smaller due to the innate buffering nature of biological systems.

Although less common, sensitivity to changes in viscosity have also been explored using sensitizing fluorophores. These are valuable in a biological setting as variation in viscosity is common during intracellular reactions.^{90,91} In addition to exploration of cellular processes, abnormal fluctuations in viscosity can identify a number of diseases.⁹² Hence, fluorophores sensitive to moderations in viscosity can be fundamental to early diagnostics. This field has included the introduction of a strategy known as molecular rotors, whereby conformational changes of a fluorophore, caused by changing viscosity, can induce variation in quantifiable fluorescence emission.⁹⁰

Detection of polarity changes is one of the most valuable uses of environmentally sensitive fluorophores.⁹³ In a biological setting, especially at a cellular level, polarity can affect the activity of many proteins, and also influence the permeability of cellular membranes. This can directly affect the higher order functionality of a biological cell. Therefore, understanding and monitoring of polarity changes in a biological setting is an important strategy for exploration at a molecular level. This could ultimately lead to a better understanding of the onset of diseases. Typically the most accessible targets for these sensitive probes are lipophilic membranes.⁹⁴ These can vary from large extracellular membranes to smaller lysosomes, which are fundamental to the interactions between enzymes and substrates.⁹⁵ Application of these probes can

therefore provide insight into the complexities of chemical and biological processes.^{93,96}

The conjugation of environmentally dependant fluorescent molecules to biologically relevant substrates is increasing in importance. Macromolecules such as DNA have been tagged with sensitive fluorophores to monitor DNA replication and protein synthesis.^{83,97} In 2013, Suzuki *et al.* attached solvatochromic fluorophores to oligonucleotides in order to monitor DNA duplex formation. Here, they demonstrated how stable base pairing within the duplex with concomitant localization of a naphthalene fluorophore enabled “switch-on” fluorescence emission.⁸³ This illustrates the relevance of environmentally sensitive fluorophores and indicates their potential for biological investigation.

The design and application of fluorophores with environmentally sensitive fluorescence emission is fundamental to the exploration of biological systems. The optimisation of these probes could improve understanding of these systems with high target specificity and accuracy. This could lead to improved strategies to address biological abnormalities, particularly in medicine, potentially culminating in disease management or treatment.

1.5 Organic fluorophores for near infra-red bio-imaging

Our understanding of biological processes is heavily dependent on our ability to comprehend these complex systems on a microscopic level. As a result, there is an increasing need to visualize biological components quantifiably in a biological context, with good spatial and temporal accuracy. Advances in fluorescence microscopy have led to a decrease in reliance on lower resolution optical microscopy, and facilitated more complex and accurate biological exploration.⁹⁸ Previously, due to the undesirable random scattering of light, imaging was limited to surface observation, restricting our understanding of *in vivo* systems. This progress in bio-imaging technology has allowed much deeper biological visualization to take place.⁵⁰ This imaging is vital for diagnostics, biological discovery and biomedical research. For

most bio-imaging applications, the fluorescent tools tend to show little to no biological activity. This minimises disruption to natural biology and ensures an accurate insight into a biological system.

Whilst fluorescent proteins^{29,50} and quantum dots^{34,36} have been used for bio-imaging with relative success, organic fluorophores are the most suited to this application. This can be attributed to the high cost, complexity and biological activity of fluorescent proteins, and poor biocompatibility and cytotoxicity of quantum dots.³⁷ Moreover organic fluorophores are relatively easy to produce on a large scale and can be conjugated to other biomolecules such as DNA, proteins or antibodies.⁴⁶ Easily controlled spectroscopic profiles enable accurate design function for specific biological targets. Variation in fluorescence spectra can predictably characterize chemical and physical behaviour of organic molecules, permitting accurate SAR driven design.

For organic fluorophores, there are some key requirements for below surface imaging of biological systems. Most importantly, detectable fluorescence emission should take place at long wavelength, ideally towards 700 nm to allow deep tissue imaging with minimal photon scattering or phototoxicity. This also applies ideally to both absorption and excitation wavelengths. Additionally, this takes advantage of the low endogenous cellular optical activity for this wavelength region. This optical window can vary based on the depth of penetration required to accurately image any given target. Furthermore, molecular selectivity for specific biological structures is highly desirable for accurate unperturbed imaging. Biocompatibility is essential to avoiding aggregation and cytotoxicity. Compatibility with other biological exploration techniques, such as cellular trafficking studies, is also desirable to permit the use of organic fluorophores in a variety of applications without severe disruption of biological systems. Fluorophores should also be sufficiently sensitive to respond to low light intensity to reduce the chances of photo-bleaching or photolytic degradation of samples. Similarly, the fluorescence emission should be easy to monitor and control, with high spatial and temporal precision. A “switch on” effect, whereby fluorescence emission increases upon binding to a target either automatically or after initiating with an external trigger, is highly advantageous. This can help minimise background

emission, improving signal-to-noise ratio to ensure highly accurate imaging of biological structures. Normally this effect is achieved by solvatochromism and/or environmentally dependent fluorescence emission.

Ideal fluorophores would possess all of these characteristics; however, it is possible to optimise light conditions to compensate for any shortcomings. These can include modification of detectors or filters to remove background signal, for example.

Many prevalent near infra-red fluorophores are cyanine based. The first of these used for *in vivo* imaging was indocyanine green, which was approved for the monitoring of cardiac output, retinal angiography and hepatic function.^{82,99} It was also shown to rapidly accumulate in malignant tissues, permitting efficient imaging of solid tumours. Moreover, indocyanine green has been employed for image guided surgery, which has enabled a dramatic improvement in the precision of the surgical removal of diseased tissue.¹⁰⁰ Cyanines have also been conjugated to tumour seeking antibodies and radioactive nucleotides. This has enabled facile fluorescence imaging of cancer cell lines.¹⁰¹ Combining cyanines with a variety of antibodies could therefore open the door to the fluorescence imaging of a range of biological targets.

Porphyrins are some of the most favoured designs for near infra-red bio-imaging. This is predominantly due to their excellent molar absorptivity and fluorescence emission towards the near infra-red.¹⁰² They are also photostable and are regularly used in PDT.⁸¹ An example of this is Verteporfin, a PDT agent that is active at 690 nm.¹⁰³ Similarly, squaraines and xanthenes have been used in bio-imaging. The former has been shown to have excellent bio-compatibility, enabling highly efficient imaging of cancer cells. They have even demonstrated the ability to target specific cellular receptors with good selectivity.^{104–106} Xanthenes have more recently become some of the most widely used fluorophores, despite their typically shorter emission wavelengths relative to other dyes. Yet, efforts have achieved analogues active at increasingly longer wavelengths.¹⁰⁷ This, combined with unusually large stokes shifts (up to ~200 nm), make xanthenes promising candidates for bio-imaging.⁸¹

Large stokes shifts have also been measured for other cell imaging fluorophores. In 2017, Abeywickrama *et al.* introduced a structurally simple pyrene based nuclear cell stain with a stokes shift of 140 nm into the red region.¹⁰⁸ This was enabled by ICT that occurred during excitation with an acceptor molecule conjugated to the pyrene core. This approach was also utilised by Ryu *et al.* where the fluorescence of a diketopyrrolopyrrole molecule was effectively controlled by a conjugated electron-rich pyrrolopyrrole.⁹³ This efficiently increased stokes shifts via charge transfer, with nitrophenyl groups within the system enabling small solvatochromic shifts in fluorescence. Polarity dependent fluorescence emission improves the suitability of a fluorophore for bio-imaging, and hence these works can provide valuable insight into the development of fluorophores for biological visualization.

There are many examples where the bio-imaging of specific cellular structures has been achieved. These range from targeting lipophilic membranes to specific cellular organelles such as lysosomes, endoplasmic reticulum or the golgi body.^{109–112} This highly selective bio-imaging is fundamental to understanding chemistry at a cellular level and has the potential to assist in the treatment and prevention of diseases with hallmarks localized to cellular organelles. Most recently, a multifunctional cinnamamide derivative was presented by Yang *et al.* with the ability to selectively target mitochondria and function as an anti-cancer agent.¹¹³ This enabled drug delivery with excellent spatial accuracy. Although photophysical activity in the near infra-red was not employed here, this study demonstrates the importance of fluorophores with highly specific targeting ability in chemical and biological research.

A variety of other organic fluorophores have been used to monitor molecular activity in the near infra-red region besides those described. Many of these are designed to rely on the increased metabolic rate, and resultant increased cellular uptake, of cancerous cells to enable specific visualization. Despite this, the scope of bio-imaging towards the near infra-red is not limited to the detection and treatment of tumours. Fluorescence technology has been used to image other diseases including Alzheimer's disease,¹¹⁴ optical abnormalities,¹¹⁵ arthritis¹¹⁶ and even for the detection of bacterial infections.¹¹⁷ These works have led to increased understanding of disease

progression, and provided new avenues for treatment potential. For example, with respect to Alzheimer's disease, fluorescent dyes have been used in near-infrared fluorescence tomography of hallmark β -amyloid plaques in live mouse models.¹¹⁴ This was highly progressive, given that Alzheimer's disease typically requires post-mortem diagnosis.¹¹⁸ These advances support the extensive potential for the development of long wavelength fluorescent probes for biological imaging.

1.6 Boron dipyrromethene

First defined in 1968 by Treibs and Kreuzer, boron dipyrromethene (BODIPY) was originally reported as a small molecule that is distinguishable by its intense fluorescence emission.¹¹⁹ Despite its apparent simplicity, it was not until 2009 that the unsubstituted BODIPY moiety was synthesised and characterised.¹²⁰ The initially described compounds were all substituted at four or more of the positions (as labelled in Figure 11).^{119,121,122}

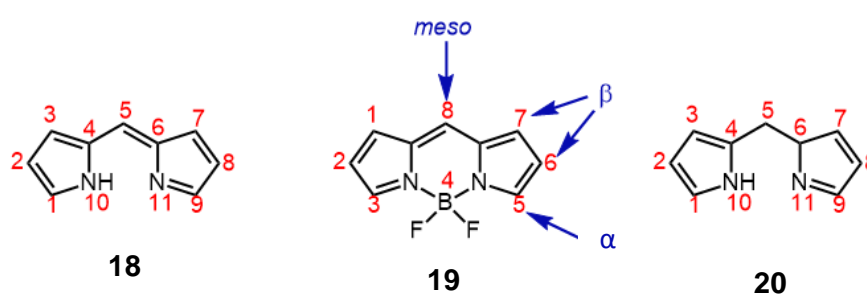


Figure 11: The dipyririn (left), BODIPY (centre) and dipyrromethene (right) cores¹²³

Although comparable in structure, the IUPAC numbering for the BODIPY core (compound **19**, 4,4-difluoro-4-bora-3a,4a-diaza-s-indacen) is different to the dipyririn and dipyrromethene (compounds **18** and **20**).¹²³ Nevertheless, the labelling of the alpha, beta and *meso* positions (the latter named as such due to analogy with porphyrin) remains the same throughout all three compounds.¹²³ The key attribute unique to the first two of these classes is the complete aromaticity throughout the BODIPY core. This complete conjugation throughout the central system accounts for the intense colours displayed by these chromophores, which are often bright red or orange.¹²⁴ Coordination of the boron difluoride to form BODIPY from the dipyririn induces rigidity in the structure. The unusually high fluorescence yields observed can be accredited to the resultant restricted flexibility.¹²⁵

1.6.1 Use of BODIPY as a fluorophore

The BODIPY scaffold has been used for a variety of applications, ranging from molecular probes and imaging agents, to dyes and lasers, and more recently in PDT.^{123,126–130} When used as fluorophores, BODIPY analogues have superior photophysical profiles compared with other long wavelength fluorophores such as fluorescein or TRITC.¹²⁴ The key advantage of using BODIPY analogues is that they can emit measurable emission that is close to 100% of the maximum fluorescence, which is not a common characteristic.¹²⁵ Combined with design dependent photo and chemical stability, BODIPY can be used for a range of applications.⁵⁰ Compounds containing BODIPY molecules often have small stokes shifts, and sharp excitation and emission peaks. Therefore, they are easily detectable by analytical techniques such as fluorescence spectroscopy. Moreover, these molecules are compatible with biological media, facilitating extensive and varied application. Furthermore, BODIPY groups are relatively non-polar, electrically neutral and often insensitive to changes in pH and solvent polarity.^{124,125,131} This results in minimal interference with the surrounding environment, making BODIPY a useful tools in a biological setting. Although BODIPY fluorophores sometimes have low molar extinction coefficients, this can be offset by other factors such as high target accuracy and good signal-to-noise ratio. The result is clear and spatially distinct fluorescence emission.

Despite its biocompatibility, BODIPY is a known DNA duplex intercalator, which is an undesirable property for an inert biological probe. Nonetheless, it is projected that when used in a cellular or tissue-based environment, negligible interaction with nuclear DNA is expected due to difficulty in penetrating the nuclear envelope. Moreover, this could be addressed by reducing the planarity of the BODIPY fluorophore, by introducing substituents, to reduce its intercalating ability.¹²⁹

Typically, BODIPY dyes are not fluorescent in their solid state, which can be attributed to the efficient fluorescence quenching power of π - π stacking interactions between adjacent BODIPY molecules. However, this has been challenged, with limited success, by the introduction of bulky substituents, reducing planarity and

subsequently minimising these π - π stacking interactions.¹³² More recently, this quenching has been rectified by entrapment of BODIPY molecules within MOFs.¹³³

An emerging application of BODIPY constructs is as near infra-red absorbing fluorophores for biochemical exploration. The core structure of the compound remains mostly unchanged, yet diverse and extensive modification has provided a range of analogues with a variety of beneficial properties. Although many BODIPY based scaffolds show little sensitivity to environmental changes, this can be successfully altered by promoting intermolecular charge transfer or photoinduced electron transfer. The result of this is often solvatochromism and/or environmentally dependent fluorescence emission. This improves the potential of BODIPY for bio-imaging by ensuring that detectable fluorescence emission is highly specific and dependent on, for example, changes in polarity or pH.¹³²

BODIPY has shown significant environmental sensitivity. This has been demonstrated by Bañuelos *et al.* and Hiruta *et al.* who presented a BODIPY fluorophore substituted at the *meso* position, which had a strong fluorescence emission response that was dependent on pH.¹³⁴ In one example, the environmental change resulted in almost complete quenching of emission.¹³⁵ It was hypothesised that this was a result of deprotonation induced movement of the enolate HOMO to sit between the HOMO-LUMO gap of the BODIPY, facilitating a PET process. Similarly, in 2011 they proposed further heavily *meso* modified BODIPY fluorophores. An increase in polarity prompted population of the red-shifted ICT state, and thus photon excitation took place from this energy level rather than the locally excited state.¹³⁵

The versatility of BODIPY has led to the development of a range of near infra-red fluorophores, ranging from small molecules that obey Lipinski's rules, to larger more lipophilic structures.¹³⁶ Some of these have shown significant environmentally dependent fluorescence emission, which has been put to effective use in bio-imaging. In some cases, emission wavelengths of towards 800 nm have been measured.¹³⁷ To date, this has been exploited for accurate bio-imaging intracellularly, including biological thiols, reactive oxygen/nitrogen species and other gaseous molecules.¹³⁸

Monitoring of cellular dynamics has played a significant role in furthering our understanding of biological events at a molecular level.¹³⁹¹⁴⁰

The BODIPY scaffold has proved to be versatile fluorescent tool for applications including the diagnosis of cancer and heart disease. For example, in 2016, Nigam *et al.* presented BODIPY derivatives that contained phosphonium ions. These BODIPY analogues showed significant affinity for mitochondrial membranes. A hallmark of cancerous and ischaemic heart cells is disruption of the mitochondrial membrane potential. The prevalent localization of BODIPY in mitochondrial membranes, combined with its environmentally sensitive fluorescence emission, permitted detection and monitoring of both malignant cells and oxygen deficient heart cells.¹⁴¹

Therapeutic uses of BODIPY are not limited to cancer detection and eradication. Rodríguez *et al.* proposed a method to track the biodistribution of the parasite responsible for Chagas disease, a condition known to infect organs including, but not limited to, the heart, oesophagus and secondary lymphoid organs.¹⁴² Known anti-Chagas chemotypes, based on the 2,3-dihydrothiazole system, were covalently bound to a BODIPY molecule. This enabled monitoring of the *in vivo* localization of the Chagas parasite in mouse models. Hence, it was possible to further understand the pharmacology of the parasite in mammalian systems. This demonstrates the broad potential of the BODIPY fluorophore in diagnostics and medicine.¹⁴²

Since then some creative methods have been utilized to further control the fluorescence emission of BODIPY molecules. Often these require *in situ* reactions to take place. A good example of this is the work of Greene *et al.* who used nucleophiles to liberate a BODIPY fluorophore from an emission quenching carbonyl substituent.¹⁴³ Perhaps one of the more innovative methods of inducing fluorescence was presented by Lincoln *et al.*¹⁴⁴ Here, they carried out nucleophilic addition to a non-fluorescent BODIPY molecule inside a mitochondrial membrane using a native protein bearing a thiol group. This caused a 350-fold increase in fluorescence emission response and allowed clear visualization of the mitochondria. This proved a valuable tool for the selective bio-imaging of mitochondria and verified the effectiveness of even a simple BODIPY fluorophore in an intelligent context.

With improvements to the design of BODIPY fluorophores, their application *in vivo* has greatly increased. Li *et al.* described a BODIPY compound with a phenyl group at the *meso* position with no detectable fluorescence emission. Upon exposure to endogenous hypochlorite ions in live cells, enhancement of fluorescence emission intensity was observed with significant hyperchromic shift.¹⁴⁵ This detection was particularly useful due to the known requirement for controlled hypochlorite levels *in vivo* in zebrafish and mice.¹³⁹ BODIPY analogues have also shown promising results when conjugated to thymidine analogues and incorporated enzymatically *in vivo* into a DNA helix.¹⁴⁶ This enabled facile visualization and determination of the native shape and intracellular distribution of newly synthesised DNA localized in *Escherichia. Coli.* cells by high-resolution electron spectroscopic imaging. In addition to this, BODIPY has been used to differentiate between different target amino acids by changing its absorption maximum when reacting with each amino acid.¹⁴⁷ Exposure of the probe to different bithiol analogues exhibited a variety of photophysical changes unique to each substrate. This illustrates the valuable high sensitivity shown by BODIPY towards changes in the environment. An interesting application of this has been molecular rotors, whereby changes in temperature and viscosity induce conformational changes at the *meso* position of the BODIPY core, leading to measurable deviations in fluorescence emission wavelength and intensity.⁹⁰

Outside of a biological setting, BODIPY has been useful in the detection of harmful substances. In 2012 Michel *et al.* presented a modified BODIPY structure capable of detecting carbon monoxide.¹⁵ Relying on liberation of a metallic fluorescence quenching palladium complex upon exposure to carbon monoxide, this probe was capable of detecting CO concentrations towards 28 ppb. With such a low detection limit, this probe had the potential to revolutionise the detection of harmful gases in a commercial setting. This is not the only example of BODIPY's ability to detect dangerous substances. Sayar *et al.* demonstrated a method to detect phosgene gas using a modified BODIPY scaffold.¹⁴⁸ This again depended on the removal of a fluorescence quenching substituent upon contact with the target gas, re-establishing the detectable fluorescence emission of the system. These works portray the real-world applications of a BODIPY fluorophore with photophysical sensitivity towards its external environment.

Modifications to the BODIPY structure can also involve the replacement of the *meso* carbon atom with a nitrogen atom, which has been successfully carried out by a number of different groups. Most interestingly, a number of these highlight the near infra-red maximum absorption wavelengths displayed by these analogues, many of which are above 700 nm.^{149–151} Whilst clearly the introduction of nitrogen into the heterocycle contributes to this bathochromic shift, the extensively conjugated nature beyond the aza-BODIPY core of the structures cannot be ignored given their known ability to increase absorption wavelengths. Hence it is possible to conclude that both the nitrogen and highly unsaturated substituents enable the shift in absorption maxima towards the infra-red region.¹⁵⁰

Over the last few years, aza-BODIPYs have featured prominently in the literature as highly functional fluorescent probes (Figure 12, compound **21**).^{144,152–154} Their photostability, high fluorescence yields and long absorption wavelengths make them ideal for bio-imaging.¹⁵⁵ In the work of Strobl *et al.* in 2015, the authors are keen to emphasise the excellent photostability of the aza-BODIPY analogues even “under extreme illumination”.¹⁴⁹ They even claim to outperform well established long wavelength chromophores, such as the cyanine dyes.¹⁴⁹



21

Figure 12: Structure of the aza-BODIPY with a nitrogen at the *meso* position

Bio-imaging using these fluorophores has been efficiently realised by Wu *et al.* with the exploitation of automatic aggregation of an aza-BODIPY probe upon contact with a lipid bilayer.¹⁴⁴ This localized aggregation enabled visualization of lipophilic cell membranes with good target selectivity. Although useful, this staining method is not particularly biocompatible, given the obvious perturbation of the cellular membrane that can accompany such extensive aggregation. Most recently, water soluble aza-

BODIPYs have been successfully used with a hydrosolubilizing group. Here, these fluorophores were used to label tumours by conjugation to an antibody.¹⁵⁶ This permitted successful and clearly detectable fluorescence imaging of tumours in mice, with excellent spatial accuracy.¹⁵⁶ Detection with BODIPY fluorophores has not been limited to cancer cells *in vivo*. Probing of β -amyloid has also been achieved in mouse models with “on/off” selectivity.¹⁵⁷ This is particularly exciting because it shows the potential for BODIPY fluorophores to cross the notoriously troublesome blood brain barrier. Hence BODIPY has clearly been shown to be a versatile chemical probe with a range of exciting biomedical capabilities.

Outside of bio-imaging, in 2018 novel approaches to PDT using BODIPY were presented. Dixit *et al.* showed how a series of BODIPY fluorophores with pyrrole and thiophene substituents could be used as photosensitizers against pancreatic cancer cells. Very low concentrations were required to achieve sufficient photocytotoxicity, further improving the attractiveness of BODIPY as an *in vivo* tool.¹⁵⁸ Ram *et al.* introduced a BODIPY scaffold covalently bonded to a platinum complex, ensuring the imperative close proximity of both photosensitizer and chemotherapeutic agent. This was able to facilitate PDT *in vitro* using near infra-red light against lung and breast cancer cells with good photocytotoxicity.¹⁵⁹ The modified BODIPY complex was prone to localization with mitochondria, showing a preference for cancer cells over healthy cells.¹⁵⁹ This enabled selective targeting of malignant cells and provided good progress towards specific cellular targeting in PDT.

Dipyrrin molecules are most commonly designed with a boron difluoride species conjugated to the two nitrogen atoms, as in the traditional BODIPY molecule. More recently however alternatives have appeared in the literature, notably incorporating heavy metals into the structure, such as in Figure 13, compounds **22** and **23**. The generation of BODIPY mimics with lower symmetry, as indicated in Figure 12, compounds **24** and **25**, were termed BOIMPY when presented by Lee *et al.*¹⁶⁰ This approach sought to remove the structural rigidity of the fluorophore and address the issue of small stokes shifts that are often measured in BODIPY fluorophores. The strategy successfully improved access to CT-type excited states, thus minimising quenching and increasing stokes shifts to almost 200 nm in some cases. As

anticipated however, this was at the expense of absorption wavelengths, with the highest maximum reaching only 460 nm. These new structures also demonstrated bio-imaging potential.

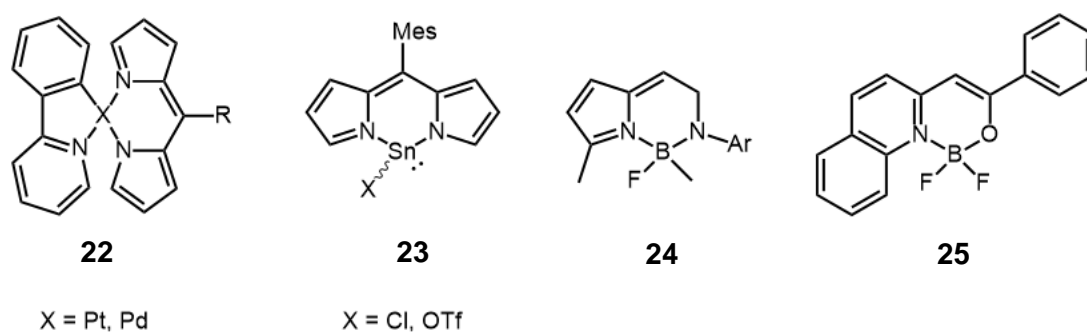


Figure 13: The structures of compounds as alternatives to the traditional BODIPY

In 2010 Bronner *et al.* presented dipyrin based scaffolds constructed by amalgamation with palladium and platinum. For both of these metals complexes, absorption maxima were measured at around 500 nm, comparable to that of BODIPY.¹⁶¹ Another example of a metal in place of boron was discussed in 2009 by Kobayashi *et al.*¹⁶² Here they used tin to complete the metallocycle (compound **23**) and, as in the case of palladium and platinum, the absorption maxima for these compounds was cited as approximately 500 nm.¹⁶²

Another approach to modification of the BODIPY core was introduced by Graser *et al.* in 2013; this involved the exchange of dipyrin for a quinolyl-enolato scaffold (compound **25**).¹⁶³ The result of this was a hypsochromic shift in the maximum absorption wavelength of almost 100 nm relative to the traditional BODIPY. Although these works provide little positive contribution to near infra-red fluorophore design, they reflect the innovative methods that can be used to develop this field further.

In 2011 Wu *et al.* introduced a novel application of BODIPY as a photosensitizer, using an iodine substituent as the heavy atom to facilitate ISC as opposed to the traditionally used metals.¹⁶⁴ These molecules proved to be valuable tools due to their intense absorption of light and long lived triplet states, allowing for efficient triplet

triplet energy transfer, and high upconversion yields. As organic molecules they are preferable to metal complexes for use in a biological setting. Their photophysical profiles remove the need to expose cells/tissue to damaging UV light as these BODIPY sensitizers were documented to absorb light between 510-629 nm.¹⁶⁴

1.7 Aims and objectives

The main aims of this project were to rationally design a series of fluorophores that are capable of fulfilling a number of photophysical objectives. The principal focus was to generate compounds with absorption/emission spectra towards the near infra-red. Primary benefits of this include permitting the use of these photolytic tools at long wavelength, opening the door to *in vivo* targets. The objective was to design fluorophores with photophysical properties that could be fine-tuned to meet the demands of specific biological applications; this was undertaken to target the unmet need for organic fluorophores that combine all the key features that facilitate effective bio-imaging. By doing this, SAR could be established to enable the highly specific design of fluorophores to address real world applications.

There have been a number of hypotheses as to how these goals can be achieved. With regards to shifting absorption wavelengths towards the infra-red region, extension of conjugated systems has been postulated as the most promising strategy to narrow the HOMO-LUMO gap. Furthermore, the introduction of heavy atoms such as iodine, and substitution of bathochromic auxochromes could contribute to increasing the wavelength of absorption maxima.^{125,165} To promote more intense detectable fluorescence emission at long wavelength, electron withdrawing groups and large conjugated systems will be used.

BODIPY is an ideal target fluorophore that can be used to determine the structural activity relationship between molecular design and photophysical properties. They are popular in bio-imaging and have desirable physical, chemical and spectroscopic properties. These include: photostability, optical activity above 500 nm, sharp absorption and fluorescence emission peaks, and good quantum yields of fluorescence. BODIPY is also a small, planar and rigid molecules that typically has a high extinction coefficient and intense fluorescence emission. These advantages combine to produce fluorophores that can be easily and precisely detected using, for example, confocal fluorescence microscopy.

Upon successful synthesis of a library of BODIPY compounds, the absorption and emission spectra for the developed compounds will be established in a range of solvents to determine absorption/emission maxima and environmental sensitivity. Establishing the relationship between chemical structures and photophysical properties will provide an understanding of the outcome of synthetic modification of BODIPY fluorophores. It has been postulated that significant solvatochromism and environmentally dependent fluorescence could be observed for many compounds. It is expected that auxochromes, such as dialkylamine substituents, will improve environmental sensitivity.¹⁶⁶ This opens the door to bio-imaging potential, with the possibility for detectable responses upon successful targeting of biological structures. It would then be possible to use confocal fluorescence microscopy, to explore how each fluorophore interacts with cellular structures. BODIPY has shown a strong affinity for membrane interactions and hence provides a viable strategy for membrane staining.¹⁶⁷ Success with a lipid bilayer mimic, such as a vesicle, will indicate the plausibility of this. This will be explored further to optimise structural design and promote affinity for lipophilic membranes. Success of all these factors could ultimately provide a means to tether inactivated substrates to a vesicle or cell and release them photolytically at a desired location. The successful synthesis of a range of different BODIPY compounds will therefore enable accurate SAR determination, facilitating the precise design of chromophores to fulfil highly specific functions.

Aside from bio-imaging, where suitable, further applications of the compounds will be explored, for example in dye sensitized solar cells. It is projected however that any drawbacks of BODIPY could be overcome by superb photophysical profiles, enabling the production of compounds capable of undertaking a series of light-activated functions with good spatial and temporal accuracy.

Chapter 2

Synthesis and characterisation of BODIPY analogues

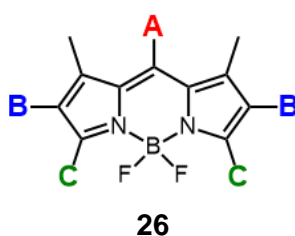
2.1 Introduction

Fluorophores based around the BODIPY scaffold are common; however, there is a distinct lack of understanding of how precise chemical modifications to BODIPY fluorophores can influence their spectroscopic properties. Here, modification of the core structure of BODIPY was carried out, with substitutions at various positions in order to efficiently explore a large chemical space. This resulted in the development of BODIPY fluorophores with a diverse range of properties and applications. This was then used to facilitate fine-tuning of the spectral and biophysical properties of the BODIPY fluorophore, which is essential for guiding an accurate structure to function design process.

A range of known and novel analogues were designed in order to develop understanding of the SAR between substituents and their location on a BODIPY molecule. These involved a selection of modifications varying in polarity, steric bulk and reactivity. The nature and positioning of substituents were projected to have a correlated effect on the resultant photophysical and biophysical properties. Modifications selected were predominantly small molecular changes, with the aim

that this would allow highly specific fine-tuning of properties with excellent precision and predictability. Particular focus was placed on molecules that are active in optical windows towards the near infra-red, have solvatochromism and have environmentally dependent fluorescence emission. This could hence be exploited to design specific molecules that are optimised to carry out highly specialised functions, such as bio-imaging, with good spatial and temporal accuracy.

Figure 14 and compound **26** depict the intended modifications to the BODIPY scaffold, with the intention to determine the SAR of the modifications on the photophysical profile of BODIPY.



A	Bromine, hydroxyl, esters, alkyls, carboxylic acids, amines and nucleosides
B	Iodine, extended alkynes, benzylic acyls, auxochromes
C	Extended alkenes, auxochromes

Figure 14: Diagram to show the planned substituents with which to modify the BODIPY core to establish photophysical profile SAR

The *meso* position (A, figure 14) is readily functionalised and can be modified using a variety of facile synthetic processes. It has also been noted that this position is particularly useful for promoting charge or electron transfer processes. Chemical modifications here could favour the population of ICT states and hence enable the generation of chromophores with environmental sensitivity. These include a variety of substituents capable of changing chemical properties such as the polarity and

electronic density of molecules. The intention was not to extend the conjugated system at the *meso* position, as poor electron overlap with the BODIPY core was unlikely to yield longer wavelengths with this strategy. Furthermore, there was also particular emphasis on reactive substituents such as bromine or hydroxyl groups because these are simple to synthesise, and their reactivity could facilitate fluorescent tagging applications.

Figure 15 (overleaf) presents compounds **27-37**, which were the target molecules with modifications at the *meso* position. These substituents were chosen due to their variation in steric bulk and polarity; however, *meso*-aryl substituents were not included here, as they are reported more extensively in the literature.^{168,169} The introduction of a variety of different substituents was planned, and different synthetic groups were to be incorporated with or without electronic conjugation to the BODIPY core.

Many compounds with simple synthetic modifications at the *meso* position are known, however their photophysical and biophysical properties have not been examined in detail, or used in the exploration of the SAR of BODIPY. Compounds **27** and **30** in particular were selected due to their high reactivity, which could ultimately lead to conjugation to larger molecules in fluorescent tagging applications. In addition, compound **29** is also a known photocage,¹⁶⁵ which indicates the diverse application potential of these molecules. Therefore, this was selected as an interesting target. It was hypothesised that this modification would also be favourable due to the introduction of an electron withdrawing group. The resultant stabilisation was expected to induce a noticeable bathochromic shift as well as a potential increase in fluorescence emission intensity. Compound **31** was the simplest proposed BODIPY fluorophore, and thus was constructed to act as a “control” molecule and provide context for any photophysical changes that occurred as a result of synthetic modifications.¹⁷⁰ Compounds **32-34** had ester groups installed adjacent to the *meso* carbon. This method aimed to introduce electron withdrawing groups closer to the BODIPY core to examine the effect on the spectroscopic properties. The outcome was expected to be a small increase in absorption wavelength, accompanied by an increase in extinction coefficient as the size of the conjugated system increased.

The structures of compounds **32-34** were very similar and the reasons for this were two-fold. The intention was to examine how minor adjustments such as the addition of a carbon atom could affect the spectroscopic profile of BODIPY; secondly, the aim was to provide multiple synthetic options to reach compound **35**. Compound **35** was designed to be analogous to compound **32** to enable direct assessment of how an increase in the polarity of the *meso* position of BODIPY could affect spectroscopic properties. Similarly, compounds **36** and **37** were targeted in order to examine the effects of distance on the impact of polar carboxylic acid groups on the photophysical profile of BODIPY. Ideally, direct comparison with compound **35** would establish the effect that proximity has on the influence of a carboxylic acid group on spectroscopic properties. With such long alkyl chains separating the carboxylic acid groups from the BODIPY core, it was not expected that the molar absorptivity or absorption wavelength would increase significantly for these compounds in comparison to other modifications. These substituents were also not conjugated to the π system and were expected to be too far from the BODIPY core to have significant inductive effects.

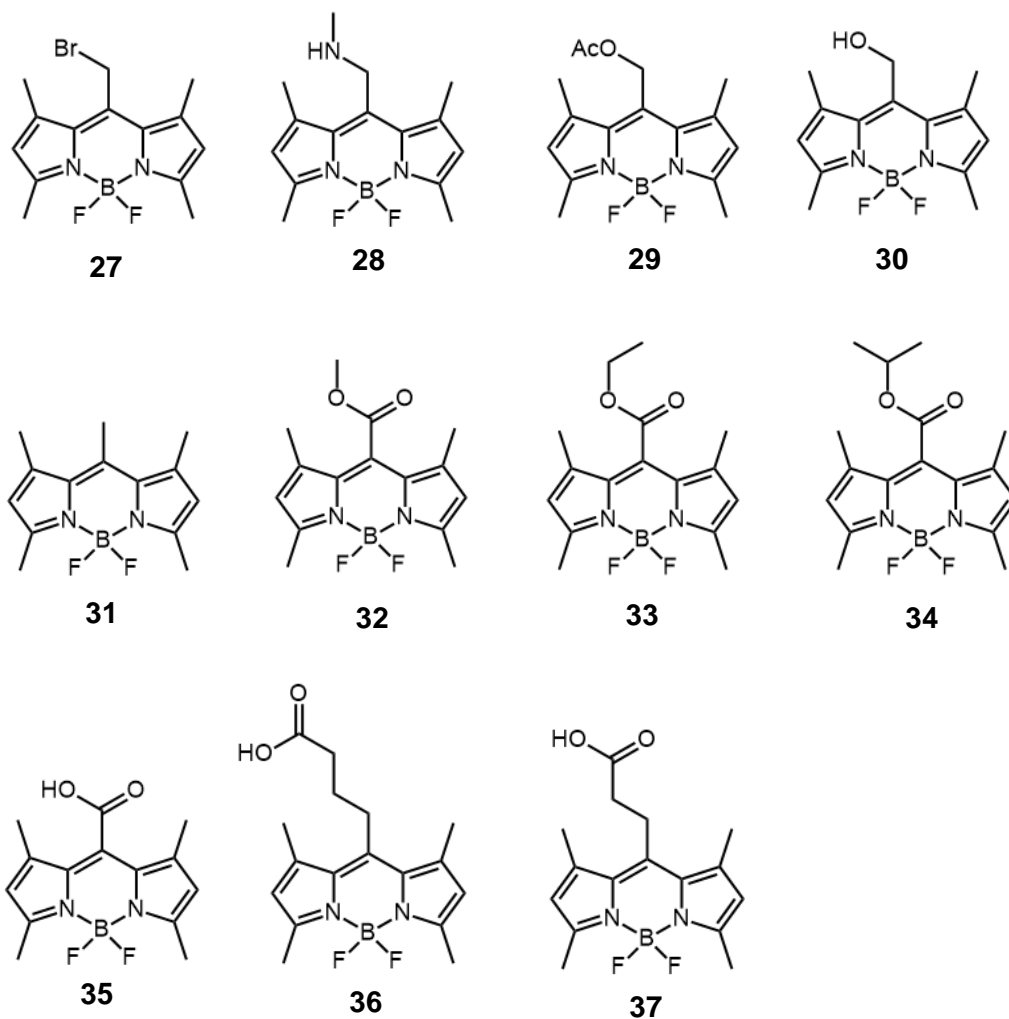


Figure 15: Planned synthetic targets with modifications at the meso position of the BODIPY core

For these *meso* modified fluorophores, it was predicted that absorption maxima would be ~500 nm.^{136,165,170–174} This can be explained by the fact that conjugation size remains fairly constant across these molecules. In addition, no auxochromes are incorporated onto the BODIPY skeleton that could interact with the conjugated system, thus solvatochromism and environmentally dependent fluorescence emission were not expected. Their main function was to provide insight into how minor changes to the structure, steric bulk and polarity of BODIPY at the *meso* position could assist in the specific design function process to achieve precise spectroscopic properties for a specialised, pre-defined application.

Functionalisation to explore the 2 and 6 positions of BODIPY was also explored (Figure 16). Here, as the BODIPY core is symmetrical, this normally permits substitution at both of these positions, which subsequently can magnify any resultant changes in the photophysical profile of the fluorophores. The most logical and simplest modification at the 2 and 6 positions of BODIPY was to introduce a halide such as iodine atom. The aim of this was to probe the effect of adding substituents at this position without an initial dramatic change to the polarity or sterics of the compound. Iodine was selected for a number of reasons: 1) the substitution of iodine onto the structure is facile and reliable, 2) iodine is electron withdrawing and relatively large, which could cause a bathochromic shift in absorption wavelength as well as an increase in fluorescence emission; Goswami *et al.* reported that an increase in absorption wavelength of almost 50 nm was observed when installing iodine atoms at the 2 and 6 positions of BODIPY.¹⁶⁵ 3) iodine is readily exchanged for other, more complex substituents. This opens the door to molecules that are highly specific and well optimised. Further, substituents such as iodine offer pathways to other more complex molecules. They permit reactions such as the Sonogashira coupling to expand the conjugated system and introduce other substituents with potentially favourable effects on photophysical profiles.

Compounds **42-44** were driven by a desire to increase the size of conjugated systems at the 2 and 6 positions of BODIPY, which has been noted as the most important factor in increasing the absorption wavelengths of BODIPY,¹⁷⁵ and also to explore the effects of carbonyl groups on the photophysical profile of BODIPY. Anderson *et al.* proposed that carbonyl groups adjacent to aromatic rings could quench fluorescence emission responses in protic solvents.¹⁷⁶ The aim of compounds **42-44** was therefore to examine the spectroscopic profiles of these compounds in protic and aprotic solvents of varying polarity, to determine whether this effect could be applied to BODIPY. The resultant environmentally dependent fluorescence emission could be a useful tool in the quest for fluorescence imaging and biological applications.

An increase in absorption maxima was also expected for compounds **43** and **44**. Incorporating an alkyne bearing either a methylbenzoate or dimethylaminobenzyl moiety was expected to also induce solvatochromism and environmentally dependent

fluorescence emission. The increased size of the conjugated system was also anticipated to increase the relative molar absorptivities of the compounds. The availability of the non-bonding electrons enables extension of the conjugated system much further than with alternative substituents without lone pairs. It was therefore expected that compound **44** would have a higher maximum absorption wavelength than compound **43**. This theory was also supported by Woodward-Fieser rules, which proposes that the addition of extra pi bonds to a conjugated system causes a correlated increase in absorption wavelength.

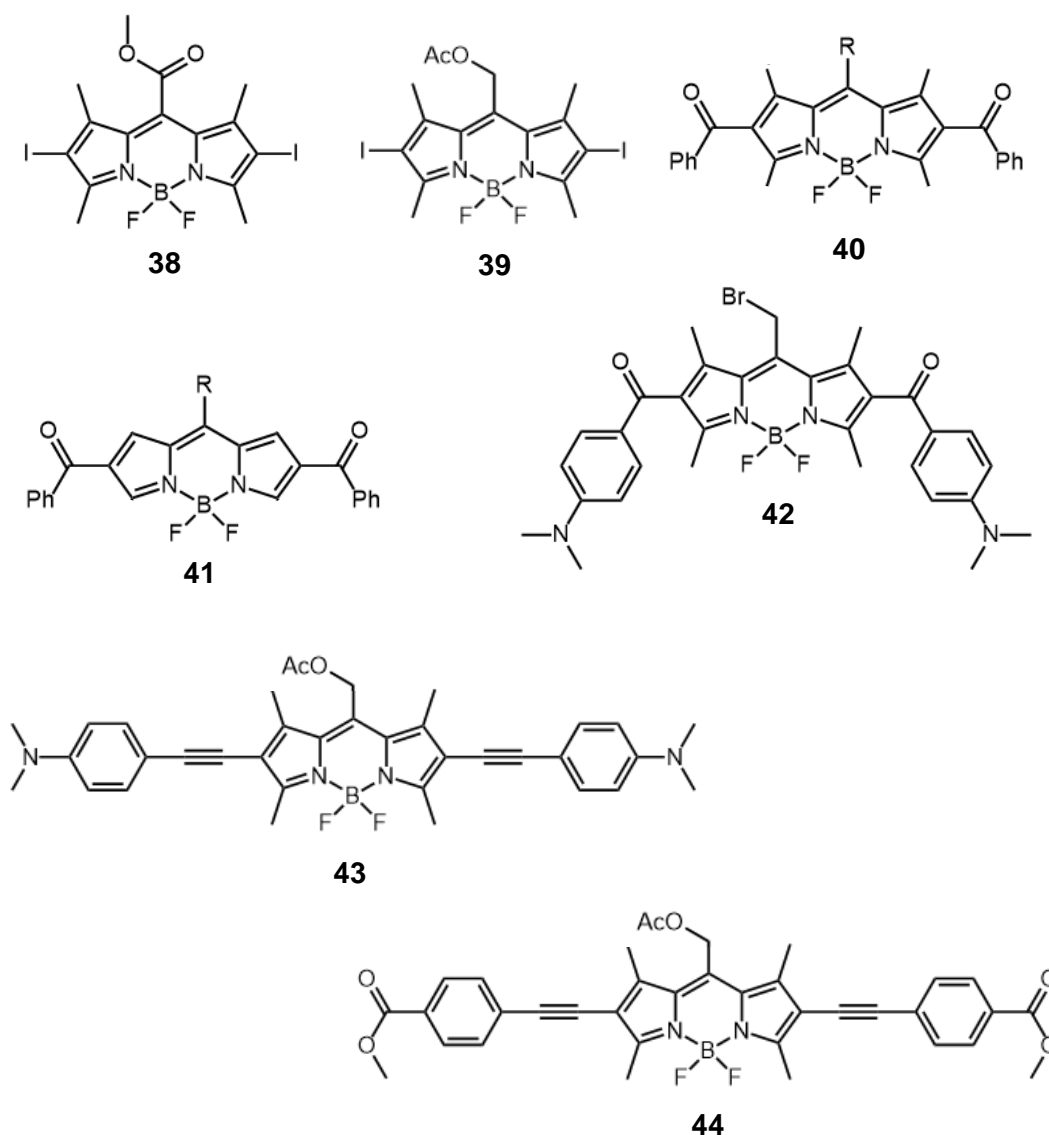


Figure 16: Planned synthetic targets with modifications at the 2 and 6 positions of the BODIPY core. R = CH₂Br, CH₂OAc or CH₂COEt

Many BODIPY analogues with near infra-red absorption maxima are large conjugated structures.¹⁰ Substitution at the 3 and 5 positions of BODIPY is reliably selective, due to the significant difference in proton acidity between the 3,5 and 1,7 positions (Figure 17).¹³⁶ Hence the theory behind substitution at the 3 and 5 positions of BODIPY was twofold. Primarily the aim was to mimic these more extensively conjugated structures to potentially stabilise a carboxylic acid moiety at the *meso* position. By doing this, another of the aims would be achieved. It was hypothesised that extending the system of conjugation would increase the maximum absorption wavelength for the compound. Further, the development of a compound with both hydrophilic and hydrophobic poles has the potential to mimic phospholipids. This combined with useful properties such as solvatochromism could provide a highly specific tool with multifunctionality. In lieu of this, Knoevenagel condensations were employed to introduce linkers bearing benzylic groups with the intention to also introduce bathochromic auxochromes. It was anticipated that this strategy had excellent potential to achieve multifunctional BODIPY fluorophores with *in vivo* potential.

Compounds **45** and **47** were expected to permit chemical conjugation to other molecules in the quest for fluorescent tags, due to the carboxylic acid and bromine *meso* substituents. Furthermore, the diethylamino auxochromes in compounds **47** and **48** were expected to introduce solvatochromism and environmentally dependent fluorescence emission.¹⁷⁷ Introducing a single modification on only the 3 position of BODIPY (compound **48**) could provide insight into the extent of which each additional “tail” changes the spectroscopic properties of BODIPY. This would complement the work carried out by Tao *et al.*, who explored the cumulative effects of styrene substituents at the 1,3,5 and 7 positions of BODIPY on the resultant spectroscopic properties of BODIPY.¹⁷⁸ Here, they discovered that further additions to the 1 and 7 positions (in addition to the 3 and 5 positions) of BODIPY did not further enhance the photophysical profile of BODIPY, with no significant further bathochromic shift in absorption maxima measured with increasing numbers of styrene substituents. As a result, no synthetic routes were undertaken to add further “tails” to the 1 and 7 positions of BODIPY; this was also because the resultant increase in lipophilicity would likely compromise bioavailability.

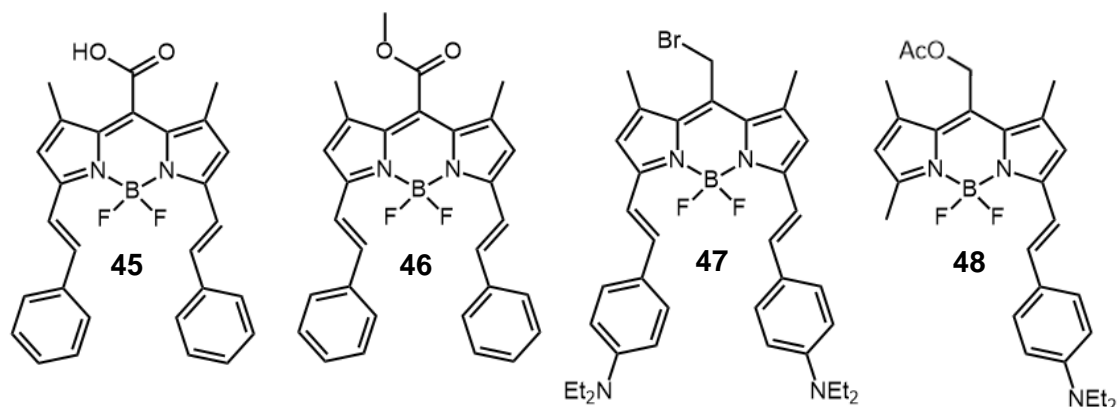


Figure 17: Planned synthetic targets with modifications at the 3 and 5 positions of the BODIPY core

Figure 18 presents the other BODIPY variations that were proposed during the design process. A series of fluorophores containing heavy metal platinum complexes were introduced. It has been documented that heavy metals can quench fluorescence emission, and this has been demonstrated in a fluorescent probe, COP-1, which had a palladium complex adjacent to the BODIPY core.¹⁵ The aim of compounds **49-52** was to build on this work and explore the effects of a heavy metal, platinum, in place of the boron of BODIPY, on the photophysical profile of the fluorophore.

The majority of molecules resembling BODIPY scaffolds are constructed from pyrrole rings. More recently there have been exceptions, making use of similar heterocycles such as isoindole.^{179,180} However, there are very few that have tried to use indole as a building block; there is a particular lack of work that uses indole in the BODIPY core. Although BODIPY fluorophores have been described containing indole heterocycles, these are normally separate to the core.^{181,182} In light of this, with the aim to expand the conjugated system of the BODIPY core and increase the potential maximum absorption wavelength, attempts were made to synthesise an indole-BODIPY fluorophore (compound **53**). It was anticipated to achieve increased absorption maxima without significantly compromising the feasibility of further reactions, such as the introduction of other substituents.

The use of BODIPY fluorophores as fluorescent tags is predominantly carried out using stable, reliable reactions such as the Sonogashira coupling to introduce fluorophores onto the nucleobase, normally at the 5 position.¹⁸³ To expand on this, efforts were made to use biological substrates such as nucleosides to prove the suitability of long wavelength BODIPY scaffolds for biological applications (Figure 18). The aim of compounds **54** and **55** was also to evaluate the effect of adjacent molecules on the spectroscopic profile. Nguyen *et al.* demonstrated that conjugation of chromophores to nucleosides did not significantly influence absorption or fluorescence profiles, and thus the same results were anticipated for BODIPY.¹⁸⁴

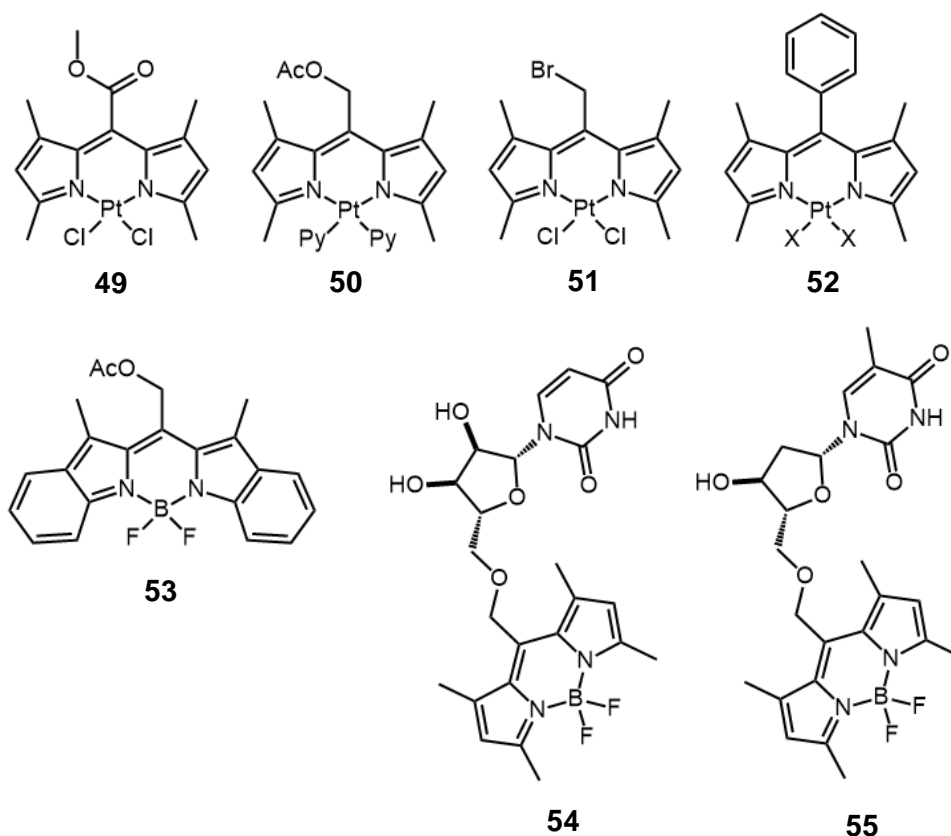


Figure 18: Planned synthetic targets with alternative structural modifications

The synthetic routes towards the successfully synthesised BODIPY analogue targets are described herein. All compounds were analysed using UV/Vis spectroscopy, followed by fluorescence spectroscopy with electronic absorption spectra measured

between 200-800 nm wavelengths. These were carried out in both polar and apolar media to monitor the effects of environmental polarity on photophysical profiles. It was anticipated that solvatochromism and environmentally dependent fluorescence emission would be observed for many compounds, particularly those with larger and more complex conjugated structures, and those containing auxochromes. The spectroscopic data for all successfully synthesised compounds are summarized in Table 5.

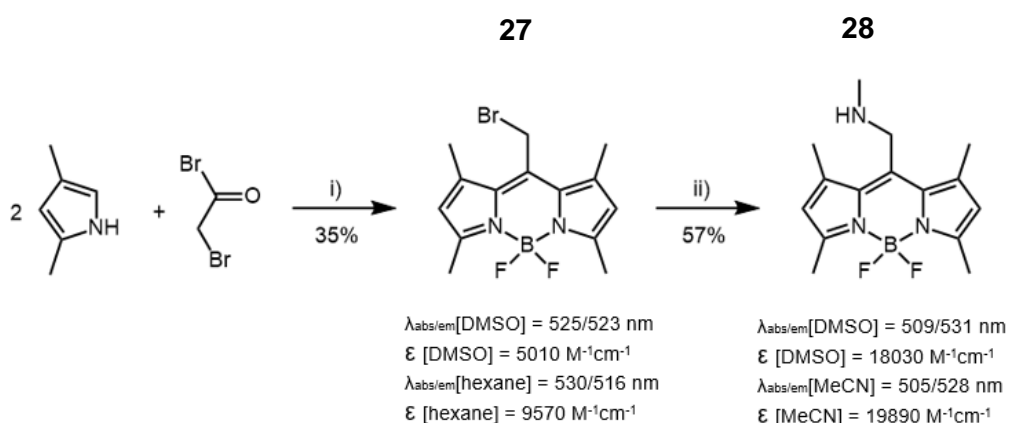
Understanding the highly specific design to function relationship of fluorophores is vital to the specificity of many applications, such as fluorophore sensing and bio-imaging. Molecules that absorb longer wavelengths of light are particularly important as they are highly compatible with *in vivo* studies – a desirable characteristic for cross disciplinary research. Often a balance must be struck between long absorption wavelength and molar absorptivity. Chromophores absorbing towards the near infra-red can also be prone to weak fluorescence emission. Hence, understanding photophysical trends resulting from small molecule design and modification can enable highly efficient and accurate SAR.

2.2 Meso – substitution of BODIPY analogues

The first series of compounds involved the synthesis of BODIPY analogues with a range of *meso* substituents. During preparation, all compounds were protected from the light to avoid unwanted photolytic decomposition.¹⁶⁵

The first of these synthesised, compound **27**, was derived using the one pot multi-step process described by Xie *et al.* in 2013 (Scheme 2).¹⁷¹ This route began with the construction of a substituted intermediate using bromoacetyl bromide and two equivalents of 2,4-dimethylpyrrole at room temperature under argon. Following the acylation of each pyrrole moiety selectively at the C2 positions, re-aromatisation of the core with a condensation reaction yielded the intermediate dipyrromethene *in situ*. TEA and $\text{BF}_3 \cdot \text{Et}_2\text{O}$ were added in excess, with the latter acting as the source of the coordinated boron difluoride. Subsequent coordination of the boron species with concomitant formation of HF afforded compound **27** in moderate yield.

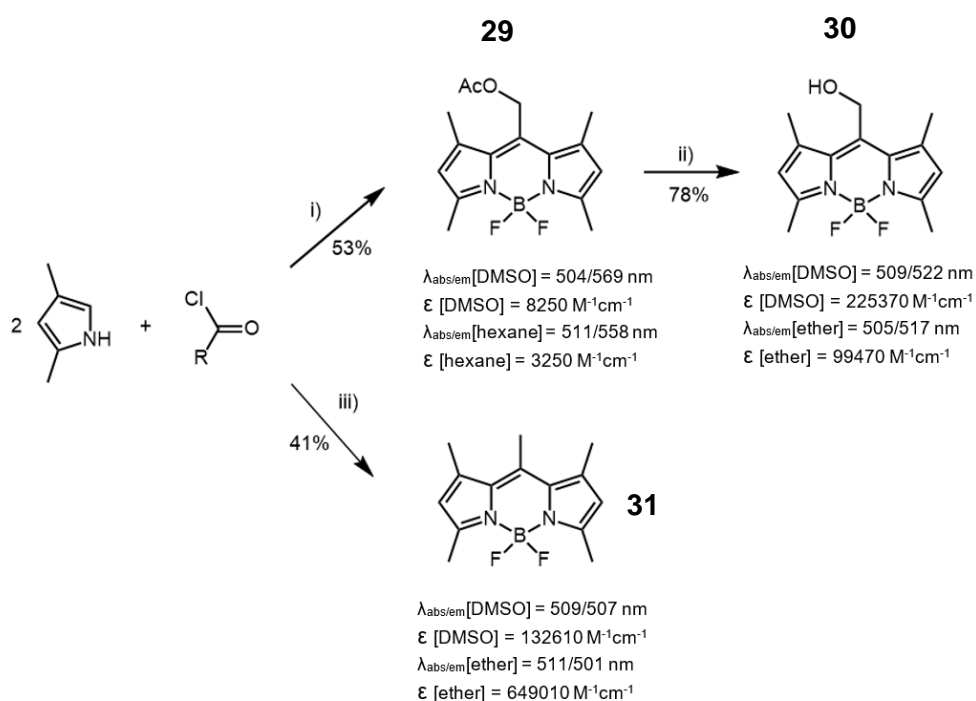
Compound **27** was subsequently used to generate compound **28**, using a Finkelstein assisted nucleophilic substitution to introduce an alternative *meso* substituent, methylamine.



Scheme 2: Synthetic routes towards compounds **27** and **28**^{171,172}: i) DCM 3h; TEA 15 min; $\text{BF}_3 \cdot \text{Et}_2\text{O}$ 3h; ii) MeNH_2 (3 eq. 2M in THF), KI, K_2CO_3 , THF, 16h

In addition to these, a similar synthesis was used to obtain compounds **29** and **31**, influenced by the work of Goswami *et al.*¹⁶⁵ Acetoxyacetyl chloride was reacted with two equivalents of 2,4-dimethylpyrrole, followed by basification and coordination to the boron difluoride moiety in a one pot synthesis.

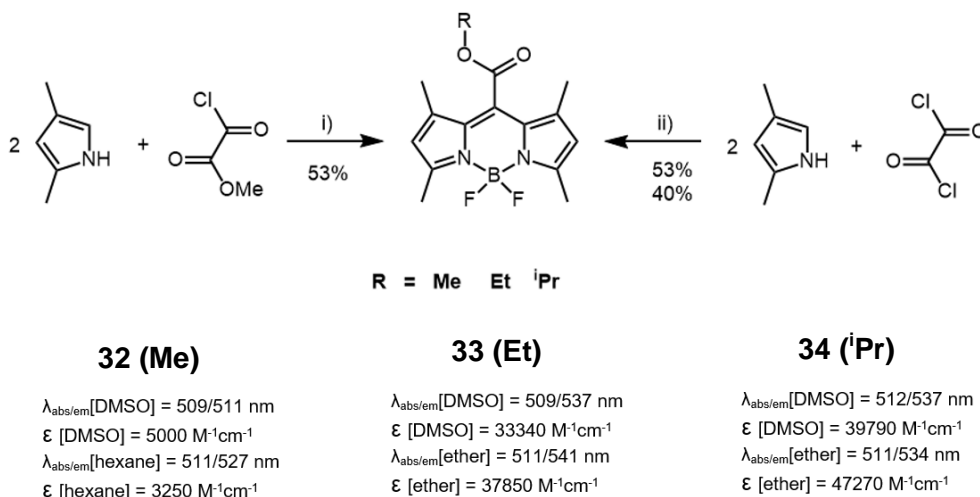
This was followed by removal of the acetyl group from compound **29** to afford compound **30**. Following this, the simplest of the BODIPY compounds was generated with only a single methyl group at the *meso* position, compound **31**, using analogous methodology (Scheme 3).



Scheme 3: Synthetic routes towards compounds **29**, **30** and **31**^{170,173}: i) DCM reflux 2h; DIPEA 15 min; $\text{BF}_3 \cdot \text{Et}_2\text{O}$ 30 min; $\text{R} = \text{CH}_2\text{OAc}$; ii) LiOH, THF/ H_2O (50:50), 4h; iii) DCM reflux 16h; TEA, $\text{BF}_3 \cdot \text{Et}_2\text{O}$ 4h; $\text{R} = \text{CH}_3$

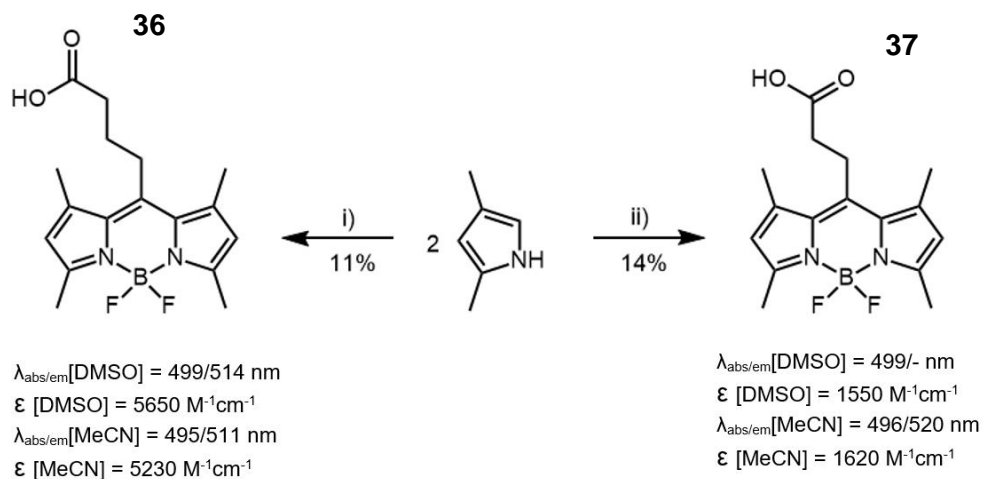
The next class of *meso* substituents reversed the ester group of compound **29** (Scheme 4) to move the carbonyl closer to the BODIPY core. The first of these, compound **32** was comprised of a methyl ester group and was built using the traditional one-pot substitution with methyl chlorooxoacetate. For compounds **33** and

34 however, an alternative method was used, employing oxalyl chloride as a starting material and treating the resultant acid chloride with the relevant alcohol. This was followed by basification with TEA and coordination to BF_2 using $\text{BF}_3 \cdot \text{Et}_2\text{O}$.



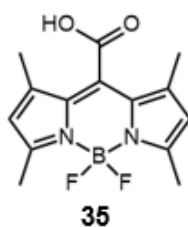
*Scheme 4: Synthetic routes towards compounds **32**, **33**, and **34**¹³⁶: i) DCM, -78°C , 4h; TEA, $\text{BF}_3 \cdot \text{Et}_2\text{O}$, 2h; ii) DCM, EtOH (**33**) or *i*PrOH (**34**), 1h; TEA, $\text{BF}_3 \cdot \text{Et}_2\text{O}$, 3h*

Alternative methods were employed to synthesised compound **36** and **37**, deviating slightly from the previously reliable acid halide starting material.¹⁸⁵ Instead, cyclic anhydrides were used for the electrophilic aromatic substitution onto 2,4-dimethylpyrrole, facilitated by $\text{BF}_3 \cdot \text{Et}_2\text{O}$ via the Lewis acid adduct. Two different analogues were made, differing in carbon chain length, using glutaric and succinic acid respectively. The resultant compounds, **36** and **37**, can be seen in Scheme 5.



*Scheme 5: Synthetic routes towards compounds **36** and **37**⁷⁴: i) succinic anhydride, DCM, $\text{BF}_3 \cdot \text{Et}_2\text{O}$, reflux; 5h, $\text{BF}_3 \cdot \text{Et}_2\text{O}$, TEA, 16h; ii) glutaric anhydride, DCM, $\text{BF}_3 \cdot \text{Et}_2\text{O}$, reflux; 5h, $\text{BF}_3 \cdot \text{Et}_2\text{O}$, TEA, 16h*

Unfortunately, efforts to synthesise compound **35** were unsuccessful; the reaction conditions and outcomes are briefly summarized in Table 1.



Compound	Reaction conditions	Outcome
35	Compounds 32-34 , Lil, EtOAc, reflux	Decomposition (TLC)
35	Compounds 32-34 , conc. HCl	Decomposition (TLC)

*Table 1: Reaction conditions for compound **35** that was not successfully synthesised*

The range of pre-designed analogues that were successfully synthesised for this series was broad enough to provide insight into the SAR arising from modification at the *meso* position. In addition, the functional groups installed have potential applications in a range of areas from conjugation to biomolecules, to dye sensitized solar cells. The resultant absorption and fluorescence spectra are presented in

Figures 19 and 20 and discussed relative to all successfully synthesised compounds in Section 2.5.

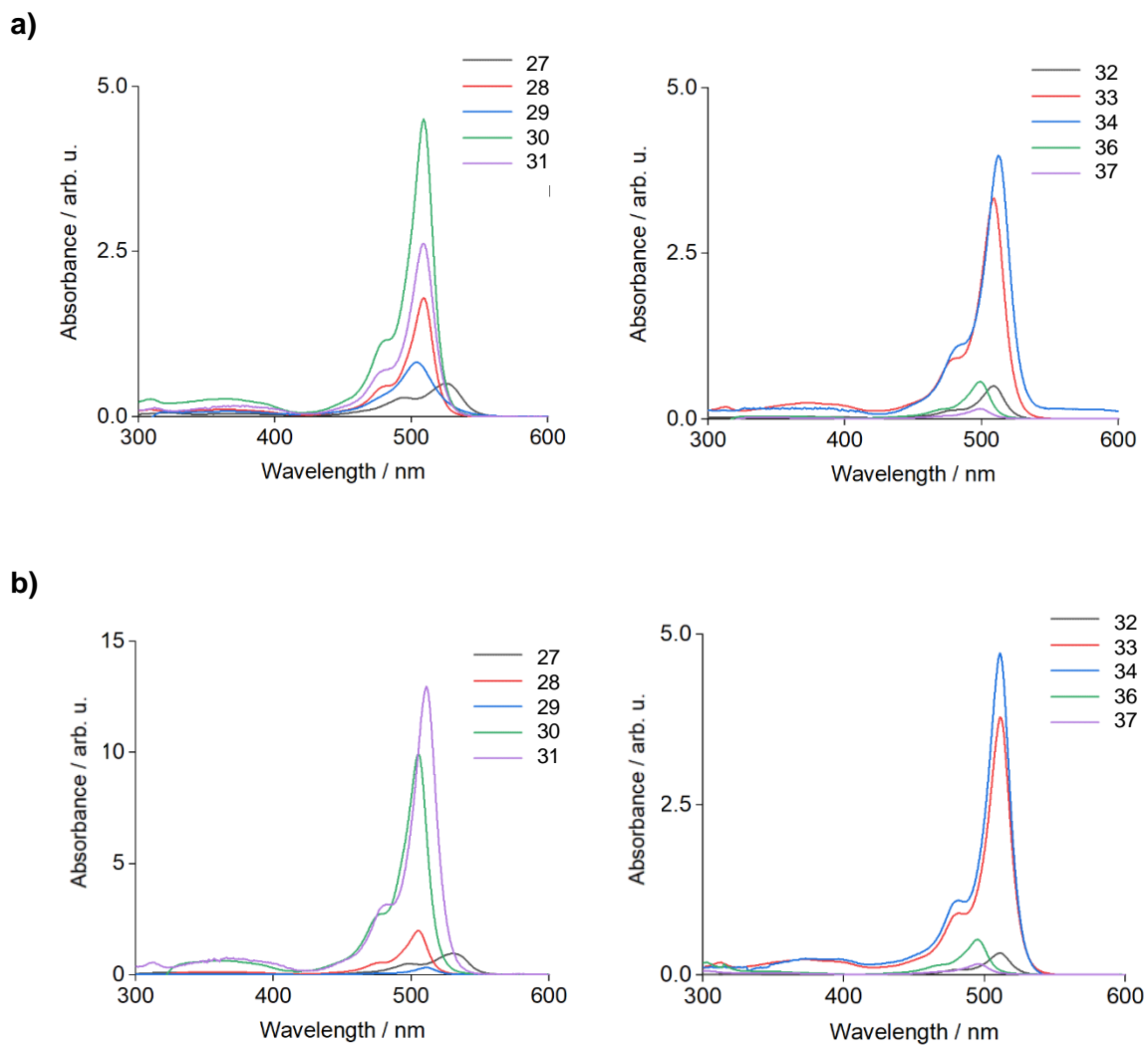


Figure 19: UV/Vis spectra of compounds **27-37**: a) polar solvent; b) apolar solvent. All data normalised to 100 μM for ease of comparison with exception of compounds **30** (polar, 5 μM) and **31** (polar, 5 μM and apolar, 20 μM)

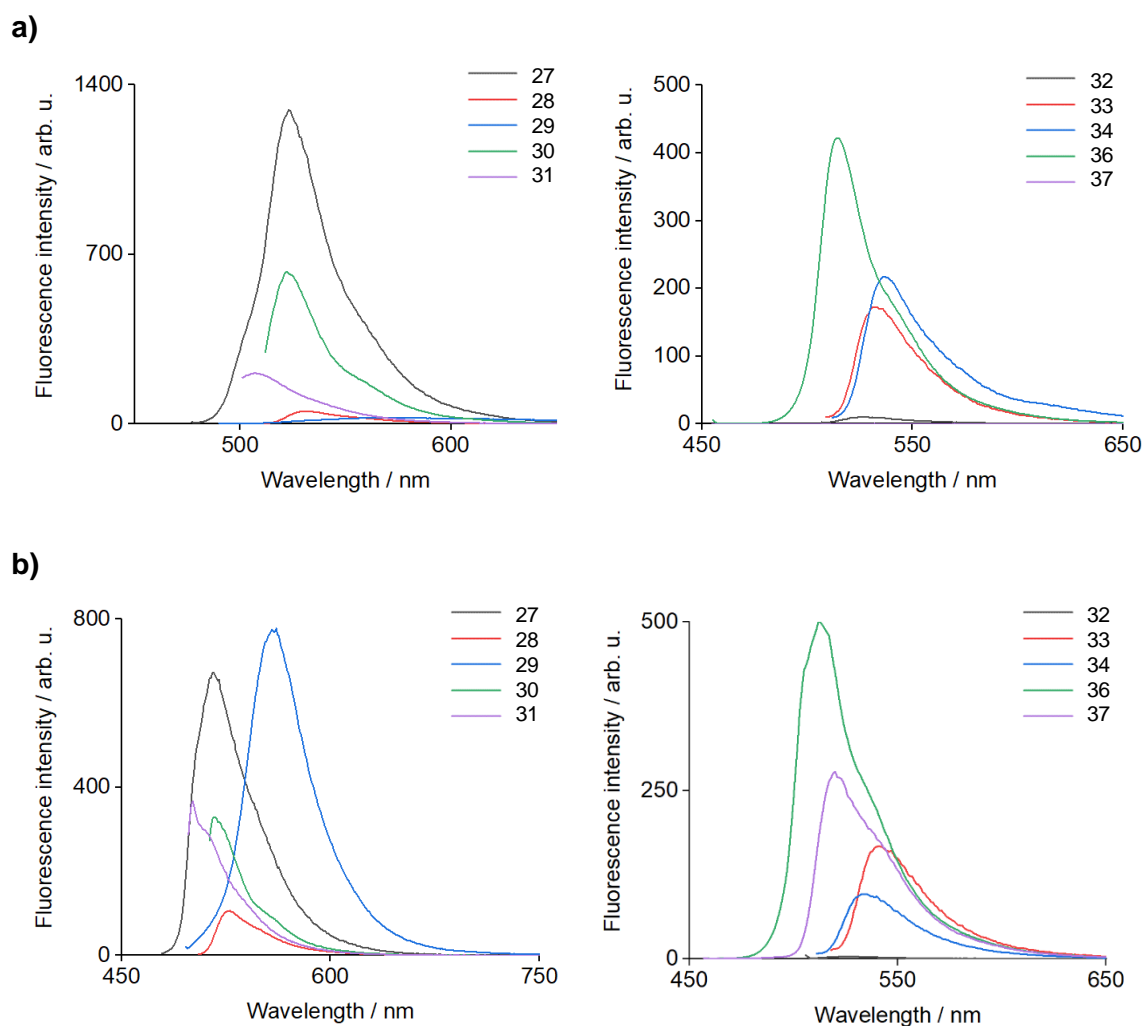
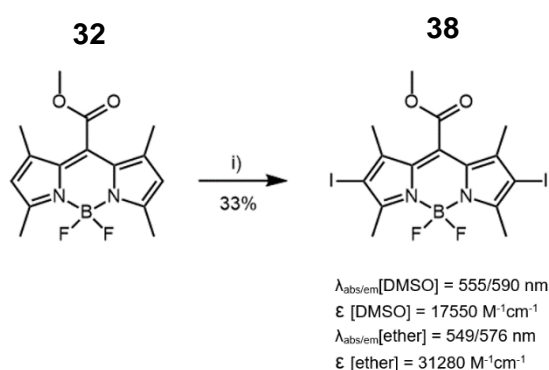


Figure 20: Fluorescence emission spectra of compounds **27-37**: a) polar solvent; b) apolar solvent. All data normalised to 100 μM for ease of comparison with exception of compound compound **27** (polar and apolar, 50 μM), compound **30** (polar, 0.2 μM and apolar, 2 μM) and compound **5** (polar, 0.5 μM and apolar, 0.1 μM)

2.3 Substitution at the 2,6 - position of BODIPY

With the *meso* position explored, attention was turned to decoration of the BODIPY scaffold at the 2 and 6 positions. Compound **32** was selected for the first reaction as this was anticipated to be the most stable, and no photolytic decay was expected from the methyl ester *meso* group. The iodine substituent was introduced using *N*-iodosuccinimide in THF at -78°C, which was allowed to reach room temperature overnight. This achieved compound **38** in moderate yield (Scheme 6).

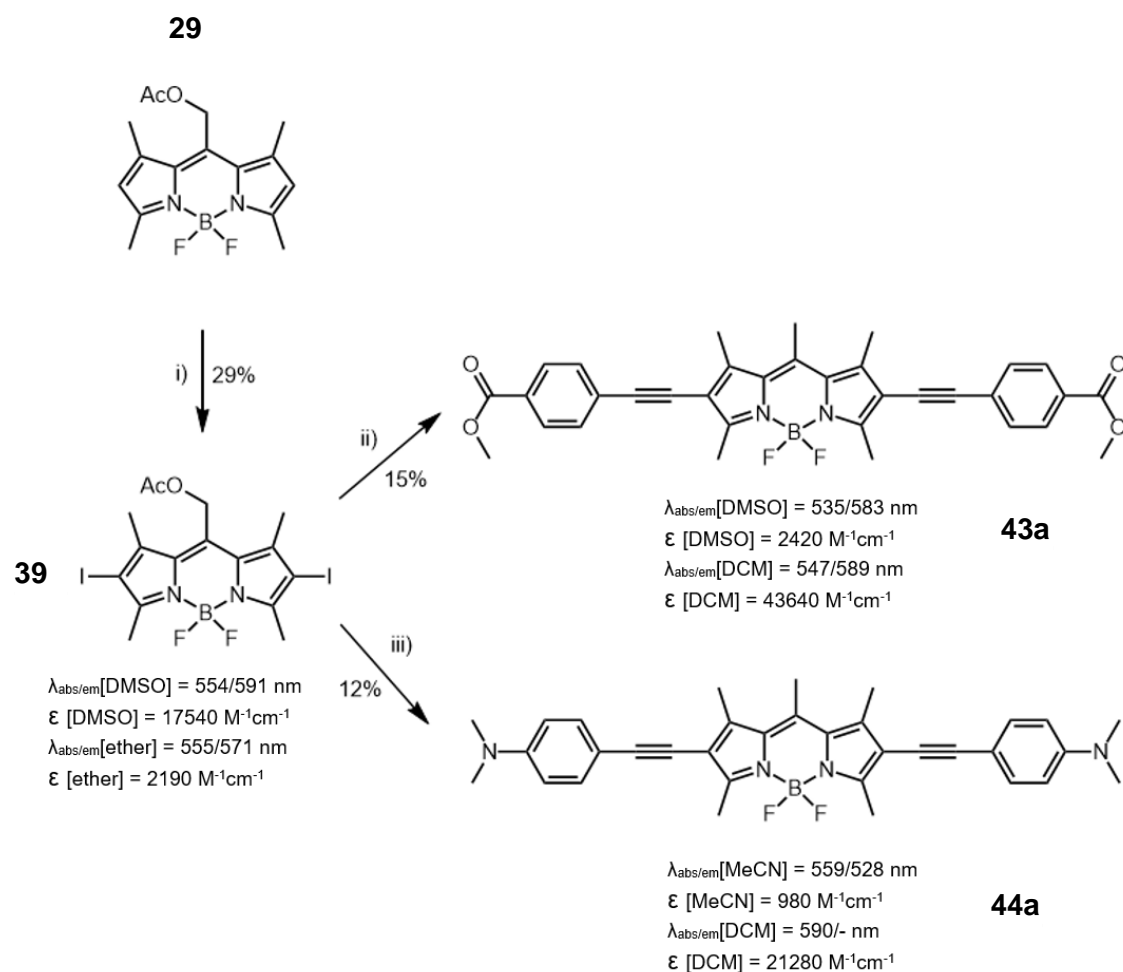


Scheme 6: Synthesis of compound **38**¹⁶⁵: i) NIS, THF, -78°C → RT, 16h

Next, compound **29** was treated using the same iodinating procedure to afford compound **39** (Scheme 7). During this reaction the acetyl group remained intact, with care taken to avoid excess exposure to the light and prevent photolytic decay.

Two further compounds with modifications at positions 2 and 6 of the BODIPY scaffold were achieved. These were obtained using Sonogashira couplings with methyl 4-ethynyl benzoate and 4-ethynyl-*N,N*-dimethylaniline to afford compounds **43a** and **44a** respectively, as opposed to compounds **43** and **44** (Scheme 7). The couplings were carried out using catalytic Pd(PPh₃)₄, facilitated by CuI in the presence of TEA overnight. Although the yields were relatively low, sufficient compound was achieved for photophysical analysis in both cases. Both compounds were purple in

colour, supporting the measured maximum absorption wavelength which was higher than those of the previous compounds, most of which were red or orange.



*Scheme 7: Synthetic routes towards compounds **39**, **43a** and **44a**¹⁶⁵: i) NIS, THF, -78°C → RT, 16h; ii) methyl 4-ethynyl benzoate, Pd(Ph₃)₄, Cul, TEA, toluene, 15h; iii) 4-ethynyl-N,N-dimethylaniline, Pd(Ph₃)₄, Cul, TEA, toluene, 15h*

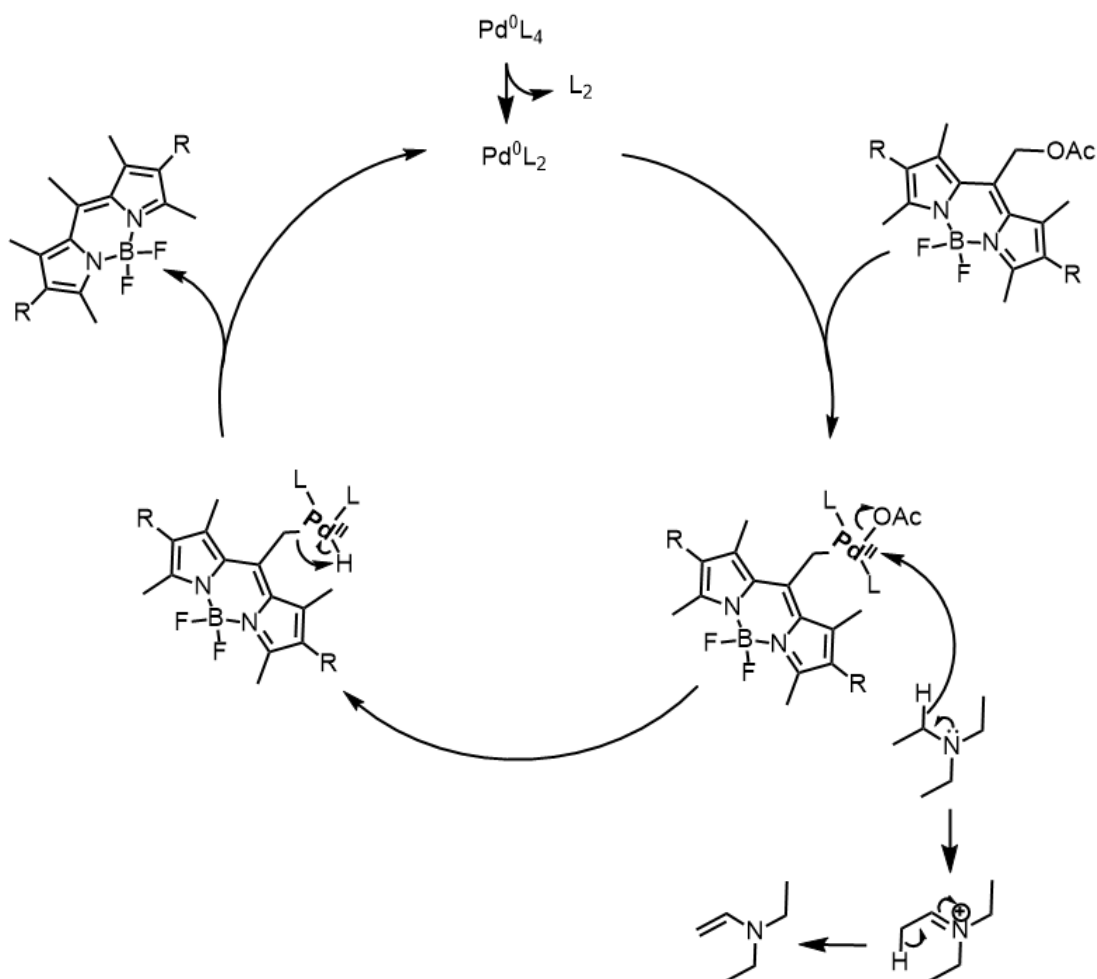
As expected, molecular symmetry resulted in the substitution of two aromatic groups, one at the 2 position and the other the 6 position of BODIPY. In the case of compound **43a**, methyl ester groups were positioned on the phenyl rings, which were expected to significantly influence the spectroscopic properties of the molecule. With compound **44a** however, bathochromic auxochromes were situated on the phenyl rings: NMe₂.

Of particular note during these reactions was the loss of the acetoxymethyl group from the *meso* position, and thus compounds **43a** and **44a** were synthesised rather than

compounds **43** and **44**. This took place completely each time the reaction was carried out. It was not assumed that this was a result of photo-uncaging upon undesired exposure to light. If this were the case, a hydroxyl group would most likely have been present or, if exposed to MeOH as in the work of Goswami *et al.*, an ether substituent.¹⁶⁵ An alternative mechanism is proposed in Scheme 8.

The mechanism begins with ligand dissociation to facilitate oxidative insertion of Pd adjacent to the acetoxy group of compound **39**. This is followed by displacement of the acetoxy moiety with a hydrogen atom, most likely sourced from the alpha position of the abundant TEA. Finally, reductive elimination liberates the free BODIPY with installed methyl group at the *meso* position.

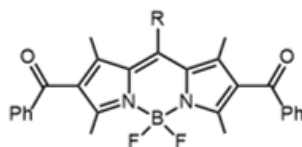
For proof of concept of this mechanism, this reaction could be carried out in deuterated TEA, with concomitant NMR analysis revealing the origin of the hydrogen atom.



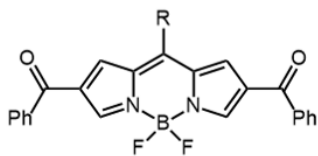
Scheme 8: Proposed mechanism for the reduction of the meso substituent during the synthesis of compounds **43a** and **44a**

Despite the unintentional modification to the *meso* position, the achieved compounds **43a** and **44a** were still extremely useful in exploring the effects of substituents on the photophysical properties of BODIPY. Instead, good comparisons can be made with control compound **31**.

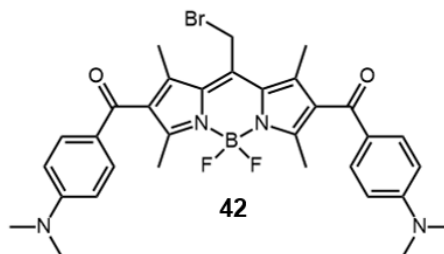
Efforts to synthesise compounds **40-42** were unfortunately unsuccessful; therefore, it was not possible to explore the fluorescence quenching potential of carbonyl groups in close proximity to the BODIPY skeleton. The reaction conditions attempted are briefly summarized in Table 2 (overleaf).



40



41



42

Compound	Reaction conditions	Outcome
40 (R = CH ₃ Br)	Compound 27 , benzoyl chloride, DBN (15 mol%), toluene, reflux	Starting material (TLC)
40 (R = CH ₃ Br)	Compound 27 , benzoyl chloride, pyridine (15 mol%), toluene, reflux	Starting material (TLC)
40 (R = CH ₃ Br)	Compound 27 , benzoyl chloride, DABCO (15 mol%), toluene, reflux	Starting material (TLC)
40 (R = CH ₃ Br)	Compound 27 , benzoyl chloride, BF ₃ ·Et ₂ O, DCM, 0°C	Starting material (TLC)
40 (R = CH ₃ Br)	Compound 27 , BuLi, -78°C, 15 min; benzoyl chloride	Decomposition (TLC)
40 (R = COOEt)	Compound 33 , benzoyl chloride, DBN (15 mol%), toluene, reflux	Starting material (TLC)
40 (R = CH ₂ OAc)	Compound 29 , benzoyl chloride, DBN (15 mol%), toluene, reflux	Starting material (TLC)
40 (R = CH ₂ OAc)	Compound 29 , benzoyl chloride, pyridine (15 mol%), toluene, reflux	Starting material (TLC)
40 (R = CH ₂ OAc)	Compound 29 , benzoyl chloride, DABCO (15 mol%), toluene, reflux	Starting material (TLC)
40 (R = CH ₂ OAc)	Compound 29 , benzoyl chloride, DMAP (15 mol%), toluene, reflux	Starting material (TLC)
40 (R = CH ₃ Br)	Compound 27 , benzoyl chloride, In(OTf) ₃ (1 mol%), MeCN, 50°C	Starting material (TLC)
40 (R = CH ₃ Br)	Compound 27 , benzoyl chloride, In(OTf) ₃ (1 mol%), AgClO ₄ (3 mol%), MeCN, 50°C	Starting material (TLC)
40 (R = CH ₃ Br)	Compound 27 , In(OTf) ₃ (1 mol%), MeCN, 50°C	Starting material (TLC)
40 (R = CH ₃ Br)	Compound 27 , In(OTf) ₃ (1 mol%), AgClO ₄ (3 mol%), MeCN, 50°C	Starting material (TLC)
40 (R = CH ₃ Br)	Compound 27 , In(OTf) ₃ (1 mol%), LiClO ₄ (4 mol%), MeCN, 50°C	Starting material (TLC)
40 (R = CH ₃ Br)	Compound 27 , In(OTf) ₃ (1 mol%), AgSbF ₆ (3 mol%), MeCN, 50°C	Starting material (TLC)
40 (R = CH ₃ Br)	Compound 27 , InCl ₃ (1 mol%), MeCN, 50°C	Starting material (TLC)

Compound	Reaction conditions	Outcome
40 (R = CH ₃ Br)	Compound 27 , InCl ₃ (1 mol%), AgClO ₄ (3 mol%), MeCN, 50°C	Starting material (TLC)
40 (R = CH ₃ Br)	Compound 27 , InCl ₃ (1 mol%), LiClO ₄ (4 mol%), MeCN, 50°C	Starting material (TLC)
40 (R = CH ₃ Br)	Compound 27 , InCl ₃ (1 mol%), AgSbF ₆ (3 mol%), MeCN, 50°C	Starting material (TLC)
40 (R = CH ₃ Br)	Compound 27 , In(OTf) ₃ (1 mol%), LiClO ₄ (4 mol%), MeNO ₂ , 50°C	Starting material (TLC)
41 (R = H)	Oxalyl chloride, 3-benzoylpyrrole, DCM, EtOH, 1h; TEA, BF ₃ ·Et ₂ O	Decomposition (TLC)
42 (R = CH ₃ Br)	Compound 27 , 4-dimethylaminobenzyl chloride, DACBO (15 mol%), toluene, reflux	Starting material (TLC)
42 (R = CH ₃ Br)	Compound 27 , 4-dimethylaminobenzyl chloride, DBN (15 mol%), toluene, reflux	Starting material (TLC)
42 (R = CH ₃ Br)	Compound 27 , BuLi, -78°C, 15 min; 4-dimethylaminobenzyl chloride	Decomposition (TLC)

*Table 2: Reaction conditions for compounds **40**, **41** and **42** that were not successfully synthesised*

Unfortunately, it was not possible to synthesise and isolate any further analogues of BODIPY with modifications at the 2 and 6 positions. There are of course a number of other different approaches that could have been used to introduce different substituents at these positions, such as metal catalysed couplings or a variety of nucleophilic or electrophilic substitutions, to name a few. The full breadth for substitution at the 2 and 6 positions of BODIPY was therefore not explored. The compounds successfully constructed would however still provide a useful insight into the effects of modifying the BODIPY core at the 2 and 6 positions. The absorption and fluorescence spectra are summarized in Figure 21 and discussed relative to all successfully synthesised compounds in Section 2.5.

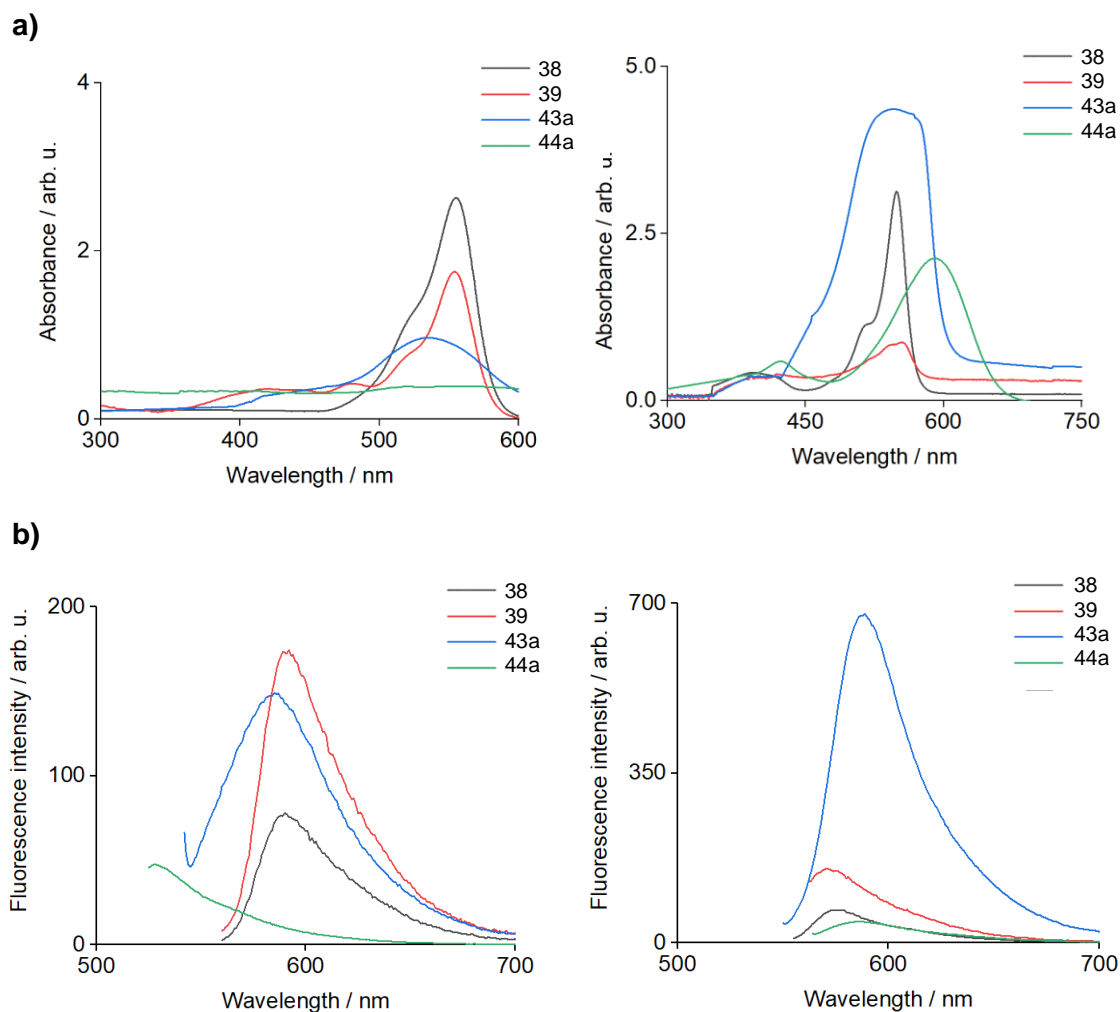
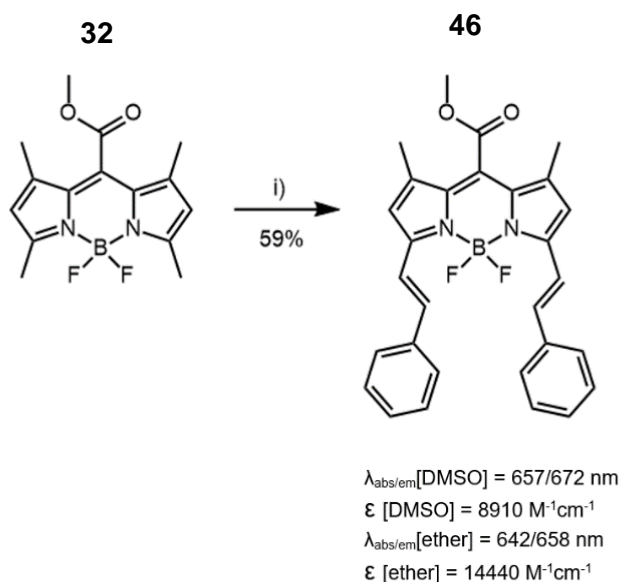


Figure 21: a) UV/Vis spectra of compounds **38-44a** in polar (left) and apolar (right) solvent. Data normalised to 100 μM with exception of compounds **39** (apolar, 400 μM), **43a** (polar, 400 μM) and **44a** (polar, 400 μM); b) fluorescence emission spectra of compounds **38-44a** in polar (left) and apolar (right) solvent. Data normalised to 100 μM with exception of compounds **43a** (apolar, 25 μM) and **44a** (200 μM)

2.4 Substitution at the 3,5 - position of BODIPY

The next series of compounds was focused on the 3 and 5 positions of the BODIPY core. It has been noted that these are relatively reliable for selective modification due to the significant proton acidity difference between positions 3 and 5, and positions 1 and 7.¹³⁶ This series promised long absorption wavelengths and the potential for phospholipid imitation, a useful characteristic for bio-imaging applications.

Compound **32** was selected as the starting material for this test reaction, partly because it was expected to be the most stable to the reaction conditions, but also because it offered the potential of a carboxylic acid *meso* substituent. The synthetic route consisted of a Knoevenagel condensation with 2.2 equivalents of benzaldehyde to maximise the chances of substitution of both methyl groups at the 3 and 5 positions. This reaction was facilitated by piperidine in the presence of acetic acid under reflux to achieve compound **46**. The synthetic route for these can be seen in Scheme 9. The synthesis of compound **46** sought to extend the size of the conjugated system for BODIPY, and hence increase the wavelength of absorption.

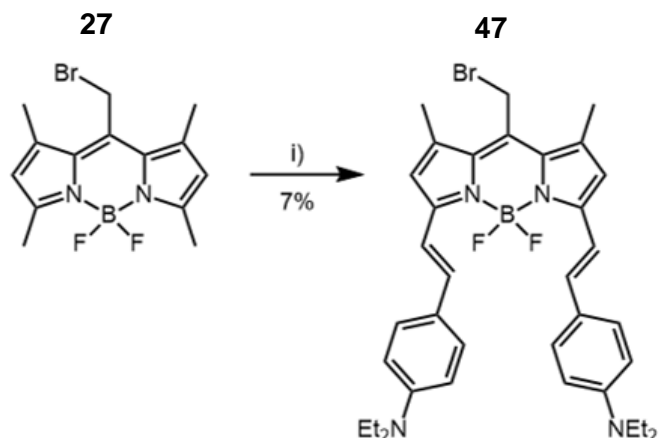


Scheme 9: Synthesis of compound 46: i) benzaldehyde (2.2 eq.), AcOH, piperidine, toluene, reflux, 16h; ii) LiI, EtOAc, reflux, 16h

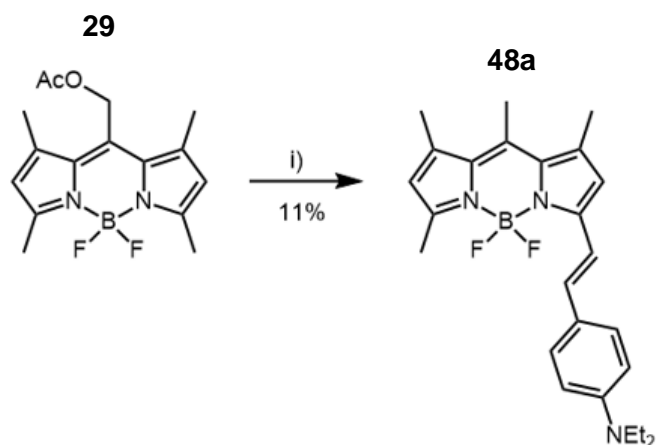
Most notable about compound **46** was that in contrast to many of the previous BODIPYs synthesised, most of which had been red, pink or purple, this compound was bright blue. This was of course promising given that this indicated optical activity at much longer wavelengths of light, towards the near infra-red.

Again, the Knoevenagel condensation reaction was used, this time reacting compound **27** with diethylaminobenzaldehyde. This successfully achieved compound **47**, once again yielding a promising blue coloured compound. As with compound **46**, both the 3 and 5 positions were successfully substituted.

Next, compound **29** was treated under the same reaction conditions of refluxing with 2.2 equivalents of diethylaminobenzaldehyde in the presence of piperidine (Scheme 10). Unfortunately, the acetoxy group proved unstable under these conditions, in a similar manner to that of compounds **43a** and **44a**. Therefore, the methyl group was instead present at the *meso* position, compound **48a**.



$\lambda_{\text{abs/em}}[\text{DMSO}] = 734/768 \text{ nm}$
 $\epsilon [\text{DMSO}] = 16130 \text{ M}^{-1}\text{cm}^{-1}$
 $\lambda_{\text{abs/em}}[\text{ether}] = 699/738 \text{ nm}$
 $\epsilon [\text{ether}] = 17880 \text{ M}^{-1}\text{cm}^{-1}$



$\lambda_{\text{abs/em}}[\text{DMSO}] = 704/738 \text{ nm}$
 $\epsilon [\text{DMSO}] = 14980 \text{ M}^{-1}\text{cm}^{-1}$
 $\lambda_{\text{abs/em}}[\text{ether}] = 679/696 \text{ nm}$
 $\epsilon [\text{ether}] = 3740 \text{ M}^{-1}\text{cm}^{-1}$

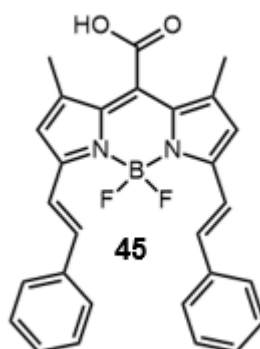
*Scheme 10: Synthetic routes towards compounds **47** and **48a**: i) diethylaminobenzaldehyde (2.2 eq.), AcOH, piperidine, toluene, reflux, 16h; ii) diethylaminobenzaldehyde (1.1 eq.), AcOH, piperidine, toluene, reflux, 16h*

For the reaction that occurs to generate compound **48a**, a palladium/Cu(I) reaction cannot be used to explain this effect. The simplest explanation for this is photolytic decomposition. Heterolytic photolysis of the carbon-oxygen bond leaves a cationic carbon, which was suggested by Goswami *et al.*¹⁶⁵ They proposed that in the presence of an alcohol such as methanol, a hydroxyl group would be substituted onto

the carbocation.¹⁶⁵ It is possible that this reaction took place as a result of undesired exposure to light, with the photolability of the acetoxo group increased by the modification of the BODIPY core. This would however require the presence of a hydride species. Alternatively, were it to be proposed that bond fission is homolytic rather than forming a tight ion pair, hydrogen abstraction from a source such as the toluene solvent could be used to explain this side reaction. Confirmation of the hydrogen atom source could be established using deuterated solvents and/or reagents alternately.

The introduction of the first diethylvinylaniline moiety contributes to the increasing electron density throughout the structure, weakening the reactivity of the other proton further. Furthermore, the loss of the acetyl group, replaced by the methyl, does not improve the acidity of the proton given its electron donating ability, which is similar to that of the acetoxo.

Unfortunately, it was not possible to synthesise compound **45**. This is most likely due to the instability of the carboxylic acid at the *meso* position, which was also observed in compound **35**. The reaction conditions are summarized in Table 3.



Compound	Reaction conditions	Outcome
45	Compound 46 , LiI, EtOAc, reflux	Decomposition (TLC)

*Table 3: Reaction conditions for compound **45** that was not successfully synthesised*

Overall three compounds with substitutions at the 3 and 5 positions were generated. Of particular use is the fact that not all contained auxochromes, allowing a clearer idea of the extent of the effect these groups have on the photophysical and biophysical properties of BODIPY. The construction of compound **48a** could be particularly useful for analysing the effects of a smaller extension to the conjugated system with only a single auxochrome and conjugated “tail”. With respect to long absorption wavelengths, these initially appeared the most promising, based on their colour. The configuration of this series of compounds also lends itself to a phospholipid mimic, in particular compounds **47** and **48a** with their diethylamino groups.

The absorption and fluorescence spectra are summarized in Figure 22 and discussed relative to all successfully synthesised compounds in Section 2.5.

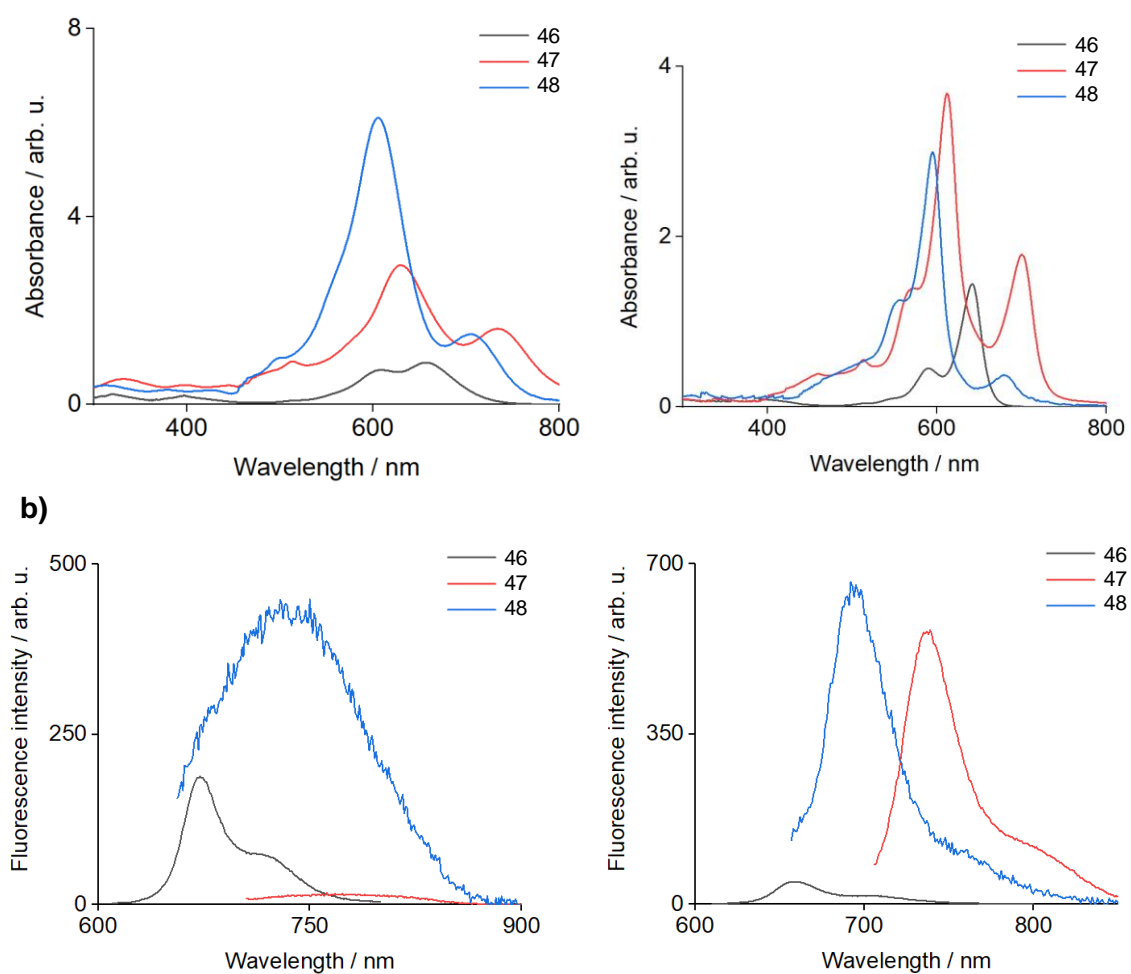
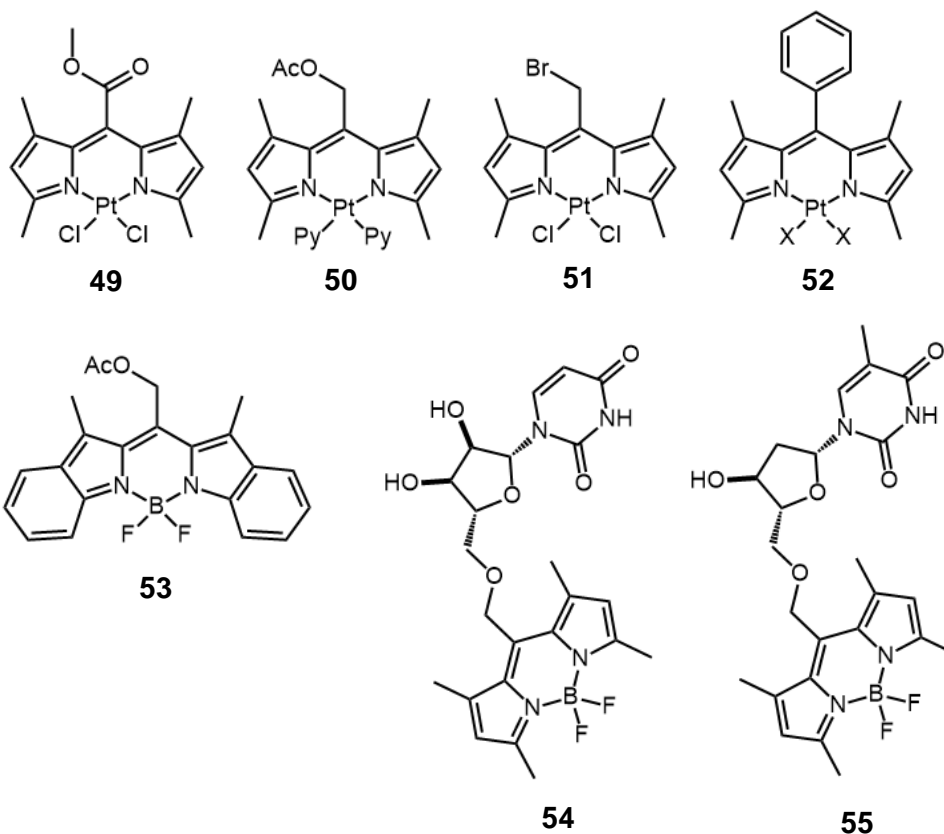


Figure 22: a) UV/Vis spectra of compounds **46-48a** in polar (left) and apolar (right) solvent; b) fluorescence emission spectra of compounds **46-48a** in polar (left) and apolar (right) solvent. All data normalised to 100 μ M.

Synthetic efforts towards compounds **49-55** were unfortunately unsuccessful. The reaction conditions used for each attempt to synthesize these compounds are summarized in Table 4.



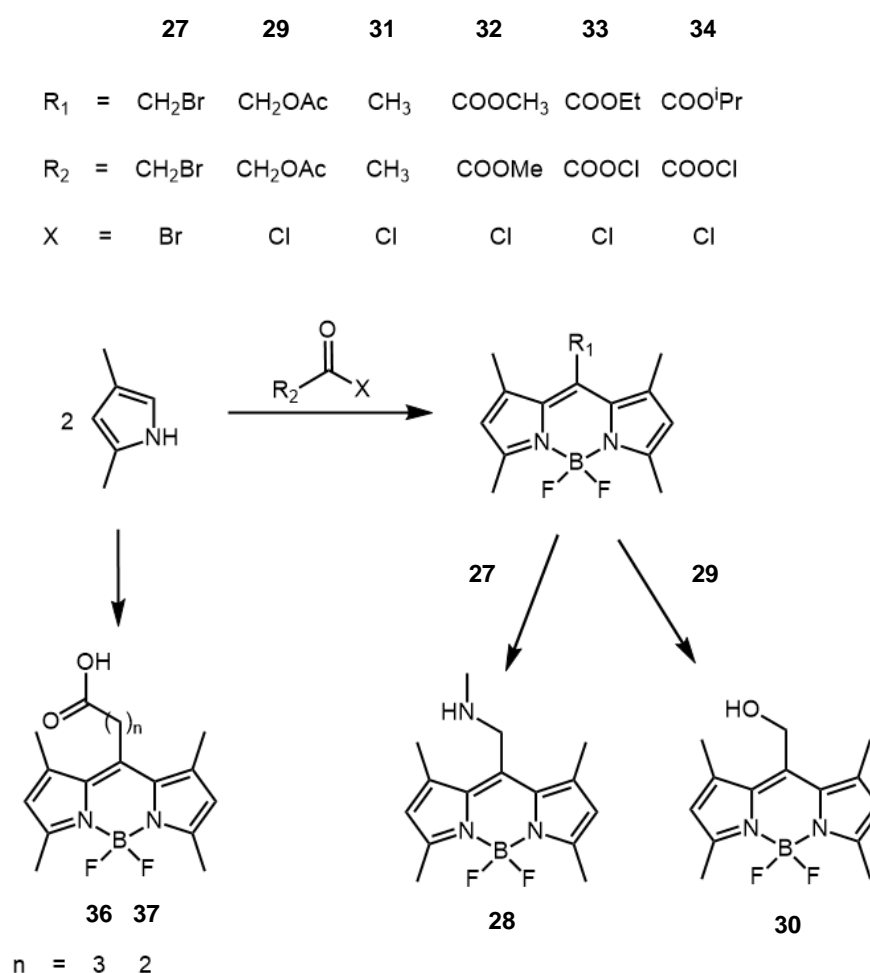
Compound	Reaction conditions	Outcome
49	2,4-dimethylpyrrole, methyl chlorooxoacetate, DCM, -78°C, 4h; TEA, 15min; PtCl ₂	Decomposition (TLC)
49	2,4-dimethylpyrrole, methyl chlorooxoacetate, DCM, -78°C, 4h; TEA, 15min; K ₂ PtCl ₄	Decomposition (TLC)
50	2,4-dimethylpyrrole, acetoxyacetyl chloride, DCM, reflux	Decomposition (TLC)
51	2,4-dimethylpyrrole, bromoacetyl bromide, DCM, reflux, 3h; DIPEA, 15min; PtCl ₂ (Py) ₂	Decomposition (TLC)
52	1) 2,4-dimethylpyrrole, HCl (0.18 M), benzaldehyde, H ₂ O; 2) PtX _x	First reaction failed (decomposition, TLC)
53	3-methylindole, acetoxyacetyl chloride, DCM, 3h; TEA, 30min; BF ₃ ·Et ₂ O	Starting material (TLC)
54	Compound 27 , uridine, Cs ₂ CO ₃ , MeCN, DCM	Starting material (TLC)
54/55	1) Compound 30 , BPFPC, DIPEA/TEA, THF; 2) uridine or 2'-deoxythymidine	Starting material (TLC)

Compound	Reaction conditions	Outcome
54/55	1) Compound 30 , CDI, DIPEA/TEA, THF; 2) uridine or 2'-deoxythymidine	Starting material (TLC)
55	Compound 27 , 2'-deoxythymidine, Cs ₂ CO ₃ , MeCN, DCM	Starting material (TLC)
55	Compound 27 , 2'-deoxythymidine, NaI, Cs ₂ CO ₃ , MeCN, DCM	Starting material (TLC)
55	Compound 27 , 2'-deoxythymidine, NaH, DMF	Starting material (TLC)
55	Compound 27 , 2'-deoxythymidine, NaH, ultra-sonication, THF	Starting material (TLC)

*Table 4: Reaction conditions for compounds **49-55** that were not successfully synthesised*

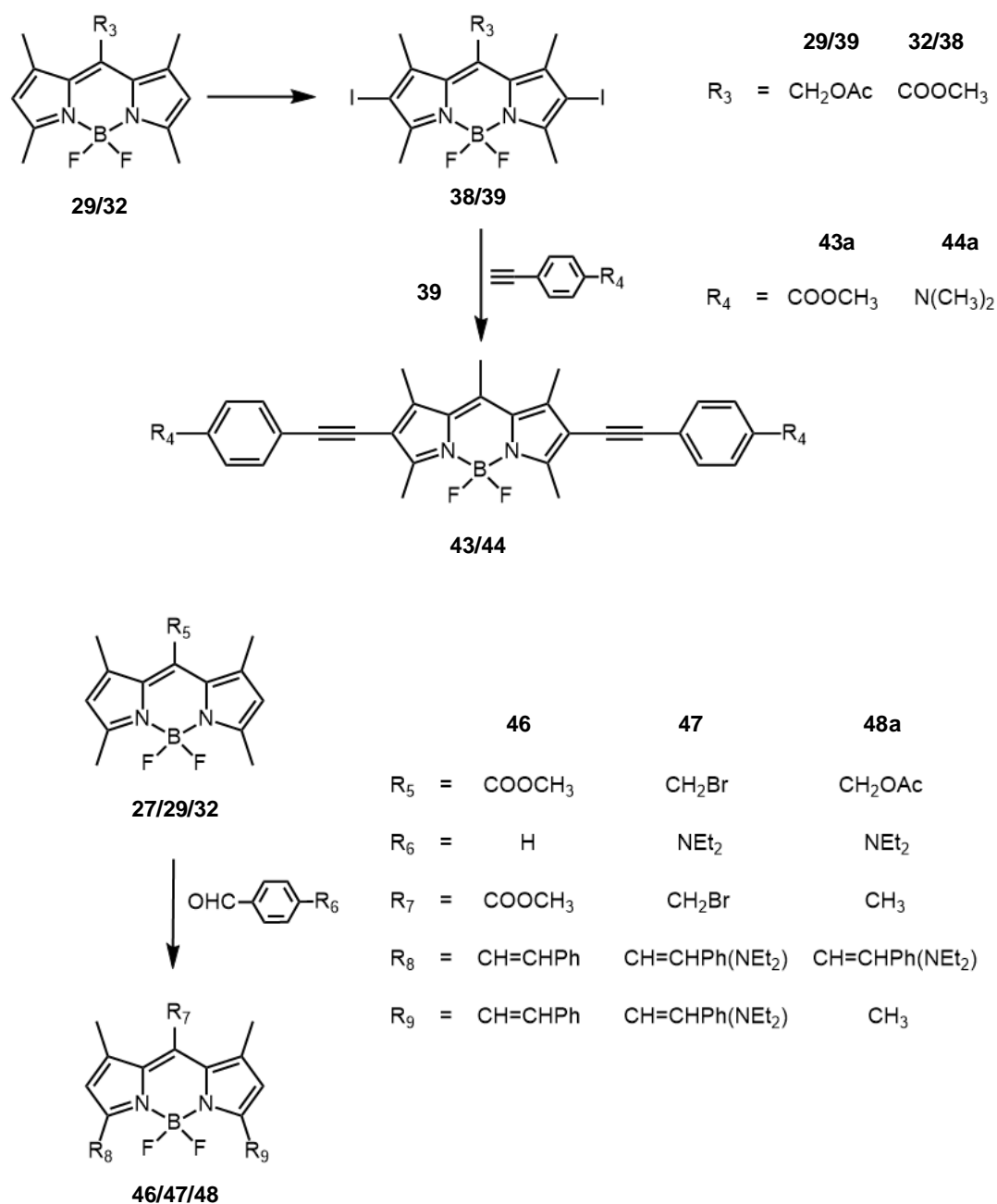
2.5 Summary and discussion

In summary, 17 analogues were successfully synthesised in the efforts to establish trends between substituents and loci on the photophysical properties of BODIPY. With respect to the *meso* position of BODIPY, these ranged from alcohols and esters to amines, halogens and carboxylic acids. Although unlikely to contribute to large increases in absorption wavelength, the varying polarities and steric bulks of these substituents will enable insight into fine-tuning of photophysical properties. The reactive nature of some moieties, such as compounds **27**, **30**, **36** and **37** could allow the combination of these tools to larger structures, for example a protein.



Scheme 11: Summary of BODIPY analogues achieved with varied *meso* substituents

Although fewer compounds were generated with modifications at the 2, 3, 5 and 6 positions, the achieved designs had desirable photophysical profiles.



Scheme 12: Summary of BODIPY analogues achieved with varied substitution and the 2, 3, 5 and 6 positions of the BODIPY core

Compounds **43a**, **44a**, **46**, **47** and **48a** were anticipated to be the most useful for establishing photophysical SAR. The presence of larger conjugated groups is potentially beneficial due to the expected inherent increase in absorption maxima

whilst the effect of auxochromes such as amines in different positions could also be determined. Furthermore, comparison between substituents at different loci will enlighten as to the most efficient strategy to achieve specific photophysical properties.

Unfortunately, not all synthetic routes were successful. It was not possible to install a carboxylic acid moiety adjacent to the BODIPY core, a difficulty that was encountered using multiple different approaches and analogues. It was therefore not possible to determine using these compounds, the effect of such close proximity of carboxylic acids or carbonyls to the BODIPY core on photophysical properties. Furthermore, it was not possible to conjugate the BODIPY analogues to species such as nucleosides, thus the effect of conjugation on the spectroscopic properties of BODIPY could not be examined.

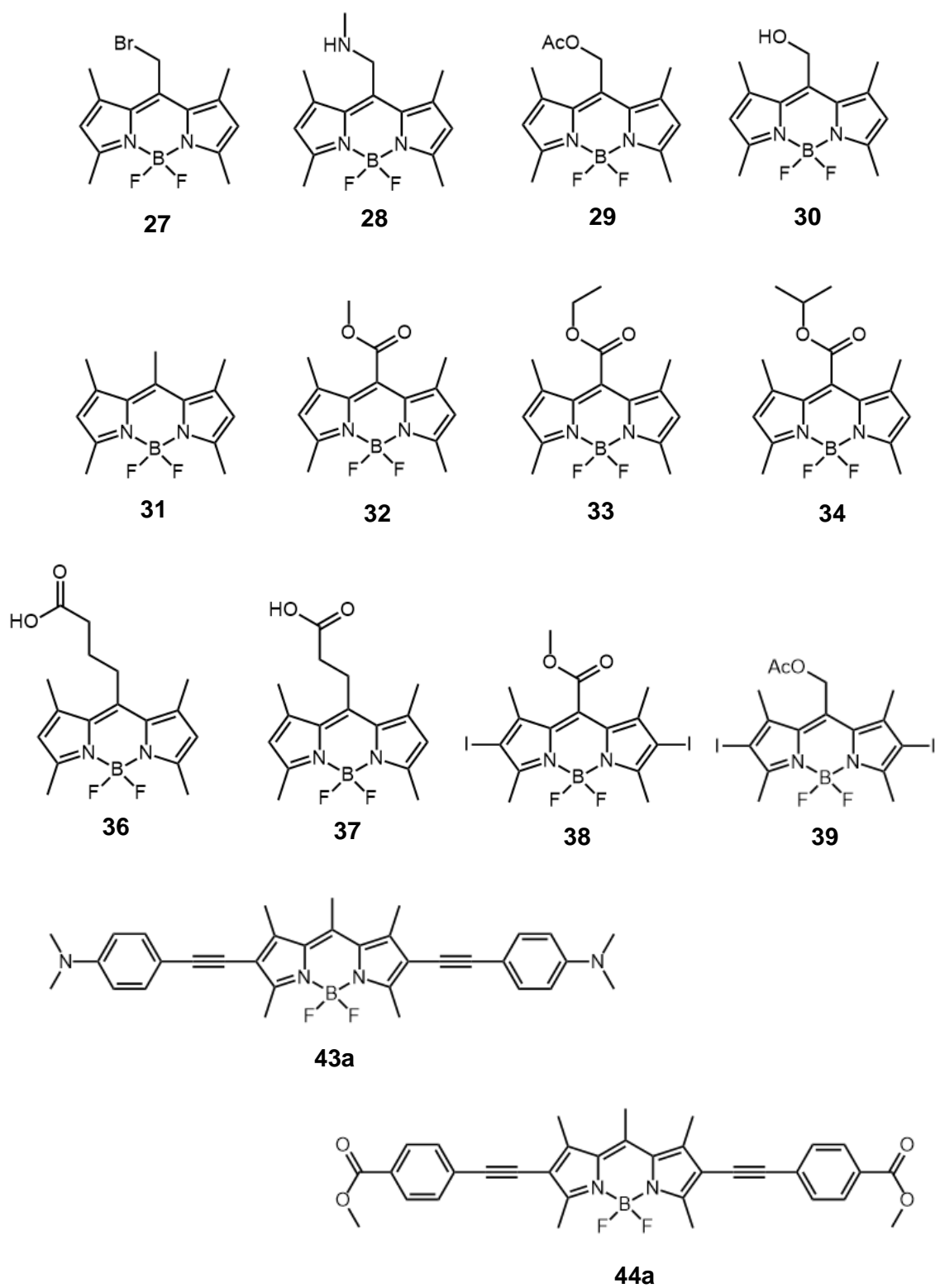
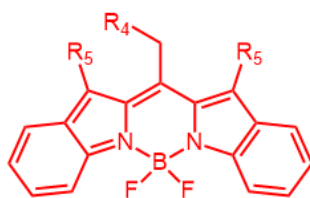
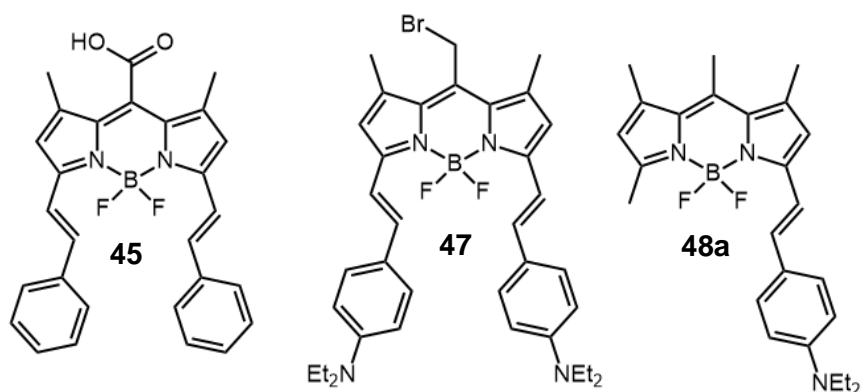


Figure 23: Summary of modifications to the BODIPY core that were successful (compounds **27-48a**) or unsuccessful



- R_1 = COOH, nucleosides
 R_2 = CPh, CPh(*p*-NMe₂)
 R_3 = Cl, Py
 R_4 = OAc, Br
 R_5 = CH₃

Figure 23: Summary of modifications to the BODIPY core that were successful (compounds **27-48a**) or unsuccessful (cont.)

The generation of expanded scaffolds using indole as a building block was also not realised. Although disappointing, this strategy was not expected to be the most efficient at improving the photophysical profile of BODIPY for biological studies. This is primarily due to only minor expansion of the conjugated system. Introducing metals such as platinum in place of boron was also not possible. The complete spectroscopic profiles of the successfully synthesised compounds are summarized in Table 5.

Compound	Solvent	λ_{\max} abs (nm)	Ext. Coeff. (M ⁻¹ cm ⁻¹)	λ_{ex} flu (nm)	λ_{em} flu (nm)	Fluorescence Intensity (a.u.)
27	DMSO	525	5,010	470	523	2,595
	Hexane	530	9,570	470	516	1,347
28	DMSO	509	18,030	500	531	53
	MeCN	505	19,890	500	528	107
29	DMSO	504	8,250	490	569	26
	Hexane	511	3,250	490	558	776
30	DMSO	509	225,370	512	522	314,500
	Pet. ether	505	99,470	513	517	16,450
31	DMSO	509	132,610	495	507	42030
	Pet. ether	511	649,010	498	501	367010
32	DMSO	509	5,000	500	511	10
	Hexane	511	3,250	500	527	3
33	DMSO	509	33,340	509	537	170
	Pet. ether	511	37,850	511	541	167
34	DMSO	512	39,790	511	537	217
	Pet. ether	511	42,270	512	534	96
36	DMSO	499	5,650	450	514	422
	MeCN	495	5,230	450	511	500
37	DMSO	499	1,550	450	n/a	n/a
	MeCN	496	1,620	450	520	278
38	DMSO	555	17,550	554	590	78.12
	Pet. ether	549	31,280	549	576	66.98
39	DMSO	554	17,540	555	591	154
	Pet. ether	555	2,190	553	571	154

Compound	Solvent	$\lambda_{\text{max abs}}$ (nm)	Ext. Coeff. ($\text{M}^{-1}\text{cm}^{-1}$)	$\lambda_{\text{ex flu}}$ (nm)	$\lambda_{\text{em flu}}$ (nm)	Fluorescence Intensity (a.u.)
43a	DMSO	535	2,420	535	583	149
	DCM	547	43,640	544	589	2,716
44a	DMSO	559	980	516	528	24
	DCM	590	21,283	580	592	22
46	DMSO	657	8,910	600	672	189
	Pet. ether	642	14,440	600	658	47
47	DMSO	734	16,130	700	768	16
	Pet. ether	699	17,880	700	738	564
48a	DMSO	704	14,980	650	738	421
	Pet. ether	679	3,740	650	696	657

Table 5: Summary of the photophysical parameters for compounds **27-48a**.

Fluorescence emission are normalised to 100 μM solutions

Compounds **27-37** explore the extent to which the *meso* group of a BODIPY scaffold can influence photophysical properties. Previous studies suggest that only small variation in spectroscopic properties is observed when modifying non-aromatic *meso* substituents.^{123,125,165,178} The data acquired here indicated that amine, hydroxyl and methyl groups at the *meso* position gave the greatest potential for high molar absorptivity. This is most clearly indicated by the absorptivities of $649,010 \text{ M}^{-1}\text{cm}^{-1}$ and $225,370 \text{ M}^{-1}\text{cm}^{-1}$ for compounds **31** and **30** respectively, in DMSO. Compounds **33** and **34** with ethyl and isopropyl esters also demonstrated promising absorption efficiencies in both polar and apolar solvent (**33**; DMSO = $33,340 \text{ M}^{-1}\text{cm}^{-1}$, Pet. Ether = $37,850 \text{ M}^{-1}\text{cm}^{-1}$; **34**; DMSO = $39,790 \text{ M}^{-1}\text{cm}^{-1}$, Pet. Ether = $42,270 \text{ M}^{-1}\text{cm}^{-1}$). Compounds **29**, **30** and **31** showed interesting properties, by which extinction coefficients dramatically varied with environmental polarity. For example, for compounds **29** and **30**, extinction coefficients increased by 2.5 and 2.3 times, respectively, when moving from apolar to polar solvent. Conversely, the extinction coefficient of compound **31** increased almost 5-fold when moving from polar to apolar

solvent. This indicates that acetyl and hydroxyl groups promote absorption of light in a more polar solvent, whereas the simple methyl group increases absorption in a less polar solvent.

Substitution at the *meso* position was also shown to have dramatic consequences for fluorescence emission. Amine and ester substituents (compounds **28**, **29**, and **32-34**) showed significant perturbation of fluorescence responses, irrespective of environmental polarity. This is clear from comparison with compound **31**; for example, in the case of compound **32**, the emission intensity was 3 arb. u. in apolar solvent, compared with 367,010 arb. u. in compound **31**. This was apparent for all carbonyl variants, with little correlation between emission response and proximity to the BODIPY core. This is clearly apparent from comparison between compounds **43a** and **32**. Compound **43a** had a decrease in fluorescence intensity of 41,881 arb. u. in polar solvent compared with unsubstituted compound **31**; similarly, compound **32** had a decrease in fluorescence intensity of 42,020 arb. u. relative to compound **31**. With respect to amine bearing compounds, compound **44a** had a significantly lower fluorescence emission intensity than compound **43a** (149 and 2,716 arb. u. for compound **43a** compared with 24 and 22 arb. u. for compound **44a** in polar versus apolar solvent). This does however support the hypothesis that both amines and carbonyls are capable of impeding fluorescence emission responses. Compounds **29** and **31** also presented environmentally dependent fluorescence emission with substantially increased responses when moving from polar to apolar solvent. In comparison, for the *meso* methyl substituent (compound **31**), this was recorded as almost a 30-fold improvement. Conversely, introduction of a hydroxyl group caused the inverse effect, with substantially magnified emission of more than 19 times in DMSO versus petroleum ether.

Solvatochromism is a desirable characteristic for a highly specialised probe; however, the constructed analogues **27-37** did not offer bathochromic or hypsochromic shifts above ~10 nm. The largest solvatochromic shift was detected for compound **27** in the bathochromic direction of only 5 nm. A shift of this magnitude is arguably negligible and hence indicates that the nature of substitution carried out at the *meso* position is incompatible with inducing solvatochromism. This was expected as none of the

compounds contained heteroatomic lone pairs within conjugative reach of the chromophore's delocalised system.

Despite having little impact on absorption wavelength, carboxylic acids **36** and **37** showed dramatic differences in photophysical profiles. With increasing alkyl chain length, here of only one carbon, there occurred an increase in extinction coefficient of 3-3.5 times ($1,620\text{ M}^{-1}\text{cm}^{-1}$ versus $5,230\text{ M}^{-1}\text{cm}^{-1}$ for compound **37** versus compound **36** in MeCN). Comparison of these two fluorophores also demonstrated the limitations of carboxylic acid fluorescence emission quenching in this context. In apolar solvent, little difference in detectable emission was observed between the two carboxylic acids, however in a polar environment, shifting the carboxylic acid one atom closer to the BODIPY core, as in compound **37**, effected dramatic fluorescence quenching. Although partial in an apolar environment ($\sim 50\%$ decrease relative to compound **36**), this fluorescence inhibition was complete in DMSO, and no detectable fluorescence response was present. This phenomenon is most likely a result of dipole-dipole electronic energy transfer between the conjugated system and carboxylic acid, restricting available energy for fluorescence emission. It is not possible to determine from this data whether this occurs via empty or molecularly occupied space, yet this could be rectified using time resolved spectroscopy. The environmental dependence for compound **37** can be explained by the proclivity for larger dipoles in a polar environment, promoting interaction of the electric fields to exacerbate fluorescence quenching. This finding was particularly exciting given the dramatic control over photophysical properties with minimal synthetic modification and little impact on the other spectroscopic properties of the core, such as absorption wavelength.

The effect of substitution at the 2 and 6 positions on fluorescence emission was clear. Iodine molecules generally reduced the emission intensity, whilst the more complex alkyne extensions caused, in most cases, a drastic perturbation of fluorescence emission. For example, emission intensity was reduced to 24 arb. u. for compound **44a** relative to 42,030 arb. u. for unsubstituted compound **31**. The only exception to this was compound **43a** in apolar solvent. This deviation from the pattern could be justified by the superior fluorescence acceptor ability of DMSO by Förster energy

transfer from the fluorophore. Regarding compound **44a**, as this environmental dependency is not observed, it can be postulated that dimethylamine substituents conjugated within the extended BODIPY molecule at these positions have a fluorescence quenching side effect, perhaps by the same electronic energy transfer mechanism as for carboxylic acids **36** and **37**. Due to conformational restrictions it is most probable that this would occur through molecularly occupied space.

For the four compounds synthesised with modifications at the 2 and 6 positions, only compound **44a** showed any discernible solvatochromism: a bathochromic shift of almost 30 nm when moving from a polar to an apolar environment. Again, this was as anticipated as this was the only compound that contained auxochromes. It was thus established that the effects of the dimethylamine auxochromes at the 2 and 6 positions were three-fold: increased absorption wavelength, decreased fluorescence emission response and bathochromic solvatochromism when moving from a polar to an apolar environment. In the case of compound **44a**, a solvatochromic shift of 31 nm was measured when moving from polar to apolar solvent; this would be useful in applications to probe the polarities of different environments, as a shift in absorption wavelength of this magnitude is distinct enough for detection.

Compounds **46**, **47** and **48a** were the most successful with respect to achieving favourable properties for biological applications. Extension of the conjugated system from positions 3 and 5 achieved absorption maxima increases of at least 150 nm relative to unmodified comparatives, such as compounds **27** and **31**. These trends are similar to those presented by Tao *et al.* where increasing conjugated system size increased absorption wavelengths and extinction coefficients.¹⁷⁸ This was supported by the clear trend in increasing wavelength with the addition of further conjugate branches. This conclusion is most succinctly derived from comparison of compounds **47** and **48a**. These structures also indicated the distinct effect of the tertiary amines. The addition of one more conjugated “tail” at the 3,5 position of BODIPY leads to an increase in absorption wavelength of 30 nm and an increase in extinction coefficient of 1150 M⁻¹cm⁻¹ in DMSO. Whilst providing a bathochromic shift for the absorption maxima, these results showed that auxochromes incorporated into BODIPY in this way have a greater effect on absorption wavelength than increasing the size of the

conjugated system. Furthermore, environmentally dependent fluorescence emission was more significant in compound **47** than compound **48a**. The percentage decrease in fluorescence for compound **48a** versus compound **47** when moving from apolar to polar solvent was 36% versus 97%. This demonstrates that compound **47** is a more sensitive fluorophore for detecting changes in polarity. Moreover, significantly higher absorption maxima of compounds **47** and **48a** compared with compound **46** in both polar and apolar solvent (differences ranging from 32 nm to 77 nm for like comparisons) reinforce that large conjugated systems with bathochromic auxochromes at the 3 and 5 position of BODIPY are effective methods to increase absorption wavelength and introduce solvatochromism and environmentally dependent fluorescence emission. Here, despite a smaller conjugated system, compound **48a** absorbed light at a wavelength almost 50 nm longer than compound **46**. This suggests that auxochromes have a more dramatic effect on absorption wavelength than adding a styrene substituent and the 3,5 position. In comparison to compound **44a**, this indicates that the induced solvatochromic effect from alkylaminophenyl substituents is reliable and irrespective of location or conjugative linker, providing there is sufficient conjugation within the electronic π system.

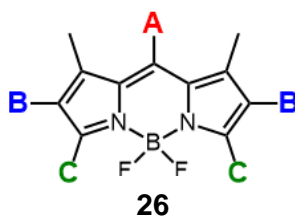
Molar extinction coefficients mostly showed an increase compared with unmodified BODIPYs, with the exception of compound **48a**. This could be accredited to conjugation size affording a greater affinity for the absorption of photons. Notably, the calculated coefficients for these analogues in apolar solvent were significantly lower than for compounds **43a** and **44a**.

In general, modification of BODIPY at the 3 and 5 positions effected a decrease in fluorescence response. This can be justified by the theory that increasing absorption wavelengths can compromise fluorescence emission, a difficult side effect to moderate given the extensive bathochromic shifts observed for these analogues. Yet for those containing auxochromes, overall this modification led to an increase in fluorescence response relative to simple phenyl groups, such as in compound **46**. Moreover, significant environmentally dependent fluorescence emission was present in compound **47**. This effect could be explained by twisted intramolecular charge-transfer, a phenomenon also observed in compounds such as Nile Red.¹⁸⁶ Although

typically prevalent in structures with long alkyl chains between donor and acceptor species, it has been noted that a special type of twisted intramolecular charge transfer state can be formed, enabling orthogonal interaction between the electronic systems of acceptor and donor molecules. This is reliant upon the successful twist around the essential single bond separating the BODIPY core from the diethylaminophenyl substituents. Twisting of the molecule away from the planar state in a polar solvent such as DMSO causes a two-fold effect. Primarily, the twisted state possesses a smaller band gap between the ground and excited states, enabling longer wavelength emission and causing the bathochromic shift. Secondly, the intensity of fluorescence emission is compromised. In a similar way to compounds 36 and 37, this could be justified by the fluorescence quenching ability of the acceptor molecule reducing fluorescence quantum yield and installing environmentally dependent fluorescence emission properties. The variation in emission wavelengths that occurs with changing solvent polarity are also likely a result of this charge transfer.¹⁸⁷

Figure 24 provides a visual representation of the photophysical trends observed based on SAR as a summary of the acquired spectroscopic data.

No major strategies were developed to increase absorption wavelengths *via* the *meso* position, with alkyl chains causing hypsochromic shifts. Most notably were the high extinction coefficients achieved by methyl and hydroxyl groups whilst bulkier groups such as carbonyls appeared to inhibit absorption efficiency, irrespective of substituent polarity. Although bulkier groups effected small bathochromic shifts, this was regularly at the expense of fluorescence emission intensity. Little solvatochromism was achieved; however, methyl and hydroxyl groups also provided the most intense fluorescence emission with most other substituents compromising the response. Significantly, it was established that incorporating carboxylic acid groups less than three carbons away from the BODIPY core at this position quenched fluorescence emission.



		λ	ϵ	Fl	Solv.
A	Methyl and hydroxyl groups	-	↑	↑	-
	Long alkyl chains	↓	-	-	-
	Bulky groups	-	↓	↓	-
	Carbonyl/amine groups	-	-	↓	-
B	Extended conjugation	↑	↓	↓	↑
	Heavy atoms	↑	↑	-	-
	Auxochromes	↑	-	↓	↑
C	Extended conjugation	↑↑	↑	↓	↑
	Auxochromes	↑	↑	↑	↑

Figure 24: Visual representation of the photophysical trends established based on modification of the BODIPY scaffold

For substitution onto the BODIPY core, many modifications here achieved an increase in absorption maxima, relative to compound **31**. In general, a larger increase was achieved via the 3 and 5 positions. Extension of the conjugated system proved the least effective method compared with the incorporation of auxochromes such as alkylamines, which efficiently induced bathochromic shifts. A similar trend was observed for extinction coefficients, by which greater improvement in molar absorptivities were observed via 3,5 modification; this was particularly poor for alkyne-based conjugation relative to unmodified BODIPY.

With the exception of heavy iodine atoms, all modifications induced a degree of solvatochromism. This was most pronounced for compounds containing auxochromes, irrespective of locus. Fluorescence profiles gave more interesting results. These larger, long wavelength chromophores presented compromised fluorescence emission without correlation to location on the BODIPY scaffold, as is often observed with such strategies. However, in compound **47**, this was offset by the presence of multiple auxochromes at the 3 and 5 positions, relative to compound **46**. These data highlight the importance of auxochromic substituents in the quest for fine-tuned photophysical profiles.

The results indicate that the most effective methods to fine-tune highly specific photophysical properties are *via* the 3 and 5 positions of the BODIPY core. This, combined with other modifications throughout the structure, could afford a broad spectrum of photolytic tools with desirable photophysical profiles for highly specialised applications. With respect to achieving long absorption maxima, reasonable extinction coefficient and solvent dependent fluorescence emission, compound **47** provided the most favourable profile. Thus, this compound has the greatest potential to be a valuable photophysical tool.

Chapter 3

Photophysical analyses

3.1 Density functional theory

Density functional theory (DFT) calculations were carried out using computational modelling to determine the HOMO and LUMO energies for each of the seventeen successfully synthesised compounds (**27-48a**). The obtained data are summarised in Figure 25 in order of compound number. Tabulated data for the obtained HOMO and LUMO energies and data organised by ascending HOMO and LUMO can be seen in the appendix (Section 6.3) for clarity of comparison and to indicate trends.

Good correlation was established between relative HOMO and LUMO energies, and UV/Vis and fluorescence spectroscopy data (Chapter 2). As expected, maximum absorption wavelength generally increased with decreasing HOMO-LUMO energy differences, due to the requirement for lower energy illumination to initiate molecular orbital transitions. Molecular orbital electron density maps for compounds **27-48a** can be found in the appendix (Section 7.3).

Clear trends were established between the nature and location of many substituents, and stabilisation (or destabilisation) of the HOMO and LUMO of the BODIPY analogues. Halogens were shown to be most successful at stabilising the HOMO. This was most evident for compounds **38** and **39** which contained two iodine atoms each, where the HOMO was lowered by more than 0.3 eV relative to BODIPY

analogues without iodine substituents (compounds **29** and **32**). Compound **27**, with a *meso* methyl bromine group also significantly stabilised the HOMO, here by 0.17 eV, compared with compound **31**, which had only a *meso* methyl group. This indicates that the effect of halogens on HOMO and LUMO energies is independent of locus on the BODIPY core.

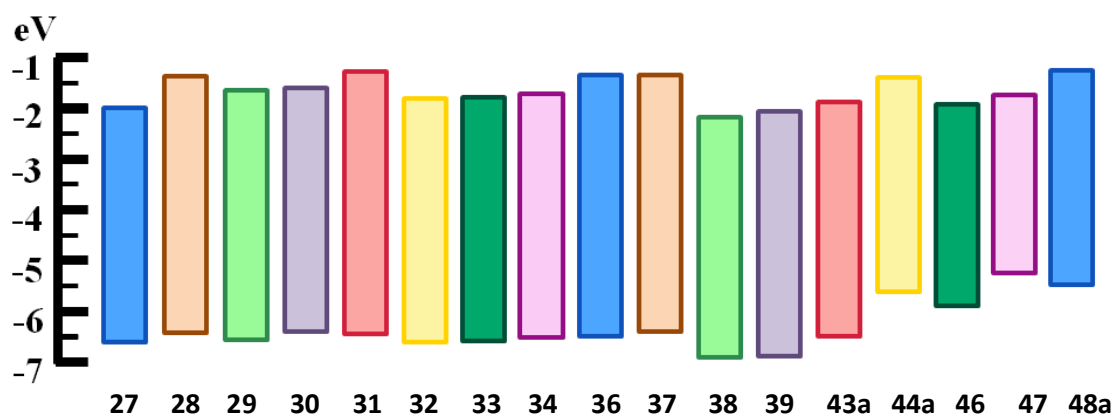


Figure 25: Representation to show the relative energies of HOMOs and LUMOs for compounds **27-48a**

The data in Figure 25 indicated that introduction of ester groups at the *meso* position (compounds **32-34**) caused partial stabilisation of the HOMO of between 0.09 and 0.13 eV, compared with compound **31** which had only a methyl group at the *meso* position. Compounds **33**, **34**, **36** and **37** contained *meso* groups comprised of a simple methyl, or alkyl groups bearing carboxylic acids respectively, yet the modifications in compounds **36** and **37** caused only partially stabilisation of the HOMO energy level (~ 0.09 eV). This suggested that the carboxylic acid groups in these compounds were physically too far from the conjugated π system to effect significant changes to molecular orbital stability. Furthermore, including electron accepting groups on the BODIPY core stabilised the HOMO. Conversely, the introduction of amine and hydroxyl species universally destabilised the HOMO of BODIPY, by an average of ~ 0.1 eV, with no significant correlation between location and efficacy.

Extension of the conjugated system destabilised the HOMO in almost all the compounds, which was intensified for extension at the 3 and 5 positions over the 2 and 6 positions. The presence of amine groups in these more complex structures also

caused dramatic increases in HOMO energies. This is most strikingly shown by comparison between compounds **43a** and **44a**, the former of which only caused a fractional HOMO destabilisation of 0.036 eV compared with compound **31**. Here, the introduction of amine substituents in place of methyl esters, as in compound **44a**, destabilised the HOMO by a further ~1 eV. This trend was also observed for compounds **46**, **48a** and **47** with HOMO energy levels tending to increase with the incorporation of additional amines. For example, comparison between compounds **46** and **47** indicates that the HOMO is destabilised by 0.65 eV when two additional amine groups are added. Although this appears to suggest that amine destabilisation is more significant *via* the 2 and 6 positions of the BODIPY scaffold, it must be acknowledged that the larger difference between compounds **43a** and **44a** (~0.4 eV greater compared to **46** and **47**) could be a result of the stabilising influence of the ester group. This makes the reasonable assumption, based on other BODIPY compounds with ester substituents, that the HOMO stabilising effect of esters at the *meso* position is similar to when they are located at the 2 and 6 positions. With respect to compound **47**, the stabilising effect of the *meso* methyl bromine substituent was insufficient to overcome destabilisation from the amine bearing conjugated extensions. This suggests that not only is HOMO stability compromised by 3,5 substitution, but that this effect cannot be overcome by the presence of stabilising halogens.

In general, weak correlation was established between calculated LUMO energies and the type and location of substituents on the BODIPY core. This is demonstrated by a variation in the LUMO energies of ± 0.6 eV compared to HOMO energies, which spanned over 1.4 eV. As with the HOMO energies, destabilisation of the LUMO occurred when substituents such as amines, hydroxyl groups and carboxylic acids were incorporated, whilst stabilisation was achieved with halogen atoms. Stabilisation of the LUMO with iodine substituents, as in compounds **38** and **39**, was ~0.2 eV, despite molecular orbital depictions indicating a lack of electron density localized over these atoms (appendix, Section 7.3). Electronic distribution of the LUMO for these two analogues was similar to un-iodinated compounds, despite the variation in orbital energies.

LUMO energy levels appeared predominantly dependent on the size of the conjugated system. For example, enlargement of the conjugated system resulted in stabilisation of the LUMO, an effect that was realised to a greater degree for compound **47**, which was substituted at the 3 and 5 positions; the energy of the LUMO was stabilised by 0.27 eV here. However, this stabilisation was partially hindered by the presence of electron donating groups, as was observed in compounds **44a** and **46**, whereby little conjugation to the phenyl group occurred. Furthermore, as with the HOMOs, incorporation of amine substituents, irrespective of loci, destabilised the molecular orbitals. This was however, to a much lesser extent than for the HOMOs. Consideration of compounds **47** and **48a** suggests that this could be overcome by a larger conjugation system, particularly as the LUMO of compound **47** is more stable than that of **48a**. This suggests that the size of a conjugated system is a more significant factor in determining LUMO energy levels than amine groups in these BODIPY fluorophores.

Overall, the greatest destabilisation of the HOMO was achieved by substitution at the 3 and 5 positions of BODIPY and the inclusion of amines, whereas the inclusion of halogen species universally improved HOMO stability. With respect to the LUMO, there was only small variation in stability; however similar trends were measured with respect to amine and halogen groups, with conjugated systems conversely providing partial stabilisation. In general, with narrowing of the HOMO-LUMO gap there was more significant destabilisation of the HOMO rather than stabilisation of the LUMO. This was exacerbated by the presence of amine groups, supported by the observation that compounds **44a** and **46**, which did not contain amine groups, experienced this effect to a lesser degree.

In 2019, Tao *et al.* reported on efforts to fine-tune the electrochemical properties of BODIPY compounds, and thus presented a series of analogues similar to compound **47**, but with a phenyl group at the *meso* position.¹⁷⁸ Here, they found that, as expected, the HOMO-LUMO energy gap decreased with the addition of styryl groups at the 3 and 5 positions of the BODIPY core. However, they observed that the progressive addition of a third and fourth styryl group did not decrease the size of the HOMO-LUMO gap to the same extent as the addition of the first and second styryl

groups at the 3 and 5 positions. This suggests that the substitution carried out to achieve compound **47** is the most efficient for achieving a narrow HOMO-LUMO gap, and that further substitution would not theoretically achieve a molecule with an absorption maximum closer to the near infra-red. In addition to this, Xuan *et al.* reported that adding substituents such as thiophene or phenyl groups could destabilise both the HOMO and LUMO, as was seen in particular in compound **44a**.¹⁸⁸ Here, they found that the HOMO of BODIPY was destabilised by ~0.65 eV, and the LUMO destabilised by ~0.5 eV. This supports the observations from compounds **43a** and **44a**, and further emphasises the stabilising effect of ester groups of the molecular orbitals of BODIPY.

Compound **47** demonstrated a photophysical profile that was the most promising. Favourable properties for biological probing combined with *in vivo* compatibility potential, facilitate a light-activated tool that could be applied to a variety of strategies. Thus, this compound was selected for more in depth DFT studies, accounting for the effects of external solvents on the molecular orbital arrangements and relative energies of the HOMO and LUMO. The oscillation strengths were also established with corresponding primary coefficients for each of the orbital transitions for compound **47** in different solvents. The obtained data are summarized in Tables 6 and 7.

Solvent	Polarity (arb. u.)	HOMO (eV)	LUMO (eV)
None	n/a	-5.253	-1.780
Ether	0.11	-5.377	-2.007
MeCN	0.46	-5.460	-2.145
MeOH	0.76	-5.458	-2.143a

Table 6: HOMO and LUMO energies for compound **47** in different solvents with varying associated polarities

Approximation to account for the global presence of solvent molecules around the BODIPY analogue, as anticipated, caused stabilisation of both the HOMO and LUMO energies by at least 0.3 eV (Table 6). The results also showed a correlation between solvent polarity and molecular orbital energies. As solvent polarity increases, both the HOMO and LUMO of compound **47** undergo minor stabilisation of less than 0.1 eV, with energy differences between the two molecular orbitals remaining negligibly constant with changing environmental polarity. Interestingly, increasing solvent polarity from MeCN to MeOH, a significant increase comparable to that from ether to MeCN, did not enable a similar improvement in molecular orbital stability for either the HOMO or LUMO.

Solvent	Transition Energy (eV)	Oscillator Strength (f)	Molecular Orbital Transition	Primary Coeff.
None	3.8260	1.15	HOMO → LUMO+1	0.52
	2.9530	0.86	HOMO-1 → LUMO	0.69
	1.8926	0.97	HOMO → LUMO (π -	0.69
Ether	3.5812	1.23	HOMO → LUMO+1	-0.67
	2.7099	1.51	HOMO-1 → LUMO	0.68
	1.5868	1.19	HOMO → LUMO (π -	0.69
MeCN	3.4733	1.08	HOMO → LUMO+1	-0.66
	2.5809	1.81	HOMO-1 → LUMO	0.68
	1.44a07	1.27	HOMO → LUMO (π -	0.69
MeOH	3.4749	1.08	HOMO → LUMO+1	-0.66
	2.5829	1.81	HOMO-1 → LUMO	0.68
	1.44a3a0	1.27	HOMO → LUMO (π -	0.69

*Table 7: Energies of quantum mechanical transitions to singlet excited states with corresponding oscillator strengths and molecular orbital transitions for compound **47***

Computational modelling of compound **47** using DFT suggested that significant redistribution of electron density takes place during π - π^* transitions. Oscillator strength can be understood as the probability that a quantum mechanical transition will occur. Exploration of transition energies with corresponding oscillator strengths indicated the potential for electronic transitions and clarified the effects of solvent polarity on these transitions. This provided insight into the feasibility of electronic excitations in compound **47** with respect to environmental polarity.

Figures 26-33 present the molecular orbital diagrams, orbital energies (LUMO+2, LUMO+1, LUMO, HOMO, HOMO-1 and HOMO-2), the orbital transition energies and, where applicable, the UV/Vis spectra for compound **47** in the absence of solvent, and in the presence of ether, MeCN and MeOH.

The results showed that with increasing polarity, the potential for quantum mechanical π - π^* transitions improves, whilst the more polar solvents more effectively stabilise the excited singlet state. This is shown by the increase in oscillator strengths from 1.19 in ether to 1.27 in MeCN and MeOH. This is also supported by the decrease in the energy of the π - π^* state that is seen with increasing solvent polarity when moving from ether to MeOH (1.59 eV to 1.44 eV). Furthermore, obtained molecular orbital depictions indicate increased localization of electron density across the conjugated π system in MeOH compared with ether (Figures 32 and 28). This suggests that the π - π^* transition is more favourable in polar environments, supporting the parameters derived in Table 7. These predictions support the UV/Vis spectra measured for compound **47** (Figures 29, 31 and 33, overleaf), which clearly demonstrate the relative intensities of the different absorption peaks (with corresponding molecular orbital transitions). These relative intensities match the oscillator strengths indicated for each transition, and thus provide an explanation for the pattern of absorption peaks observed on UV/Vis spectroscopy.

In the absence of solvent, the largest transition energy (HOMO \rightarrow LUMO+1) was the most favourable, with an oscillator strength of 1.15. For models accounting for external solvent molecules, the π - π^* transition was not calculated to be the most

favourable molecular orbital transition. There is a greater probability of quantum mechanical transition for HOMO-1 \rightarrow LUMO compared with the π - π^* , suggested by this increase in oscillator strength. The difference between these two transitions was 0.54 for MeCN and MeOH, and 0.33 for ether; this demonstrates that the HOMO-1 \rightarrow LUMO is more favourable to an even greater extent in polar solvents than apolar solvents. This also justifies the ratios of transition states observed in the UV/Vis spectra, where an absorption peak of shorter wavelength is also detected with a greater absorption intensity (Figures 27, 29 and 31). Despite this, the relative transition energies show that the HOMO-1 \rightarrow LUMO transition, as expected, is less stable, with values more than 1.1 eV larger than the π - π^* transition, making these two singlet state excitations more comparable in proclivity.

The π - π^* transition is the most valuable molecular orbital transition in the pursuit of fluorophores active towards the near infra-red. This is because excitation from the LUMO to the HOMO requires the longest wavelength of light compared with other molecular orbital transitions. In the case of compound **47**, in polar and apolar solvents, the π - π^* transition represents absorption wavelengths of 734 and 699 nm, respectively. Here, the oscillator strengths for π - π^* transition in ether and MeOH was measured as 1.27 and 1.19, respectively. Although the π - π^* transition is not the most favoured, an oscillator strength of 1.19 is high for a BODIPY fluorophore. In comparison to other BODIPY compounds, Bañuelos *et al.* reported that the simple BODIPY core (compound **31**) had an oscillator strength of 0.53, most likely such as low value because of poor HOMO-LUMO orbital overlap.¹⁸⁹ Shao *et al.* in 2011 and Chen *et al.* in 2019 presented BODIPY molecules with similar structures to compound **47**, with conjugated substituents at the 3,5 positions of the BODIPY core. Here however, much weaker oscillator strengths were reported of less than 1.^{190,191} This suggests that despite the π - π^* transition not being the most favourable transition, it is still highly likely to occur compared with other BODIPY fluorophores. The oscillator strengths measured here are also significantly stronger than for similar fluorophores, such as those presented by Ksenofontova *et al.*¹⁹² In comparison to compound **47** which has an oscillator strength of 0.97 for the π - π^* transition in the absence of solvent, the highest oscillator strength presented by Ksenofontova *et al.* was 0.609 (also a π - π^* transition). This indicates that the photophysical profile of compound **47** is

stronger than these other BODIPYs, and that excitation to the HOMO prior to fluorescence emission is more favourable in compound **47**. Most significantly, however, was the fact that the HOMO-1 \rightarrow LUMO and HOMO \rightarrow LUMO oscillator strengths were very similar (0.605 versus 0.600) for the compounds presented by Ksenofontova *et al.* This is in stark contrast to the values reported for compound **47**, where a difference in oscillator strength of 0.11 was measured between these two molecular orbital transitions.

The data suggest that not only is compound **47** is a viable candidate for a long wavelength fluorophore, but it is optically active at more than one wavelength. This could be a valuable characteristic in a biological application where, for example, triggering a fluorescence response in different areas of the body *in vivo* would require the use of different wavelengths of length as a result of varied depth of penetration requirements.

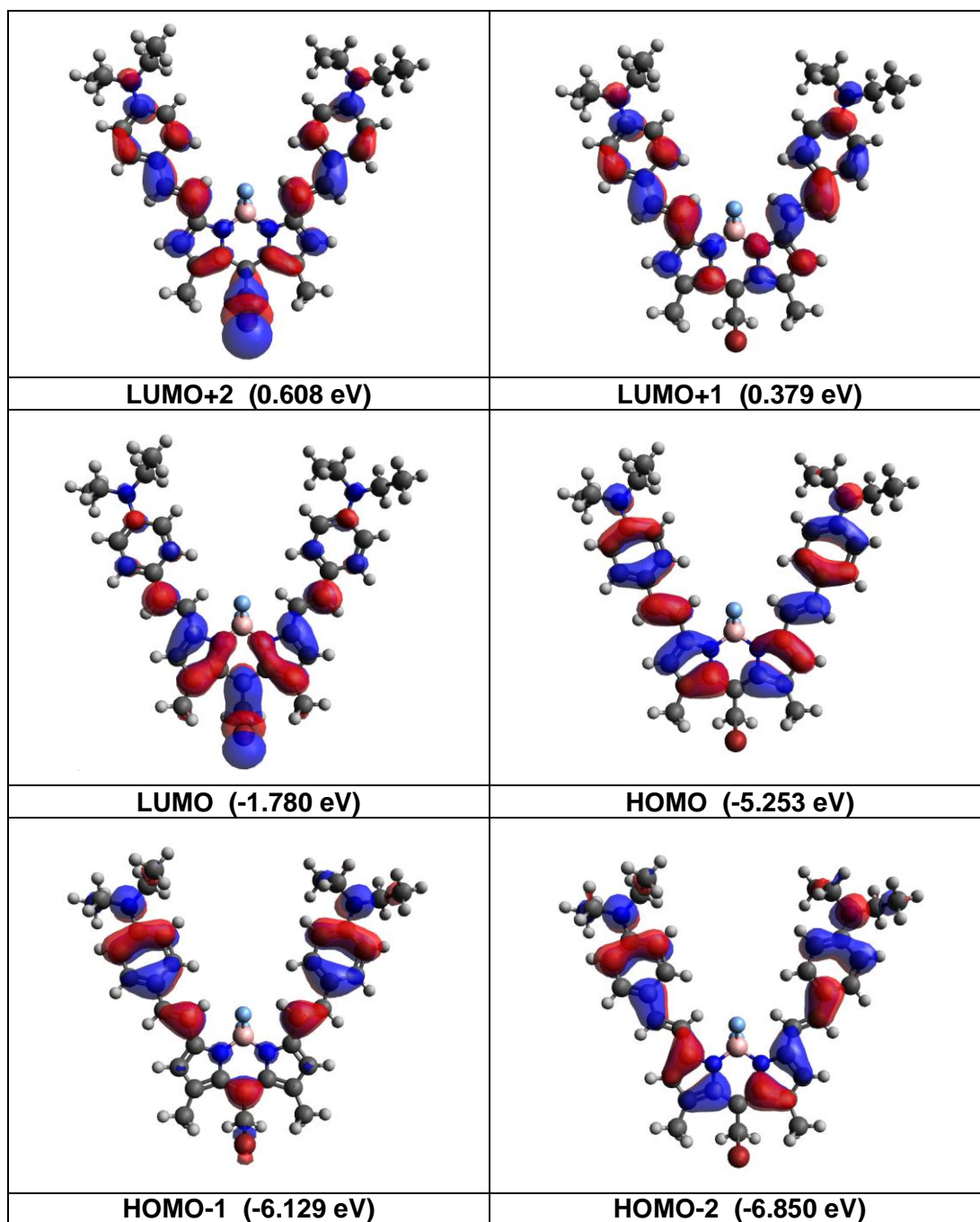


Figure 26: Molecular orbital diagrams and energies for compound **47** without solvent

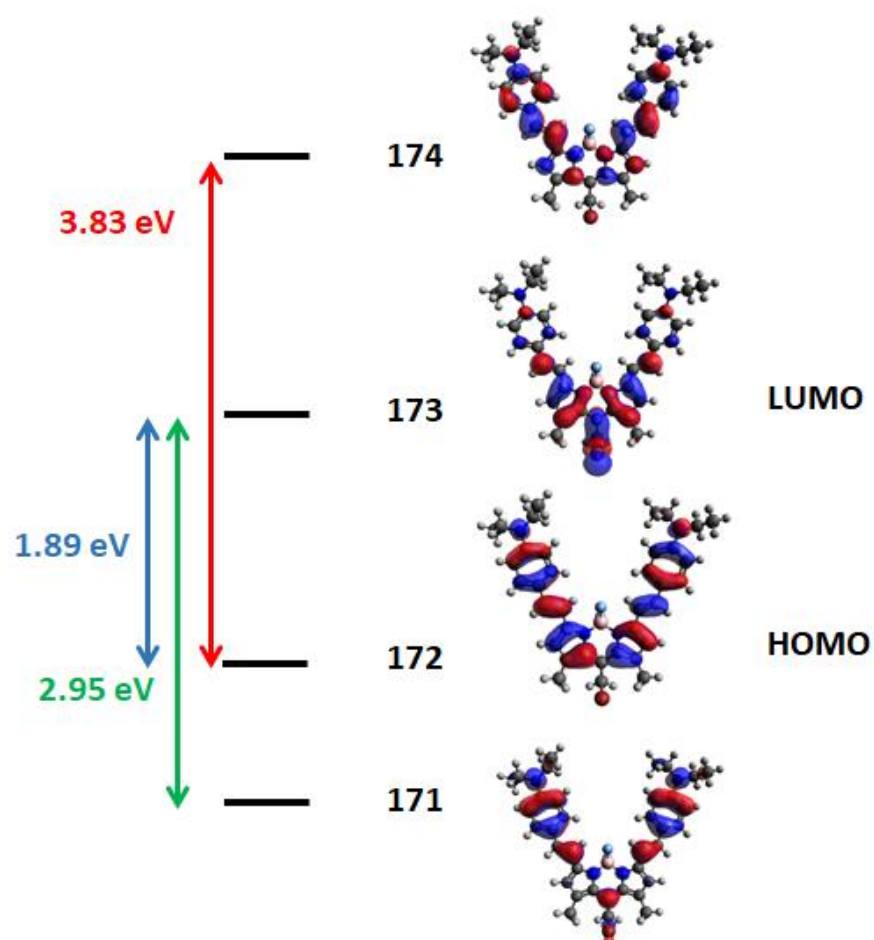


Figure 27: Orbital transition energies of compound **47** without solvent

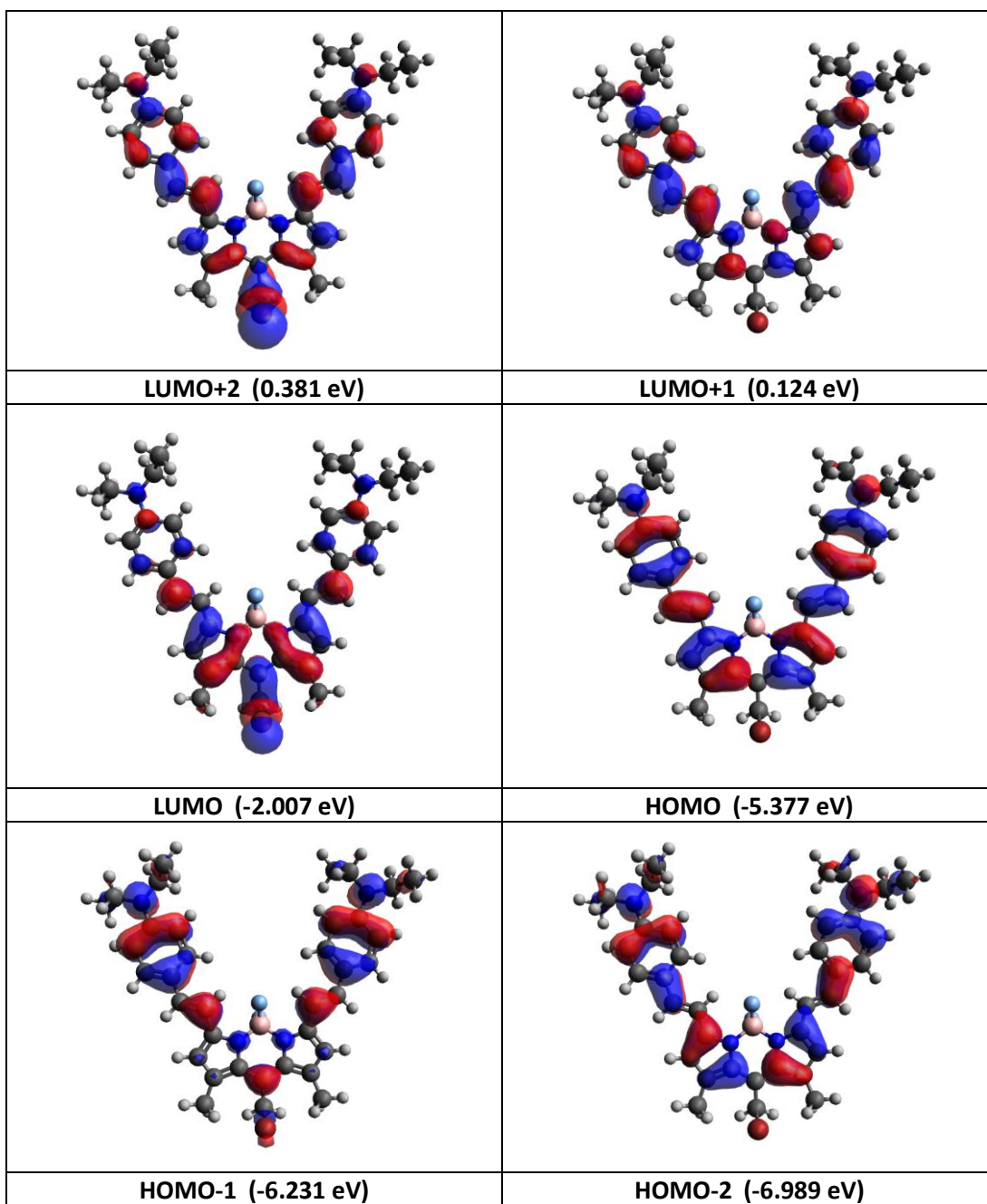


Figure 28: Molecular orbital diagrams and energies for compound **47** in ether

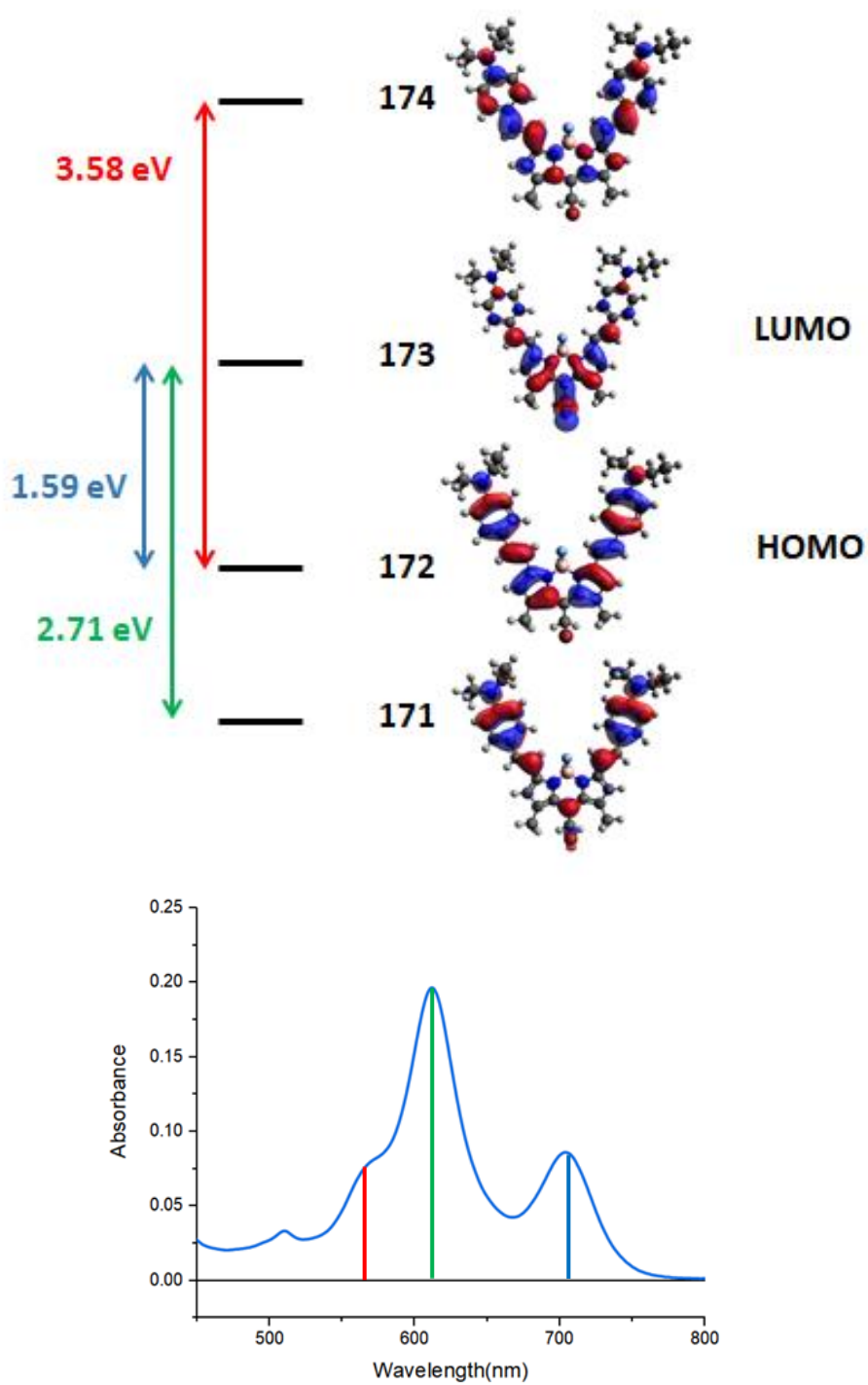


Figure 29: Molecular orbital transitions energies of compound **47** in ether with assignment of transitions to absorption spectrum

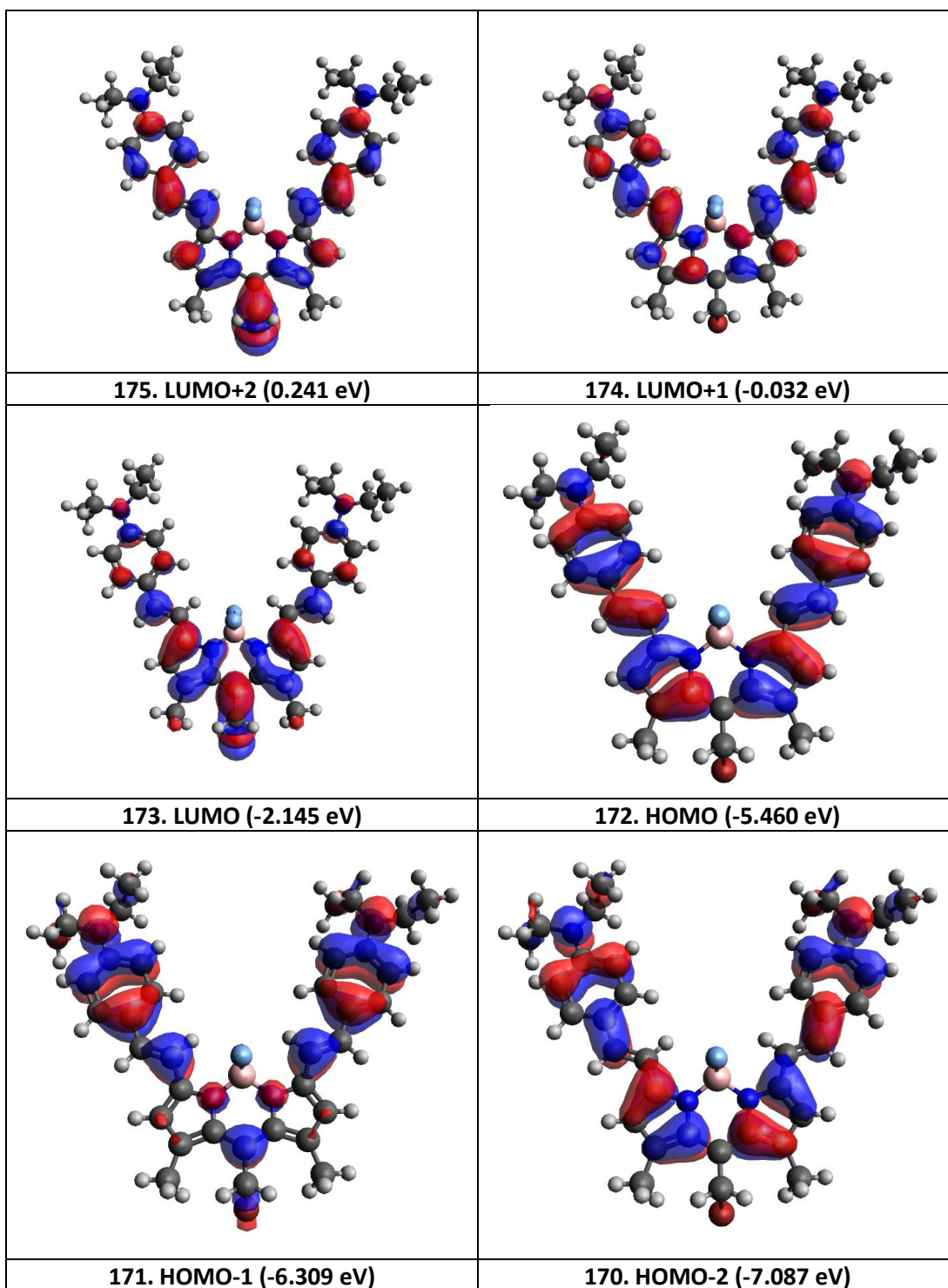


Figure 30: Molecular orbital diagrams and energies for compound **47** in MeCN

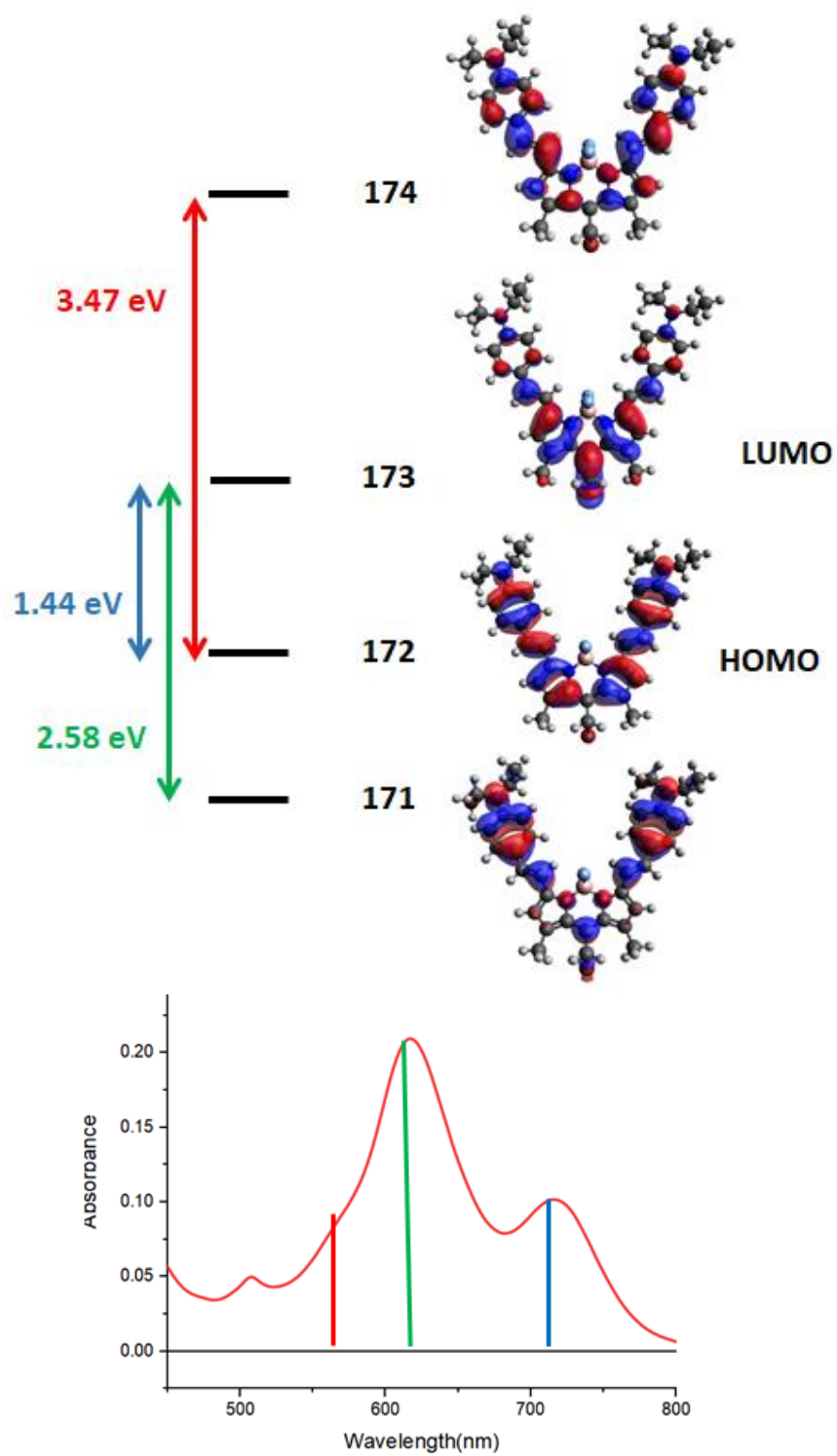


Figure 31: Molecular orbital transitions energies of compound **47** in MeCN with assignment of transitions to absorption spectrum

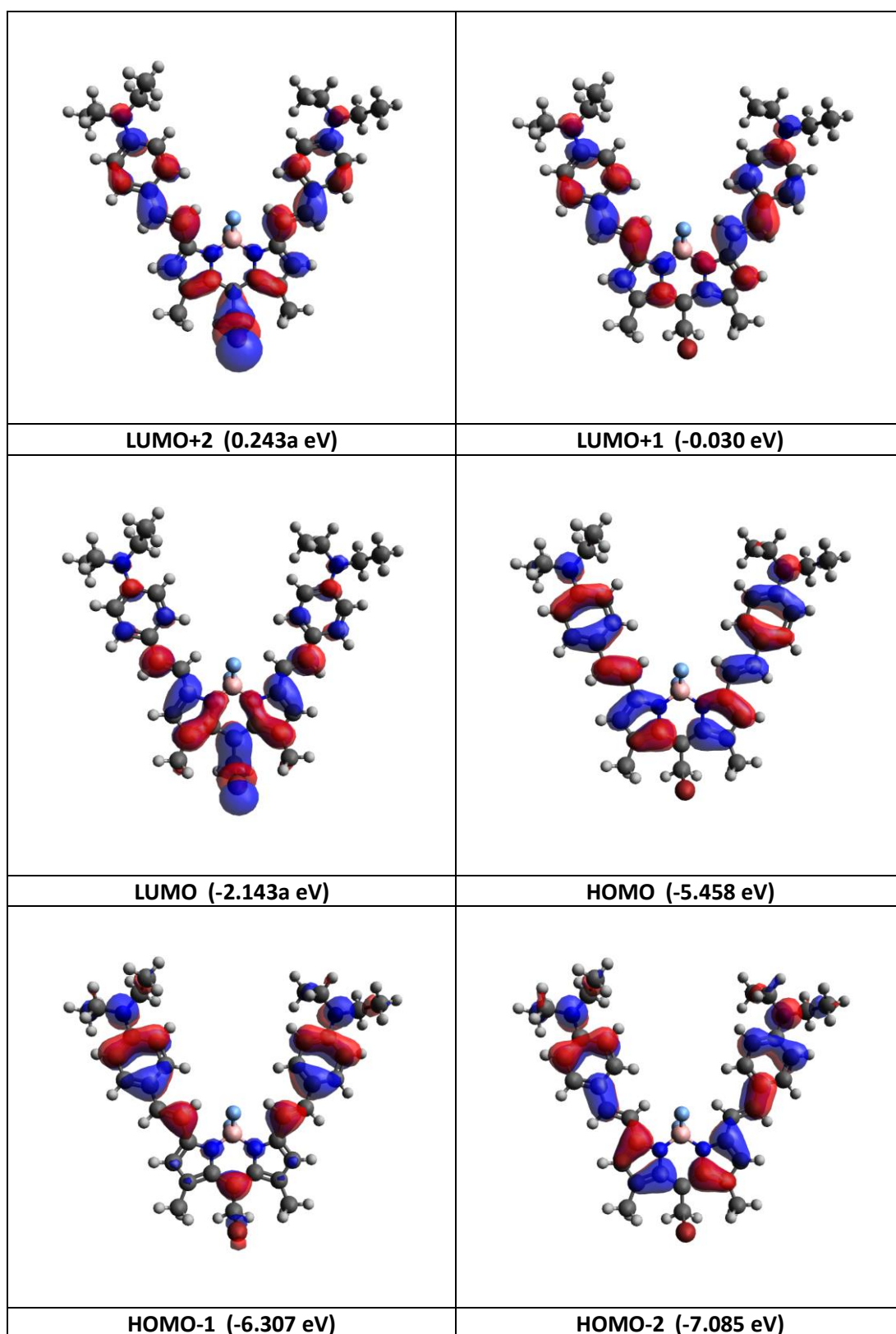


Figure 32: Molecular orbital diagrams and energies for compound **47** in MeOH

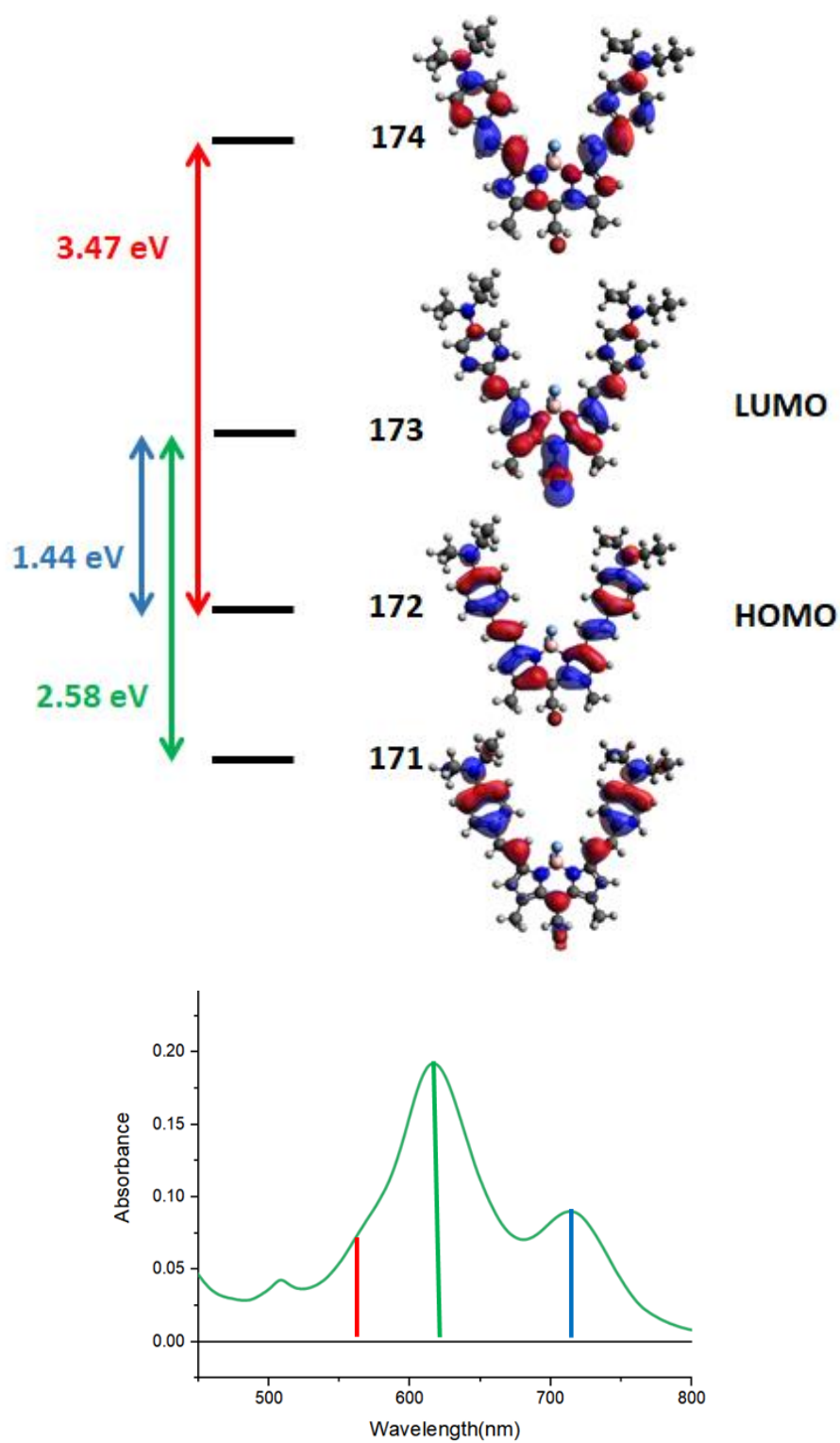


Figure 33: Molecular orbital transitions energies of compound **47** in MeOH with assignment of transitions to absorption spectrum

3.2 Transient absorption spectroscopy

Transient absorption spectroscopy (TAS) was utilised to monitor the dynamics of transient changes in absorption upon excitation using a pulsed laser. During this technique, an initial laser pulse is followed by a probe pulse after a time delay, by which a fraction of the molecules are promoted to their excited state. The resultant absorption profile, upon removing ground state absorption spectra as a background trace, indicates the nature of the photoexcited charges. The location of excited electrons (either in the singlet or triplet state) could suggest the potential fluorescence emission yield after excitation, with fluorescence emission favoured by increased maintenance of electrons in the singlet prior to relaxation. Here, absorption is monitored over time to track any changes until complete relaxation of electrons to the ground state. Significant variation of absorption response over time can indicate both the presence and electronic properties of intermediate excited states, such as triplet state occupation as a result of intersystem crossing. Tracking and recording of the absorption dynamics multiple times before averaging of the signal provides a representative depiction of the electronic kinetics under photoexcitation. Modification of the probe pump enables spectra to be collected over a range of wavelengths, providing insight into the effects of excitation wavelength on the nature of excited states. This method was selected to improve the potential to detect dark, or non-emissive, states.

TAS was carried out on compound **47** in MeCN and DMSO at room temperature (~298 K) using a Xe lamp (75 W) for sample illumination. An Si PIN photodiode was used to measure fluctuations in transmitted light after application of the UV laser pulse with intensity 0.5-36 $\mu\text{J cm}^{-2}$. Excitation was carried out at 700 and 630 nm for MeCN and DMSO respectively.

In both solvents, compound **47** did not suggest the detectable occupation of an excited triplet state. The spectra (Figure 34) effectively show background “noise” with little evidence of intersystem crossing. The range of wavelengths recorded at, from 650 to 1600 nm, demonstrates no detectable emission in the vis-IR region that would

indicate alternative transient changes. This suggests that undetectable numbers of photons are being lost to phosphorescence, and therefore more excited photons are available for fluorescence emission.

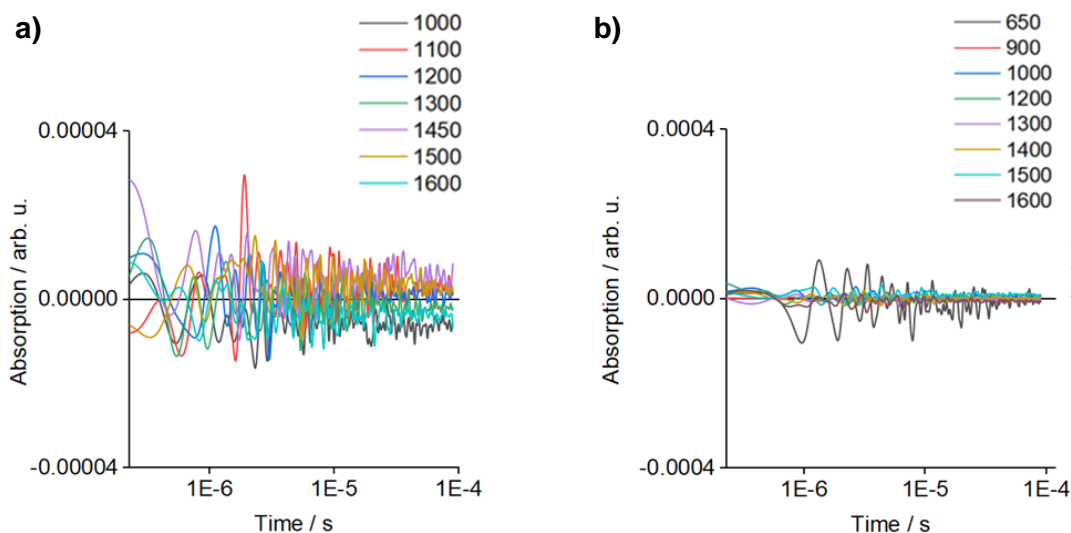


*Figure 34: Transient absorption spectra for compound **47** in MeCN (a) and DMSO (b) indicating that little intersystem crossing to the triplet excited state is occurring*

The results here were not unexpected. There have been reports of very poor triplet state population and little detectable intersystem crossing occurring in BODIPY compounds.¹²⁵ Further, the majority of work that addresses population of the triplet state of BODIPY does so in compounds containing heavy atoms or heavy metals, which are known to promote intersystem crossing.^{193,194} The lack of heavy atoms or metals in compound **47** therefore, could explain the undetectable levels of ISC.

3.3 Time correlated single photon counting and photoluminescence quantum yield

Monitoring of the excited states was not successful using transient absorption spectroscopy; therefore, alternative strategies were employed to provide a clearer picture of the excited states. Time correlated single photon counting (TCSPC) was utilised as a method to detect single photons of light initiated by a pulsed laser. Excitation of a sample enables detection of these photons by measuring their arrival times with respect to a reference signal in order to determine the relative lifetimes of a fluorescent response. Repetition of this stimulus allows construction of fluorescence decay curves based on the arrival time of photons at a detector.

Compound **47** was hence analysed using TCSPC in three different solvents: MeOH, MeCN and petroleum ether. The aim was to determine the effect of solvent polarity on emission decay pathways upon excitation and subsequent detection with multiple wavelength tuned emission probes. The employment of multiple probes enables monitoring of more than one molecular orbital transition. The obtained data are summarized in Table 8. The profiles demonstrate that whilst all decays occur on a nanosecond time scale, a clear trend was established whereby increasing environmental polarity increases photoluminescent decay. Rise times were shown to be less dependent on environmental polarity with slight decreases in time taken for excimer formation. However, these are restricted by the detection limits of the spectrometer with rise times defined as time taken for photon detection to reach 1000 (arb. u.) for ease of comparison. Thus, they are not perfectly reliable and do not provide valuable insight into the excited states of compound **47**. With respect to decay times, significant variation was established in timescale/half-life as a result of global solvent. In apolar solvent petroleum ether, decay lifetimes of 2.04 and 2.76 nanoseconds were recorded with detection wavelengths of 720 and 640 nm respectively. However, increasing the polarity of the solvent dramatically reduced the decay lifetime; in MeCN, recuperation of electrons to the ground state was achieved in 1.00 nanoseconds or less. This decreased even further in the most polar solvent MeOH, where the average decay time was 4.97 nanoseconds.

Solvent	$\lambda_{\text{detection}}$ (nm)	τ_{rise} (ns)	τ_{decay} (ns)
Ether	640	5.13	2.76 ± 0.39
	720	5.32	2.04 ± 0.38
MeCN	730	5.02	0.78 ± 0.10
	792	5.01	1.00 ± 0.09
MeOH	660	4.97	0.57 ± 0.15
	760	5.03	0.64 ± 0.12

Table 8: Fluorescence lifetime measurements for compound **47** in three solvents with different detection wavelengths

Correlation of transition states showing HOMO-1 \rightarrow LUMO, as calculated from DFT modelling, supports the conclusion that absorption peaks at 630 and 612 nm for DMSO and Pet. ether respectively are a result of this quantum mechanical transition. It was established that excitation using wavelengths at 630 nm and below excited electrons from the HOMO-1 to the LUMO, whereas illumination above this wavelength stimulated the π - π^* transition. This is supported by the relative transition energy calculations (Figure 35b-d).

The measured fluorescence lifetimes were shorter than for some of the compounds previously reported in the literature. Large conjugated systems similar to, but slightly larger than, compound **47** have reported fluorescence lifetimes of between 3.2 and 4.3 ns. These are significantly larger than those measured here, which are less than 1 ns for similar solvent polarities. This suggests that, although compound **47** has a strong photophysical profile when it comes to probability of molecular orbital transitions, the fluorescence emission is short lived relative to other BODIPY compounds.¹⁹⁴ In contrast, the fluorescence lifetimes of the simplest BODIPY compound (comparable to compound **31** without the methyl group at the *meso* position) have been explored in multiple solvents.¹⁹⁵ The results indicate that the fluorescence lifetime increases in a less complex and less conjugated structure. For example, decay lifetimes were measured as 7.48a and 7.58 ns in MeCN and MeOH

respectively, significantly higher than for compounds **47**, which had an average fluorescence lifetime of ~5 ns in MeCN and MeOH.

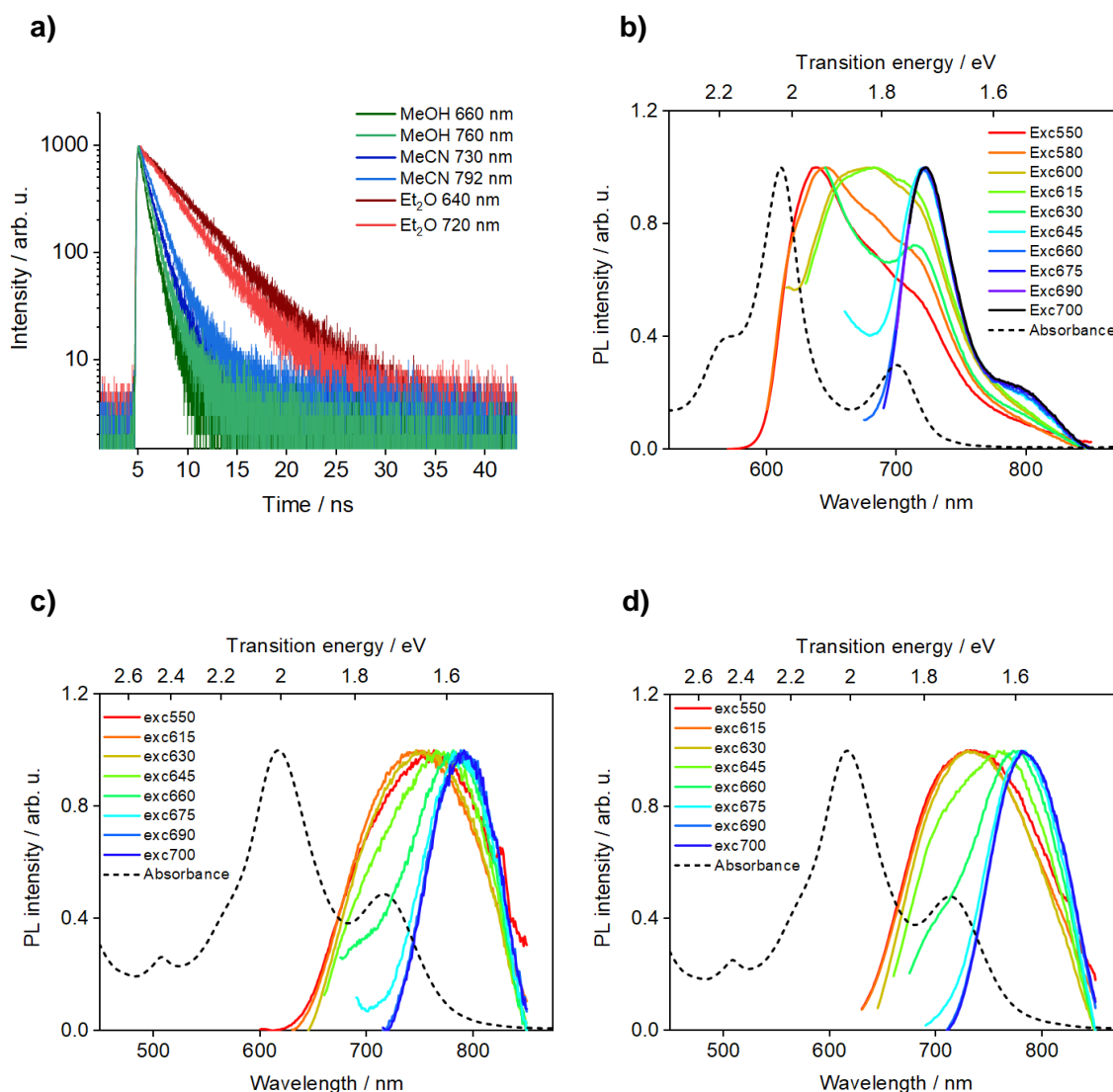


Figure 35: a) Time correlated single photon counting decays of compound **47** in three different solvents, excited at 44a3a nm and measured at various wavelengths (see Figure legend); b)-d) Photoluminescence spectra of compound **47** with excitation wavelengths from 550-700 nm in ether (b), MeCN (c) and MeOH (d) with corresponding absorption spectra and transition energies. All obtained PL data has been normalised.

Photoluminescence spectra were used to calculate photoluminescence quantum yields (PLQY) for compound **47** in the three solvents. The data were extracted using Excel Macro software by taking the quantity of photons emitted by the sample as a proportion of the photons used during excitation. This was carried out using data obtained with and without fluorophore sample to provide controls. Yields were derived using the closest detection probe to the emission wavelength for each excitation profile. The data are shown in Table 9.

As anticipated based on previously acquired data, yields of emission were poorer in more polar solvents. This was particularly striking upon comparison between petroleum ether and MeOH, where PLQY dropped more than 13 times with increasing solvent polarity. Similarly to the molecular orbital energies, linear correlation in line with polarity indexes was not observed, with MeCN achieving a much poorer PLQY, closer to MeOH, despite polarity being approximately between MeOH and ether. This can also account for the poorer fluorescence emission yields observed during fluorescence spectrometry.

Ether	MeCN	MeOH
635 nm = 9.4%	616 nm = 1.9%	720 nm = 0.6%
725 nm = 7.9%	716 nm = 1.5%	786 nm = 0.6%

*Table 9: Photoluminescence quantum yield (PLQY) for compound **47** in three solvents: ether, MeCN and MeOH using detection probes of varying wavelengths*

Despite little difference between the molecular orbital transitions in MeCN and MeOH, PLQY still varies between 1.5% and 9.4%, indicating that this photon deficit after excitation is not only a result of transition energies but also some interaction with the environment. A possible explanation for this is Förster electron transfer to solvent molecules, or by collisional or static interactions between the BODIPY analogue and the solvent molecules. It is expected that Förster electron transfer would be more prevalent in polar solvents given the inherent stronger dipoles within the system.

In 2015, Sajjad *et al.* presented a series of BODIPY compounds with polymeric chains, all of which had PLQYs of between 55-75%.¹⁹⁶ In comparison, the PLQY of compound **47** is low, with a maximum of 9.4% measured in ether. Furthermore, PLQYs of 50% and above have been reported in BODIPY fluorophores with large bulky structures that are comparable to compound **47**.¹⁹⁷ This demonstrates that the PL profile of compound **47** is weak compared with other BODIPY fluorophores in the literature; this could be attributed to low favourability of the π - π^* transition that was calculated using DFT (Table 7).

Overall, it has been possible to establish trends in spectroscopic properties, both absorption and fluorescence, based on nature and loci of substituents on the BODIPY scaffold. In addition, the effect of these varied substitutions on the HOMO and LUMO energies has been determined, enabling compound design with the aim of stabilisation or destabilisation of molecular probes as required. Further, the most promising compound (**47**) has been explored more thoroughly to establish the effects of environmental polarity on the probability and quantum efficiencies of molecular orbital transitions, with correlation to spectroscopic data. The results indicate that with increasing polarity comes greater stability of the molecular orbitals; however, with this occurs faster decay of photon emission and loss of quantum efficiency. This information will assist with highly specific design to function strategy for the development of light-activated molecular probes with precisely tuneable properties to meet selective application demands.

DFT, TAS, TCSPC and PLQY calculations were carried out in collaboration with Dr José Marin Beloqui. DFT, TAS, TCSPC and PLQY experiments and data extraction carried out by Dr José Marin Beloqui

Chapter 4

Lipid membrane interactions

4.1 Introduction

With the photophysical characteristics of the BODIPY compounds established, their potential as probes for biological environments was explored. The most logical approach for these experiments was to generate a series of lipid vesicles with which the BODIPY analogues could be incubated. The estimated TPSA values (calculated using ChemBioDraw Ultra) suggested that the structures would be significantly more inclined to associate with apolar environments. This was supported by predications of logP values using of ALOGPS 2.1, which suggested ranges of 5.11-6.76. Although the high lipophilicity of these compounds has the potential to compromise bioavailability, it indicates that BODIPY compounds will preferentially associate with lipid membranes. Hence, it was hypothesised that when in the presence of lipophilic membranes in aqueous media, these BODIPY analogues would favourably situate within the lipid bilayer. Previous work showed that the intensity of fluorescence emission is dependent on environmental polarity (Chapter 2). Therefore, in the case of these some BODIPY analogues, fluorescence emission was only observed in a sufficiently apolar environment. It was postulated that these BODIPY fluorophores would experience fluorescence quenching in aqueous solution (as was observed in polar solvents such as DMSO), with the re-establishment of fluorescence emission upon insertion into an apolar lipid membrane. It is therefore possible that exposing

these BODIPY analogues to biological systems *in vitro* could enable precise staining of cellular components, a useful outcome for bio-sensing.

4.2 Insertion of BODIPY fluorophores into synthetic lipid membranes

1-palmitoyl-2-oleoyl-sn-glycero-3-phosphocholine (POPC) was selected as the most suitable synthetic model for lipophilic membrane interactions, as this lipid is known to form relatively rigid vesicles in comparison to other lipids analogues.¹⁹⁸ Small unilamellar vesicles (SUVs) were prepared by concentration of the lipid solution and re-suspension under sonication in buffer (1 x PBS). Two approaches were used for the insertion of the compounds into the synthetic membranes: the first involved incubation with the fluorophore for one hour after vesicle formation and the second involved the addition of the compound prior to vesicle preparation. Giant unilamellar vesicles (GUVs) were also prepared by electroformation. As with the SUVs, the BODIPY fluorophore was introduced using two different methods, the first prior vesicle preparation in the sucrose buffer, and the second after electroformation. Samples were prepared containing a high fluorophore concentration of 800 μM ; this was for initial proof of concept. The aim was to saturate the lipid membranes with fluorophore, maximising fluorescence emission and ensuring a detectable fluorescence response.

The fluorescence response for these samples was monitored using bulk measurements in buffer (1 x PBS) against a control of POPC GUVs and SUVs that had not been treated with any fluorophore. For both SUVs and GUVs, no detectable fluorescence emission was measured using this method. Therefore, it was also not possible to determine whether adding the compound pre or post vesicle formation had a significant impact on membrane insertion. This method was hence determined as unsuitable for measuring fluorophore-membrane interactions.

4.2.1 Confocal fluorescence microscopy with GUVs

As an alternative, confocal fluorescence microscopy was used to monitor the presence of fluorophores in membranes. Preliminary experiments were carried out using synthetic lipophilic stain, Nile Red (Figure 36, compound **56**). This fluorophore is part of the oxazine family of fluorophores; its extended conjugated structure permits a long maximum absorption wavelength of ~571 nm. Diethylamine groups (similar to those used in compounds **44a**, **47** and **48a**) are bathochromic auxochromes, capable of increasing absorption wavelengths. Further, the lone pair of the nitrogen atoms induces solvatochromism as well as environmentally dependent fluorescence emission. This fluorophore is known to interact with lipid membranes and therefore Nile Red therefore provided an appropriate control molecule for membrane bio-imaging studies using confocal fluorescence microscopy.¹⁶⁶

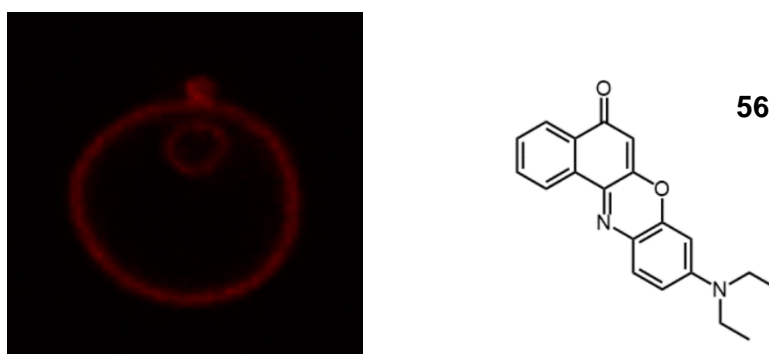


*Figure 36: Confocal microscopy image of POPC GUV after incubation with Nile Red (**56**) showing insertion into the lipid membrane. Excitation using 532 nm laser*

Nile Red was clearly detectable after incubation with POPC GUVs. This method was therefore employed for the synthesised BODIPY analogues.

4.2.2 Insertion of BODIPY fluorophores into synthetic lipophilic membranes

Eight of the analogues previously synthesised (Figure 36) showed significant environmentally dependent fluorescence emission. These were selected for membrane insertion experiments.

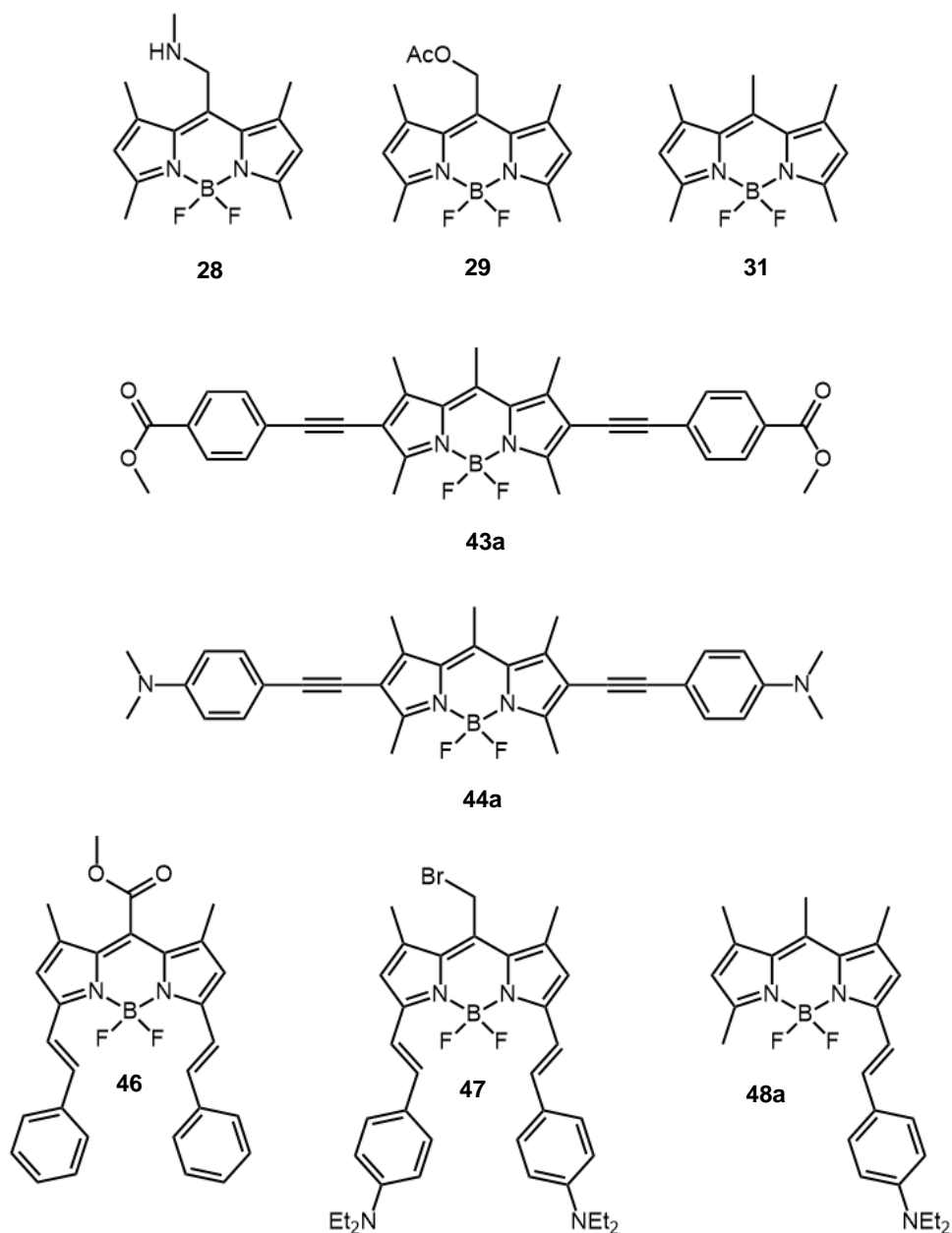
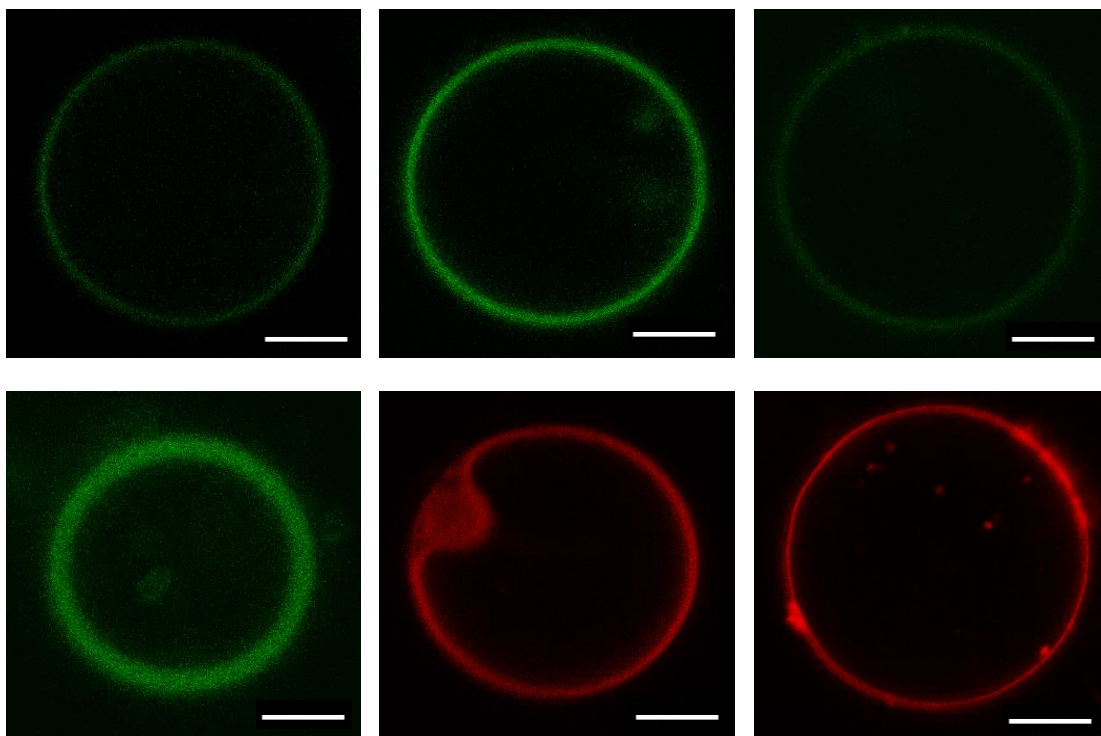


Figure 37: BODIPY analogues chosen for lipid membrane insertions, selected based on their environmentally dependent fluorescence emission profiles

Based on the photophysical profiles for each compound, it was anticipated that in all cases apart from compound **46**, measurable fluorescence emission would be detected upon insertion into the lipid membrane. For the case of compound **46**, fluorescence emission intensity decreased significantly (189 arb.u. to 47 arb.u.) when moving from polar to apolar environments, and this was expected to be reflected in the microscopy images.

All compounds were incubated with POPC GUVs for five minutes at a concentration of 100 μ M prior to visualization by confocal fluorescence microscopy. Compounds **28**, **29**, **31**, **43a** and **44a** were excited using a 532 nm laser and compounds **46**, **47** and **48a** were excited using a 635 nm laser. For most compounds, imaging was achieved within the five minutes without the need for washing to remove the excess dye to reduce background fluorescence. Good signal-to-noise ratio enabled clear visualization of the vesicles with little background interference. This demonstrates the efficient staining power of BODIPY for visualizing lipophilic environments. The resultant images are illustrated in Figure 38.

Images are false coloured green and red respectively to indicate wavelengths of light emitted (Figure 38). In the case of compounds **31** and **46**, no fluorescence emission was detected, hence these images have not been included but are available, with all full overlaid images, in the appendix (Figures A1-A3).



*Figure 38: Confocal microscopy images of POPC GUVs incubated with 100 μ M solutions of each compound. Compounds **28-44a** excited with 532 nm laser and compounds **46-48a** a 635 nm laser. Top row L \rightarrow R: compound **28**, compound **29**, compound **43a**; Bottom row L \rightarrow R: compound **44a**, compound **47**, compound **48a**. Scale bar 8 μ M*

Due to the differences in fluorescence emission intensity during fluorescence spectroscopy measurements, direct comparison between the membrane-inserting ability of the compounds is difficult. This is exacerbated by the fact that two different lasers were required as a result of the varied photophysical profiles. Attempts to normalise these data have been carried out by dividing the emission intensities of the membrane insertions by the intensities from the fluorescence spectroscopy. This allows a more direct comparison between membrane inserting affinity of the different BODIPY fluorophores. The results of these membrane insertion experiments are quantified in Table 10 to enable clearer comparison between the BODIPY analogues and to determine the suitability of each for the staining of membranes.

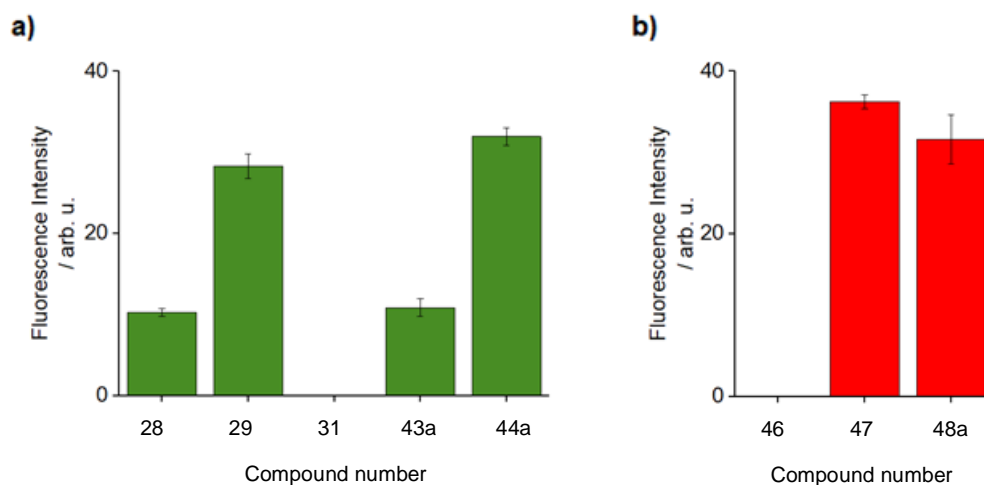


Figure 39: Relative fluorescence emission intensity produced by BODIPY analogues upon incubation with POPC GUVs using 100 μ M solutions of dyes for five minutes. a) Compounds **28-44a** all excited at 532 nm; b) Compounds **46-48a** all excited at 635 nm

Compound	$\lambda_{\text{abs/em}}$ (nm)	In_{flu} (arb. u.) ^a	In_{mem} (arb. u.) ^b	Norm. ($\div 10^3$ arb. u.)
28	505/528	107	10.26	95.89
29	511/558	776	28.33	36.51
43a	547/589	2,716	10.86	4.00
44a	590/592	5	31.96	6.39
47	699/738	564	36.28	64.33
48a	679/696	657	31.62	48a.13

Table 10: Comparison of fluorescence intensities for compounds **28-48a** and normalized to allow more accurate comparison. ^aemission intensity measured using fluorescence spectrometry and normalised to 100 μ M solutions, ^bemission intensity measured using confocal fluorescence microscopy images (Figure 38)

The easiest to analyse are compounds **31** and **46**. The former of these was anticipated to enact a strong response due to its excellent emission intensity in apolar conditions under fluorescence spectrometry (emission intensity of 367010 arb. u.). However, no detectable fluorescence emission was observed on confocal microscopy, indicating that compound **31** interacts weakly with lipid membranes. Compound **46** also did not permit membrane visualization, which could be also explained firstly by poor membrane insertion. In addition to this, compound **46** showed a significant decrease in fluorescence emission when moving from polar to apolar environments of 189 to 47 arb.u., and hence at least a poor signal-to-noise ratio was expected. For both compounds, even increasing the laser intensity and signal/background contrast failed to reveal the vesicles.

Compounds **28** and **29** both provided a facile means to visualize the GUVs using green light. The confocal microscopy results in Figure 38 and Table 10 indicated that compound **29** has ~2.8 times greater fluorescence emission intensity upon insertion into the lipid membrane compared with compound **28**. However, it is inconclusive as to whether this is due to greater localization within the membrane. Fluorescence spectroscopy (Chapter 2) showed that compound **29** has an emission response in apolar solution that is over seven times more intense than that of compound **28**. Despite this, the detectable emission for compound **29** upon insertion into the membrane was only ~2.8 times more than compound **28**. It could hence be argued that an amine group at the *meso* position of BODIPY, despite decreasing fluorescence emission intensity, leads to an increased affinity for lipid membrane localization.

Compound **43a** demonstrated excellent potential on fluorescence spectroscopy, with intense environmentally dependent fluorescence emission (Chapter 2, 2716 arb. u. in apolar solvent and 149 arb. u. in polar solvent). Compound **44a** on the other hand had a weak fluorescence response in both a polar and apolar environment (24 and 22 arb.u., respectively). However, compound **44a** showed superior vesicle staining, with more than a three-fold increase compared with compound **43a** (Figure 38, Table 10). This indicates that the affinity for membrane insertion is improved by the presence of dimethylamine groups compared with ester groups. In addition,

auxochromic substituents have shown capability to improve the binding of dyes to structures by electrolytic dissociation throughout the molecule, further supporting this hypothesis. Although confocal microscopic images showed some evidence of weak signal-to-noise ratios, it can be concluded that compound **44a** shows promise as a building block for a biological membrane stain. Despite this, compounds **43a** and **44a** were not selected for biological studies due to their poor solubility in apolar solutions; as a result, fluorescence spectroscopy in an apolar solvent (Chapter 2) was carried out in DCM and compared with DMSO as the polar solvent. It was feared that the low lipophilicity of compounds **43a** and **44a** could result in intracellular aggregation and subsequently, cytotoxicity. However, these compounds provide a basis for the future design of more biologically compatible fluorophores as well as an insight into methods that can be used to improve the lipophilic membrane affinity of BODIPY fluorophores. With careful modification to increase hydrophilicity, compound **44a** could be a promising membrane specific stain.

Compounds **47** and **48a** showed strong staining of the lipid membranes compared with compound **46**. Given that fluorescence emission intensity tends to decrease with increasing wavelength, the intense fluorescence emission on confocal microscopy for compounds **47** and **48a** (36.28 and 31.62 arb. u., respectively) were amongst the highest for the fluorophores examined (Figure 38). These data demonstrate the membrane staining efficiency of these longer wavelength BODIPY fluorophores. Their large lipophilic design lends itself to effective membrane insertion with intense fluorescence emission upon reaching a target. These results support the theory, suggested by the confocal microscopy images from compounds **43a** and **44a**, that dialkylamine groups promote anchoring of BODIPY fluorophores within a membrane. This is further reinforced by the slightly lower emission intensity measured using spectrometry for compound **48a** (Chapter 2), suggesting that membrane uptake is higher for compound **47** (compound **47**, 564 arb. u.; compound **48a**, 657 arb. u.). In addition, areas of greater fluorescence emission observed within the membrane for compound **48a** could indicate increased membrane localization, potentially as a result of aggregation. It is possible that this event could artificially influence the fluorescence emission response, depending on the density of aggregation and resultant fluorescence quenching from any π - π stacking interactions.

It was projected therefore that compound **47** provided a more desirable bio- and photophysical profile than compound **48a**, due to it having the highest fluorescence emission intensity upon membrane insertion out of all the compounds (Table 10). The other key reason for this is the greater environmentally dependent fluorescence shown by compound **47**, whereby moving from polar to apolar solvent evokes a more than 35-fold increase in emission intensity. This increase is less than 1.5 for compound **48a**. Additionally, in apolar solution, the emission wavelength for compound **47** is ~20 nm higher, permitting its use towards the infra-red. Compound **47** also boasts a higher extinction coefficient in an apolar environment (more than five times that of compound **48a**). The bromine *meso* group also gives potential for chemical conjugation to other species, such as small molecules or proteins. This could broaden the use of compound **47** for a wide variety of procedures from fluorescent tagging to bio-modification.

Overall, compound **47** gave the most favourable profile with respect to long absorption wavelength, high intensity fluorescence emission, strong specific association with lipid membranes, good solubility in polar and apolar extremes, and low signal-to-noise ratio upon imaging. These characteristics are fundamental for a successful fluorescent membrane probe.¹⁹⁹ The compact amphiphilic design also counters common issues of long wavelength fluorophores of large and predominantly lipophilic structures. Common issues can include poor biological compatibility, low intensity fluorescence emission and limited retention within lipophilic membranes.⁴⁶ It was expected that compound **47** could offer a means to combat these and provide an alternative tool for biological membrane visualization. Furthermore, the 13-fold increase in PLQY for compound **47** in apolar environments relative to polar environments (Chapter 3, Table 9) further supports the hypothesis that this analogue could allow excellent signal-to-noise ratios upon target binding. Hence, compound **47** was selected as the lead structure for more in-depth biological studies *in vitro*.

4.3 Visualization of cytoplasmic membranes with BODIPY compound **47**

4.3.1 Staining of live cells

The suitability of these BODIPY analogues to selectively visualize lipophilic membranes was confirmed for compounds **28-48a** using vesicles as biological membrane mimics. As the best candidate, compound **47** was used to visualize lipid bilayers in biological cells *in vitro*. Hypopharyngeal squamous carcinoma cells (FaDu) were selected given their slow growth rate, versatility and stability.²⁰⁰ Initial experiments in live cells used compound **47** at a concentration of 10 μ M. This low concentration was selected as it is suspected that BODIPY could be toxic to cells above this.²⁰¹ For each plate, co-staining was carried out using nuclear stain DAPI in order to precisely determine the location of cells whilst minimising background noise. This stain was selected as it does not possess a fluorescence profile that overlaps with compound **47**. It is therefore possible to use separate lasers to achieve a fluorescence response for the different stains. All experiments were carried out in triplicate with incubation periods of either five, seven, thirty or sixty minutes. Images were achieved using 633 nm and 405 nm lasers for BODIPY and DAPI respectively. The results are shown in Figure 40.

The resultant confocal microscopy images clearly indicate that sufficient and selective visualization of cell membranes was achieved within an incubation time of five minutes (Figure 40). Compound **47** provided clear and specific staining of the extracellular membrane of the cells. The overlaid images supported this with little localized overlap between the nuclear and BODIPY stains. The increased incubation periods demonstrated a clear correlation between increasing detectable fluorescence emission and incubation time. With live cells, it was clear that for incubation periods above thirty minutes, localization of compound **47** was achieved to an extent that oversaturated detection of the fluorescence response. This could have the potential to perturb the detection of other fluorophores if used in multi-channel experiments. Hence, it was clear that long incubation times were not required for the visualization

of live cell membranes with compound **47**. This is particularly beneficial not just for staining efficiency, but it also increases compatibility with other time sensitive protocols.

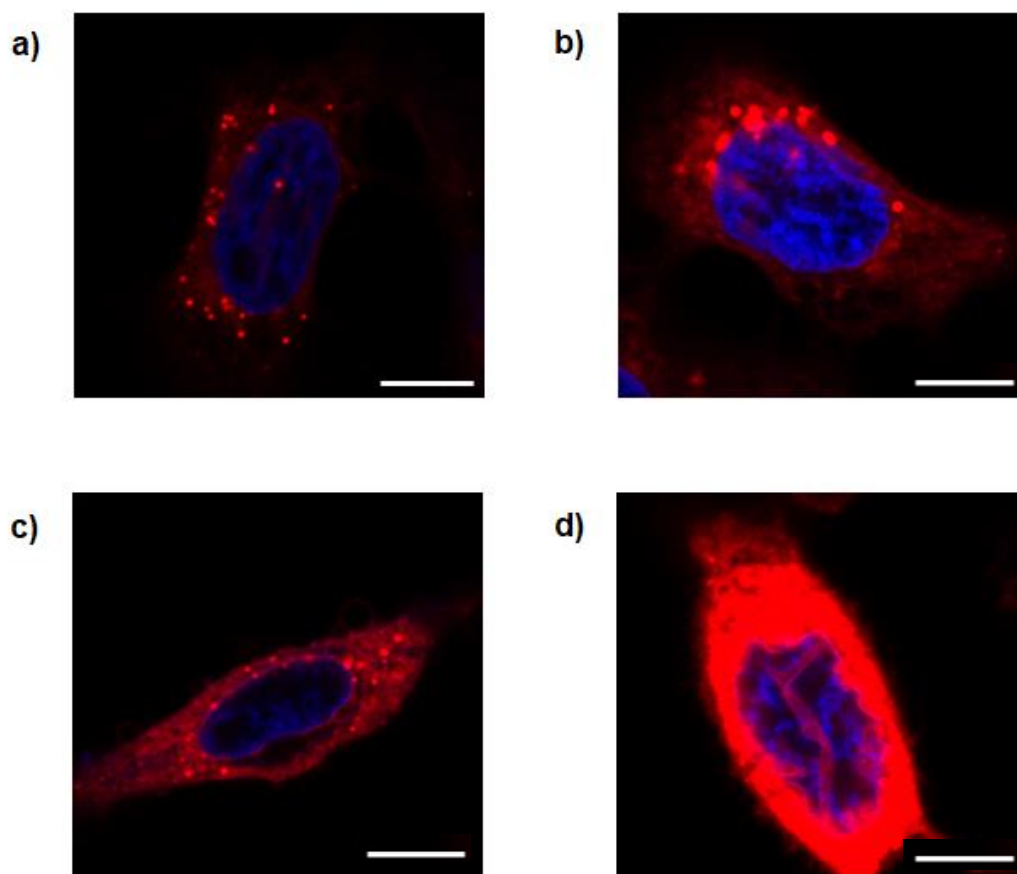


*Figure 40: Confocal microscopy images of live FaDu cells after incubation with 10 μ M solution of compound **47** for 5 (a), 7 (b), 30 (c) and 60 (d) min. Excitation using 633 nm laser beam for red channel and 405 nm laser beam for blue channel. Single channel images available in the appendix. Scale bar 10 μ M. for all except 60 min, 8 μ M*

4.3.2 Cell viability studies using MTT assays

MTT assays were carried out to confirm the non-toxicity of the dye towards FaDu cells. This was done using concentrations of compound **47** of up to 50 μM , five times the concentration which was shown to be required for the sufficient staining of live cells. The assays were incubated for 24 hours and carried out in duodecuplicate. From baseline up to 24 hours, cells treated with up to 50 μM solutions of compound **47** showed little sign of metabolic stress or change in percentage proliferation in comparison to untreated control cells (0 mM). This study demonstrates the suitability of compound **47** as a non-cytotoxic *in vitro* probe due to no evidence of impacted cell viability. A summary of the assay readout can be seen in Figure 41.

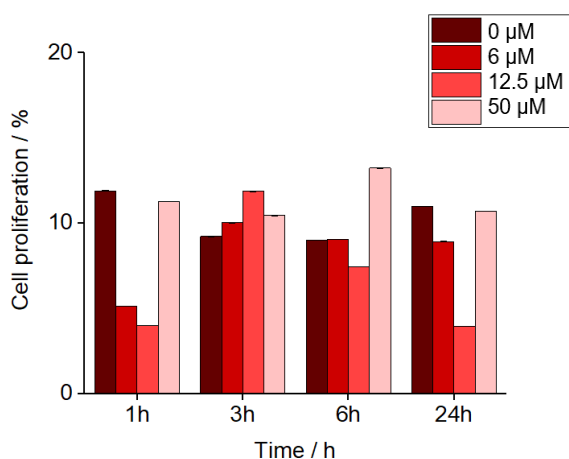


*Figure 41: MTT assay readout for the treatment of FaDu cells with compound **47** over 24 hours. Cells showed little increase in proliferation at up to five times the concentration used for live cell staining in comparison to untreated cells. The data represent averages and standard deviations from duodecuplicate repetition of the experiment*

4.3.3 Interaction of compound **47** with FaDu cells pre and post fixation

To explore the potential of membrane visualization with compound **47**, the robustness and limitations of its staining ability were explored further. This initially involved determining whether staining of the lipid membrane was retained during the fixation process. Live FaDu cells were treated with compound **47** (10 μ M solution in 1 x PBS) for 5, 30 and 60 minutes before fixation with para-formaldehyde (3.75%). The results are shown in Figure 42.

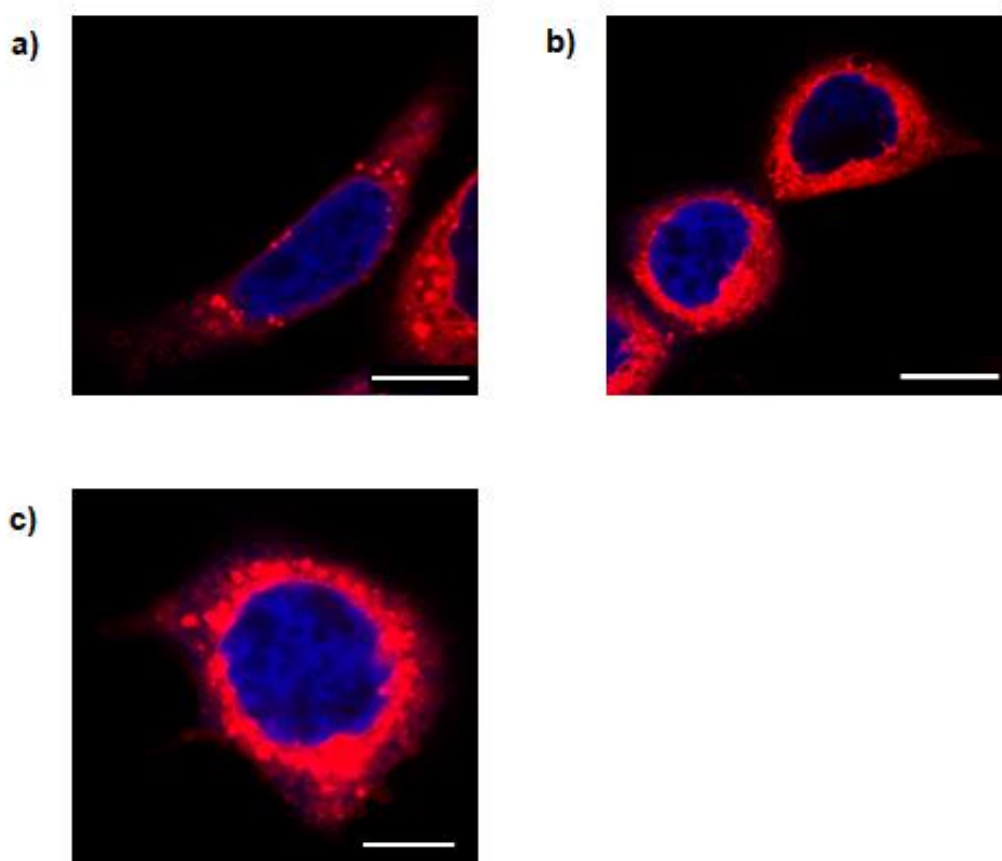
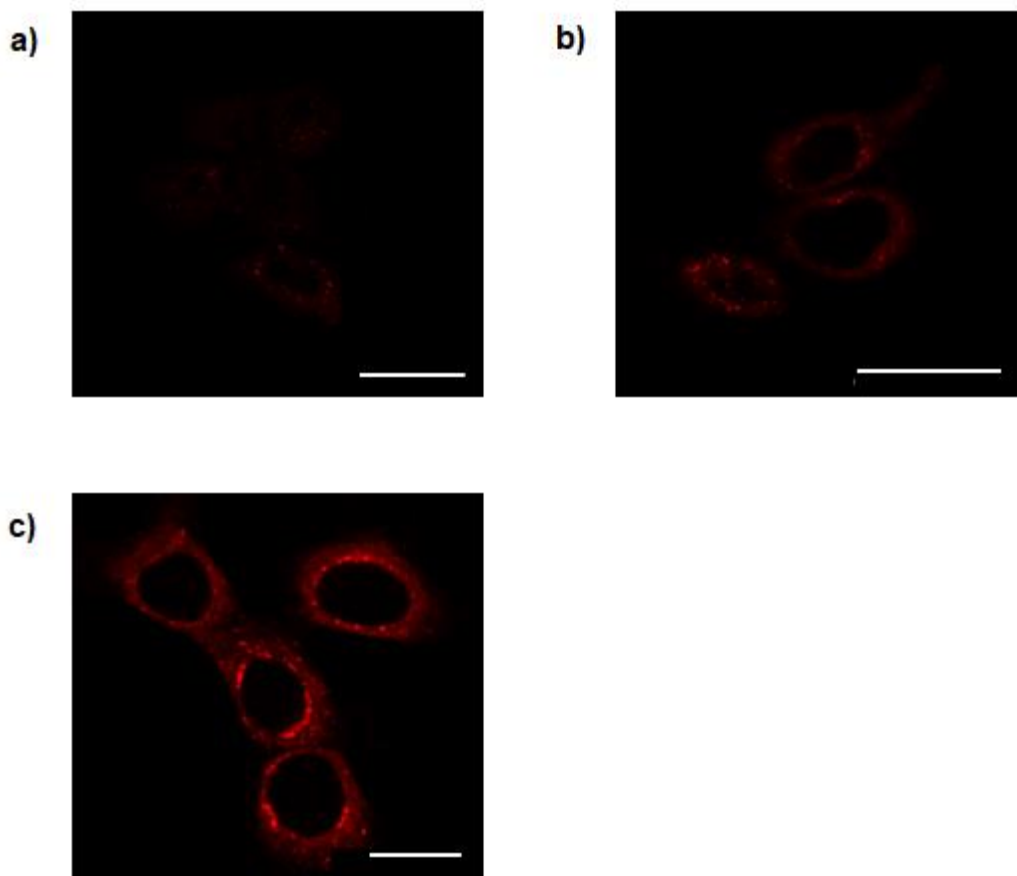


Figure 42: Confocal microscopy images of FaDu cells after incubation with 10 μ M solution of compound **47** for 5 (a), 30 (b) and 60 (c) min followed by immediate fixation with paraformaldehyde (3.75%). Excitation using 633 nm laser beam for red channel and 405 nm laser beam for blue channel. Single channel images available in the appendix. Scale bar for 5 and 30 min images, 10 μ m. For 60 min image, 8 μ m

For all samples, excellent retention of the BODIPY dye in the membrane was observed, with detectable fluorescence emission in all cases. With this success, efforts were turned to the staining of cells after fixation. Here, para-formaldehyde (3.75%) was used to fix FaDu cells, which were subsequently treated with compound **47** (10 μ M solution in 1 x PBS) for 5, 30 and 60 minutes (Figure 43).



*Figure 43: Confocal microscopy images of FaDu cells after fixation with paraformaldehyde (3.75%) followed by incubation with 10 μ M solution of compound **47** for 5 (a), 30 (b) and 60 (c) min. Excitation using a 633 nm laser beam. Single channel images only have been included to aid visualization. Full single channel and overlaid images available in the appendix. Scale bar, 25 μ m*

Single channel images are shown here for clarity. For the five minute incubation period, the detection of the fixed cells using compound **47**, was significantly less successful than for live cells. However, although detection of the fixed cells was

possible, it could be improved by increasing incubation times, increasing fluorophore concentration, or altering the confocal microscope settings to increase contrast or fluorescence intensity. This was not carried out here in order to permit reliable comparisons of fluorescence emission intensity between the cells undergoing each treatment. After 30 minutes however, staining of the fixed FaDu cells was clear, permitting visualization of the cell membranes.

The comparative fluorescence emission intensity between live FaDu cells and cells stained pre and post fixation is quantified in Figure 44. In all three of the experimental conditions, an increase in detectable fluorescence emission took place with increasing incubation time, as anticipated.

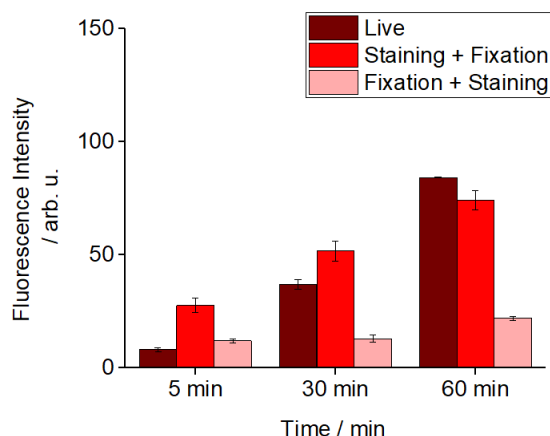


*Figure 44: Effect of incubation time on fluorescence intensity in live cells, cells fixed post-staining (staining + fixation) and cells fixed pre-staining (fixation + staining). All incubations carried out using 10 μ M solutions of compound **47** in 1 x PBS buffer. The data represent averages and standard deviations from quadruple repetition of experiment*

Of particular interest is the increased fluorescence intensity for FaDu cells fixed after incubation (staining + fixation) relative to the live cells. This was most apparent for samples incubated for 5 and 30 minutes. The most logical explanation for this is a side effect of molecular retention of the fluorophore within the lipid bilayer. Despite multiple washes, it is possible that unbound BODIPY dye was present during the

fixation process, artificially amplifying the fluorescence response by the increasing the incubation time unintentionally.

Although staining after fixation permitted visualization of the cytoplasmic membrane and intracellular compartments, the intensity was significantly lower. This can be attributed to reduced accessibility to the membrane for the dye, caused by the cross-linked bilayer structure.

Although fast and efficient staining of fixed cells (fixation + staining) is desirable for many biological applications, it is not essential. The excellent staining of live FaDu cells and the clear retention of compound **47** within the membrane during subsequent exposure to para-formaldehyde support the desirability of this probe. Thus, the data suggests that this BODIPY compound is compatible with the sensitive staining of bilayers in both live and fixed cells, and is retained during the fixation process.

4.3.4 Permeabilization studies

A fundamental aspect of many cellular assays requires the permeabilization of the cell membrane, normally with detergent, to facilitate the movement of larger molecules into the cell. This is vital particularly for larger substrates such as antibodies during immunofluorescence microscopy that are too large for passive diffusion through an intact lipid bilayer. Hence it is beneficial for a membrane stain to be sufficiently resistant to detergent induced lipid bilayer disruption. Typical permeabilizing detergent, Triton X, was used for this study. Cells were first incubated with compound **47** under the previously used conditions (10 μ M solution in 1 x PBS) for 30 minutes, followed by fixation with para-formaldehyde (3.75%). Treatment of the cells was carried out during visualization in order to monitor the effects of permeabilization over time. A 0.2% solution of Triton X was used, twice the concentration normally required for this protocol. This was done to fully realise the effects of membrane perturbation on the detection of cellular membranes using compound **47**. Data was collected using continuous scanning and response detection over the course of 10 minutes. This long time period was selected as sufficient

permeabilization of the extracellular membrane for studies such as biological trafficking is typically achieved in much shorter time frames.

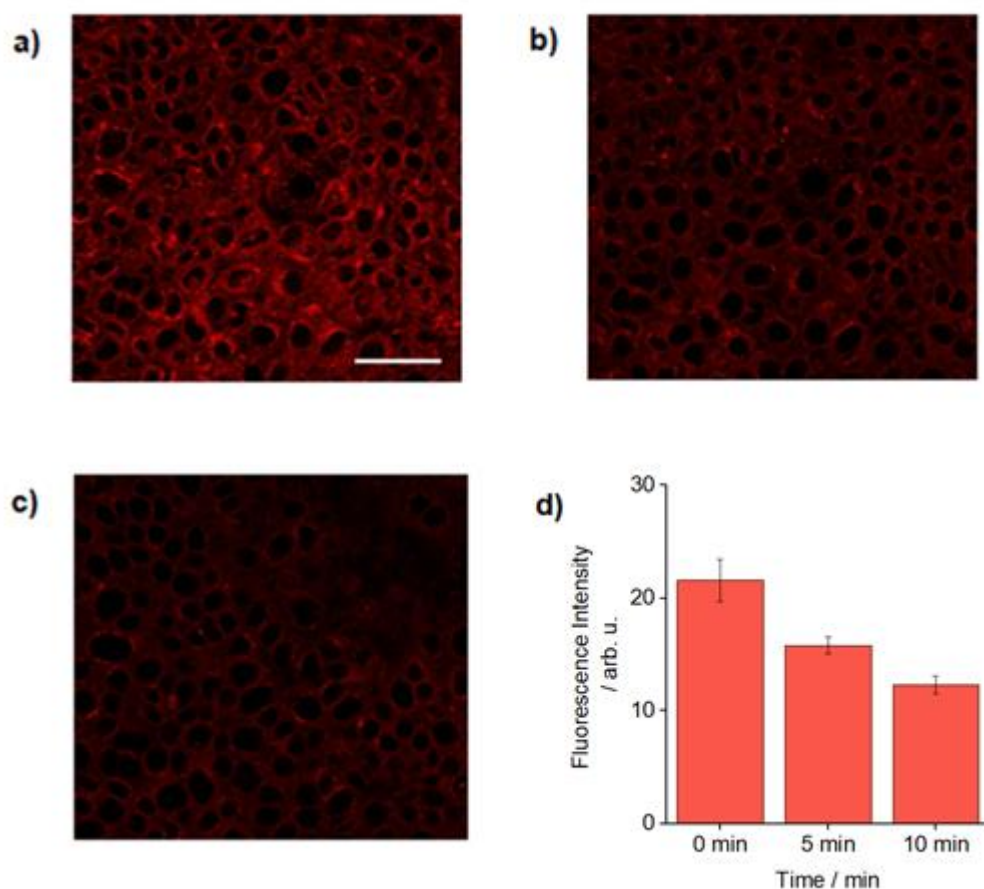


*Figure 45: Confocal microscopy images of FaDu cells before treatment (a) and after treatment with 0.2% Triton X for 5 (b) and 10 min (c), after staining with compound **47** for 30 min. A concentration of 0.2% Triton-X is higher than 0.1% usually used for permeabilization. Scale bar 50 μ m; d) effect of permeabilization on fluorescence intensity over time. The data represent averages and standard deviations from quadruple repetition of sampling*

Over the course of the 10 minutes (Figure 45), the images clearly indicated a decrease in fluorescence emission intensity over ten minutes. Despite this small decrease in intensity (less than 50%), the cell membranes were still clearly visible under the confocal microscopy. This resistance to permeabilization is unusual for membrane dyes, which are often not retained in the lipid bilayer during lipid

perturbation. Notably, during the continuous scanning, depletion of the DAPI nuclear stain response was also observed. It is possible that loss of fluorescence response was exacerbated by the continuous excitation with the laser. This could have caused photo-bleaching of the fluorophores and, with the lack of antifade agents to reduce this effect, could explain the decrease in emission intensity in response.

As an alternative, stained and fixed FaDu cells (under the same staining conditions as previously described) were treated with Triton X and visualized after 10 minutes without continuous exposure to the laser. This proved much more successful; the results of this are shown in Figure 46.

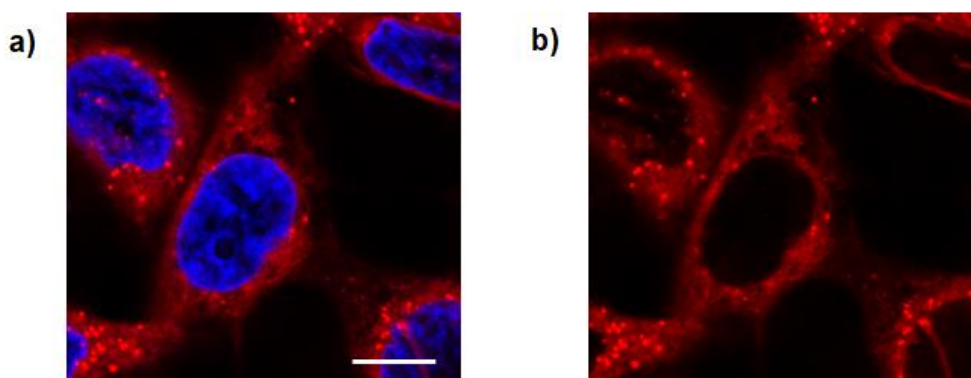


Figure 46: Confocal microscopy images of cells fixed with para-formaldehyde (3.75%), incubated for 60 min with compound 47 and treated with 0.1% Triton X. Imaging was carried out after 10 minutes. The images show a) DAPI (blue channel) and compound 47 (red channel); b) compound 47 (red channel) only

These confocal images taken without continuous excitation/scanning with the laser gave a clearer picture of effect of permeabilization on the retention of compound 47 in the membrane. Very little fluorescence emission was lost during this protocol despite perturbation of the membrane. Hence it was determined that compound 47 was a suitable tool for more advanced cell biological studies.

4.3.5 Cell membrane trafficking with immunofluorescence microscopy

After establishing compatibility with permeabilization methods, the suitability of compound **47** for use in combination with other cellular exploratory tools was established. The BODIPY dye was therefore used in an immunofluorescence microscopy assay to explore the compatibility of compound **47** with other cell biological techniques. Live FaDu cells were first incubated with a 10 μ M solution of compound **47** in PBS (1x solution) for one hour to ensure maximized detectable insertion of the fluorophore into the lipid bilayer. This was followed by a complete immunofluorescence preparatory protocol, including fixation with paraformaldehyde (3.75% solution), permeabilization with Triton X (0.1% solution) and blocking with BSA. The latter process was undertaken to minimize non-specific binding of antibodies and ensure that any positive immunofluorescence responses were genuine. The chosen primary antibody was LAMP1-H483 from rabbit, active against lysosomal membranes. This was used in conjugation with secondary antibody Donkey A488 anti-rabbit, which contained the Alexa488 fluorophore. This particular fluorophore was selected due to lack of overlap between nuclear stain DAPI and compound **47**, permitting the use of three individual channels on the confocal fluorescence microscope.

The resultant images (Figure 47) indicated that despite a reduction in fluorescence emission intensity, compound **47** was clearly retained within the cell membrane during this procedure. Visualization of the membrane was therefore still possible during immunofluorescence microscopy. The results also demonstrated that the trafficking of antibodies into the cell is unperturbed by the presence of BODIPY fluorophore **47**. This shows the excellent biocompatibility and promising application of this fluorophore.

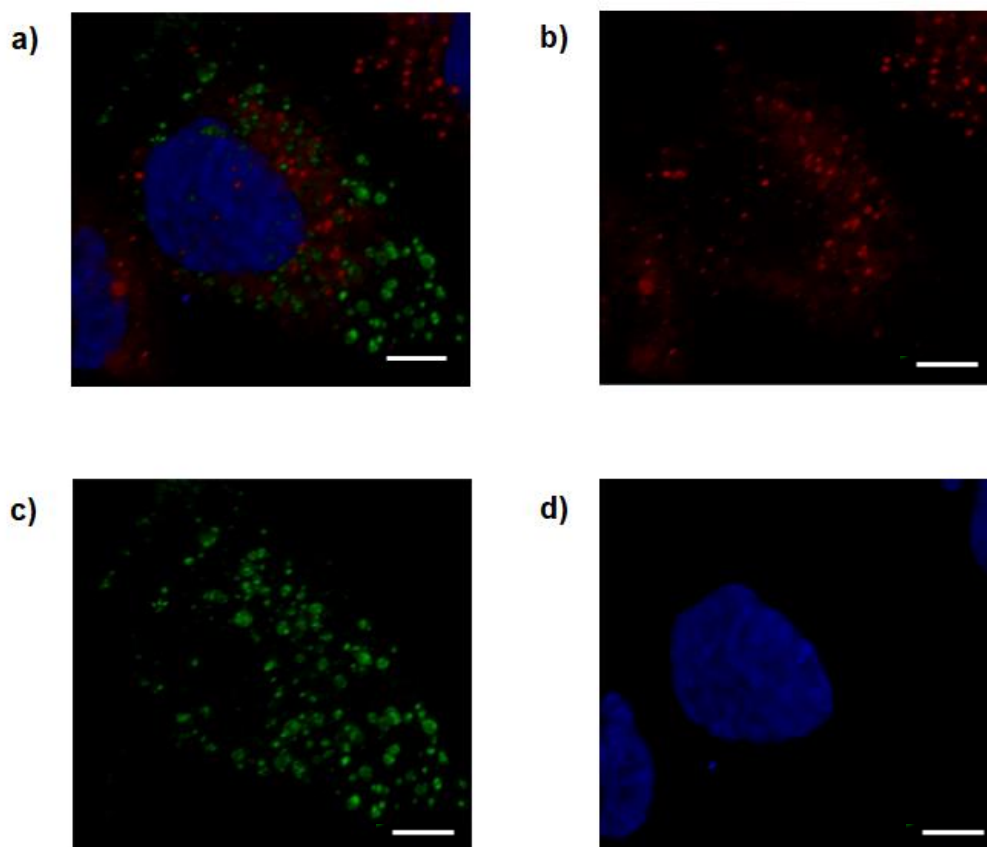


*Figure 47: Immunofluorescence microscopy. Confocal microscopy images of FaDu cells fixed with paraformaldehyde (3.75%) before 60 min incubation with compound **47**, treatment with 0.1% Triton X, blocking with BSA (5% in PBS) and incubation with LAMP1-H48a3 antibody followed by Donkey A48a8 anti-rabbit secondary antibody. The colour channels are 405 nm for DAPI (blue), 532 nm for A48a8 (green) and 633 nm for compound **47** (red). Single-channel images are included to show sufficient retention of the fluorophore in the membrane after permeabilization and successful antibody trafficking. a) all channels; b) compound **47** (red); c) A48a8 (green); d) DAPI (blue). Scale bar 5 μ m.*

Further to this, the nature of immunofluorescence microscopy protocols requires experiment lengths of at least a few days. Typically, staining of the membrane would need to be carried out during the earliest stages of the protocol. The retention of BODIPY fluorophore **47** within the membrane during this time demonstrates the longevity of staining, which is not eradicated over time. This further supports the suitability of compound **47** as a versatile cell biological stain.

The secondary intention of this cell trafficking was to establish an explanation for the increased localization of compound **47** in particular areas of the lipid bilayer. This was consistently observed in all staining experiments and showed a significant increase with increasing incubation times. It was hypothesized that co-localization with lysosomes within the extracellular membrane could indicate a more highly specialized and facile alternative to fluorophore-labelled antibodies. The overlaid images from the immunofluorescence however do not indicate a correlation between lysosomal membranes active towards LAMP1-H483 antibodies and the BODIPY dye. This suggests that compound **47** is not preferentially staining these particular targets. Although it must be acknowledged that the root cause of this accumulation could be aggregation within the membrane, it could be possible to determine an alternative cause for this increased localization by carrying out immunofluorescence microscopy with a range of different antibodies until a “match” is detected. Despite this, if aggregation is the cause, the MTT studies indicate that this is not accompanied by cytotoxicity, due to the lack of metabolic disruption suggested by the MTT assay readout. Hence, compound **47** retains its status as a smart switchable near infra-red fluorophore for the specific and sensitive imaging of membranes.

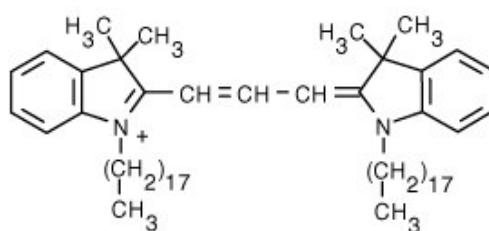
4.4 Discussion

Compound **47** has proven to be a smart, switchable near infra-red fluorophore that has been successfully used for the sensitive and target specific bio-imaging of cells *in vitro* at low concentrations. Staining of synthetic membranes (GUVs) and live and fixed cancer cells (FaDu) has been achieved with excellent signal-to-noise ratio, with compound **47** retained in the lipid membrane for 72 hours. This is vital in the accurate visualization of cellular structures to reduce the chances of “false positives” or off-target staining. Compound **47** also survives both the fixation and permeabilization processes; the low cytotoxicity, as determined using MTT assays, furthers the value of this BODIPY fluorophore. Its compatibility with cell biological studies, such as immunofluorescence microscopy, with minimal interference to antibody trafficking, has not been demonstrated for many cell biological stains.²⁰²

Other BODIPY fluorophores that have been used for bio-imaging have often required extensive washing to remove all traces of fluorophore to prevent background fluorescence emission.²⁰² This is vital to ensure high target accuracy and prevent off-target visualization. In contrast to this, the high signal-to-noise ratio of compound **47** means that membrane staining can be carried out without the risk of background fluorescence emission. In addition to this, many other BODIPY fluorophores have required longer than 5 minutes for visualization to occur, sometimes up to 30 minutes to achieve sufficient detectable fluorescence emission.^{202–204} Furthermore, resistance to fixation is not a characteristic seen in all BODIPY membrane fluorophores; for example in 2016, Hirata *et al.* presented a promising near infra-red BODIPY fluorophore, however it did not survive the fixation or even the washing process.^{202,205}

A key commercial competitor for compound **47** is currently marketed as CellBrite 640 and is a fluorophore from the cyanine family that is active at 640 nm.²⁰⁶ Figure 48 provides a direct comparison between CellBrite 640 and compound **47**. Some key characteristics of CellBrite 640 are similar to those of compound **47**: long absorption

wavelengths, biological compatibility and fast incubation times, which are all crucial to a successful fluorescent probe used for bio-imaging.



	CellBrite 640	47
Long absorption wavelength	Yes	Yes
Compatible with cells	Yes	Yes
Fast incubation (< 5mins)	Yes	Yes
Survives fixation	Yes	Yes
Survives permeabilization	Yes	Yes
Live and fixed cells	No	Yes
Specific extracellular localisation	No	Yes

*Figure 48: Comparison of the fluorophore profiles of CellBrite 640 (pictured) and compound **47***

However, a key shortcoming of CellBrite 640 is that it cannot be used to stain fixed cells. In addition to this, the dye becomes internalized into the cell if used to stain live cells for more than 24 hours.²⁰⁶ In contrast, compound **47** was retained in the

membrane for up to 72 hours and has a longer absorption wavelength in apolar solvent of 699 nm. Moreover, the specific localization of compound **47** within certain components of the cellular membrane is not observed in CellBrite. In the future, if this increased localization was found to be a co-localization with a specific cellular component, this could dramatically improve the value of compound **47**. This would be particularly notable if the increased staining affinity were to be to a cellular component that is a hallmark of a certain disease or cellular process. This could therefore open the door to a diagnostic application for compound **47**. Despite this, at present, compound **47** does not have the capacity to significantly challenge the commercial market as a superior bio-imaging agent for cell membranes. It does however provide a platform for the development of membrane targeting fluorophores that are based around the BODIPY scaffold. The SAR developed during this work will therefore assist in the intelligent design of fluorophores with properties optimized for applications including, but not limited to, biological imaging.

Cell biological studies were carried out with the support of Dr Loris Rizello

Chapter 5

Conclusions and further work

5.1 Summary

The aim of this work was to develop a series of small molecules capable of performing as long wavelength fluorophores with a range of applications. A series of seventeen analogues based on the BODIPY scaffold were successfully synthesised and characterised to develop photophysical profiles. This involved UV/Vis spectroscopy, fluorescence spectroscopy and DFT modelling to establish HOMO/LUMO energies and electronic distributions. Correlation between nature and loci of substituents and resultant photophysical properties was established.

In summary, increasing the size of the conjugated system, as anticipated, effected an increase in maximum absorption wavelength. This was achieved at both the 2,6 and 3,5 positions of BODIPY, but was most efficiently carried out at the 3 and 5 positions. The increases in absorption wavelengths ranged from 35 nm at the 2 and 6 positions, to 209 nm at the 3 and 5 positions of the BODIPY core. A significant improvement was observed when auxochromes such as dialkylamine groups were introduced. Here, an increase in absorption wavelength of 77 nm was measured when two diethylamine groups were incorporated into the conjugated system. An improvement in molar absorptivity was also observed with methyl or hydroxyl groups at the *meso* positions and by heavy atoms such as iodine at the 2 and 6 positions. With respect to fluorescence emission, increases in emission intensity were observed with methyl

and hydroxyl *meso* groups. Auxochromes also caused an intensity increase; however, this was mostly measured when substituents were located at the 3 and 5 positions. With increasing conjugation size and number of amine groups also occurred environmentally dependent fluorescence emission, where a more intense response was measured in an apolar solvent, sometimes with complete fluorescence quenching in a polar environment.

Overall, the greatest destabilisation of the HOMO was achieved by substitution at the 3 and 5 positions of BODIPY and incorporation of amines, whereas the inclusion of halogen species universally improved HOMO stability. LUMO energies varied to a lesser degree; however, similar trends were established with respect to amine and halogen groups, with conjugated systems conversely providing partial stabilisation. In general, narrowing of HOMO-LUMO gaps was typically a destabilisation of the HOMO, and seemed particularly exacerbated by amine groups.

Eight of the analogues that showed environmentally dependent fluorescence emission were used to image lipid bilayer mimics. These GUVs were characterised using confocal fluorescence microscopy and it was determined that amine groups significantly improved the proclivity of BODIPY compounds for membrane insertion.

The most spectroscopically promising compound (**47**) was used for more extensive studies. These involved measuring HOMO and LUMO energy levels in different solvents using DFT. Moreover, the probability of molecular orbital transitions, the fluorescence decay lifetimes, and PLQY were determined using DFT and TCSPC/PL respectively. Increasing the polarity of the global solvent was shown to have key impacts on the photophysics of compound **47**: the probability of π - π^* transitions improved by 20%, decay lifetimes were shortened by 3% when moving from ether to MeOH and photoluminescence yields were lowered by almost 9%. The latter two factors suggest that compound **47** would possess a more useful photophysical profile in an apolar environment, supporting its use as a probe for lipophilic environments. Unfortunately, it was not possible to detect the presence of excited triplet states for compound **47** using TAS; however, this indicates that photons are not significantly lost to phosphorescence and are instead available for fluorescence emission.

In light of these results, cell biological membrane staining was carried out. This was successful typically within five minutes in live cells and when staining cells pre and post fixation, although the latter showed a marked decrease in fluorescence emission intensity. The BODIPY fluorophore also showed little cytotoxicity and was stable to membrane permeabilization. It also demonstrated good compatibility with other cell biological techniques, and when immunofluorescence microscopy was used to monitor cellular trafficking of antibodies, this was unperturbed by the presence of the fluorophore in the membrane. Furthermore, visualization of compound **47** was still possible after the study, over the course of three days, indicating the robust nature of the cell staining which has the potential to challenge commercially available near infra-red membrane stains. These factors overall demonstrate the versatility and suitability of compound **47** as a long wavelength probe for the selective staining of cell membranes.

5.2 Future outlook

Although many aims were achieved during this work, it was unfortunately not possible to synthetically achieve all designed analogues. Further work in this area would primarily strive towards the achieving BODIPY fluorophores with carbonyls adjacent to the BODIPY core. This could enable exploration into the fluorescence quenching ability of carbonyl groups on BODIPY. Furthermore, conjugation of nucleosides to the longer wavelength BODIPY moieties such as compound **47** could be explored in more detail. This would not only improve our understanding of fluorophores, but also demonstrate their suitability as fluorescent tags on biological molecules.

Expansion of synthetic designs based on photophysical profiles could also be achieved. For biological membrane targeting, this could include for example, even larger conjugated systems at the 3 and 5 positions of the BODIPY core with the incorporation of auxochromes such as amine groups. Both of these would be expected to contribute to increasing maximum absorption wavelength and improving *in vivo* potential. Moreover, the dialkylamine auxochromes, as established here,

would also be anticipated to improve membrane affinity, allowing greater targeting efficiency.

Further exploration of the potential of compound **47** would also be valuable. Ideally, biological membrane staining could be expanded to include other cell lines. This could also permit establishment of concentration limits, to monitor the minimum concentration required for sufficient bio-imaging. These studies could be carried out in tandem with determining the longevity of membrane retention of compound **24**, which here was determined to be at least three days. Whilst showing compatibility with cell biological techniques such as immunofluorescence microscopy, the limits of this could be investigated. This would include use of the fluorophore with, for example, radioactive tracing or enzyme immunoassays. Finally, a full comprehensive study into the precise localization of compound **47** within lipophilic membranes could be carried out. This would establish the reasons, if more complex than aggregation, behind the increased localization of the BODIPY fluorophore in particular portions of the membrane.

With these future works, it could be possible to ultimately produce a long wavelength multi-functional fluorescent probe that is able to precisely target specific cellular components. This could lead to specialised drug delivery that could be easily monitored with excellent spatial and temporal control.

In addition, a project exploring the synthetic methodology could be undertaken, particularly for compounds **43a**, **44a** and **48a** in order to determine and rationalise the mechanisms occurring during loss of the acetoxy group from the *meso* position.

Further to this, compounds **36** and **37** have been successfully used as sensitizing dyes in dye sensitized solar cells (DSSCs).²⁰⁷ BODIPY compounds **36** and **37** have both been successfully employed in the clean conversion of light to electricity within a DSSC. Although efficiencies were not as high as other sensitizing dyes in the literature, it has proved the potential for BODIPY analogues active towards the near infra-red for use in DSSCs. Ideally a dye used in these photoelectrodes would also absorb light at even longer wavelengths, in order to promote the most efficient light

harvesting. However, this set-up is still useful, and provides a means to generate power.

Whilst power conversion efficiencies were fairly low ($\sim 0.05\%$), the fill factor readings suggest that these dyes are promising. In order to improve solar cell efficiency and maximise the harvesting of light, steps could be taken to reduce electron recombination within the cell. These could include incorporating additional photoelectron trapping centres (such as AuNPs), reducing the incidence of I_3^- reaching the TiO_2 surface using a molecular monolayer such as polphenylene, or modifying protocols to minimise the occurrence of dye aggregation.

To improve efficiencies further, longer wavelength BODIPY analogues could be generated by further modifications to compounds **36** and **37**, or adapting compounds **47** or **48a** to allow them to be used in DSSCs by adding carboxylic acid groups. In addition to this, incorporating a range of dyes and additives with a variety of absorption wavelengths could in fact create a wider range over which light is absorbed. This could in turn improve the efficiency of light harvesting, and thus demonstrates that even chromophores active under green light can be a beneficial addition to DSSCs.

Chapter 6

Bibliography

1. Ellis-Davies, G. C. R. Caged compounds: photorelease technology for control of cellular chemistry and physiology. *Nat. methods*. **4**, 619–28 (2007).
2. Imming, P., Sinning, C. & Meyer, A. Drugs, their targets and the nature and number of drug targets. *Nat. Rev. Drug Discov.* **5**, 821–834 (2006).
3. Melorose, J., Perroy, R. & Careas, S. *Textbook of Receptor Pharmacology. Statewide Agricultural Land Use Baseline* (2015).
4. Anderson, R. R. & Parrish, J. A. The Optics of Human Skin. *J. Invest. Dermatol.* **77**, 13–19 (1981).
5. Abrahamse, H. & Harith, M. A. Photodynamic cancer therapy—recent advances. in *AIP Conf. Proc.* vol. 1380 5–11 (2011).
6. Altshuler, G. B. & Yaroslavsky, I. Absorption characteristics of tissues as a basis for the optimal wavelength choice in photodermatology. *Palomar Medical Technologies Inc.* (2004).
7. Mustafa, F. H. & Jaafar, M. S. Comparison of wavelength-dependent penetration depths of lasers in different types of skin in photodynamic therapy. *Indian J. Phys.* **87**, 203–209 (2013).
8. Chen, A. C.-H. *et al.* Low level laser therapy activates NF- κ B via generation of reactive oxygen species in mouse embryonic fibroblasts. *PLoS One* **6**, e22453 (2011).
9. Fournier, L. *et al.* Coumarinylmethyl caging groups with redshifted absorption. *Chem. - A Eur. J.* **19**, 17494–17507 (2013).
10. Peterson, J. A. *et al.* Family of BODIPY photocages cleaved by single photons of visible/near-infrared light. *J. Am. Chem. Soc.* **140**, 7343–7346 (2018).
11. Maciejewski, A. & Steer, R. P. The photophysics, physical photochemistry, and related spectroscopy of thiocarbonyls. *Chem. Rev.* **93**, 67–98 (1993).
12. Sumalekshmy, S. & Gopidas, K. R. Photoinduced intramolecular charge transfer in donor–acceptor substituted tetrahydropyrenes. *J. Phys. Chem. B* **108**, 3705–3712 (2004).
13. Ulises Acuña, A., Amat-Guerri, F., Morcillo, P., Liras, M. & Rodríguez, B. Structure and formation of the fluorescent compound of *lignum nephriticum*. *Org. Lett.* **11**, 3020–3023 (2009).
14. Jaffe, H. H. & Miller, A. L. The fates of electronic excitation energy. *J. Chem. Educ.* **43**, 469–473 (1966).
15. Michel, B. W., Lippert, A. R. & Chang, C. J. A reaction-based fluorescent probe for selective imaging of carbon monoxide in living cells using a palladium-mediated carbonylation. *J. Am. Chem. Soc.* **134**, 15688–15671 (2012).
16. Christov, C., Ianev, D., Shosheva, A. & Atanasov, B. *pH-dependent quenching of the fluorescence of tryptophan residues in class A-lactamase from E. coli (TEM-1)*. *Z. Naturforsch* vol. 59 <http://www.znaturforsch.com> (2004).
17. Hanagodimath, S. M., Siddlingeshwar, B., Thipperudrappa, J., Kumar, S. &

- Hadimani, B. Fluorescence-quenching studies and temperature dependence of fluorescence quantum yield, decay time and intersystem crossing activation energy of TPB. *J. lum* **129**, 335–339 (2009).
18. Lakowicz, J. R. & Weber, G. Quenching of fluorescence by oxygen. A probe for structural fluctuations in macromolecules. *Biochemistry* **12**, 4161–4170 (1973).
 19. Solov, K. N. Intramolecular heavy-atom effect in the photophysics of organic molecules. *UFN* **175**, 247–270 (2005).
 20. Shimomura, O., Johnson, K. H. & Saiga, Y. O. Extraction, purification and properties of Aequorin, a bioluminescent protein from the luminous hydromedusan, *Aequorea*. *J. Cell. Comp. Physiol.* **59**, 223–239 (1962).
 21. Prasher, D. C., Eckenrode, V. K., Ward, W. W., Prendergast, F. G. & Cormier, M. J. Primary structure of the *Aequorea victoria* green-fluorescent protein. *Gene* **111**, 229–233 (1992).
 22. Miyawaki, A., Shcherbakova, D. M. & Verkhusha, V. V. Red fluorescent proteins: chromophore formation and cellular applications. *Curr. Opin. Struct. Biol.* **22**, 679–688 (2012).
 23. Kremers, G.-J., Gilbert, S. G., Cranfill, P. J., Davidson, M. W. & Piston, D. W. Fluorescent proteins at a glance. *J. Cell Sci.* **124**, 157–160 (2011).
 24. Arun, K. H. S., Kaul, C. L. & Ramarao, P. Green fluorescent proteins in receptor research: An emerging tool for drug discovery. *J. Pharmacol. Toxicol. Methods* **51**, 1–23 (2005).
 25. Patterson, G. H., Knobel, S. M., Sharif, W. D., Kain, S. R. & Piston, D. W. Use of the green fluorescent protein and its mutants in quantitative fluorescence microscopy. *Biophys. J.* **73**, 2782–2790 (1997).
 26. Snapp, E. Design and use of fluorescent fusion proteins in cell biology. *Curr Protoc Cell Biol* **21–24**, 1–17 (2005).
 27. Mishin, A. S. *et al.* The first mutant of the *Aequorea Victoria* green fluorescent protein that forms a red chromophore. *Biochemistry* **47**, 4666–4673 (2008).
 28. Snapp, E. L. Fluorescent proteins: A cell biologist's user guide. *Trends Cell Biol.* **19**, 649–655 (2009).
 29. Lin, M. Z. Beyond the rainbow: new fluorescent proteins brighten the infrared scene. *Nat. Methods* **8**, 726–728 (2011).
 30. Zhang, J., Campbell, R. E., Ting, A. Y. & Tsien, R. Y. Creating new fluorescent probes for cell biology. *Nat. Rev. Mol. Cell Biol.* **3**, 906–918 (2002).
 31. Ekimov, A. I., O. Quantum size effect in three-dimensional microscopic semiconductor crystals. *Theor Phys Lett* **34**, 345–349 (1981).
 32. Resch-Genger, U., Grabolle, M., Cavaliere-Jaricot, S., Nitschke, R. & Nann, T. Quantum dots versus organic dyes as fluorescent labels. *Nat. methods.* **5**, 763–775 (2008).
 33. Zhou, J., Yang, Y. & Zhang, C.-Y. Toward biocompatible semiconductor quantum dots: from biosynthesis and bioconjugation to biomedical application. *Chem. Rev.* **115**, 11669–11717 (2015).
 34. Michalet, X. *et al.* Quantum dots for live cells, in vivo imaging, and diagnostics. *Science*. **307**, 538–544 (2005).
 35. Stefani, F. D., Hoogenboom, J. P. & Barkai, E. Beyond quantum jumps: Blinking nanoscale light emitters. *Phys. Today* **62**, 34–39 (2009).
 36. Rosenthal, S. J., Chang, J. C., Kovtun, O., McBride, J. R. & Tomlinson, I. D. Biocompatible quantum dots for biological applications. *Chem. Biol.* **18**, 10–24 (2011).
 37. Jensen, E. C. Use of fluorescent probes: their effect on cell biology and limitations. *Anat. Rec.* **295**, 2031–2036 (2012).
 38. Li, Y. *et al.* Mechanism-oriented controllability of intracellular quantum dots formation: the role of glutathione metabolic pathway. *ACS Nano* **7**, 2240–2248 (2013).

39. Bao, H., Hao, N., Yang, Y. & Zhao, D. Biosynthesis of biocompatible cadmium telluride quantum dots using yeast cells. *Nano Res* **3**, 481–489 (2010).
40. Ma, N., Dooley, C. J. & Kelley, S. O. RNA-templated semiconductor nanocrystals. *J. Am. Chem. Soc.* **128**, 12598–12599 (2006).
41. Lee, K. G. *et al.* In vitro biosynthesis of metal nanoparticles in microdroplets. *ACS Nano* **6**, 6998–7008 (2012).
42. Ma, N., Marshall, A. F. & Rao, J. Near-infrared light emitting luciferase via biomineralization. *J. Am. Chem. Soc.* **132**, 6884–6885 (2010).
43. Zhang, P. *et al.* Click-functionalized compact quantum dots protected by multidentate-imidazole ligands: conjugation-ready nanotags for living-virus labeling and imaging. *J. Am. Chem. Soc.* **134**, 8388–8391 (2012).
44. Kaufman, T. S. & Rúveda, E. A. The quest for quinine: Those who won the battles and those who won the war. *Angew. Chemie - Int. Ed.* **44**, 854–885 (2005).
45. Lavis, L. D. & Raines, R. T. Bright ideas for chemical biology. *ACS Chem. Biol.* **3**, 142–155 (2008).
46. Luo, S., Zhang, E., Su, Y., Cheng, T. & Shi, C. A review of NIR dyes in cancer targeting and imaging. *Biomaterials* **32**, 7127–7138 (2011).
47. Levitus, M. & Ranjit, S. Cyanine dyes in biophysical research: the photophysics of polymethine fluorescent dyes in biomolecular environments. *Q. Rev. Biophys.* **44**, 123–151 (2011).
48. Chen, X. *et al.* Photostabilities of novel heptamethine 3H-indolenine cyanine dyes with different N-substituents. *J. Photochem. Photobiol. A Chem.* **181**, 79–85 (2006).
49. Nani, R. R., Shaum, J. B., Gorka, A. P. & Schnermann, M. J. Electrophile-integrating smiles rearrangement provides previously inaccessible C4'-O-alkyl heptamethine cyanine fluorophores. *Org. Lett.* **17**, 302–305 (2015).
50. Martinić, I., Eliseeva, S. V. & Petoud, S. Near-infrared emitting probes for biological imaging: Organic fluorophores, quantum dots, fluorescent proteins, lanthanide(III) complexes and nanomaterials. *J. Lumin.* **189**, 19–43 (2017).
51. Volkova, K. D. *et al.* Spectroscopic study of squaraines as protein-sensitive fluorescent dyes. *Dye. Pigment.* **72**, 285–292 (2007).
52. Umezawa, K., Citterio, D. & Suzuki, K. Water-soluble NIR Fluorescent Probes Based on Squaraine and Their Application for Protein Labeling. *Anal. Sci.* **24**, 213–217 (2008).
53. Lee, H., Berezin, M. Y., Henary, M., Strekowski, L. & Achilefu, S. Fluorescence lifetime properties of near-infrared cyanine dyes in relation to their structures. *J. Photochem. Photobiol. A Chem.* **200**, 438–444 (2008).
54. Wang, Z. *et al.* A highly specific and sensitive turn-on fluorescence probe for hypochlorite detection based on anthracene fluorophore and its bioimaging applications. *Dye. Pigment.* **161**, 172–181 (2019).
55. Benedetti, E., Kocsis, L. S. & Brummond, K. M. Synthesis and photophysical properties of a series of cyclopenta[b] naphthalene solvatochromic fluorophores. *J. Am. Chem. Soc.* **134**, 12418–12421 (2012).
56. Chao, J. *et al.* A pyrene-based colorimetric and fluorescent pH probe with large stokes shift and its application in bioimaging. *Talanta* **189**, 150–156 (2018).
57. Mehta, P. K., Hwang, G. W., Park, J. & Lee, K.-H. Highly sensitive ratiometric fluorescent detection of indium(III) using fluorescent probe based on phosphoserine as a receptor. *Anal. Chem.* **90**, 11256–11264 (2018).
58. Liu, L.-N., Tao, H., Chen, G., Chen, Y. & Cao, Q.-Y. An amphiphilic pyrene-based probe for multiple channel sensing of mercury ions. *J. Lumin.* **203**, 189–194 (2018).
59. Bo, Y. *et al.* Surfactant modulation effect on the fluorescence emission of a dual-fluorophore: Realizing a single discriminative sensor for identifying different proteins in aqueous solutions. *Sensors Actuators B Chem.* **295**, 168–

- 178 (2019).
60. Móczár, I. & Huszthy, P. Optically active crown ether-based fluorescent sensor molecules: A mini-review. *Chirality* **31**, 97–109 (2019).
 61. Grimm, J. B., Heckman, L. M. & Lavis, L. D. The Chemistry of Small-Molecule Fluorogenic Probes. in *Progress in Molecular Biology and Translational Science, Volume 113* 1–34 (2013).
 62. Naderi, F. & Farajtabar, A. Solvatochromism of fluorescein in aqueous aprotic solvents. (2016) doi:10.1016/j.molliq.2016.05.071.
 63. May, B. C. H. *et al.* Structure-activity relationship study of 9-aminoacridine compounds in scrapie-infected neuroblastoma cells. *Bioorganic Med. Chem. Lett.* **16**, 4913–4916 (2006).
 64. Chozinski, T. J., Gagnon, L. A. & Vaughan, J. C. Twinkle, twinkle little star: photoswitchable fluorophores for super-resolution imaging. *FEBS Lett.* **588**, 3603–3612 (2014).
 65. Yan, F. *et al.* Fluorescein applications as fluorescent probes for the detection of analytes. *Trends Anal. Chem.* **97**, 15–35 (2017).
 66. Mondal, S. B. *et al.* Real-time fluorescence image-guided oncologic surgery. in *Advances in Cancer Research, Volume 124* 171–211 (2014).
 67. Li, H. *et al.* Novel coumarin fluorescent dyes: synthesis, structural characterization and recognition behavior towards Cu(II) and Ni(II). *Dye. Pigment.* **91**, 309–316 (2011).
 68. O'brien, J., Wilson, I., Orton, T. & Ois Pognan, F. Ě. Investigation of the Alamar Blue (resazurin) fluorescent dye for the assessment of mammalian cell cytotoxicity. *Eur. J. Biochem.* **267**, 5421–5426 (2000).
 69. Hara, K. *et al.* Molecular Design of Coumarin Dyes for Efficient Dye-Sensitized Solar Cells. *J. Phys. Chem. B* **107**, 597–606 (2003).
 70. Raviña Rubira, E. *The evolution of drug discovery: from traditional medicines to modern drugs.* (Wiley-VCH, 2011).
 71. Lee, D.-N., Kim, G.-J. & Kim, H.-J. A Fluorescent coumarinylalkyne probe for the selective detection of mercury(II) ion in water. *Tetrahedron Lett.* **50**, 4766–4768 (2009).
 72. Huang, S. *et al.* Highly sensitive and selective fluorescent chemosensor for Ag⁺ based on a coumarin–Se2N chelating conjugate. *Chem. Commun.* **47**, 2408–2410 (2011).
 73. Tamima, U. *et al.* A benzocoumarin based two-photon fluorescent probe for ratiometric detection of bisulfite. *Sensors Actuators, B Chem.* **277**, 576–583 (2018).
 74. Westblom, T. U., Barthelt, J. S., Haveyt, A. D., Gonzalez, F. J. & Tarka, E. F. Cresyl fast violet staining method for campylobacter like organisms. *J. Clin. Pathol.* **40**, 353–356 (1987).
 75. Ho Park, M. *et al.* Prototype nerve-specific near-infrared fluorophores. *Theranostics* **4**, 823–833 (2014).
 76. Vogelsang, J., Cordes, T., Forthmann, C., Steinhauer, C. & Tinnefeld, P. Controlling the fluorescence of ordinary oxazine dyes for single-molecule switching and superresolution microscopy. *PNAS* **106**, 8107–8112 (2009).
 77. Lavis, L. D., Chao, T.-Y. & Raines, R. T. Latent blue and red fluorophores based on the trimethyl lock. *ChemBioChem.* **7**, 1151–1154 (2006).
 78. Marazzi, M., Gattuso, H. & Monari, A. Nile blue and Nile red optical properties predicted by TD-DFT and CASPT2 methods: static and dynamic solvent effects. *Theor. Chem. Acc.* **135**, 57 (2016).
 79. Huang, H., Song, W., Rieffel, J. & Lovell, J. F. Emerging applications of porphyrins in photomedicine. *Front. Phys.* **3**, 1–15 (2015).
 80. Pansare, V. J., Hejazi, S., Faenza, W. J. & Prud'homme, R. K. Review of Long-Wavelength Optical and NIR Imaging Materials: Contrast Agents, Fluorophores, and Multifunctional Nano Carriers. *Chem. Mater.* **24**, 812–827

- (2012).
81. Escobedo, J. O., Rusin, O., Lim, S. & Strongin, R. M. NIR dyes for bioimaging applications. *Curr. Opin. Chem. Biol.* **14**, 1–11 (2010).
 82. Zhang, X., Bloch, S., Akers, W. & Achilefu, S. Near-infrared molecular probes for in vivo imaging. *Curr. Protoc. Cytom.* **60**, 1–28 (2012).
 83. Suzuki, A. *et al.* Synthesis of solvatofluorochromic 7-arylethynylated 7-deaza-2'- deoxyadenosine derivatives: Application to the design of environmentally sensitive fluorescent probes forming stable DNA duplexes. *Tetrahedron Lett.* **54**, 2348–2352 (2013).
 84. Lee, M. H. *et al.* Direct fluorescence monitoring of the delivery and cellular uptake of a cancer-targeted RGD peptide-appended naphthalimide theragnostic prodrug. *J. Am. Chem. Soc.* **134**, 12668–12674 (2012).
 85. Jana, A., Sanjana, K., Devi, P., Maiti, T. K. & Singh, N. D. P. Perylene-3-ylmethanol: fluorescent organic nanoparticles as a single-component photoresponsive nanocarrier with real-time monitoring of anticancer drug release. *J. Am. Chem. Soc.* **134**, 7656–7659 (2012).
 86. Abo, M. *et al.* Development of a highly sensitive fluorescence probe for hydrogen peroxide. *J. Am. Chem. Soc.* **133**, 10629–10637 (2011).
 87. Eser, S. *et al.* In vivo diagnosis of murine pancreatic intraepithelial neoplasia and early-stage pancreatic cancer by molecular imaging. *PNAS* **108**, 9945–9950 (2011).
 88. Junyan Han and Kevin Burgess. Fluorescent indicators for intracellular pH. *Chem. Rev.* **110**, 2709–2728 (2010).
 89. Aydinler, B. & Seferoğlu, Z. Proton sensitive functional organic fluorescent dyes based on coumarin-imidazo[1,2-a]pyrimidine; syntheses, photophysical properties, and investigation of protonation ability. *European J. Org. Chem.* **2018**, 5921–5934 (2018).
 90. Vu, T. T., Mé Allet-Renault, R., Clavier, G., Trofimov, B. A. & Kuimova, M. K. Tuning BODIPY molecular rotors into the red: sensitivity to viscosity vs. temperature. *J. Mater. Chem. C* **4**, 2828–2833 (2016).
 91. Wang, X., Song, F. & Peng, X. A versatile fluorescent probe for imaging viscosity and hypochlorite in living cells. *Dye. Pigment.* **125**, 89–94 (2016).
 92. Kuimova, M. K., Yahioglu, G., Levitt, J. A. & Suhling, K. Molecular rotor measures viscosity of live cells via fluorescence lifetime imaging. *J. Am. Chem. Soc.* **130**, 6672–6673 (2008).
 93. Gun Ryu, H. *et al.* Bidirectional solvatofluorochromism of a pyrrolo[3,2-b]pyrrole– diketopyrrolopyrrole hybrid. *J. Phys. Chem. C* **122**, 13424–13434 (2018).
 94. Zhu, H. *et al.* d-PET-controlled 'off-on' polarity-sensitive probes for reporting local hydrophilicity within lysosomes. *Nat. Publ. Gr.* **6**, 1–10 (2016).
 95. Li, M. *et al.* A ratiometric fluorescence probe for lysosomal polarity. *Biomaterials* **164**, 98–105 (2018).
 96. Signore G1, Nifosì R, Albertazzi L, B. R. A novel coumarin fluorescent sensor to probe polarity around biomolecules. *J Biomed. Nanotechnol.* **5**, 722–729 (2009).
 97. Riedl, J., Pohl, R. & Hocek, M. Synthesis and photophysical properties of biaryl-substituted nucleos(t)ides. Polymerase synthesis of DNA probes bearing solvatochromic and pH-sensitive dual fluorescent and ¹⁹F NMR labels. *J. Org. Chem.* **77**, 1026–1044 (2011).
 98. Ntziachristos, V. Going deeper than microscopy: the optical imaging frontier in biology. *Nat. Methods* **7**, 603–614 (2010).
 99. Feenstra, D. J. *et al.* Indocyanine green molecular angiography of choroidal neovascularization. *Exp. Eye Res.* **180**, 122–128 (2019).
 100. Van Der Vorst, J. R. *et al.* Near-infrared fluorescence-guided resection of colorectal liver metastases. *Cancer* **119**, 3411–3418 (2013).

101. Xu, H., Eck, P. K., Baidoo, K. E., Choyke, P. L. & Brechbiel, M. W. Toward preparation of antibody-based imaging probe libraries for dual-modality positron emission tomography and fluorescence imaging. *Bioorg. Med. Chem.* **17**, 5176–5181 (2009).
102. Tanaka, Y., Shin, J.-Y. & Osuka, A. Facile synthesis of largemeso-pentafluorophenyl-substituted expanded porphyrins. *European J. Org. Chem.* **2008**, 1341–1349 (2008).
103. Allison, R. R. *et al.* Photosensitizers in clinical PDT. *Photodiagnosis Photodyn. Ther.* **1**, 27–42 (2004).
104. Liu, T. *et al.* Far-red-to NIR-emitting adamantyl-functionalized squaraine dye: J-aggregation, dissociation, and cell imaging. *European J. Org. Chem.* 4095–4102 (2018).
105. Shaw, S. K. *et al.* Non-covalently pre-assembled high-performance near-infrared fluorescent molecular probes for cancer imaging. *Chem. - A Eur. J.* **24**, 13821–13829 (2018).
106. Cong, Z. *et al.* Highly efficient crystal red fluorescent 1,2-squaraine dyes with excellent biocompatibility and bioimaging. *Dye. Pigment.* **162**, 654–661 (2019).
107. Niu, G. *et al.* Deep-red and near-infrared xanthene dyes for rapid live cell imaging. *J. Org. Chem.* **81**, 7393–7399 (2016).
108. Abeywickrama, C. S., Wijesinghe, K. J., Stahelin, R. V. & Pang, Y. Bright red-emitting pyrene derivatives with a large Stokes shift for nucleus staining. *Chem. Commun.* **53**, 5886–5889 (2017).
109. Zhu, H., Fan, J., Du, J. & Peng, X. Fluorescent probes for sensing and imaging within specific cellular organelles. *Acc. Chem. Res.* **49**, (2016).
110. Shim, S.-H. *et al.* Super-resolution fluorescence imaging of organelles in live cells with photoswitchable membrane probes. *PNAS* **109**, 13978–13983 (2012).
111. Samanta, S. *et al.* Fluorescent probes for nanoscopic imaging of mitochondria. *Chem.* **5**, 1697–1726 (2019).
112. Yan, P., Xie, A., Wei, M. & Loew, L. M. Amino(oligo)thiophene-based environmentally sensitive biomembrane chromophores. *J. Org. Chem.* **73**, 6587–94 (2008).
113. Yang, K., Li, Y., Tang, Q., Zheng, L. & He, D. Synthesis, mitochondrial localization of fluorescent derivatives of cinnamamide as anticancer agents. *Eur. J. Med. Chem.* **170**, 45–54 (2019).
114. Raymond, S. B., Kumar, A. T. N., Boas, D. A., Bacsikai, B. J. & Org, B. Optimal parameters for near infrared fluorescence imaging of amyloid plaques in Alzheimer's disease mouse models. *Phys Med Biol.* **24**, 6201–6216 (2009).
115. Tarnawska, D. *et al.* Endogenous fluorescence can differentiate the keratoconic cornea. *Exp. Eye Res.* **181**, 178–184 (2019).
116. Gompels, L. L. *et al.* In vivo fluorescence imaging of E-selectin: Quantitative detection of endothelial activation in a mouse model of arthritis. *Arthritis Rheum.* **63**, 107–117 (2011).
117. Baird, F. J., Wadsworth, M. P. & Hill, J. E. Evaluation and optimization of multiple fluorophore analysis of a *Pseudomonas aeruginosa* biofilm. *J Microbiol Methods.* **90**, 192–196 (2012).
118. Lee, J. S., Lee, B. II & Park, C. B. Photo-induced inhibition of Alzheimer's β -amyloid aggregation in vitro by rose bengal. *Biomaterials* **38**, 43–49 (2015).
119. Treibs, A. & Kreuzer, F. Difluoroboryl-komplexe von di- und tripyrrylmethenen. *Justus Liebigs Ann. der Chemie.* **718**, 208–223 (1968).
120. Arroyo, I. J., Hu, R., Merino, G., Zhong Tang, B. & Pe~ Na-Cabrera, E. The smallest and one of the brightest. Efficient preparation and optical description of the parent borondipyrrromethene system. *J. Org. Chem* **74**, 5719–5722 (2009).
121. Schmitt, A., Hinkeldey, B., Wild, M. & Jung, G. Synthesis of the core compound

- of the BODIPY dye class: 4,4'-difluoro-4-bora-(3a,4a)-diazas-indacene. *J. Fluoresc.* **19**, 755–758 (2009).
122. Tram, K., Yan, H., Jenkins, H. A., Vassiliev, S. & Bruce, D. The synthesis and crystal structure of unsubstituted 4,4-difluoro-4-bora-3a,4a-diazas-indacene (BODIPY). *Dye. Pigment.* **82**, 392–395 (2009).
 123. Loudet, A. & Burgess, K. BODIPY dyes and their derivatives: syntheses and spectroscopic properties. *Chem. Rev.* **107**, 4891–4932 (2007).
 124. The Molecular Probes Handbook. (2010).
 125. Ulrich, G., Ziesel, R. & Harriman, A. The chemistry of fluorescent bodipy dyes: versatility unsurpassed. *Angew. Chemie. Int. Ed.* **47**, 1184–1201 (2008).
 126. Ono, M., Watanabe, H., Kimura, H. & Saji, H. BODIPY-based molecular probe for imaging of cerebral β -amyloid plaques. *ACS Chem. Neurosci.* **3**, 319–324 (2012).
 127. Kamkaew, A. *et al.* BODIPY dyes in photodynamic therapy. *Chem. Soc. Rev.* **42**, 77–88 (2013).
 128. Yee, M. C., Fas, S. C., Stohlmeyer, M. M., Wandless, T. J. & Cimprich, K. A. A cell-permeable, activity-based probe for protein and lipid kinases. *J. Biol. Chem.* **280**, 29053–29059 (2005).
 129. Zhao, C., Zhang, Y., Wang, X. & Cao, J. Development of BODIPY-based fluorescent DNA intercalating probes. *J. Photochem. Photobiol. A Chem.* **264**, 41–47 (2013).
 130. Zhao, W. & Carreira, E. M. Conformationally restricted aza-bodipy: a highly fluorescent, stable, near-infrared-absorbing dye. *Angew. Chemie - Int. Ed.* **44**, 1677–1679 (2005).
 131. Karolin, J., B-A Johansson, L., Leif Strandberg, J. & Ny, T. Fluorescence and absorption spectroscopic properties of dipyrrometheneboron difluoride (BODIPY) derivatives in liquids, lipid membranes, and proteins. *J. Am. Chem. Soc.* **116**, 7801–7806 (1994).
 132. Jorge Banuelos. BODIPY dye, the most versatile fluorophore ever? *Chem. Rec.* **16**, 335–348 (2016).
 133. Glembockyte, V. *et al.* Highly photostable and fluorescent microporous solids prepared via solid-state entrapment of boron dipyrromethene dyes in a nascent metal-organic framework. *J. Am. Chem. Soc.* **140**, 16882–16887 (2018).
 134. Hiruta, Y. *et al.* Near IR emitting red-shifting ratiometric fluorophores based on borondipyrromethene. *Org. Lett.* **17**, 3022–3025 (2015).
 135. Bañ, J. *et al.* Photophysical study of new versatile multichromophoric diads and triads with BODIPY and polyphenylene groups. *J. Phys. Chem. A* **112**, 10816–10822 (2008).
 136. Ni, Y. *et al.* Meso-ester and carboxylic acid substituted BODIPYs with far-red and near-infrared emission for bioimaging applications. *Chem. - A Eur. J.* **20**, 2301–2310 (2014).
 137. Gibbs, J. H. *et al.* Synthesis, spectroscopic, and in vitro investigations of 2,6-diiodo-BODIPYs with PDT and bioimaging applications. *J. Photochem. Photobiol. B* **145**, 35–47 (2015).
 138. Kolemen, S. & Akkaya, E. U. Reaction-based BODIPY probes for selective bio-imaging. *Coord. Chem. Rev.* **354**, 121–134 (2018).
 139. Sansalone, L. *et al.* A photoactivatable far-red/Near-infrared BODIPY to monitor cellular dynamics in vivo. *ACS Sens* **3**, 1347–1353 (2018).
 140. Yu, C., Miao, W., Wang, J., Hao, E. & Jiao, L. PyrrolylBODIPYs: syntheses, properties, and application as environment-sensitive fluorescence probes. *ACS OMEGA* **2**, 3551–3561 (2017).
 141. Nigam, S. *et al.* Structurally optimised BODIPY derivatives for imaging of mitochondrial dysfunction in cancer and heart cells. *Chem. Commun.* **52**, 7114–7117 (2016).
 142. Rodriguez, G. *et al.* Synthesis and in vivo proof of concept of a BODIPY-based

- fluorescent probe as a tracer for biodistribution studies of a new anti-Chagas agent. *RSC Adv.* **7**, 7983–7989 (2017).
143. Greene, L. E., Lincoln, R., Krumova, K. & Cosa, G. Development of a fluorogenic reactivity palette for the study of nucleophilic addition reactions based on meso-formyl BODIPY dye. *ACS OMEGA* **2**, 8618–8624 (2017).
 144. Lincoln, R., Greene, L. E., Zhang, W., Louisia, S. & Cosa, G. Mitochondria alkylation and cellular trafficking mapped with a lipophilic BODIPY–acrolein fluorogenic probe. *J. Am. Chem. Soc.* **139**, 16273–16281 (2017).
 145. Li, Y. *et al.* A sensitive BODIPY-based fluorescent probe suitable for hypochlorite detection in living cells. *J. Photochem. Photobiol. A Chem.* **352**, 65–72 (2018).
 146. Loukanov, A., Mladenova, P., Toshev, S., Udono, H. & Nakabayashi, S. Visualization of the native shape of bodipy-labeled DNA in Escherichia coli by correlative microscopy. *Microsc. Res. Tech.* **81**, 267–274 (2018).
 147. Zhang, J. *et al.* Pyridinium substituted BODIPY as NIR fluorescent probe for simultaneous sensing of hydrogen sulphide/glutathione and cysteine/homocysteine. *Sensors Actuators B* **257**, 1076–1082 (2018).
 148. Sayar, M. *et al.* A BODIPY-based fluorescent probe to visually detect phosgene: toward the development of a handheld phosgene detector. *Chem. - A Eur. J.* **24**, 3136–3140 (2018).
 149. Strobl, M., Rappitsch, T., Borisov, S. M., Mayr, T. & Klimant, I. NIR-emitting aza-BODIPY dyes – new building blocks for broad-range optical pH sensors. *Analyst.* **140**, 7150–7153 (2015).
 150. Bellier, Q. *et al.* Near-infrared nitrofluorene substituted aza-boron-dipyrromethenes dyes. *Org. Lett.* **13**, 22–25 (2011).
 151. Alejandro, D. *et al.* Synthesis of a class of core-modified aza-BODIPY derivatives. *J. Org. Chem.* **79**, 8932–8936 (2014).
 152. Daly, H. C. *et al.* BF₂-azadipyrromethene NIR-emissive fluorophores with research and clinical potential. *Eur. J. Med. Chem.* **135**, 392–400 (2017).
 153. Wu, D. & O'Shea, D. F. Comparative triad of routes to an alkyne-BF₂ azadipyrromethene near-infrared fluorochrome. *Tetrahedron Lett.* **58**, 4468–4472 (2017).
 154. Wu, D. *et al.* A DIE responsive NIR-fluorescent cell membrane probe. *Biochim. Biophys. Acta - Biomembr.* **1860**, 2272–2280 (2018).
 155. Wu, D. & O'Shea, D. F. Fluorogenic NIR-probes based on 1,2,4,5-tetrazine substituted BF₂-azadipyrromethenes. *Chem. Commun* **53**, 10804 (2017).
 156. Pliquett, J. *et al.* A promising family of fluorescent water-soluble aza-BODIPY dyes for in vivo molecular imaging. *Bioconjug. Chem.* **30**, 1061–1066 (2019).
 157. Ren, W. *et al.* Fluorescent imaging of β -amyloid using BODIPY based Near-infrared off-On fluorescent probe. *Bioconjug. Chem.* **29**, 3459–3466 (2018).
 158. Dixit, S., Mahaddalkar, T., Lopus, M. & Agarwal, N. Synthesis, photophysical studies of positional isomers of heteroaryl BODIPYs, and biological evaluation of di-pyrrolyl BODIPY on human pancreatic cancer cells. *J. Photochem. Photobiol. A Chem.* **353**, 368–375 (2018).
 159. Ramu, V., Gautam, S., Garai, A., Kondaiah, P. & Chakravarty, A. R. Glucose-appended platinum(II)-BODIPY conjugates for targeted photodynamic therapy in red light. *Inorg. Chem.* **57**, 1717–1726 (2018).
 160. Lee, B. *et al.* BOIMPY: fluorescent boron complexes with tunable and environment-responsive light-emitting properties. *Chem. - A Eur. J.* **22**, 17321–17328 (2016).
 161. Bronner, C. *et al.* Dipyrin based luminescent cyclometallated palladium and platinum complexes. *Dalt. Trans.* **39**, 180–184 (2010).
 162. Kobayashi, J., Kushida, T. & Kawashima, T. Synthesis and reversible control of the fluorescent properties of a divalent tin dipyrromethene. *J. Am. Chem. Soc.* **131**, 10836–10837 (2009).

163. Graser, M. *et al.* Efficient fluorophores based on pyridyl-enolato and enamido difluoroboron complexes: simple alternatives to boron-dipyrromethene (BODIPY) dyes. *Inorganica Chim. Acta.* **405**, 116–120 (2013).
164. Wu, W., Guo, H., Wu, W., Ji, S. & Zhao, J. Organic triplet sensitizer library derived from a single chromophore (BODIPY) with long-lived triplet excited state for triplet triplet annihilation based upconversion. *J. Org. Chem.* **76**, 7056–7064 (2011).
165. Goswami, P. P. *et al.* BODIPY-derived photoremovable protecting groups unmasked with green light. *J. Am. Chem. Soc.* **137**, 3783–3786 (2015).
166. Fletcher, K. A., Storey, I. A., Hendricks, A. E., Pandey, S. & Pandey, S. Behavior of the solvatochromic probes Reichardt's dye, pyrene, dansylamide, nile red and 1-pyrenecarbaldehyde within the room-temperature ionic liquid bmimPF₆. *Green Chem.* **3**, 210–215 (2001).
167. Hughes, L. D., Rawle, R. J. & Boxer, S. G. Choose your label wisely: water-soluble fluorophores often interact with lipid bilayers. *PLoS One* **9**, e87649 (2014).
168. Hu, W. *et al.* Attaching electron donating groups on the meso-phenyl and meso-naphthyl make aryl substituted BODIPYs act as good photosensitizer for singlet oxygen formation. *J. Lumin.* **194**, 185–192 (2018).
169. Descalzo, A. B. *et al.* Phenanthrene-fused boron-dipyrromethenes as bright long-wavelength fluorophores. *Org. Lett.* **10**, 1581–1584 (2008).
170. Guo, B. *et al.* Synthesis and spectral properties of new boron dipyrromethene dyes. *Dye. Pigment.* **73**, 206–210 (2007).
171. Xie, R., Yi, Y., He, Y., Liu, X. & Liu, Z.-X. A simple BODIPY-imidazole-based probe for the colorimetric and fluorescent sensing of Cu(II) and Hg(II). *Tetrahedron.* **69**, 8541–8546 (2013).
172. Oshikawa, Y. & Ojida, A. PET-dependent fluorescence sensing of enzyme reactions using the large and tunable pK_a a shift of aliphatic amines. *Chem. Commun. Chem. Commun* **49**, 11373–11375 (2013).
173. Krumova, K. & Cosa, G. Bodipy dyes with tunable redox potentials and functional groups for further tethering: preparation, electrochemical, and spectroscopic characterization. *J. Am. Chem. Soc.* **132**, 17560–17569 (2010).
174. Pakhomov, A. A. *et al.* Synthesis and photophysical properties of a new BODIPY-based siloxane dye. *Tetrahedron Lett.* **57**, 979–982 (2016).
175. Swavey, S., Quinn, J., Coladipietro, M., Cox, K. G. & Kyle Brennaman, M. Tuning the photophysical properties of BODIPY dyes through extended aromatic pyrroles. *RSC Adv.* **7**, 173–179 (2017).
176. Anderson, R. S., Nagirimadugu, N. V. & Abelt, C. J. Fluorescence quenching of carbonyl-twisted 5 - acyl-1-dimethylaminonaphthalenes by alcohols. *ACS Omega* **4**, 14067–14073 (2019).
177. Fournier, L. *et al.* Coumarinylmethyl caging groups with red shifted absorption. *Chem. - A Eur. J.* **19**, 17494–17507 (2013).
178. Tao, J. *et al.* Tuning the photo-physical properties of BODIPY dyes: Effects of 1, 3, 5, 7- substitution on their optical and electrochemical behaviours. *Dye. Pigment.* **168**, 166–174 (2019).
179. Yu, C. *et al.* Red to near-infrared isoindole BODIPY fluorophores: synthesis, crystal structures, and spectroscopic and electrochemical properties. *J. Org. Chem.* **81**, 3761–3770 (2016).
180. Yu, C. *et al.* Isoindole-BODIPY dyes as red to near-infrared fluorophores. *Chem. - A Eur. J.* **18**, 6437–6442 (2012).
181. Ni, Y., Zeng, W., Huang, K. W. & Wu, J. Benzene-fused BODIPYs: synthesis and the impact of fusion mode. *Chem. Commun.* **49**, 1217–1219 (2013).
182. Zhao, C. *et al.* Development of an indole-based boron-dipyrromethene fluorescent probe for benzenethiols. *J. Phys. Chem. B* **115**, 642–647 (2011).
183. Dziuba, D., Pohl, R. & Hocek, M. Bodipy-labeled nucleoside triphosphates for

- polymerase synthesis of fluorescent DNA. *Bioconjug. Chem.* **25**, 1984–1995 (2014).
184. Nguyen, H. P. *et al.* A photo-responsive small-molecule approach for the opto-epigenetic modulation of DNA methylation. *Angew. Chemie* **131**, 6692–6696 (2019).
 185. Li, Z., Mintzer, E. & Bittman, R. First synthesis of free cholesterol-BODIPY conjugates. *J. Org. Chem.* **71**, 1718–1721 (2006).
 186. Guido, C. A., Mennucci, B., Jacquemin, D. & Adamo, C. Planar vs. twisted intramolecular charge transfer mechanism in Nile Red: New hints from theory. *Phys. Chem. Chem. Phys.* **12**, 8016–8023 (2010).
 187. Turro, N. J., Ramamurthy, V. & Scaiano, J. C. *Modern molecular photochemistry of organic molecules*. (2016).
 188. Xuan, S. *et al.* Synthesis and spectroscopic investigation of a series of push–pull boron dipyrromethenes (BODIPYs). *J. Org. Chem.* **82**, 2545–2557 (2017).
 189. Bañuelos, J., Lopez Arbeloa, F., Arbeloa, T., Martinez, V. & Arbeloa, I. L. BODIPY Laser dyes applied in sensing and monitoring environmental properties. in *Chapter 19* 645 (2012).
 190. Shao, J., Guo, H., Ji, S. & Zhao, J. Styryl-BODIPY based red-emitting fluorescent OFF-ON molecular probe for specific detection of cysteine. *Biosens. Bioelectron.* **26**, 3012–3017 (2011).
 191. Chen, X.-X., Niu, L.-Y., Shao, N. & Yang, Q.-Z. BODIPY-based fluorescent probe for dual-channel detection of nitric oxide and glutathione: visualization of cross-talk in living cells. *Anal. Chem.* **91**, 3 (2019).
 192. Ksenofontova, K. V., Ksenofontov, A. A., Khodov, I. A. & Rumyantsev, E. V. Novel BODIPY-conjugated amino acids: Synthesis and spectral properties. *J. Mol. Liq.* **283**, 695–703 (2019).
 193. Chen, K. *et al.* Triplet excited state of BODIPY accessed by charge recombination and its application in triplet-triplet annihilation upconversion. *J. Phys. Chem. A* **121**, 7550–7564 (2017).
 194. Zhao, J., Xu, K., Yang, W., Wang, Z. & Zhong, F. Triplet excited state of Bodipy: formation, modulation and application. *RSC Adv.* **7**, 173–179 (2017).
 195. Zhang, X. F. & Zhu, J. BODIPY parent compound: Fluorescence, singlet oxygen formation and properties revealed by DFT calculations. *J. Lumin.* **205**, 148–157 (2019).
 196. Muhammad T. Sajjad , Pavlos P. Manousiadis , Clara Orofi no, D. C.-L., Alexander L. Kanibolotsky , Sujana Rajbhandari , Dimali Amarasinghe, H. C., Grahame Faulkner , Dominic C. O'Brien , Peter J. Skabara, G. A. T. & Samuel, and I. D. W. Fluorescent red-emitting BODIPY oligofluorene star-shaped molecules as a color converter material for visible light communications. *Adv. Optitcal Mater.* **3**, 536–540 (2015).
 197. Vithanage, D. *et al.* BODIPY star-shaped molecules as solid state colour converters for visible light communications. *Appl. Phys. Lett.* **109**, 013302 (2016).
 198. Niggemann, G., Kummrow, M. & Helfrich, W. The bending rigidity of phosphatidylcholine bilayers: dependences on experimental method, sample cell sealing and temperature. *J. Phys. II EDP Sci.* **5**, 413–425 (1995).
 199. Hong, G., Antaris, A. L. & Dai, H. Near-infrared fluorophores for biomedical imaging. *Nat. Biomed. Eng.* **1**, 1–22 (2017).
 200. Rangan, S. R. S. A new human cell line (FaDu) from a hypopharyngeal carcinoma. *Cancer* **29**, 117–121 (1972).
 201. Alford, R. *et al.* Toxicity of organic fluorophores used in molecular imaging: literature review. *Mol. Imaging* **8**, 341–354 (2009).
 202. Kaur, P. & Singh, K. Recent advances in the application of BODIPY in bioimaging and chemosensing. *J. Mater. Chem. C* **7**, 11361–11405 (2019).

203. Tümay, S. O. *et al.* Naked-eye fluorescent sensor for Cu(II) based on indole conjugate BODIPY dye. *Polyhedron* **117**, 161–171 (2016).
204. Li, J. *et al.* Nucleoside-based ultrasensitive fluorescent probe for the dual-mode imaging of microviscosity in living cells. *Anal. Chem.* **88**, 5554–5560 (2016).
205. Hirata, T. *et al.* Protein-coupled fluorescent probe to visualize potassium ion transition on cellular membranes. *Anal. Chem.* **88**, 2693–2700 (2016).
206. Biotium. CellBrite™ Fix Membrane Stains. <https://biotium.com/product/cellbrite-fix-membrane-stains>. Accessed: 02/03/2019.
207. Ambroz, F., Donnelly, J. L., Wilden, J. D., Macdonald, T. J. & Parkin, I. P. Carboxylic acid functionalization at the meso-position of the bodipy core and its influence on photovoltaic performance. *Nanomaterials* **9**, (2019).

Chapter 7

Appendix

7.1 General Experimental

Chemicals and solvents

All solvents and reagents were obtained from Sigma Aldrich, Acros Organics, Alfa Aesar or Thermo Fischer Scientific. Values are reported to three significant figures and all materials were used as received unless otherwise stated.

Chromatography

Monitoring of all reactions was achieved using 60 F254 silica coated aluminium TLC plates by Merck. Visualisation of these was carried out using UV light of wavelength of 254 and/or 365 nm. Purification was achieved by flash column chromatography using silica gel (43-60 μm) from Merck.

LCMS/HRMS

All reverse phase UPLC-MS measurements were carried out using an Acquity Ultra Performance LC Waters system equipped with a UPLC BEH C18 column (50 x 2.1 mm, 1,7 μm beads). Gradient conditions were run using two mobile phases; mobile

phase A: 0.1% formic acid in water; mobile phase B: 95% acetonitrile-5% water. Sample injections of 1 μ L were used. Flow from the column immediately entered a mass spectrometer, the Waters SQ Detector, which was configured with an electrospray ionisation source with nitrogen used as the nebuliser gas. Mass spectra were obtained by scanning at a speed of 10,000 Da/sec up to 2,000 Da. The Waters MassLynx Mass Spectrometry Software was used for data acquisition post analysis. All EI and CI mass spectrometry was carried out using the Thermo Finnigan MAT900 magnetic sector. ESI was carried out using the Waters Autosampler Manager 2777C with Waters LCT Premier Q-TOF. Where relevant, ammonia was used as the reagent gas prior to analysis.

Spectroscopy

All ^1H , ^{13}C , ^{11}B and ^{19}F nuclear magnetic resonance spectra were recorded at 600 MHz using the Bruker Avance III 600 Cryo or at 700 MHz the Bruker Avance Neo 700. Instruments are clearly indicated for each spectra. Chemical shifts are reported in ppm relative to the internal standard TMS as follows: chemical shift, multiplicity (s = singlet, d = doublet, t = triplet, q = quartet, sep = septet, m = multiplet), coupling constant(s), integration and assignment using either CDCl_3 or $\text{DMSO}-d^6$ as a solvent and TMS as an internal standard. Infrared spectra were obtained using the FT-IR (Shimadzu 8700) in the ATR mode, with a range of 7800 - 350 cm^{-1} , and resolution of up to 0.5 cm^{-1} . All UV-vis spectra were obtained using the Cary 100 UV/Vis spectrophotometer between 800-200 nm. Data was analysed using the Agilent Cary WinUV software.

Fluorescence spectroscopy

All fluorescence spectroscopy was measured using the Agilent Cary Eclipse Fluorescence Spectrophotometer with emission measured between 1000-200 nm. Data was analysed using the Agilent Cary WinFLR software.

Vesicle procedures

General procedure for the formation of SUVs

A solution of POPC with a concentration of 20 mg/mL (5 μ L) was added to an oven dried round bottomed flask (5 mL). The solvent was removed *in vacuo* until complete dryness, allowing a thin film to form. 1 x PBS buffer (1 mL) was added and the lipid re-suspended, sonicated for 10 minutes at room temperature and used as such in subsequent experiments.

Insertion of compounds into the lipid bilayers of SUVs

Two methods were used to incorporate compounds into lipid bilayers: a) after thin film formation, an 800 μ M solution of test compound (in 1 x PBS buffer) was added prior to sonication and then incubated at room temperature for one hour. b) 0.8 μ mol of compound was added to the cholesterol solution prior to drying and vesicle formation.

General procedure for the formation of GUVs

All giant unilamellar vesicles (GUVs) were prepared by electroformation. Two aliquots of POPC (6 μ L, 25.4 mM in CHCl_3) were deposited on an indium tin oxide glass plate inside two rubber rings and the solvent was left to evaporate. The rings were flooded with sucrose (600 μ L, 1 M in water) and another indium tin oxide glass plate placed on top. The protocol for the electroformation involved a 3 minute rise time to a frequency of 10 Hz and amplitude of 3 mV in a sinusoidal fashion, which was held for 120 minutes. A fall time of 5 minutes returned the GUVs to conditions to be removed. This was done using the Nanion Vesicle Prep Pro electroformation equipment and generated vesicles of between 1-30 μ m.

Insertion of compounds into the lipid bilayers of GUVs

Two methods were used to incorporate compounds into lipid bilayer: a) the compound was dissolved in the sucrose buffer used prior to electroformation. b) the compound was added to the solution of GUVs after electroformation. Concentrations from 100 μ M (method a) to 800 μ M (method b only) were used. Successful experiments were carried out using method a.

Cell culture of mammalian cells

Pharynx squamous carcinoma cell lines (FaDu) obtained from the American Type Culture Collection (ATCC HTB-43) were grown in DMEM with 10% fetal bovine serum (FBS). Growth media was supplemented with 2 mM L-glutamine, 1 mM sodium pyruvate, 100 U/mL penicillin and 100 g/mL streptomycin. Cell lines were sub-cultured, or seeded, for further analyses by incubation with trypsin-EDTA solution. Cell fixation was carried out by incubation with para-formaldehyde (3.75%) in PBS (1 x solution) for seven minutes, followed by extensive washing (1 x PBS).

MTT cell viability assays

Assay based MTT (3-(4,5-Dimethylthiazol-2-yl)-2,5-diphenyltetrazolium bromide) was used to determine cell viability upon exposure to compound **47**. Samples of 8 x 10⁴ cells/well were seeded overnight on 96 well plates before incubation with compound **47** at final concentrations of 0, 6, 12.5 and 50 μ M. Batches were incubated for 1, 3, 6 and 24 hours in octuplicate. The plates were scanned using a well-plate spectrophotometer with reading at wavelength of 570 nm. Data were normalized to account for control (untreated) cells. T-test was used for statistical analyses to compare groups with control samples.

Confocal microscopy

Confocal fluorescence microscopic analyses were carried out using the SPEinv (inverted SPE) microscopy (for vesicle experiments) or the Leica TCS SP8 (for cell experiments), using single photon irradiation with sequential scanning. Visualization of giant unilamellar vesicles was carried out in buffer (0.5% TAE, 500 mM NaCl). Visualization of cells was carried out in PBS (1 x solution). Images were taken using samples on fluorodish cell culture dishes, purchased from World Precision Instruments. Images were taken using excitation wavelengths of 532 or 635 nm (vesicles), or 405, 532 and 633 nm (cells). Data were analysed using LAS-X (Leica Application Suite X) software.

Density functional theory (DFT)

Computational modelling carried out with optimisation of molecular geometry using CAM-B3LYP/6-31G software with application of the SCRF method and the PCM (polarizable continuum model) with adjustment for the relevant solvents where appropriate. Excitation energies for ground state to singlet transitions with corresponding oscillator strengths were acquired using time dependent DFT (with CAM-B3LYP/6-31G software) and accounting for DMSO, acetonitrile or petroleum ether solvents where necessary.

Transient absorption spectroscopy (TAS)

Transient absorption spectra were obtained using a HELIOS (Ultrafast systems) transient absorption spectrometer equipped Xe lamp (75 W) with integrated monochromator to enable wavelength selection. Laser pulses were used with a width of 6 ns at an excitation wavelength of 700 nm. Data was obtained using an Nd: YAG laser with intensity of $\sim 500 \mu\text{J cm}^{-2} \text{ pulse}^{-1}$. Changes in transmitted light were monitored using a Si PIN photodiode upon excitation.

Time correlated single photon counting (TCSPC)

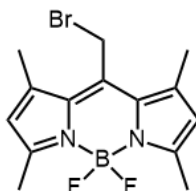
Decay lifetimes were established using TCSPC with a photoluminescence spectrometer equipped with a CCD. Excitation was carried out at 443 nm (1 MHz repetition rate, $80 \mu\text{Wcm}^{-2}$ average intensity) and high pass emission detection at 660 and 760 nm (MeOH), 792 and 730 nm (MeCN) and 720 and 640 nm (ether).

Photoluminescence measurements and photoluminescence quantum yield (PLQY)

Photoluminescence spectra were achieved using a photoluminescence spectrometer with excitation wavelengths between 550 and 700 nm in ether, MeCN and MeOH with PLQY established using Excel Macro software.

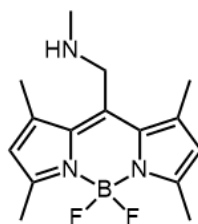
7.2 Synthetic experimental details

Compound 27¹⁷¹



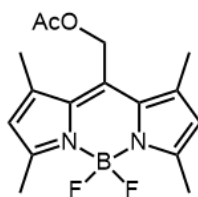
Dry DCM (150 mL) was evacuated with argon. Bromoacetyl bromide (0.170 mL, 1.90 mmol, 1.00 eq.) and 2,4-dimethylpyrrole (0.400 mL, 3.90 mmol, 2.00 eq.) were added dropwise and the dark red reaction mixture was stirred at room temperature under argon and protected from the light for three hours. The solvent was reduced to ~50 mL under vacuum and TEA (4.00 mL, 29.0 mmol, 15.0 eq.) was added. After 15 minutes of stirring under argon, $\text{BF}_3 \cdot \text{Et}_2\text{O}$ (8.00 mL, 65.0 mmol, 33.0 eq.) was added dropwise. The reaction mixture was stirred for a further three hours under argon and protected from the light. DCM was used to extract the organic material, which was washed with distilled water, dried over MgSO_4 , filtered and concentrated *in vacuo*. The crude red product was purified by flash column chromatography on silica gel; eluent: hexane/DCM from a ratio of 80/20 to 50/50. The fractions containing product were combined and concentrated by evaporation to afford 10-(bromomethyl)-5,5-difluoro-1,3,7,9-tetramethyl-5H-4 λ^4 ,5 λ^4 -dipyrrolo[1,2-c:2',1'-f][1,3,2]diazaborinine (224 mg, 0.660 mmol, 35%) as a red amorphous solid. ^1H -NMR (600 MHz, CDCl_3) δ_{H} 6.09 (s, 2H, ArH), 4.69 (s, 2H, CH_2Br), 2.54 (s, 12H, 4CH₃) ppm; ^{13}C -NMR (151 MHz, CDCl_3) δ_{C} 156.6, 141.0, 137.3, 131.1, 122.4, 24.7, 16.1, 14.8 ppm; ^{11}B -NMR (224 MHz, CDCl_3) δ_{B} 0.62 (t, $J = 32.5$ Hz) ppm; ^{19}F -NMR (658 MHz, CDCl_3) δ_{F} -146.7 (q, $J = 33.1$ Hz) ppm MS (EI) $\text{C}_{14}\text{H}_{16}\text{BBBrF}_2\text{N}_2$ (m/z 340.1, $[\text{M}\{^{79}\text{Br}\}+\text{H}]^+$; m/z 342.1, $[\text{M}\{^{81}\text{Br}\}+\text{H}]^+$; m/z 261.1, $[\text{M}-\text{Br}+\text{H}]^+$); UV/Vis λ_{max} (DMSO) = 525 nm, λ_{max} (hexane) = 530 nm; R_f (hexane/DCM:50/50) = 0.4

Compound 28¹⁷²



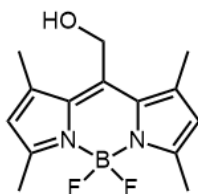
10-(bromomethyl)-5,5-difluoro-1,3,7,9-tetramethyl-5*H*-4λ⁴,5λ⁴-dipyrrolo[1,2-*c*:2',1'-*f*][1,3,2]diazaborinine (70.0 mg, 0.200 mmol), KI (58.0 mg, 0.348 mmol, 1.70 eq.) and K₂CO₃ (160 mg, 1.10 mmol, 5.80 eq.) were dissolved in dry THF (15.0 mL) and flushed with argon. Methylamine (0.300 mL, 1M in THF, 3.00 eq.) was added dropwise. The reaction mixture was stirred overnight. The solvent was removed *in vacuo* and the crude purified by flash column chromatography on silica gel; eluent: hexane/EtOAc:10/90. The fractions containing product were combined and concentrated to afford 1-(5,5-difluoro-1,3,7,9-tetramethyl-5*H*-4λ⁴,5λ⁴-dipyrrolo[1,2-*c*:2',1'-*f*][1,3,2]diazaborinin-10-yl)-*N*-methylmethanamine as a purple solid (34.0 mg, 0.117 mmol, 57%). ¹H NMR (600.130 MHz, CDCl₃) δ_H 6.07 (s, 2H, ArH), 3.90 (s, 2H, CH₂), 2.56 (s, 3H, CH₃), 2.52, (s, 6H, 2CH₃), 2.47 (s, 6H, 2CH₃) ppm; ¹¹B-NMR (224 MHz, CDCl₃) δ_B 0.56 (t, *J* = 33.3 Hz) ppm; ¹⁹F-NMR (658 MHz, CDCl₃) δ_F -146.6 (q, *J* = 32.5 Hz) ppm; UV/Vis λ_{max} (DMSO) = 509 nm, λ_{max} (MeCN) = 505 nm; IR (N-H) = 2921.98 cm⁻¹; R_f (hexane/DCM:20/80) = 0.1

Compound 29¹⁷³



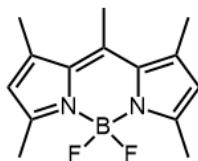
A solution of dry DCM (30 mL) was degassed using argon for 10 minutes before 2,4-dimethylpyrrole (0.220 mL, 2.10 mmol, 2.00 eq.) was added followed by acetoxyacetyl chloride (0.140 mL, 1.30 mmol, 1.20 eq.). The reaction mixture was left to reflux for two hours under argon, after which it was cooled to room temperature. DIPEA (0.730 mL, 4.20 mmol, 4.00 eq.) was added dropwise prior to stirring for 15 minutes under argon. Finally $\text{BF}_3 \cdot \text{Et}_2\text{O}$ (0.530 mL, 4.20 mmol, 4.00 eq.) was added and the reaction mixture was stirred for 30 minutes under a flow of argon and protected from the light. The solvent was removed *in vacuo* to yield a dark red solid which was purified by flash column chromatography on silica gel; eluent: hexane/DCM from a ratio of 70/30 to 30/70 to afford (5,5-difluoro-1,3,7,9-tetramethyl-5H-4 λ^4 ,5 λ^4 -dipyrrolo[1,2-c:2',1'-f][1,3,2]diazaborinin-10-yl)methyl acetate (182 mg, 0.570 mmol, 53%) as a red solid. ^1H -NMR (600 MHz, CDCl_3) δ_{H} 6.09 (s, 2H, ArH), 5.30 (s, 2H, CH_2), 2.54 (s, 6H, 2 CH_3), 2.36 (s, 6H, 2 CH_3), 2.14 (s, 3H, CH_3) ppm; ^{11}B -NMR (224 MHz, CDCl_3) δ_{B} 0.56 (t, $J = 33.3$ Hz) ppm; ^{19}F -NMR (658 MHz, CDCl_3) δ_{F} -146.4 (q, $J = 32.5$ Hz) ppm; UV/Vis λ_{max} (DMSO) = 504 nm, λ_{max} (hexane) = 506 nm; IR (C=O) = 1738.72 cm^{-1} ; R_f (hexane/DCM:20/80) = 0.5.

Compound 30¹⁷³



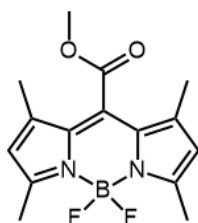
A solution of compound 3 (255 mg, 0.800 mmol, 1.00 eq.) in THF (8.00 mL) was flushed with argon for 10 minutes. LiOH (95.0 mg, 4.00 mmol, 5.00 eq.) was dissolved in distilled water (8.00 mL) and the two solutions were combined and stirred at room temperature under argon and protected from the light for four hours. The organic material was extracted using EtOAc and the organic layers were washed with brine (3 x 20.0 mL) and saturated NH₄Cl (1 x 20.0 mL) before being dried over MgSO₄, filtered under vacuum and the solvent removed *in vacuo*. The crude red solid was purified by flash column chromatography on silica gel; eluent: hexane/DCM from a ratio of 20/80 to 0/100. The fractions containing product were combined and concentrated under vacuum to yield (5,5-difluoro-1,3,7,9-tetramethyl-5*H*-4λ⁴,5λ⁴-dipyrrolo[1,2-*c*:2',1'*f*][1,3,2]diazaborinin-10-yl)methanol (172 mg, 0.620 mmol, 78%) as a red solid. ¹H NMR (600 MHz, *d*⁶-DMSO) δ_H 6.24 (s, 2H, ArH), 5.56 (t, *J* = 5.2 Hz, 1H, OH), 4.71 (d, *J* = 5.2 Hz, 2H, CH₂), 2.49 (s, 6H, 2CH₃), 2.41 (s, 6H, 2CH₃) ppm; ¹¹B-NMR (224 MHz, CDCl₃) δ_B -1.66 ppm; ¹⁹F-NMR (658 MHz, CDCl₃) δ_F -146.4 (q, *J* = 32.2 Hz) ppm; UV/Vis λ_{max} (DMSO) = 512 nm, λ_{max} (Pet. ether) = 513 nm; IR (O-H) = 3548.59 cm⁻¹; R_f (hexane/DCM:20/80) = 0.1.

Compound 31¹⁷⁰



Acetyl chloride (0.700 mL, 9.75 mmol) and 2,4-dimethylpyrrole (2.00 mL, 19.5 mmol, 2.00 eq.) were dissolved in dry DCM (30.0 mL) under argon. The reaction mixture was heated under reflux overnight. $\text{BF}_3 \cdot \text{Et}_2\text{O}$ (8.00 mL, 65.0 mmol, 33.0 eq.) and TEA (4.00 mL, 29.0 mmol, 15.0 eq.) were added and the reaction stirred for a further four hours. The solvent was removed under vacuum and the crude was purified by flash column chromatography on silica gel; eluent: hexane/DCM(60/40). The fractions containing product were combined and concentrated *in vacuo* to afford 5,5-difluoro-1,3,7,9,10-pentamethyl-5H-4 λ^4 ,5 λ^4 -dipyrrolo[1,2-*c*:2',1'-*f*][1,3,2]diazaborinine (1.06 g, 4.04 mmol, 41%). ^1H NMR (700 MHz, CDCl_3) δ_{H} 6.05 (s, 2H, ArH), 2.58 (s, 3H, CH_3), 2.52 (s, 6H, 2 CH_3), 2.42 (s, 6H, 2 CH_3) ppm; ^{11}B -NMR (224 MHz, CDCl_3) δ_{B} 0.62 (t, J = 33.3 Hz) ppm; ^{19}F -NMR (658 MHz, CDCl_3) δ_{F} -146.7 (q, J = 33.1 Hz) ppm; UV/Vis λ_{max} (DMSO) = 495 nm, λ_{max} (Pet. ether) = 498 nm; R_{f} (hexane/DCM:70/30) = 0.1.

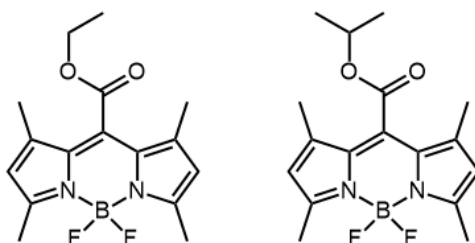
Compound 32¹³⁶



Compound 32: Dry DCM (60.0 mL) which was flushed with argon for 10 minutes. The reaction flask was cooled to -78°C and to the solution was added methyl chlorooxoacetate (0.180 mL, 1.90 mmol, 1.00 eq.) and 2,4-dimethylpyrrole (0.400 mL, 3.90 mmol, 2.50 eq.). The reaction was stirred at this temperature for four hours

before TEA (1.08 mL, 7.76 mmol, 4.00 eq.) was added, followed by $\text{BF}_3 \cdot \text{Et}_2\text{O}$ (3.00 mL, 24.0 mmol, 12.5 eq., excess). The reaction mixture was allowed to reach room temperature and stir for a further two hours prior to the removal of solvent *in vacuo*. The crude product was purified by flash column chromatography on silica gel; eluent: hexane/DCM:50/50 and the fractions containing product were combined and concentrated by evaporation to afford methyl 5,5-difluoro-1,3,7,9-tetramethyl-5*H*-4 λ^4 ,5 λ^4 -dipyrrolo[1,2-*c*:2',1'-*f*][1,3,2]diazaborinine-10-carboxylate (309 mg, 1.00 mmol, 53%) as a red solid. ^1H NMR (600 MHz, CDCl_3) δ_{H} 6.07 (s, 2H, ArH), 3.97 (s, 3H, OCH_3), 2.53 (s, 6H, 2 CH_3), 2.12 (s, 6H, 2 CH_3) ppm; ^{13}C NMR (151 MHz, CDCl_3) δ_{C} 165.9, 157.8, 141.2, 128.7, 128.7, 121.3, 53.3, 14.9, 12.7 ppm; ^{11}B -NMR (224 MHz, CDCl_3) δ_{B} 0.55 (t, $J = 33.3$ Hz) ppm; ^{19}F -NMR (658 MHz, CDCl_3) δ_{F} -146.3 ppm; UV/Vis λ_{max} (DMSO) = 509 nm, λ_{max} (hexane) = 511 nm; IR (C=O) = 1737.61 cm^{-1} ; R_f (hexane/DCM:50/50) = 0.2.

Compounds 33 and 34¹³⁶



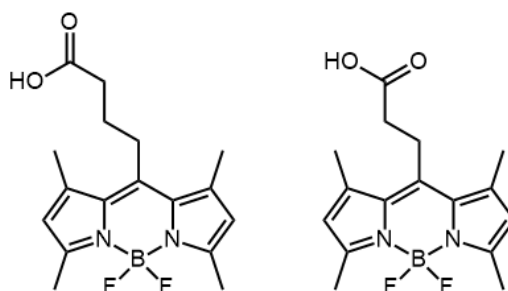
2,4-dimethylpyrrole (0.500 mL, 5.00 mmol, 2.00 eq.) and oxalyl chloride (0.220 mL, 2.50 mmol, 1.00 eq.) were dissolved in dry DCM (20.0 mL) and degassed with argon. Dry alcohol (2.50 mmol, 1.00 eq.) was added and the reaction mixture was stirred at room temperature for one hour. TEA (2.00 mL) and $\text{BF}_3 \cdot \text{Et}_2\text{O}$ (3.00 mL) were added dropwise and the reaction was stirred at room temperature under argon for three hours. The solvent was subsequently removed under vacuum and the crude was purified by flash column chromatography on silica gel; eluent: hexane/DCM:50/50.

Compound **33**: ethyl 5,5-difluoro-1,3,7,9-tetramethyl-5*H*-4 λ^4 ,5 λ^4 -dipyrrolo[1,2-*c*:2',1'-*f*][1,3,2]diazaborinine-10-carboxylate (309 mg, 1.00 mmol, 53%) as an amorphous

red solid. ^1H NMR (600 MHz, CDCl_3) δ_{H} 6.07 (s, 2H, ArH), 4.43 (q, $J = 7.2$ Hz, 2H, CH_2), 2.54 (s, 6H, 2CH_3), 2.14 (s, 6H, 2CH_3), 1.43 (t, $J = 7.2$ Hz, 6H, CH_3) ppm; ^{11}B -NMR (224 MHz, CDCl_3) δ_{B} 0.27 (t, $J = 33.8$ Hz) ppm; UV/Vis λ_{max} (DMSO) = 509 nm, λ_{max} (Pet. ether) = 511 nm; IR (C=O) = 1737.70 cm^{-1} ; R_f (hexane/DCM:50/50) = 0.2.

Compound **34**: isopropyl 5,5-difluoro-1,3,7,9-tetramethyl-5H-4 λ^4 ,5 λ^4 -dipyrrolo[1,2-*c*:2',1'-*f*][1,3,2]diazaborinine-10-carboxylate (322 mg, 1.00 mmol, 40%) as an amorphous red solid. ^1H NMR (600 MHz, CDCl_3) δ_{H} 6.08 (s, 2H, ArH), 5.25 (spt, $J = 6.3$ Hz, 1H, CH), 2.54 (s, 6H, 2CH_3), 2.19 (s, 6H, 2CH_3), 1.43 (t, $J = 7.2$ Hz, 6H, 2CH_3) ppm; ^{11}B -NMR (224 MHz, CDCl_3) δ_{B} 0.27 (t, $J = 33.8$ Hz) ppm; IR (C=O) = 1737.68 cm^{-1} ; UV/Vis λ_{max} (DMSO) = 511 nm, λ_{max} (Pet. ether) = 512 nm; R_f (hexane/DCM:50/50) = 0.2.

Compounds 36 and 37¹⁷⁴



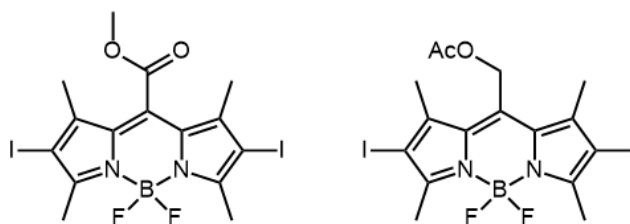
2,4-dimethylpyrrole (0.120 mL, 1.20 mmol, 2 eq.) and glutaric or succinic anhydride (0.600 mmol, 1 eq.) were dissolved in dry DCM (10.0 mL) under argon. $\text{BF}_3 \cdot \text{Et}_2\text{O}$ (0.500 mL, 4.00 mmol) and TEA (0.420 mL, 3.00 mmol) were added and the reaction was heated under reflux for five hours. The organic material was washed with water, dried over MgSO_4 , filtered and concentrated *in vacuo* before purification by flash column chromatography on silica gel; eluent: hexane/EtOAc/AcOH:50/50/0 to 0/97/3.

Compound **36**: 4-(5,5-difluoro-1,3,7,9-tetramethyl-5H-4 λ^4 ,5 λ^4 -dipyrrolo[1,2-*c*:2',1'-*f*][1,3,2]diazaborinin-10-yl)butanoic acid (22.0 mg, 0.066 mmol, 11%). ^1H NMR (600.130 MHz, CDCl_3) δ_{H} 6.06 (s, 2H, ArH), 2.82-2.78 (m, 2H, CH_2), 2.57-2.54 (m,

2H, CH₂), 2.52 (s, 6H, 2CH₃), 2.43 (s, 6H, 2CH₃), 2.04-1.99 (m, 2H, CH₂) ppm; UV/Vis λ_{\max} (DMSO) = 499 nm, λ_{\max} (MeCN) = 495 nm; IR (C=O) = 1687.50 cm⁻¹, (O-H) = 3266.48 cm⁻¹; R_f (EtOAc) = 0.3 (stained with bromocresol green).

Compound **37**: 3-(5,5-difluoro-1,3,7,9-tetramethyl-5H-4I4,5I4-dipyrrolo[1,2-c:2',1'-f][1,3,2]diazaborinin-10-yl)propanoic acid (27.0 mg, 0.084 mmol, 14%). ¹H NMR (600.130 MHz, CDCl₃) δ_{H} 6.06 (s, 2H, ArH), 3.36-3.33 (m, 2H, CH₂), 2.71-2.69 (m, 2H, CH₂), 2.52 (s, 6H, 2CH₃), 2.45 (s, 6H, 2CH₃) ppm; UV/Vis λ_{\max} (DMSO) = 499 nm, λ_{\max} (MeCN) = 496 nm; IR (C=O) = 1688.71 cm⁻¹, (O-H) = 3266.60 cm⁻¹; R_f (EtOAc) = 0.3 (stained with bromocresol green).

Compounds 38 and 39¹⁶⁵



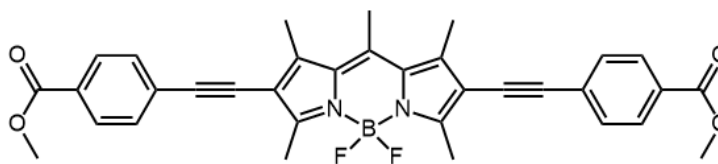
Compound **32** or **29** was dissolved in dry THF (10.0 mL) under argon and cooled to -78°C. NIS (3.90 eq.) was added and the reaction warmed to room temperature overnight. The solvent was evaporated, and the crude purified by flash column chromatography on silica gel; eluent: hexane/DCM:50/50.

Compound **38**: (5,5-difluoro-2,8-diiodo-1,3,7,9-tetramethyl-5H-4 λ^4 ,5 λ^4 -dipyrrolo[1,2-c:2',1'-f][1,3,2]diazaborinin-10-yl)methyl acetate (61.0 mg, 0.109 mmol, 33%) ¹H NMR (600.130 MHz, CDCl₃) δ_{H} 4.01 (s, 3H, OCH₃), 2.64 (s, 6H, 2CH₃), 2.14 (s, 6H, 2CH₃) ppm; ¹¹B-NMR (224 MHz, CDCl₃) δ_{B} 0.38 (t, *J* = 30.5 Hz) ppm; ¹⁹F-NMR (658 MHz, CDCl₃) δ_{F} -145.7 (q, *J* = 31.6 Hz) ppm; UV/Vis λ_{\max} (DMSO) = 554 nm, λ_{\max} (Pet. ether) = 549 nm; IR (C=O) = 1737.11 cm⁻¹; R_f (hexane/DCM:50/50) = 0.2.

Compound **39**: methyl 5,5-difluoro-2,8-diiodo-1,3,7,9-tetramethyl-5H-4 λ^4 ,5 λ^4 -dipyrrolo[1,2-c:2',1'-f][1,3,2]diazaborinine-10-carboxylate (52.0 mg, 0.091 mmol,

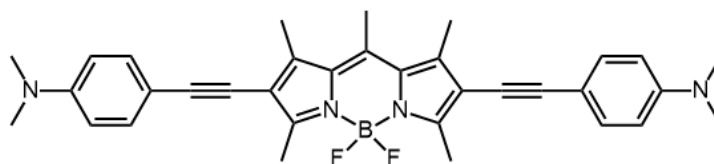
29%) ^1H NMR (600.130 MHz, CDCl_3) δ_{H} 5.32 (s, 2H, CH_2), 2.63 (s, 6H, 2 CH_3), 2.40 (s, 6H, 2 CH_3), 2.15 (s, 3H CH_3) ppm; ^{13}C NMR (151 MHz, CDCl_3) δ_{C} 170.4, 158.1, 143.6, 132.9, 132.7, 87.4, 58.4, 20.7, 18.3, 16.5 ppm; ^{11}B -NMR (224 MHz, CDCl_3) δ_{B} 0.36 (t, $J = 33.3$ Hz) ppm; ^{19}F -NMR (658 MHz, CDCl_3) δ_{F} -145.6 (q, $J = 31.6$ Hz) ppm; UV/Vis λ_{max} (DMSO) = 555 nm, λ_{max} (Pet. ether) = 553 nm; IR (C=O) = 1740.76 cm^{-1} ; R_{f} (hexane/DCM:50/50) = 0.4.

Compound 43a



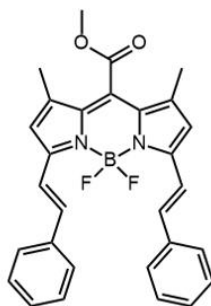
A solution of compound **3** (100 mg, 0.310 mmol) was prepared in dry toluene (300 mL). Methyl 4-ethynyl benzoate (124 mg, 0.775 mmol, 2.50 eq.), $\text{Pd}(\text{Ph}_3)_4$ (10.4 mg, 0.00900 mmol, 3.00 mol%), CuI (3.00 mg, 0.0160 mmol, 5.00 mol%) and TEA (3.00 mL) were added and the reaction mixture stirred under reflux overnight. The reaction mixture was filtered through a plug of celite using EtOAc and the crude product dried under vacuum. The material was purified using flash column chromatography on silica gel; eluent: hexane/EtOAc:10/90. The fractions containing product were combined and concentrated *in vacuo* to afford 4,4'-((5,5-difluoro-1,3,7,9,10-pentamethyl-5*H*-4 λ^4 ,5 λ^4 -dipyrrolo[1,2-*c*:2',1'-*f*][1,3,2]diazaborinine-2,8-diyl)bis(ethyne-2,1-diyl))dibenzoate as an amorphous purple solid (27.0 mg, 0.0467 mmol, 15%). ^1H -NMR (700 MHz, CDCl_3) δ_{H} 8.03 (d, 4H, $J = 8.5$ Hz, PhH), 7.57 (d, 4H, $J = 8.5$ Hz, PhH), 3.94 (s, 6H, COOCH_3), 2.71 (s, 3H, CH_3), 2.70 (s, 6H, 2 CH_3), 2.60 (s, 6H, 2 CH_3) ppm; ^{11}B -NMR (224 MHz, CDCl_3) δ_{B} 0.59 (t, $J = 30.5$ Hz) ppm; ^{19}F -NMR (658 MHz, CDCl_3) δ_{F} -146.6 (q, $J = 31.6$ Hz) ppm; UV/Vis λ_{max} (DMSO) = 535 nm, λ_{max} (DCM) = 544 nm; IR (C=O) = 1719.33 cm^{-1} ; R_{f} (hexane/EtOAc:20/80) = 0.1

Compound 44a



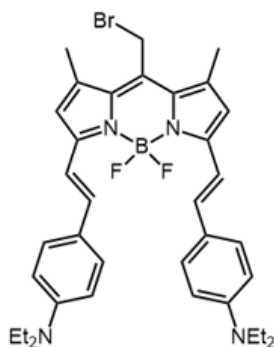
A solution of compound **3** (100 mg, 0.310 mmol) was prepared in dry toluene (30 mL). 4-ethynyl-*N,N*-dimethylaniline (113 mg, 0.775 mmol, 2.50 eq.), Pd(Ph₃)₄ (10.4 mg, 0.009 mmol, 3.0 mol%), CuI (3.00 mg, 0.0160 mmol, 5.00 mol%) and TEA (3.00 mL) were added and the reaction mixture stirred under reflux overnight. The reaction mixture was filtered through a plug of celite using EtOAc and the crude product dried under vacuum. The material was purified using flash column chromatography on silica gel; eluent: hexane/EtOAc:50/50. The fractions containing product were combined and concentrated by evaporation to yield 4,4'-((5,5-difluoro-1,3,7,9,10-pentamethyl-5*H*-4λ⁴,5λ⁴-dipyrrolo[1,2-*c*:2',1'-*f*][1,3,2]diazaborinine-2,8-diyl)bis(ethyne-2,1-diyl))bis(*N,N*-dimethylaniline) as an amorphous purple solid (21.0 mg, 0.0383 mmol, 12%). ¹H-NMR (700 MHz, CDCl₃) δ_H 7.40 (d, 4H, *J* = 8.9 Hz, PhH), 6.67 (d, 4H, *J* = 8.7 Hz, PhH), 3.00 (s, 12H, 2N(CH₃)₂), 2.68 (s, 6H, 2CH₃), 2.67 (s, 3H, CH₃), 2.56 (s, 6H, 2CH₃) ppm; ¹¹B-NMR (224 MHz, CDCl₃) δ_B 0.46 (t, *J* = 33.3 Hz) ppm; ¹⁹F-NMR (658 MHz, CDCl₃) δ_F - 146.9 (q, *J* = 31.9 Hz) ppm; UV/Vis λ_{max} (DMSO) = 561 nm, λ_{max} (DCM) = 590 nm; R_f (hexane/EtOAc:50/50) = 0.2

Compound 46



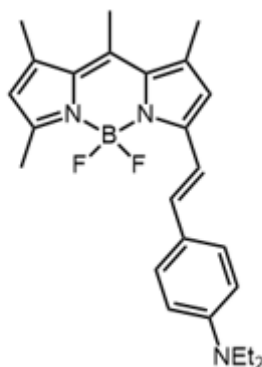
An oven dried round bottomed flask was equipped with a Dean-Stark trap and charged with benzaldehyde (0.110 mL, 1.10 mmol, 2.20 eq.), piperidine (2.00 mL) and AcOH (2.00 mL). The flask was flushed with argon before compound **32** (150 mg, 0.490 mmol, 1.00 eq.) in dry toluene (20.0 mL) was added. The flask was equipped with a Dean and Stark trap and the reaction mixture was heated under reflux for 16 hours. After cooling to room temperature, the reaction mixture was washed with distilled water (3 x 20.0 mL) and the organic material was extracted with DCM, dried over MgSO₄, filtered and concentrated *in vacuo*. The residue was purified by flash column chromatography on silica gel; eluent: DCM/MeOH from a ratio of 100/0 to 90/10. The fractions containing product were combined and concentrated by evaporation to afford methyl 5,5-difluoro-1,9-dimethyl-3,7-di((E)-styryl)-5H-4λ⁴,5λ⁴-dipyrrolo[1,2-c:2',1'-f][1,3,2]diazaborinine-10-carboxylate as a blue solid (140 mg, 0.290 mmol, 59%). ¹H-NMR (700 MHz, CDCl₃) δ_H 7.70 (d, *J* = 16.4 Hz, 2H, C=CH), 7.53 (d, *J* = 16.3 Hz, 4H, PhH), 7.42 (m, 6H, PhH), 7.10 (d, *J* = 16.4 Hz, 2H, C=CH), 6.72 (s, 2H, ArH), 4.01 (s, 3H, CH₃), 2.20 (s, 6H, 2CH₃) ppm; ¹¹B-NMR (224 MHz, CDCl₃) δ_B 0.98 (t, *J* = 33.3 Hz) ppm; ¹⁹F-NMR (658 MHz, CDCl₃) δ_F -138.3 ppm; (MS (ESI) C₂₉H₂₅BF₂N₂O₂ (*m/z* 483.2, [M+H]⁺); UV/Vis λ_{max} (DMSO) = 656 nm, λ_{max} (Pet. ether) = 642 nm; IR (C=O) = 1735.80 cm⁻¹; R_f (DCM) = 0.2

Compound 47



Dry toluene (30.0 mL) was degassed with argon for 30 minutes. 10-(bromomethyl)-5,5-difluoro-1,3,7,9-tetramethyl-5*H*-4 λ^4 ,5 λ^4 -dipyrrolo[1,2-*c*:2',1'-*f*][1,3,2]diazaborinine (80.0 mg, 0.235 mmol) was added followed by diethylaminobenzaldehyde (92.0 mg, 0.517 mmol, 2.20 eq.). AcOH (2.00 mL) and piperidine (2.00 mL) were added and the reaction mixture was stirred under reflux and under argon overnight. The organic material was extracted using DCM and the organic layers washed with water, dried over MgSO₄, filtered and concentrated by evaporation. The crude solid was purified by flash column chromatography on silica gel; eluent: hexane/DCM. The fractions containing product were combined and concentrated under vacuum to afford 4,4'-((1*E*,1'*E*)-(10-(bromomethyl)-5,5-difluoro-1,9-dimethyl-5*H*-4 λ^4 ,5 λ^4 -dipyrrolo[1,2-*c*:2',1'-*f*][1,3,2]diazaborinine-3,7-diyl))bis(ethene-2,1-diyl))bis(*N,N*-diethylaniline) as a green/blue solid (10.0 mg, 0.0160 mmol, 7%). ¹H-NMR (700 MHz, CDCl₃) δ_{H} 7.47 (d, *J* = 8.8 Hz, 4H, PhH), 7.45 (d, *J* = 16.7 Hz, 2H, C=CH), 7.20 (d, *J* = 16.1 Hz, 2H, C=CH), 6.67 (s, 2H, CH), 6.64 (d, *J* = 8.8 Hz, 4H, PhH) 3.72 (s, 2H CH₂Br), 3.40 (q, *J* = 7.1 Hz, 8H, CH₂CH₃), 2.51 (s, 6H, CH₃), 1.19 (t, *J* = 7.1 Hz, 12H, CH₂CH₃) ppm; ¹¹B-NMR (224 MHz, CDCl₃) δ_{B} 0.86 (t, *J* = 33.3 Hz) ppm; ¹⁹F-NMR (658 MHz, CDCl₃) δ_{F} -142.5 ppm; UV/Vis λ_{max} (DMSO) = 734 nm, λ_{max} (Pet. ether) = 699 nm; *R*_f (hexane/EtOAc:60/40) = 0.3.

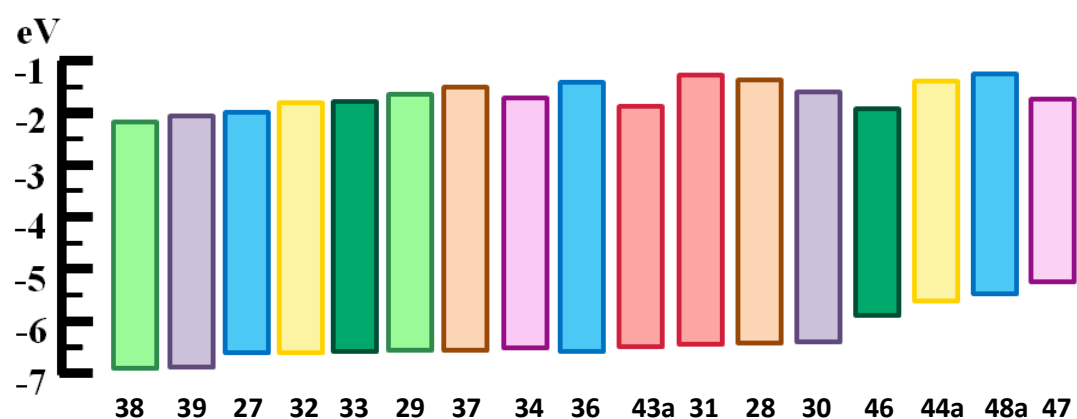
Compound 48a



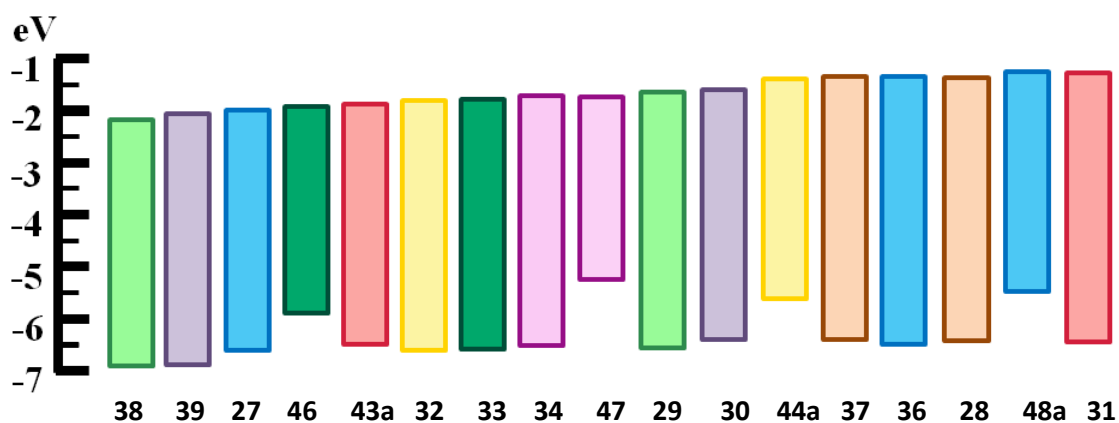
Dry toluene (30.0 mL) was degassed with argon for 30 minutes. Compound **3** (50.0 mg, 0.156 mmol) was added followed by diethylaminobenzaldehyde (30.5 mg, 0.172 mmol, 1.10 eq.). AcOH (2.00 mL) and piperidine (2.00 mL) were added and the reaction mixture was stirred under reflux and under argon overnight. The organic material was extracted using DCM and the organic layers washed with water, dried over MgSO₄, filtered and concentrated by evaporation. The crude solid was purified by flash column chromatography on silica gel; eluent: hexane/DCM from a ratio of 10/90 to 40/60. The fractions containing product were combined and concentrated under vacuum to afford (E)-4-(2-(5,5-difluoro-1,7,9,10-tetramethyl-5H-5λ⁴,6λ⁴-dipyrrolo[1,2-c:2',1'-f][1,3,2]diazaborinin-3-yl)vinyl)-N,N-diethylaniline as a blue gum (7.00 mg, 0.0166 mmol, 11%). ¹H-NMR (700 MHz, CDCl₃) δ_H 7.46 (d, *J* = 8.9 Hz, 2H, PhH), 7.42 (d, *J* = 16.1 Hz, 1H, C=CH), 7.18 (d, *J* = 16.3 Hz, 1H, C=CH), 6.67 (s, 1H, ArH), 6.63 (d, *J* = 8.9 Hz, 2H, PhH), 6.03 (s, 1H, ArH), 3.40 (q, *J* = 7.1 Hz, 4H, 2CH₂), 2.59 (s, 3H, CH₃), 2.55 (s, 3H, CH₃), 2.46 (s, 3H, CH₃), 2.42 (s, 3H, CH₃), 1.19 (t, *J* = 7.0 Hz, 6H, 2CH₃) ppm; ¹¹B-NMR (224 MHz, CDCl₃) δ_B 0.87 (q, *J* = 33.29 Hz) ppm; ¹⁹F-NMR (658 MHz, CDCl₃) δ_F - 143.0 ppm (q, *J* = 31.9 Hz); UV/Vis λ_{max} (DMSO) = 704 nm, λ_{max} (Pet. ether) = 679 nm; R_f (hexane/DCM:50/50) = 0.3

7.3 Density functional theory

HOMO/LUMO representations arranged by ascending HOMO



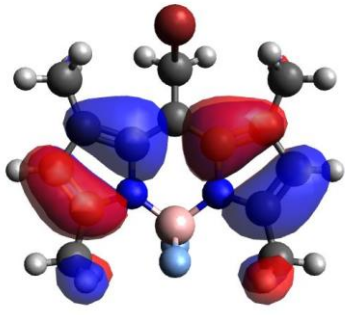
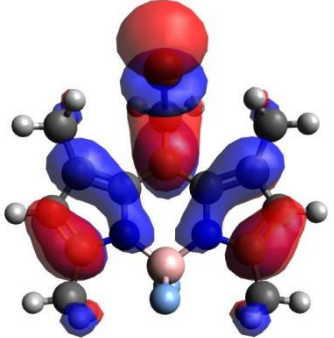
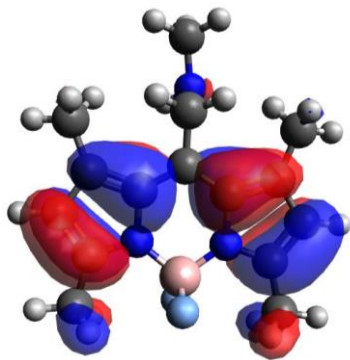
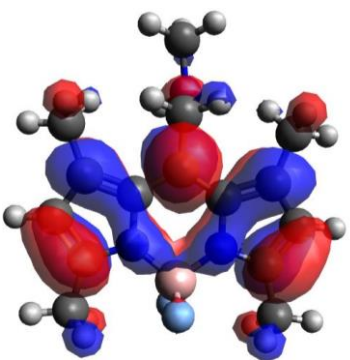
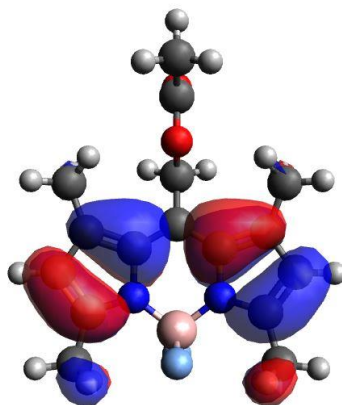
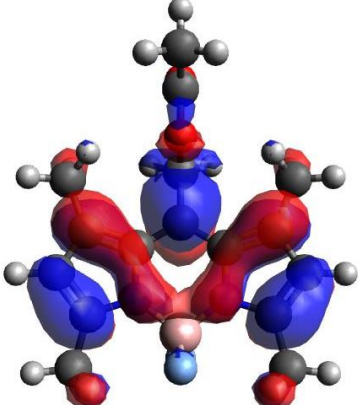
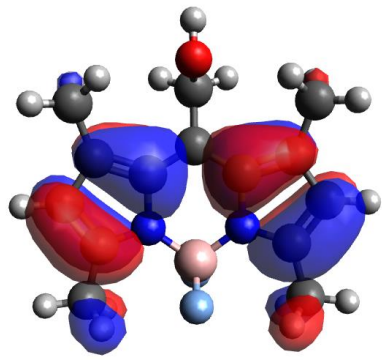
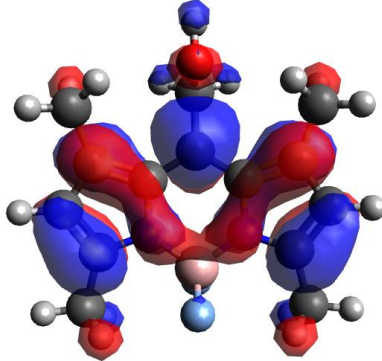
HOMO/LUMO representations arranged by ascending LUMO

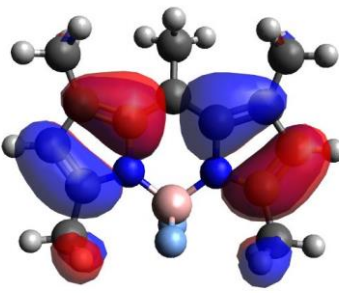
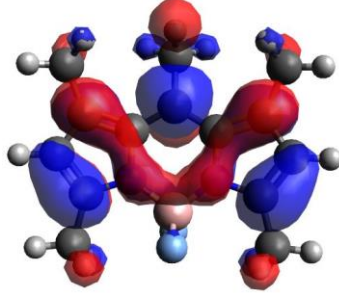
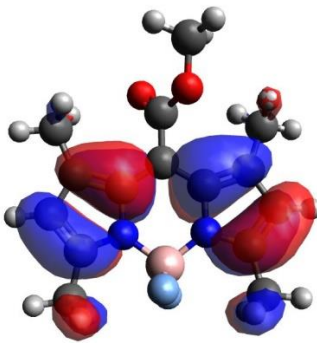
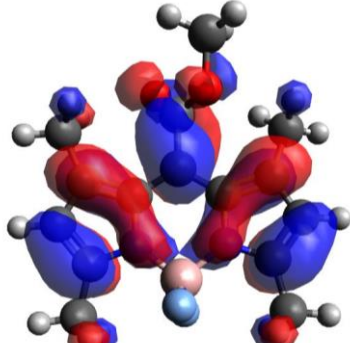
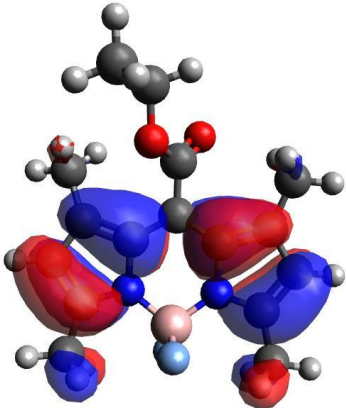
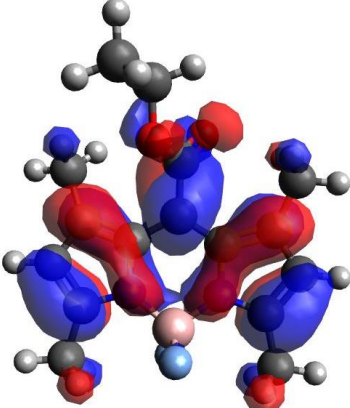
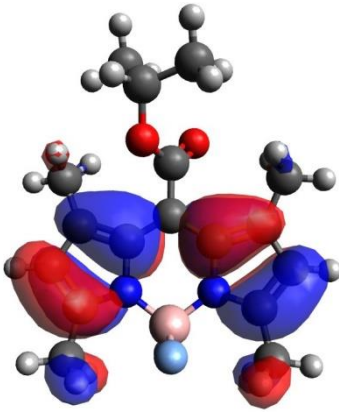
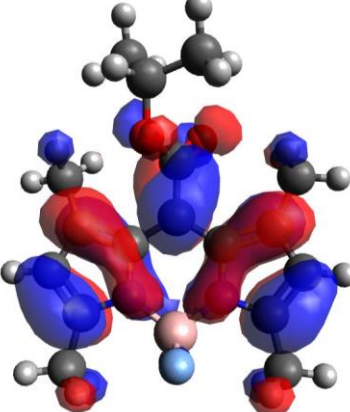


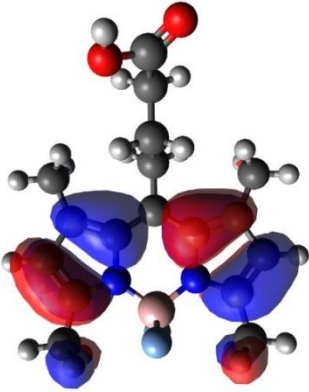
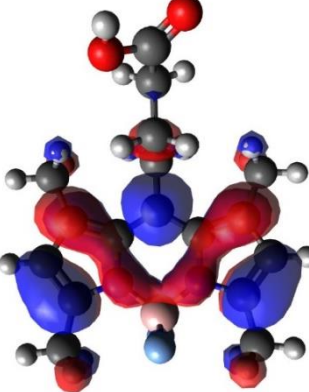
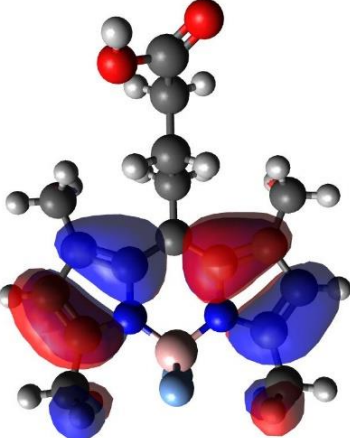
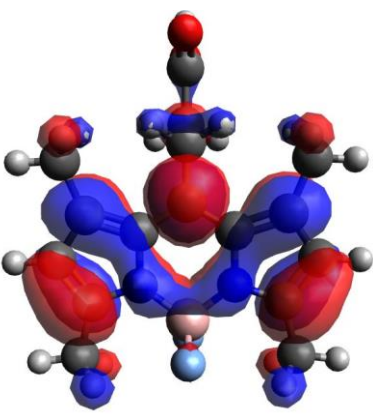
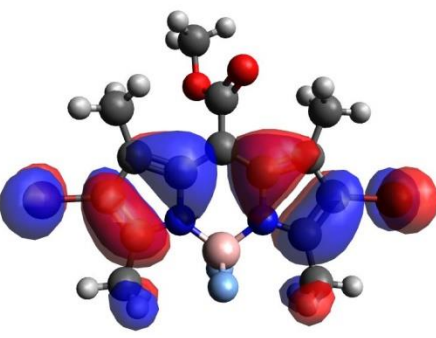
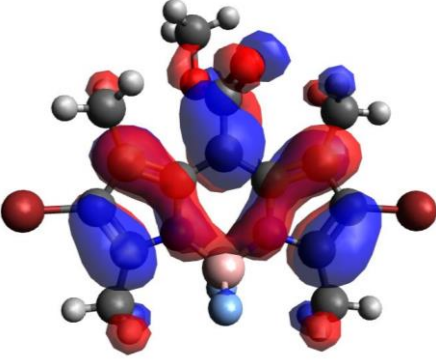
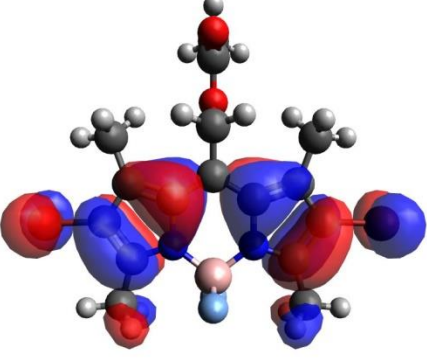
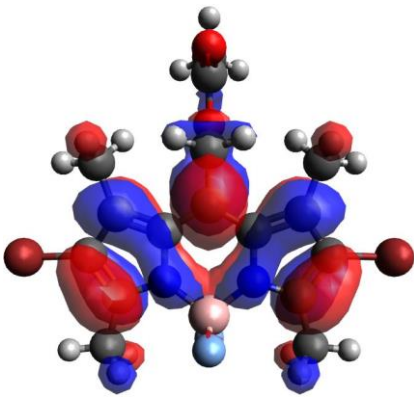
Compound	HOMO (eV)	LUMO (eV)
27	-6.637	-2.028
28	-6.453	-1.421
29	-6.576	-1.681
30	-6.442	-1.526
31	-6.467	-1.334
32	-6.594	-1.841
33	-6.578	-1.806
34	-6.554	-1.778
36	-6.552	-1.427
37	-6.559	-1.428
38	-6.917	-2.209
39	-6.889	-2.101
43a	-6.503	-1.892
44a	-5.644	-1.441
46	-5.911	-1.969
47	-5.257	-1.762
48a	-5.530	-1.335

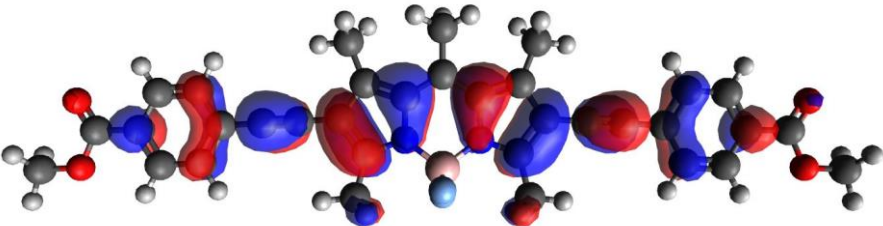
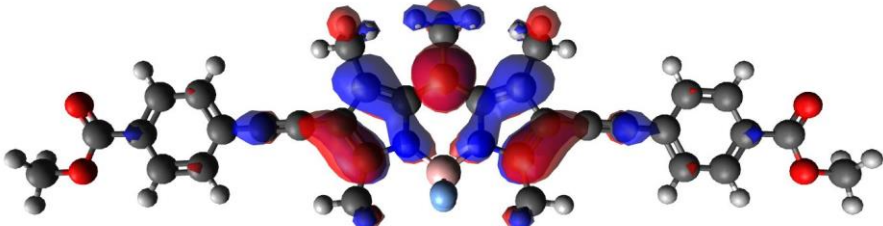
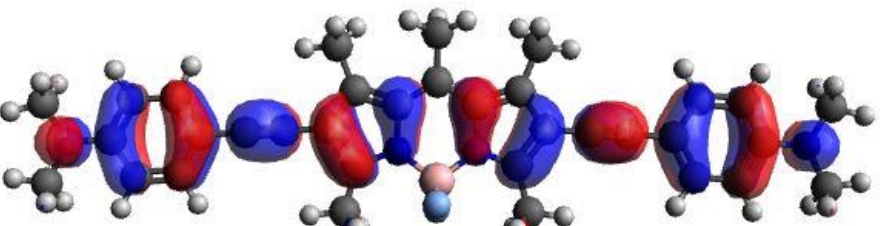
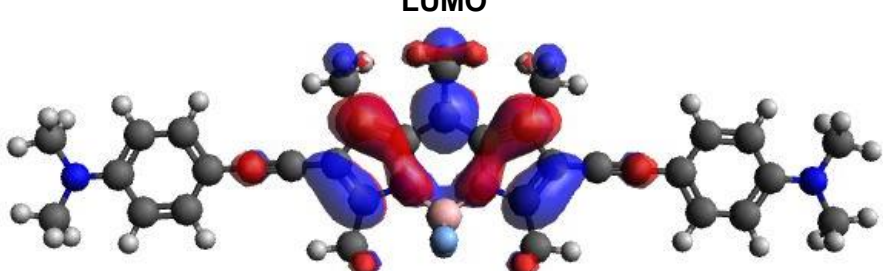
*Table A1: HOMO and LUMO energies for compounds **27-48a***

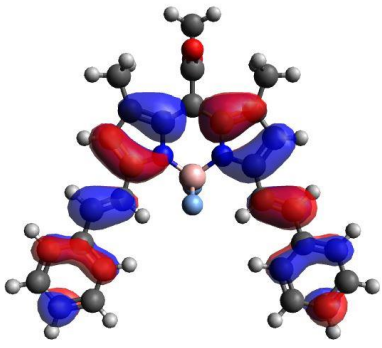
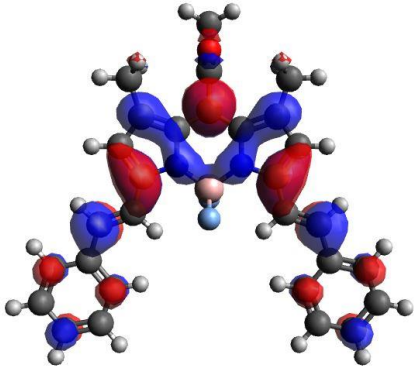
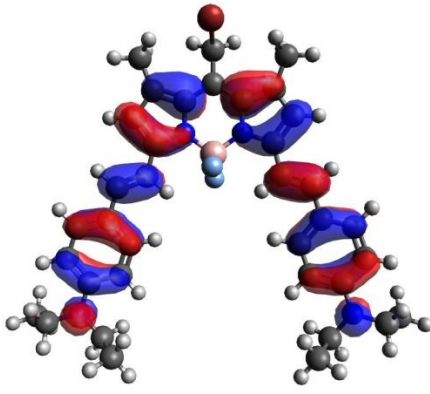
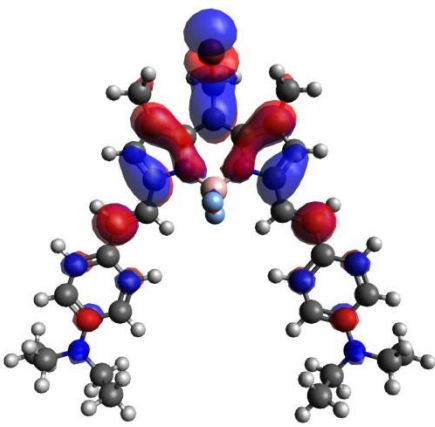
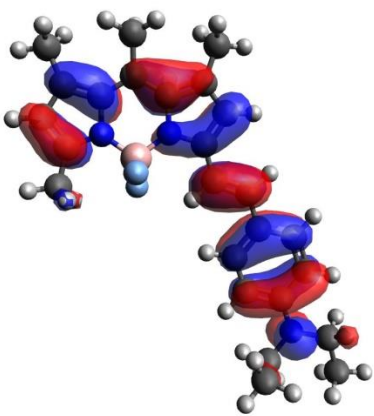
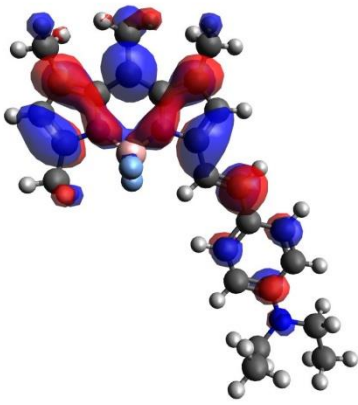
Molecular orbitals of compounds 27-48

	HOMO	LUMO
Compound 27		
Compound 28		
Compound 29		
Compound 30		
	HOMO	LUMO

Compound 31		
Compound 32		
Compound 33		
Compound 34		

	HOMO	LUMO
Compound 36		
Compound 37		
Compound 38		
Compound 39		

<p>Compound 43a</p>	<p>HOMO</p> 
	<p>LUMO</p> 
<p>Compound 44a</p>	<p>HOMO</p> 
	<p>LUMO</p> 

	HOMO	LUMO
Compound 46		
Compound 47		
Compound 48a		

7.4 Confocal fluorescence microscopy

Vesicle staining

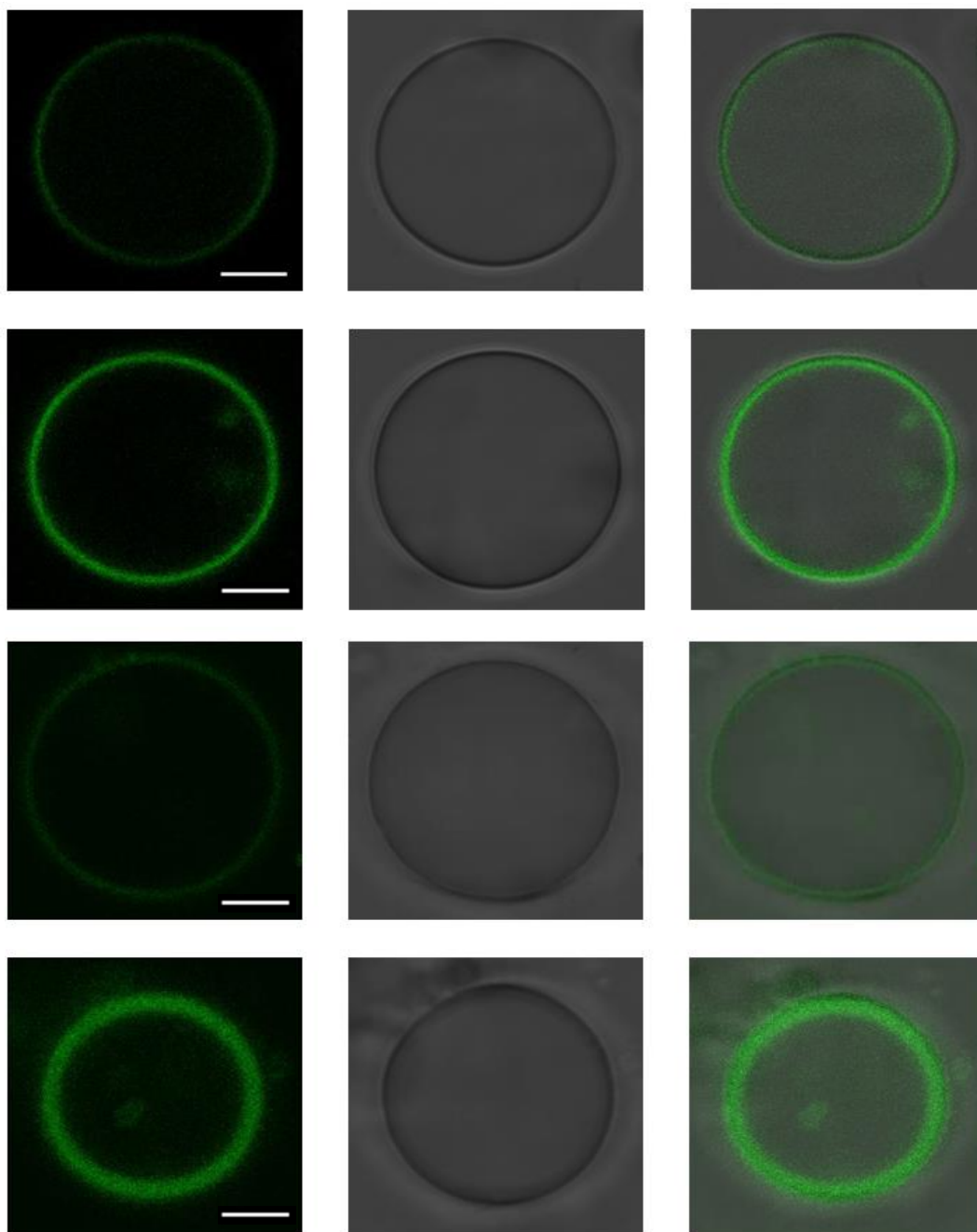


Figure A1: Confocal microscopy images; top to bottom: compounds **28**, **29**, **43a**, and **44a**. L \rightarrow R: Single channel (532 nm excitation), single channel (visible), overlaid images. Scale bar 8 μ M.

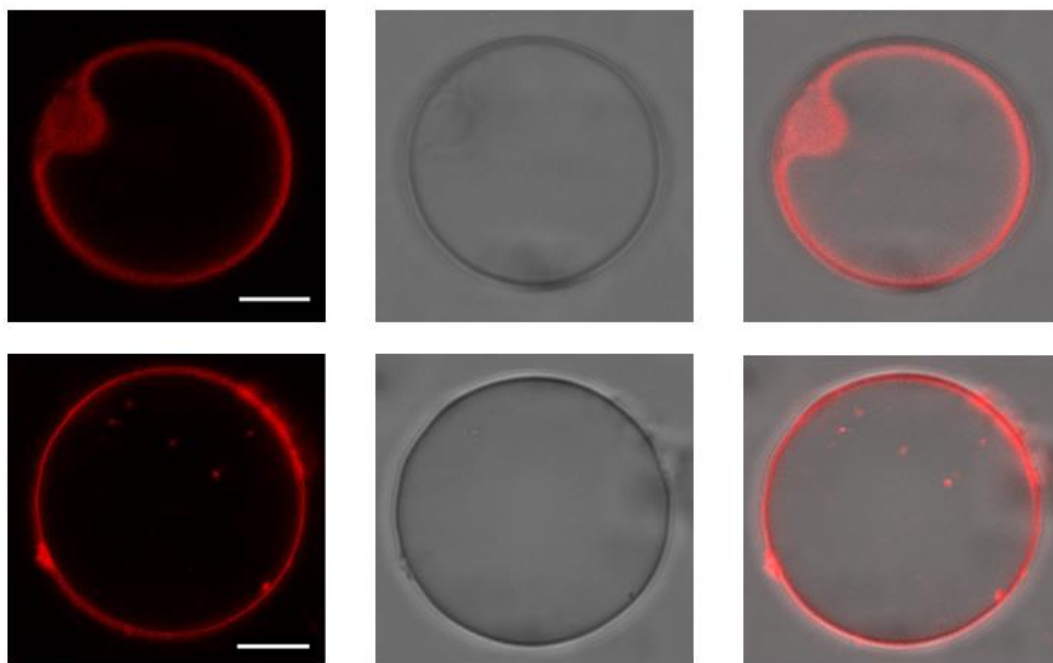
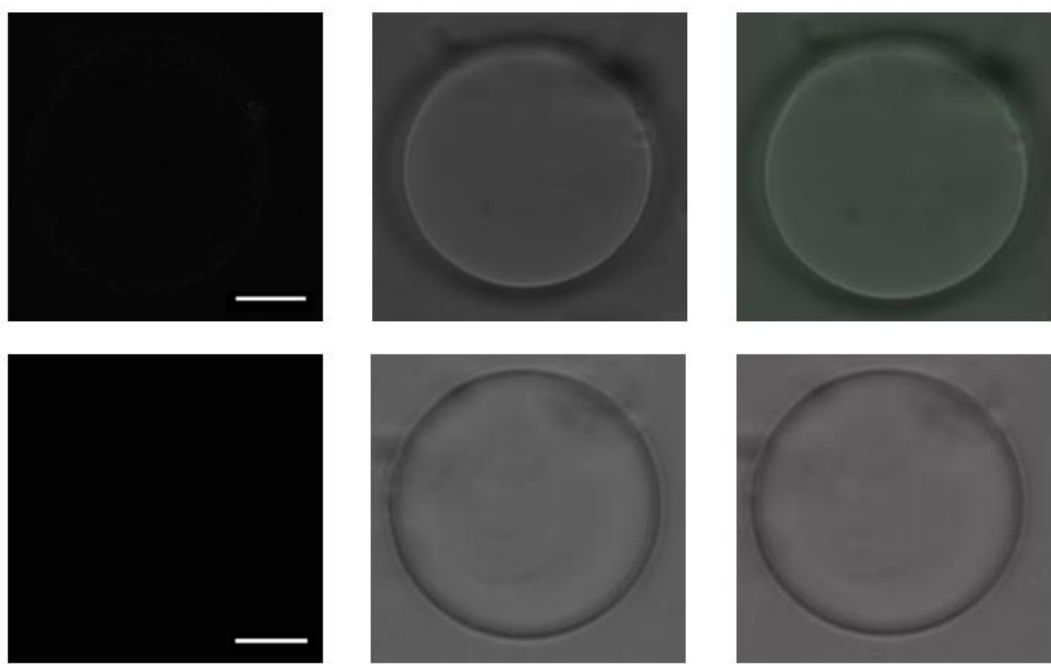


Figure A2: Confocal microscopy images for compounds **47** (top) and **48a** (bottom). L
→ R: Single channel (635 nm excitation), single channel (visible), overlaid images.
Scale bar 8 μ M



*Figure A3: Confocal microscopy images for compounds **31** (top) and **46** (bottom). L → R: Single channel (532 nm (a) or 635 nm (b) excitation), single channel (visible), overlaid images. Scale bar 8 μ M*

Live cells

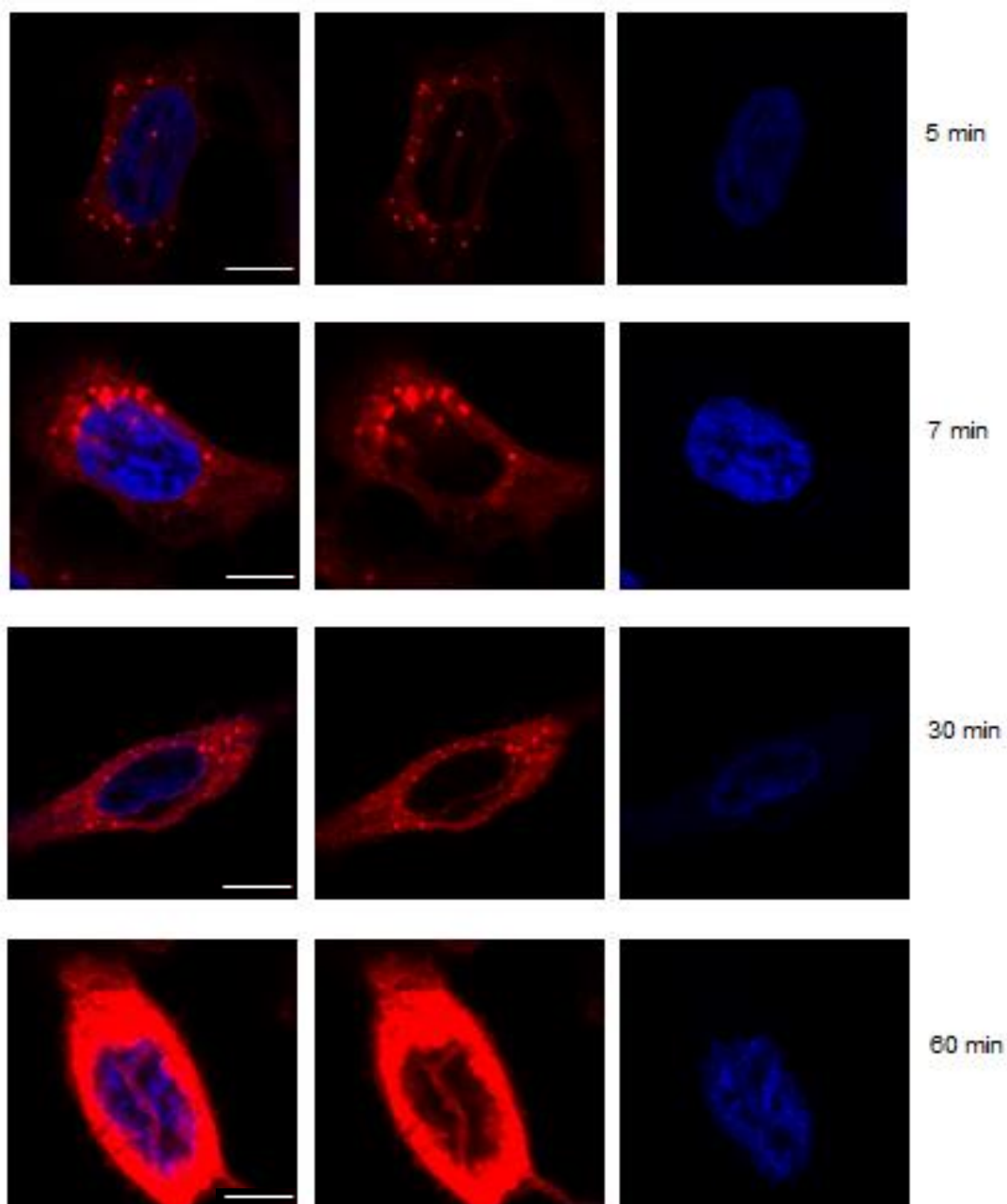
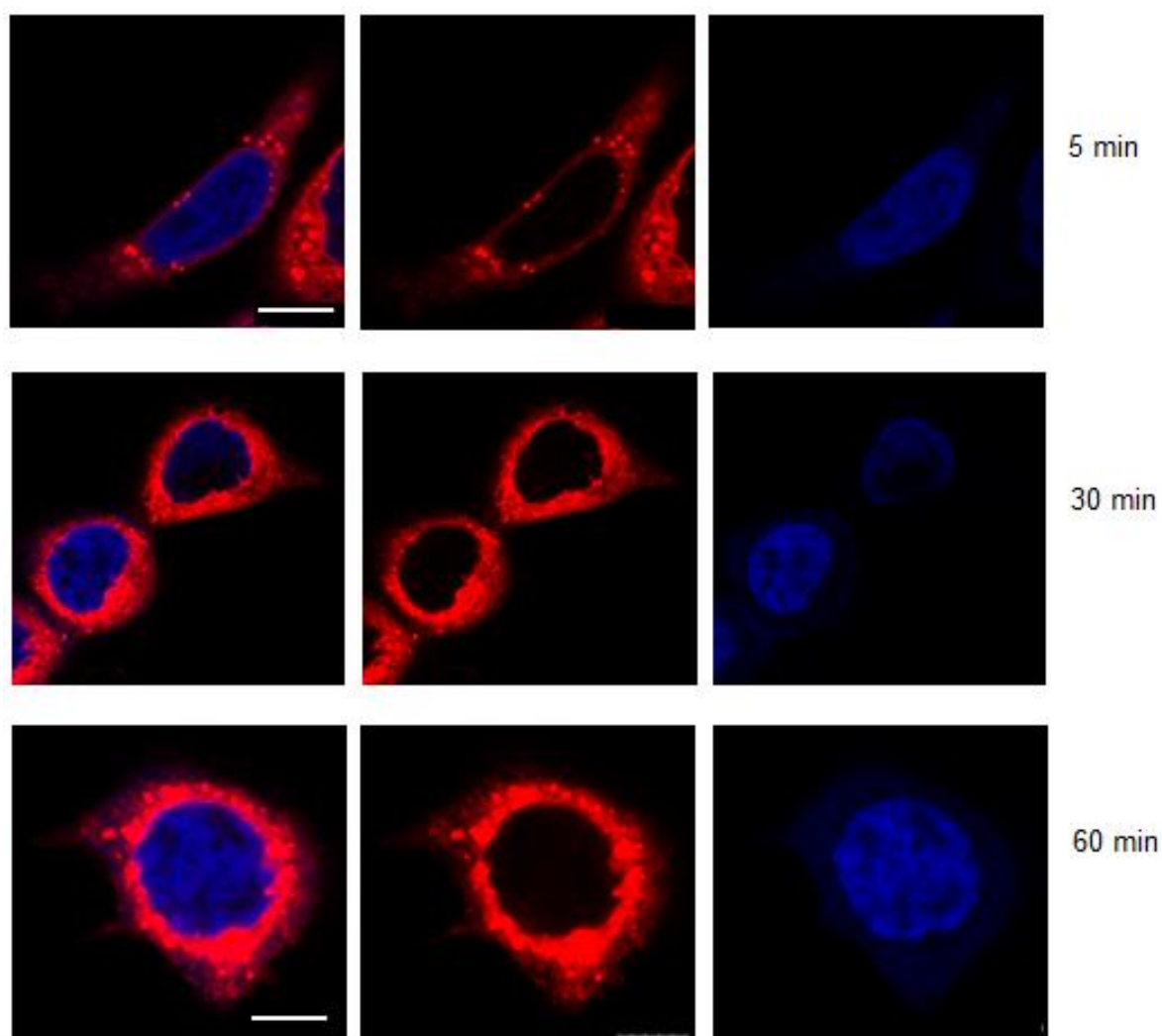


Figure A4: Confocal microscopy images of live FaDu cells after incubation with 10 μ M solution of compound **47** for 5, 7, 30 and 60 min. Excitation using 633 nm laser beam. Left to right: overlay, single 633 nm laser channel, DAPI channel. Scale bar 10 μ m for all except 60 min, 8 μ m

Staining + fixation



*Figure A5: Confocal microscopy images of FaDu cells after incubation with 10 μ M solution of compound **47** for 5, 7, 30 and 60 min followed by immediate fixation with paraformaldehyde. Excitation using 633 nm laser beam. Left to right: overlay, single 633 nm laser channel, DAPI channel. Scale bar 10 μ m for all except 60 min, 8 μ m.*

Fixation + staining

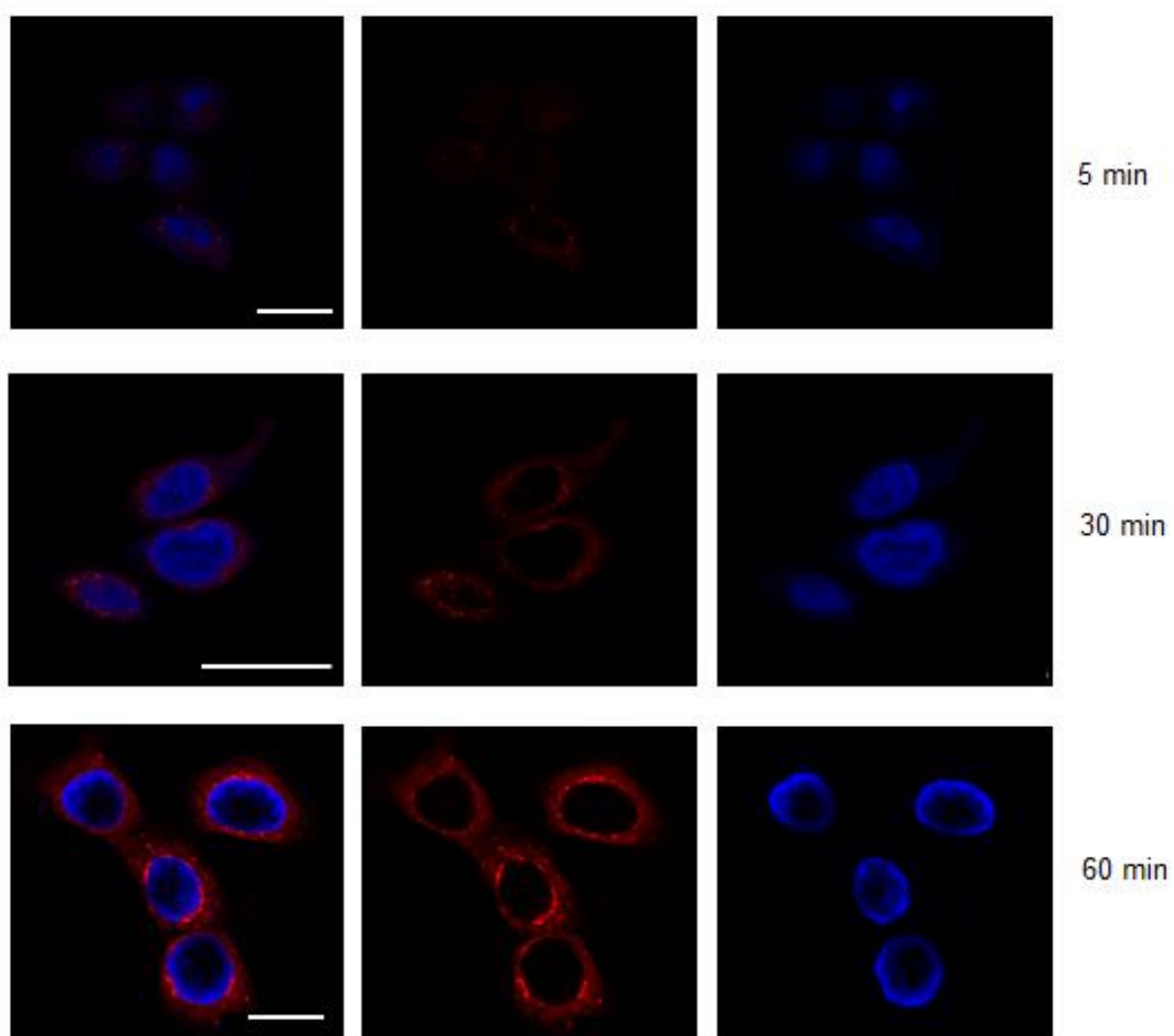


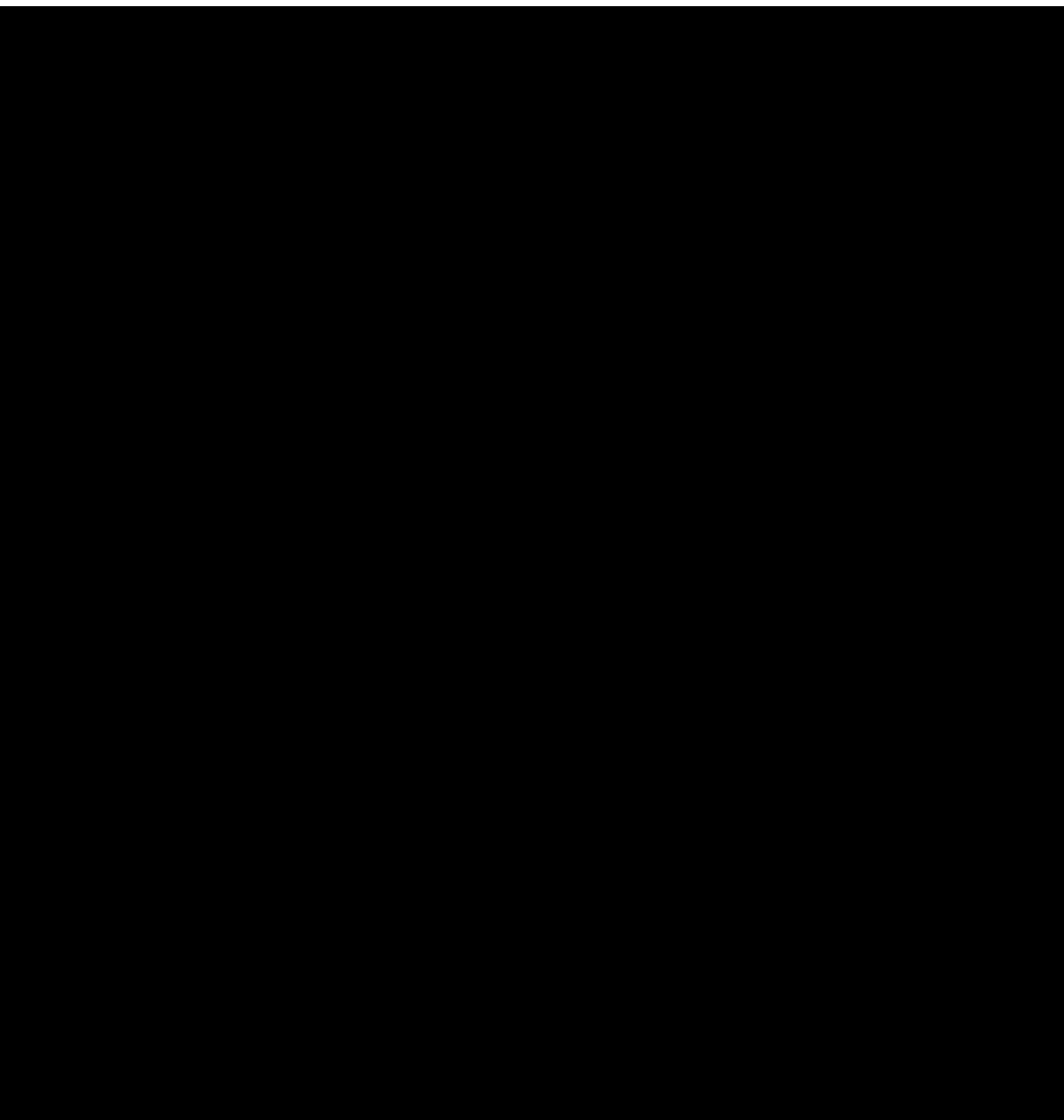
Figure A6: Confocal microscopy images of FaDu cells after fixation with paraformaldehyde followed by incubation with 10 μ M solution of compound **47** for 5, 7, 30 and 60 min. Excitation using a 633 nm laser beam. Left to right: overlay, single 633 nm laser channel, DAPI channel. Scale bar 25 μ m.

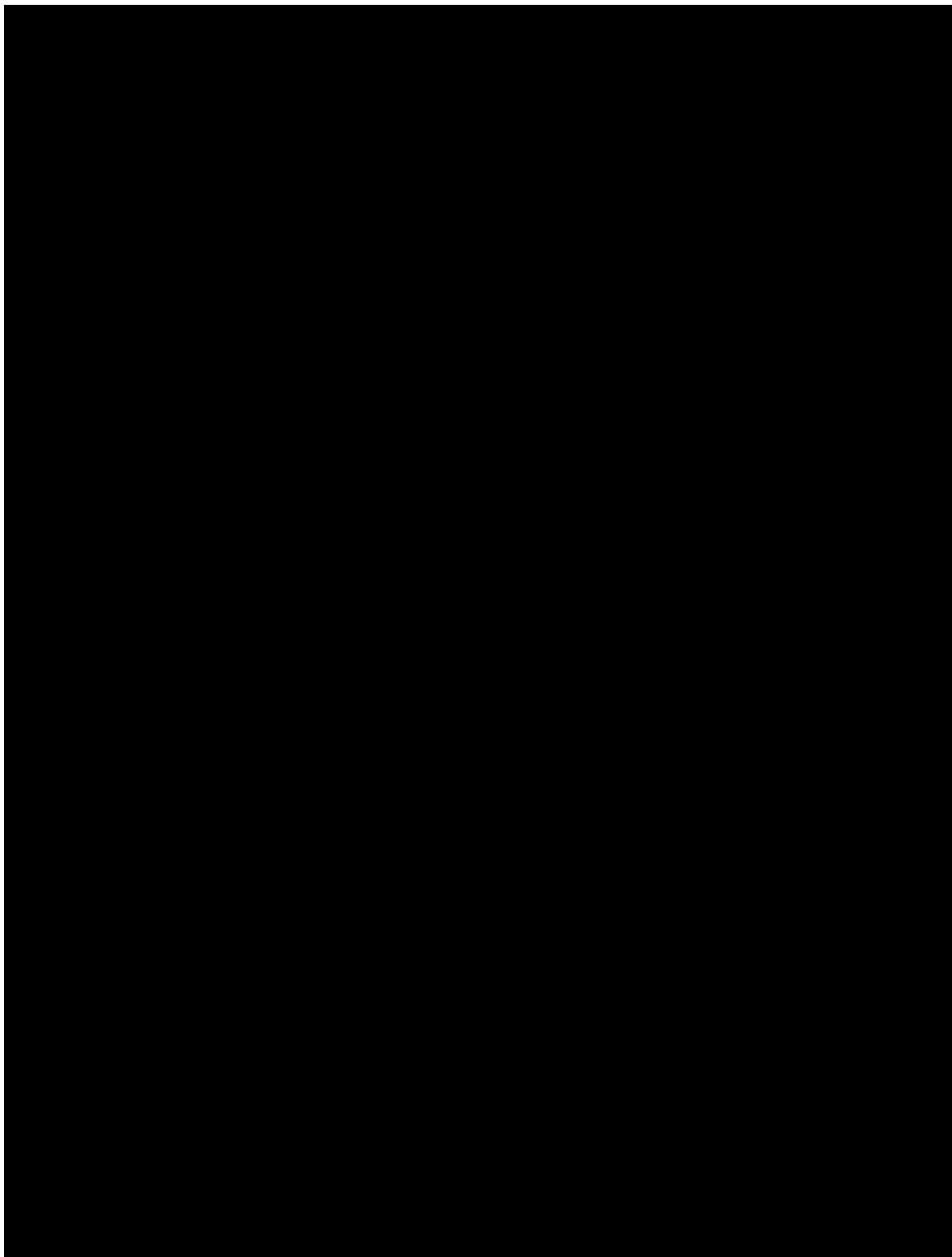
7.5 Publications

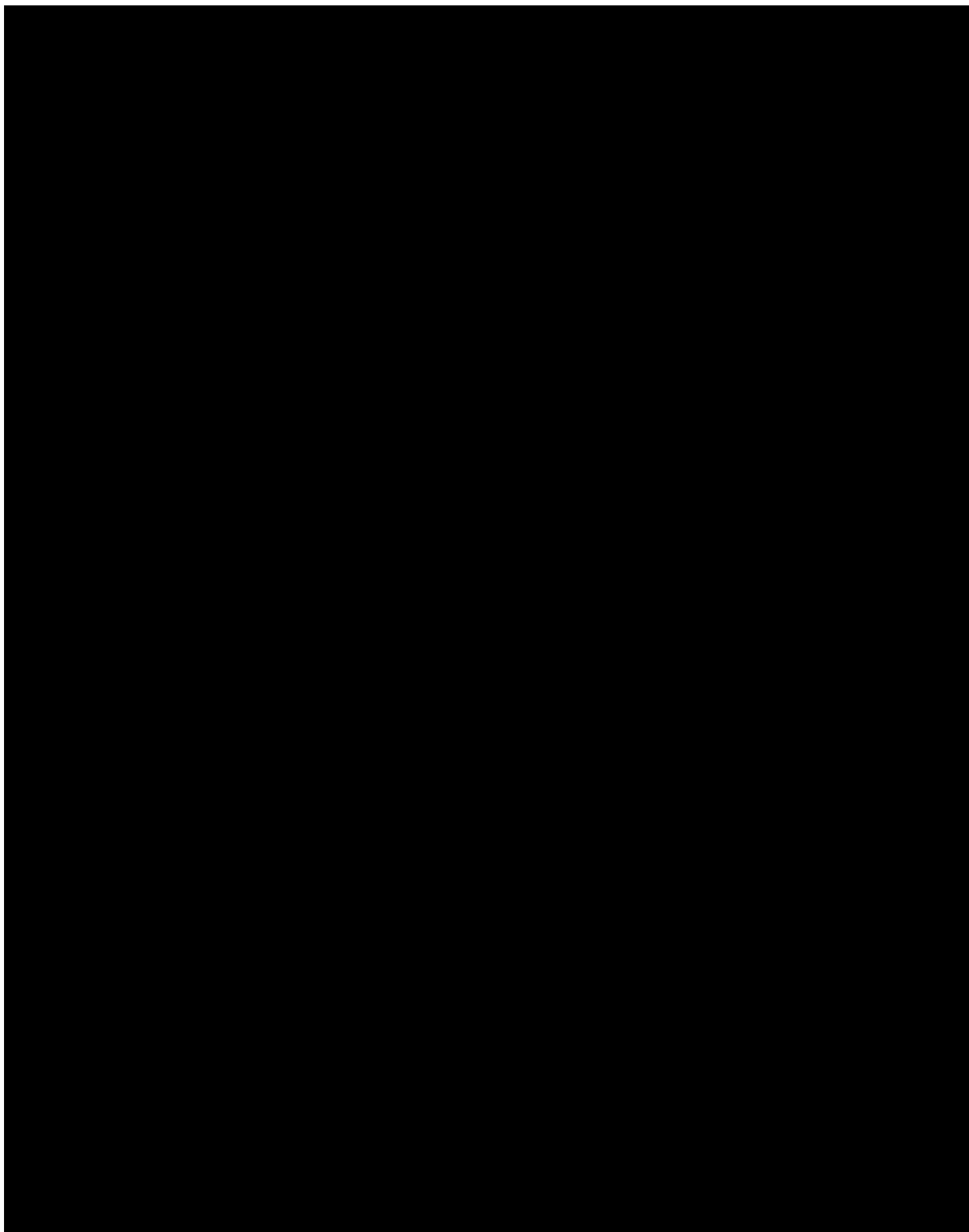
■ Bioimaging

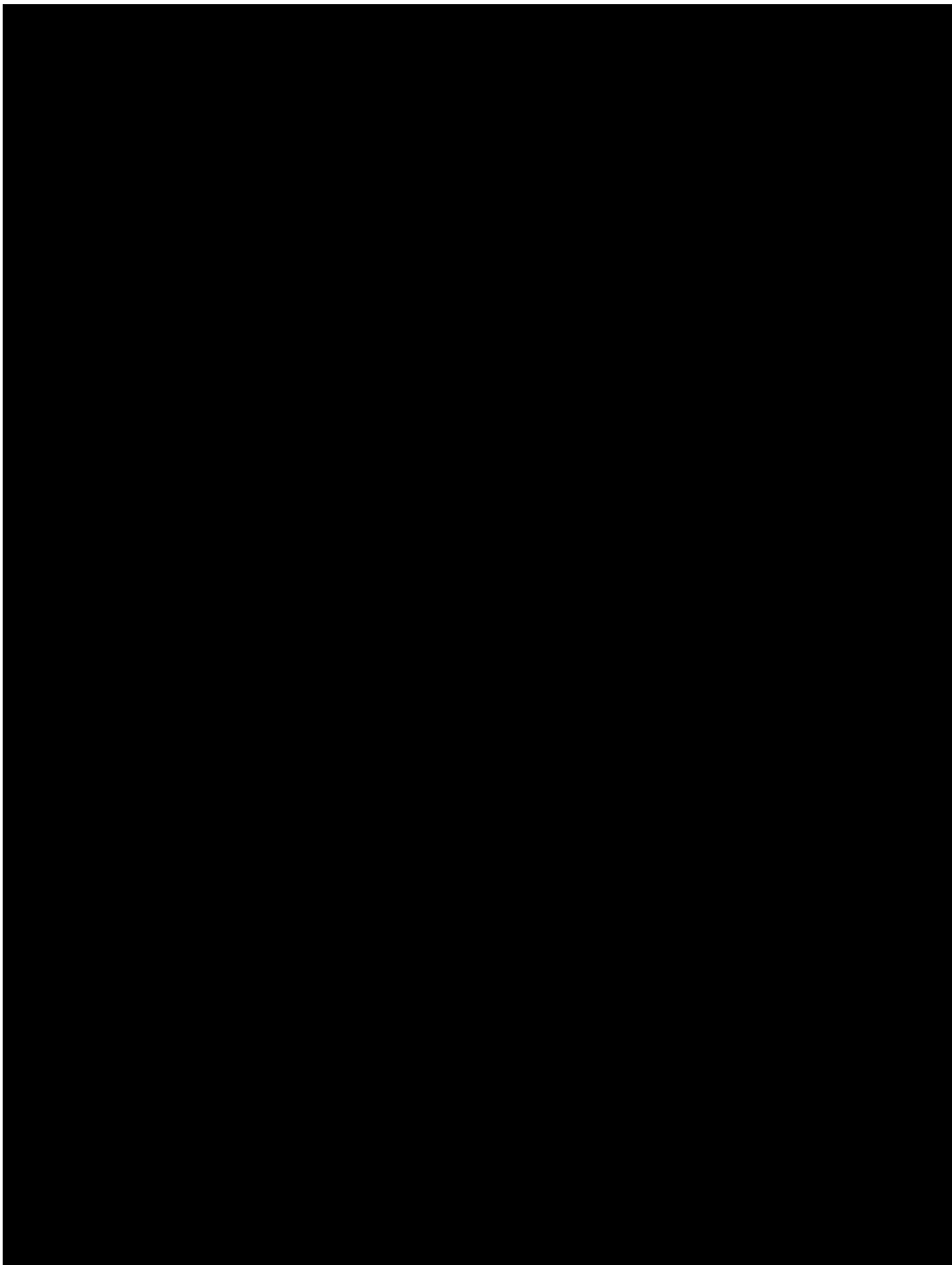
Exploring the Relationship between BODIPY Structure and Spectroscopic Properties to Design Fluorophores for Bioimaging

Joanna L. Donnelly,^[a, b] Daniel Offenbartl-Stiegert,^[a, b] José M. Marín-Beloqui,^[a] Loris Rizzello,^[a, c, d] Guiseppe Battaglia,^[a, c, d, e] Tracey M. Clarke,^[a] Stefan Howorka,^{*, [a, b]} and Jonathan D. Wilden^{*, [a, b]}

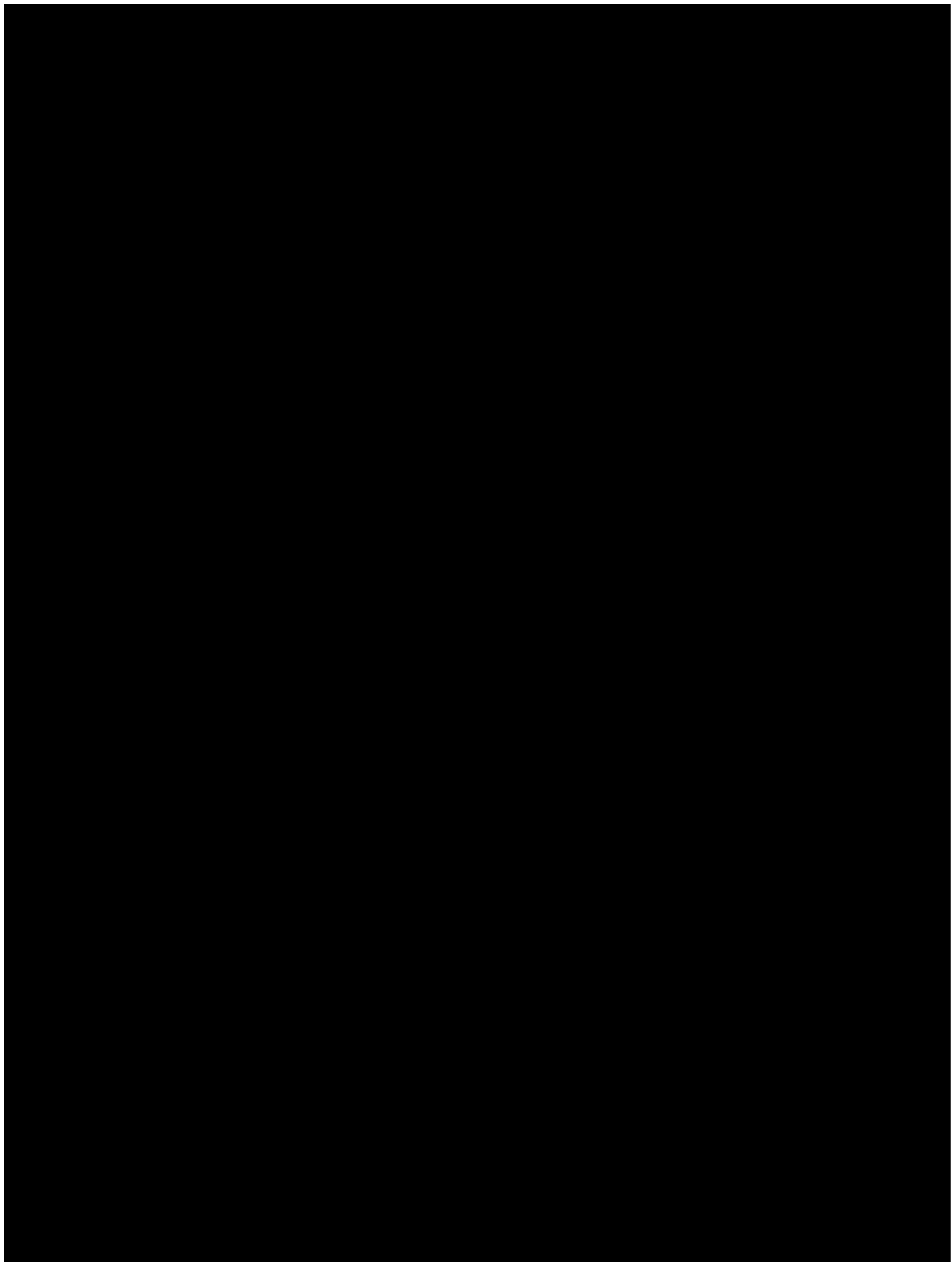


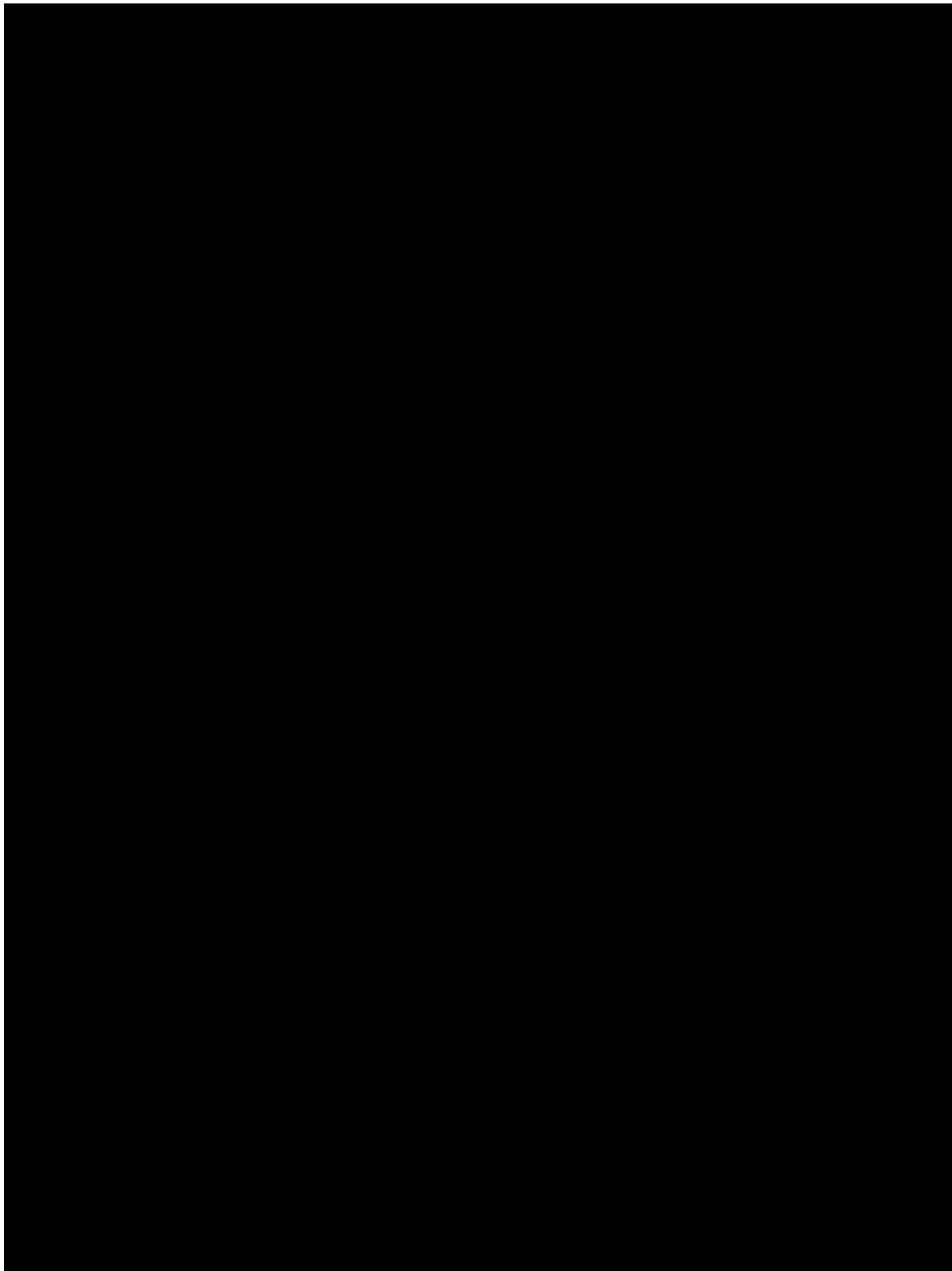


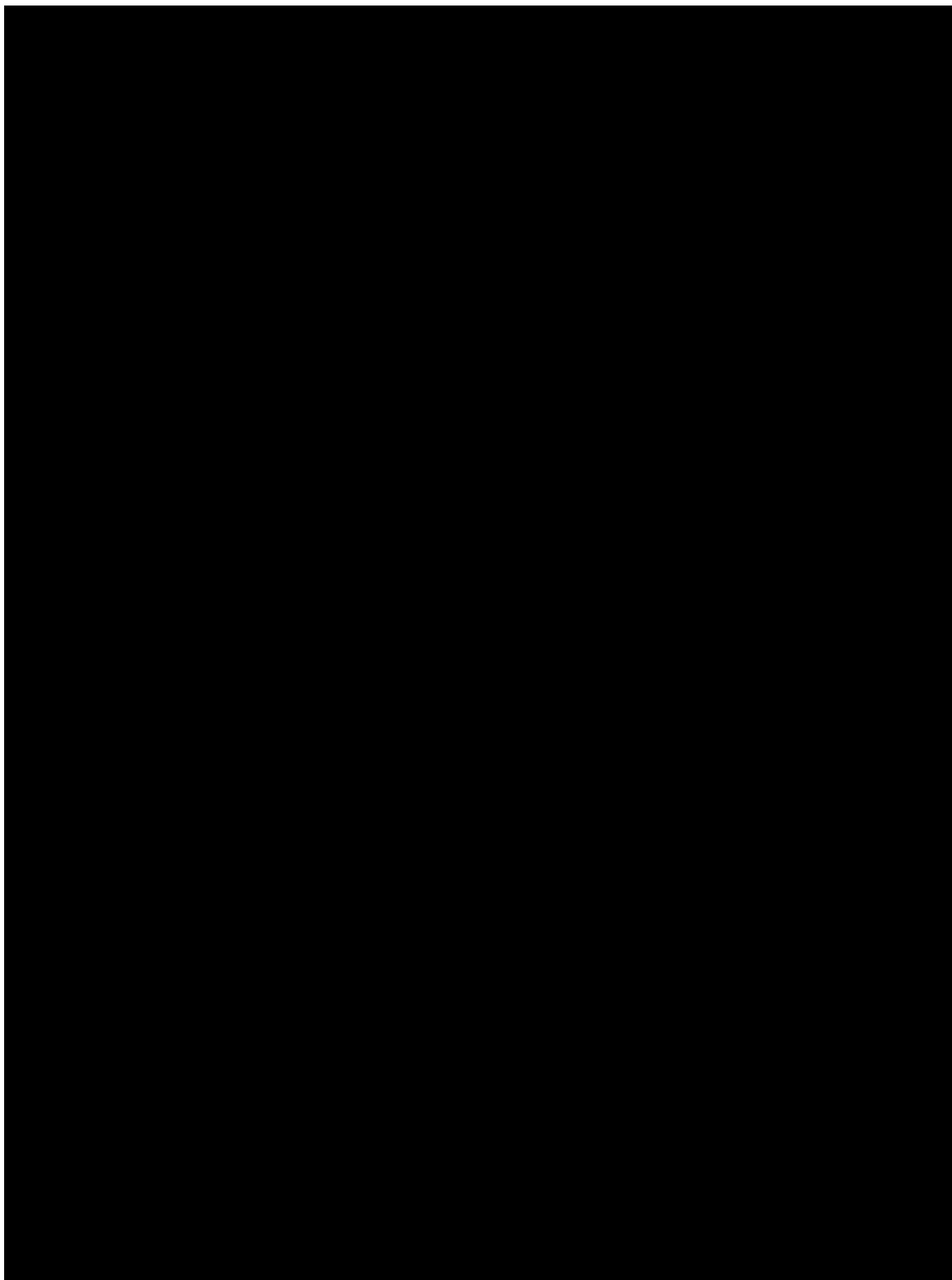




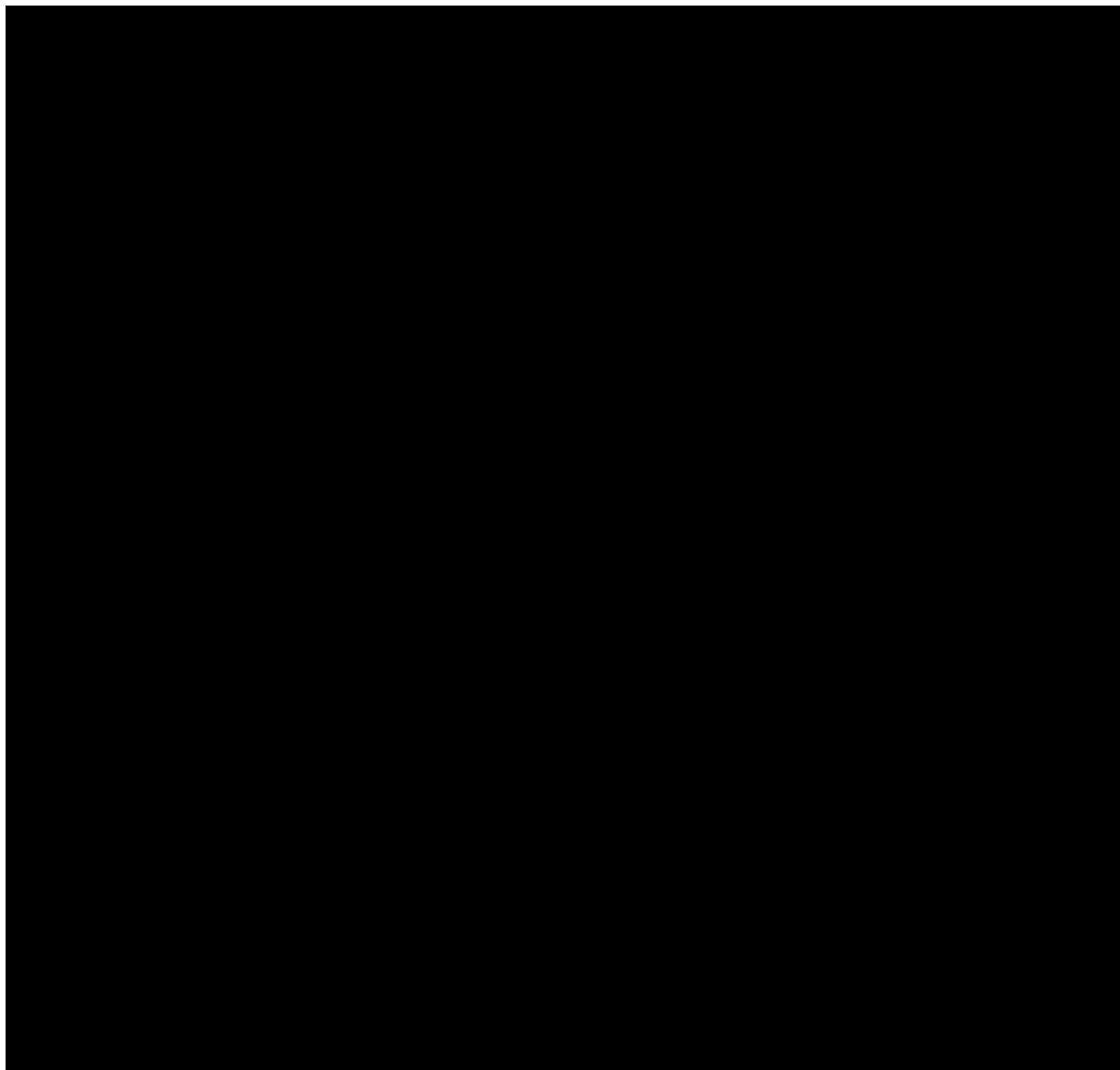














Article

Carboxylic Acid Functionalization at the *Meso*-Position of the Bodipy Core and Its Influence on Photovoltaic Performance

Filip Ambroz, Joanna L. Donnelly, Jonathan D. Wilden, Thomas J. Macdonald * and Ivan P. Parkin *

Department of Chemistry, University College London 20 Gordon St., London WC1H 0AJ, UK; filip.ambroz.16@ucl.ac.uk (F.A.); joanna.donnelly.15@ucl.ac.uk (J.L.D.); j.wilden@ucl.ac.uk (J.D.W.)

* Correspondence: tom.macdonald@ucl.ac.uk (T.J.M.); i.p.parkin@ucl.ac.uk (I.P.P.)

Received: 18 August 2019; Accepted: 17 September 2019; Published: 20 September 2019



Abstract: Two bodipy dyes with different carboxylic acids on the *meso*-position of the bodipy core were prepared and used to sensitize TiO₂ photoelectrodes. On the basis of spectroscopic characterization, the photoelectrodes were used to fabricate photoelectrochemical cells (PECs) for solar light harvesting. Photovoltaic measurements showed that both bodipy dyes successfully sensitized PECs with short-circuit current densities (J_{SC}) two-fold higher compared to the control. The increase in generated current was attributed to the gain in spectral absorbance due to the presence of bodipy. Finally, the influence of co-sensitization of bodipy and N719 dye was also investigated and photovoltaic device performance discussed.

Keywords: Dye-sensitized solar cells; bodipy dye; co-sensitization; N719 dye; photoelectrochemical cells

1. Introduction

Over the last few decades numerous types of photoelectrochemical cells (PECs) that convert sunlight to electricity have been extensively explored as an alternative photovoltaic technology to silicon [1,2]. The most promising include, dye-sensitized solar cells (DSSCs) [3,4], metal chalcogenide solar cells [5,6], organic/polymer solar cells [7–9], and perovskite solar cells [10,11]. While significant research has been conducted for their progress, they all have drawbacks in certain aspects that hinder large scale market employment [12]. For DSSCs in particular, the main efforts have been related to improving cell efficiencies where investigations have focused on two main components, such as the dye sensitizer and semiconducting electrode [13,14]. The foremost step in achieving high efficiencies is the light absorption by the dye molecules that should ideally cover as much of the visible spectrum as possible. To complement this, ruthenium-based dyes such as Di-tetrabutylammonium cis-bis(isothiocyanato)bis(2,2'-bipyridyl-4,4'-dicarboxylato)ruthenium(II) (best known as N719) and other ruthenium-based derivatives have been the most successful candidates thus far [15–17]. While N719 dye has been extensively used in DSSCs research since it shows promise of high efficiency, the limited supply, fluctuation in price, and environmental impact of ruthenium have all prompted investigations into other alternatives [18]. Possible choices to replace ruthenium-based dyes include porphyrin [19,20], squaraine [21,22], and boron dipyrromethene (bodipy) dye complexes [23,24]. As a result of many unique features that bodipy dyes possess, they have emerged as an attractive class of functional dyes that can be used for a variety of applications [25,26]. They are known to exhibit characteristics such as ease of structural modification, minimum triplet state formation, photostability, low rates of intersystem crossing, and more [27], which renders them promising for use in the future [28]. In the past decade, a variety of bodipy dyes have been synthesized for use in solar cell

applications, however most attempts were not prosperous since the efficiencies were shown to be poor [29]. This was mostly a result of insufficient light harvesting since efforts to design a metal free organic dye that would achieve panchromatic absorption proved to be rather ambitious [30]. Therefore, bodipy dyes were separately engineered to cover a particular absorption spectral range and co-sensitized together in a PEC with the aim to obtain high efficiency [31]. In addition, structural modifications and functionalization of the bodipy core was also shown to have a notable influence on the photovoltaic performance of PECs. For instance, by replacing fluorine on the bodipy core with long alkoxy groups, losses due to charge recombination can be minimized resulting in efficiencies in the range of 5.75% as reported by Ziessel et al [32].

Herein, we report the details of the synthesis and characterization of two bodipy sensitizers with different carboxylic acids at the *meso*-position [29] of the bodipy core. In addition, spectroscopy results of bodipy-sensitized TiO₂ photoelectrodes are discussed followed by PEC fabrication and characterization using simulated sunlight. Finally, the influence of bodipy and N719 dye co-sensitization on the performance of PECs is also investigated.

2. Experimental Section

2.1. Materials

All chemicals used in this study were obtained from Sigma Aldrich (St. Louis, MO, USA), Acros Organics (Geel, Belgium), Alfa Aesar (Haverhill, MA, USA) or Thermo Fischer Scientific (Waltham, MA, USA). They were used as received unless otherwise stated.

2.2. Synthesis of Bodipy Dye 1 and 2

2,4-dimethylpyrrole (0.120 mL, 1.20 mmol, 2 eq.) and glutaric or succinic anhydride (0.600 mmol, 1 eq.) were dissolved in dry dichloromethane (DCM, 10.0 mL) under argon. BF₃·Et₂O (0.500 mL, 4.00 mmol) and TEA (0.420 mL, 3.00 mmol) were added and the reaction was heated under reflux for five hours. The organic material was washed with water, dried over MgSO₄, filtered and concentrated in vacuo before purification by flash column chromatography on silica gel; eluent: Hexane/EtOAc/AcOH:50/50/0 to 0/97/3.

2.2.1. Bodipy Dye 1

4-(5,5-difluoro-1,3,7,9-tetramethyl-5H-4l4,5l4-dipyrrolo[1,2-c:2',1'-f][1,3,2]diazaborinin-10-yl) butanoic acid (22.0 mg, 0.066 mmol, 11%). ¹H NMR (600.130 MHz, CDCl₃) δ_H 6.06 (s, 2H, ArH), 2.82–2.78 (m, 2H, CH₂), 2.57–2.54 (m, 2H, CH₂), 2.52 (s, 6H, 2CH₃), 2.43 (s, 6H, 2CH₃), 2.04–1.99 (m, 2H, CH₂) ppm; R_f (EtOAc) = 0.1 (stained with bromocresol green).

2.2.2. Bodipy Dye 2

3-(5,5-difluoro-1,3,7,9-tetramethyl-5H-4l4,5l4-dipyrrolo[1,2-c:2',1'-f][1,3,2]diazaborinin-10-yl) propanoic acid (27.0 mg, 0.084 mmol, 14%). ¹H NMR (600.130 MHz, CDCl₃) δ_H 6.06 (s, 2H, ArH), 3.36–3.33 (m, 2H, CH₂), 2.71–2.69 (m, 2H, CH₂), 2.52 (s, 6H, 2CH₃), 2.45 (s, 6H, 2CH₃) ppm; R_f (EtOAc) = 0.1 (stained with bromocresol green).

2.3. Preparation of Photoelectrochemical Cells (PECs)

PEC fabrication followed the procedures already reported in our previous work [14]. Briefly, TiO₂ photoelectrodes were prepared by doctor blading commercially available TiO₂ paste (GreatCell Solar, DSL-18NRT, Queanbeyan, Australia) onto pre-cleaned fluorine-doped tin oxide (FTO) glass followed by sintering at 500 °C for 30 min which resulted in a uniform layer of anatase TiO₂ nanoparticles (NPs) labelled as a transparent layer. On this layer, an additional layer of bigger-sized TiO₂ NPs (WER2-0 paste, GreatCell Solar, Queanbeyan, Australia) was deposited (doctor blading technique) followed by another sintering at 500 °C for 30 min. The second layer was labelled as light-scattering

layer. The photoelectrodes were then subject to treatment with an aqueous solution of titanium tetrachloride (TiCl_4 , 40 mM) for 30 min at $\approx 70^\circ\text{C}$ followed by another sintering at 500°C for 30 min. It should be noted that the active solar cell area of the photoelectrodes was 0.1256 cm^2 . Control (unsensitized) PECs (see procedures below for dye sensitization), were directly eclipsed with counter electrodes (Pt-coated FTO glass, GreatCell Solar, Queanbeyan, Australia) with a thermoplastic sealant (GreatCell Solar, MS004610, Queanbeyan, Australia) following by heating at $\approx 100^\circ\text{C}$ for 10 min to seal the sealant. An electrolyte consisting of iodine (I_2 , 0.05 M), 1,2-dimethyl-3-propylimidazolium iodide (DMPII, 0.6 M), guanidium thiocyanate (0.10 M) and 4-tert-Butylpyridine (TBP, 0.5 M) in a mixture of acetonitrile and valeronitrile (volume ratio, 85:15) was injected between the sealed electrode via vacuum filling.

2.4. Dye Sensitization

Bodipy dye 1 and 2 sensitized photoelectrodes underwent dye sensitization with a solution of a relevant dye (0.5 mM) in acetonitrile for 20 h in the dark.

Control (sensitized only with N719) photoelectrodes underwent dye sensitization with a solution of ruthenizer 535-bisTBA (Solaronix 0.5 mM, Aubonne, Switzerland) in absolute ethanol for 20 h in the dark.

Bodipy dye 1 and 2 co-sensitized photoelectrodes underwent dye sensitization with a solution that was a mixture of bodipy dye 1 or 2 solution in absolute ethanol (0.5 mM)—5 vol% and a solution of ruthenizer 535-bisTBA (0.5 mM, Solaronix, Aubonne, Switzerland) in absolute ethanol for 20 h in the dark.

3. Characterisation

Monitoring of all reactions was achieved using 60 F254 silica coated aluminium TLC plates by Merck. Visualisation of these was carried out using UV light of wavelength of 254 and/or 365 nm. Purification was achieved by flash column chromatography using silica gel (43–60 μm) from Merck.

All ^1H , ^{13}C , ^{11}B and ^{19}F nuclear magnetic resonance spectra were recorded at 600 MHz using the Bruker Avance III 600 Cryo or at 700 MHz with the Bruker Avance Neo 700. Instruments clearly indicated for each spectra. Chemical shifts are reported in ppm relative to the internal standard TMS as follows: chemical shift, multiplicity (s = singlet, d = doublet, t = triplet, q = quartet, sep = septet, m = multiplet), coupling constant(s), integration, and assignment using either CDCl_3 or $\text{DMSO}-d_6$ as a solvent and TMS as an internal standard.

X-Ray photoelectron spectroscopy (XPS) analysis was carried out using a Thermo Scientific K-alpha photoelectron spectrometer with monochromatic Al-K_α radiation. Peak positions were calibrated to carbon (284.8 eV) and plotted using the CasaXPS software. The measurements were performed on control and sensitized photoelectrodes. X-Ray diffraction (XRD) analysis was performed with a Bruker D8 discovery X-Ray diffractometer using monochromatic $\text{Cu K}_{\alpha 1}$ and $\text{Cu K}_{\alpha 2}$ radiation of wavelengths 1.54056 and 1.54439 Å, respectively.

The UV/Vis absorption spectra were taken on a Perkin Elmer Lambda 950 instrument with a measurement interval of 1 nm.

The photoluminescence (PL) spectra were recorded using Horiba FluoroMax-4 spectrofluorometer equipped with a PMT detector.

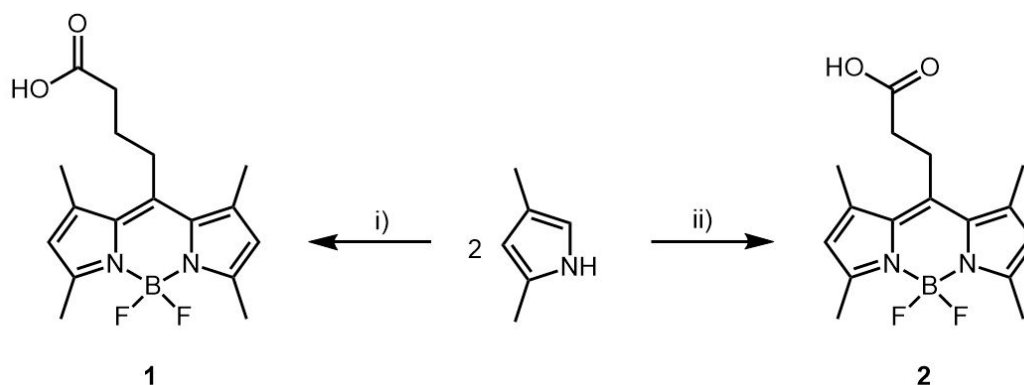
Fourier-transform infrared (FTIR) spectra were recorded with a Bruker FTIR Spectrometer Alpha II with an attenuated total reflection (ATR) attachment. Measurements were performed in the mid-IR region (4000–400 cm^{-1}).

J–V measurements were performed under one-sun (AM 1.5G) illumination using a LOT calibrated solar simulator with a Xenon lamp. Devices were connected to a Keithley 2400 source meter to output the data. Photocurrent measurements were obtained with a halogen lamp chopped to a frequency of 188 Hz through a Newport monochromator; a 4-point probe in connection with a lock-in amplifier is used to collect data. The monochromatic beam is calibrated using a Silicon photo-diode.

4. Results and Discussion

4.1. Synthesis

The synthesis of bodipy dye 1 and 2 is depicted in Scheme 1 and is based on previously reported synthetic strategies [33,34]. (See Supplementary Materials for more details) Molecular structures of the obtained compounds were characterized by spectroscopic methods, such as NMR which is shown in Supplementary Materials Figure S1 and S2. Singlet peaks integrating to two protons at 6.06 ppm for both compounds confirm the successful construction of the BODIPY scaffold.



Scheme 1. Synthetic routes towards bodipy dyes 1 and 2. (1) Succinic anhydride, dichloromethane (DCM), $\text{BF}_3 \cdot \text{Et}_2\text{O}$, reflux 5h, $\text{BF}_3 \cdot \text{Et}_2\text{O}$, TEA, 16 h. (2) Glutaric anhydride, DCM, $\text{BF}_3 \cdot \text{Et}_2\text{O}$, reflux 5h, $\text{BF}_3 \cdot \text{Et}_2\text{O}$, TEA, 16 h.

4.2. Optical Properties

The absorption and PL emission spectra of solutions of bodipy dyes 1 and 2 are illustrated in Figure 1a,b. Both dyes exhibit three absorption features (more pronounced for dye 1 due to higher molar attenuation coefficients (ϵ) at those particular wavelengths—Table 1) with two located in the UV region and one in the visible (green) portion of the electromagnetic spectrum. From the absorption onset of the dyes, their band gap values were determined to be ≈ 2.4 eV (Table 1). Due to Stokes shift, where the position of the band maxima of the absorption was at ≈ 495 nm, the emission of the dyes resulted to be 514 nm for dye 1 and 520 nm for dye 2. The bodipy dyes were then used for PECs, by sensitizing TiO_2 photoelectrodes in a dye solution and their corresponding UV/Vis spectra are shown in Figure 1c,d. To evaluate if the TiO_2 photoelectrodes successfully absorbed the dyes, comparison was made to the untreated (unsensitized) TiO_2 photoelectrodes. As can be seen in Figure 1c,d, both sensitized TiO_2 photoelectrodes exhibited a broad absorption feature in the visible spectrum allowing the harvesting of more energy from photons. This can be attributed to the dye absorption (λ_{max} at 502 and 504 nm for bodipy dyes 1 and 2, respectively). Compared to the bodipy solutions, sensitized TiO_2 photoelectrodes exhibited a bathochromic shift that occurred as a result of the interaction, between the dye and TiO_2 nanoparticles (suppression of H-aggregation). [35] Moreover, to investigate the molecular packing of dye molecules [36] X-Ray diffraction (XRD) was also performed. Supplementary Materials Figure S4 shows the XRD diffraction patterns for unsensitized and sensitized TiO_2 photoelectrodes where no difference between the samples was observed.

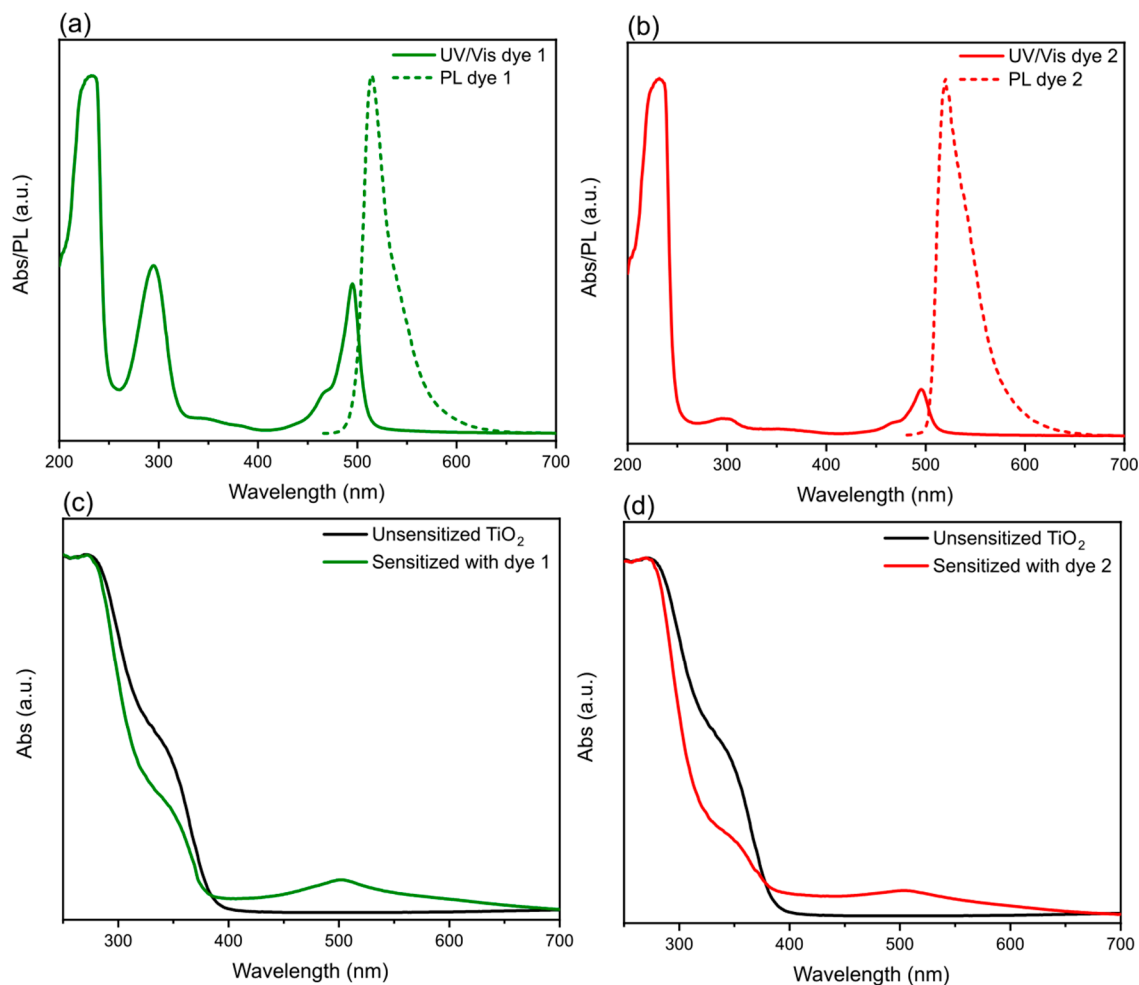


Figure 1. UV/Vis absorption (solid line) and photoluminescence (PL) emission (dotted lines) spectra of bodipy (a) dye 1 and (b) dye 2 solutions. (Excitation wavelength for PL emission was 400 nm) UV/Vis absorption spectra of TiO₂ sensitized photoelectrodes of bodipy (c) dye 1 and (d) dye 2, respectively. Black lines represent untreated TiO₂ photoelectrodes where green (dye 1) and red (dye 2) lines correspond to TiO₂ sensitized photoelectrodes.

Table 1. Summary of spectral properties of bodipy dye 1 and 2 in ethanol solution (0.5 mM) and on photoelectrodes. The band gap values (E_g) were determined following the procedure reported elsewhere [37] and also from the Tauc plots (Supplementary Materials Figure S3) where the obtained values were comparable.

Sensitizer	Solution Abs λ_{\max} (nm)	Solution PL λ_{\max} (nm)	Photoelectrode Abs λ_{\max} (nm)	E_g (eV)	ϵ (M ⁻¹ cm ⁻¹)
Dye 1	232, 295, 495	514	502	2.39	6124 (at 495 nm)
Dye 2	232, 295, 496	520	504	2.38	1350 (at 496 nm)

4.3. Spectroscopy Characterization

FTIR spectroscopy was used to obtain infrared spectra (% transmittance) of synthesized bodipy dyes which can be seen in Figure 2. A broad band in the region of around 3500–2500 cm⁻¹ can be observed (Figure 2a) which is a typical characteristic for compounds containing a carboxyl group (O–H stretch) [38]. Since this band is in the same region as the C–H stretching bands, a slightly distorted absorption pattern is observed where the former band is superimposed on the sharp C–H stretching bands. Furthermore, a strong peak appeared around 1700 cm⁻¹ for both dyes which was assigned to

C=O stretching of the carbonyl group [35]. Additional peaks that were identified for both spectra were located in the regions of around 1400, 1200, and 910 cm^{-1} (see Supplementary Materials Table S1 for the exact values) and were assigned to O–H bend, C–O stretch, and O–H bend, respectively.

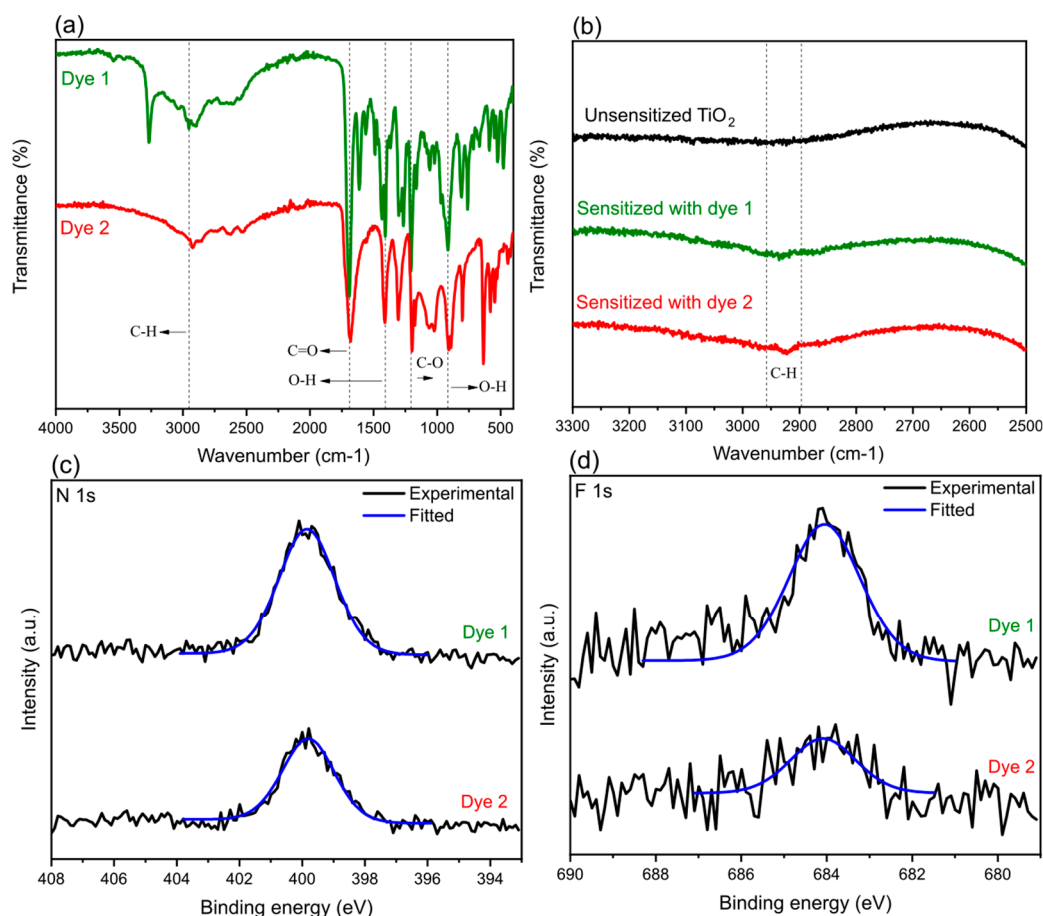


Figure 2. Fourier-transform infrared (FTIR) spectra of bodipy (a) dye 1 (green curve) and dye 2 (red curve) in a powder form along with the inset (b) of untreated (black curve) and sensitized TiO₂ photoelectrodes on glass substrate. The whole range for the FTIR spectra of TiO₂ photoelectrodes can be seen in Supplementary Materials Figure S5. The high-resolution (c) N 1s and (d) F 1s X-ray photoelectron spectroscopy (XPS) spectra for sensitized TiO₂ photoelectrodes.

FTIR measurements were also performed with the intention to investigate interaction of individual dyes on sensitized TiO₂ electrodes. However, our results showed that the substrates used for TiO₂ deposition strongly absorbed below 2500 cm^{-1} which prevented characterization in this region (Supplementary Materials Figure S5). Despite this, by comparing regions of around 3000 cm^{-1} between sensitized and untreated TiO₂ photoelectrodes, a slight increase in absorbance was observed for both sensitized TiO₂ photoelectrodes. (Figure 2b) These bands were assigned to C–H stretching of the dye compounds.

X-Ray photoelectron spectroscopy (XPS) was carried out to identify relevant elements present on the surface of untreated and sensitized TiO₂ photoelectrodes. Elements (N and F) associated to the compounds of the dyes were identified on both sensitized TiO₂ photoelectrodes (Figure 2c) while only noise was observed in the same binding energy regions for the untreated TiO₂ photoelectrode. (Figure S6). It is noteworthy that efforts related to the detection of boron resulted to be negative. However, such results are not surprising since it is notoriously difficult to detect B1's peak due to its very low sensitivity.

4.4. Photoelectrochemical Properties

Photoelectrochemical cells (PECs) were fabricated using bodipy dyes 1 and 2 as photosensitizers for nanocrystalline TiO₂ photoelectrodes. Figure 3a shows the photocurrent–voltage (J – V) curves of PECs and the photovoltaic parameters are summarized in Table 2. Compared to control (unsensitized), PECs sensitized with bodipy dyes showed a significant increase in J_{SC} values (≈ 2.5 -fold increase for dye 1 and ≈ 2 -fold increase for dye 2). Such a phenomenon is primarily attributed to the improved light harvesting due to the presence of the bodipy dyes. Moreover, the fill factor (FF) also increased for sensitized PECs while V_{OC} decreased. The latter can be related to the changes in the band gap energy (E_g) where an E_g decrease results in higher J_{SC} and lower V_{OC} . Nevertheless, the overall power conversion efficiency (PCE) of bodipy sensitized PECs doubled compared to the control. On the other hand, the results indicate that the proximity of the carboxylic acid group to the bodipy core notably influenced the photovoltaic parameters for PECs. Specifically, PECs sensitized with a bodipy dye 1 (distance of three carbons) were shown to exhibit better J_{SC} as opposed to the bodipy dye 2 (distance of two carbons) sensitized PECs that had higher V_{OC} and FF. Nevertheless, the overall PCE was not influenced by such changes (Table 2). It is noteworthy that the average values of the photovoltaic parameters for different batches of devices, shown in Figure S7, did not show a change in the trends, as discussed herein. Furthermore, the values of PV parameters for bodipy sensitized PECs were low where one of the reasons together with the nature of the absorption onset of the dyes can be related to their aggregation on the TiO₂ photoelectrodes, thus increasing charge recombination and reducing electron injection to the n-type layer of the photoelectrode [39,40].

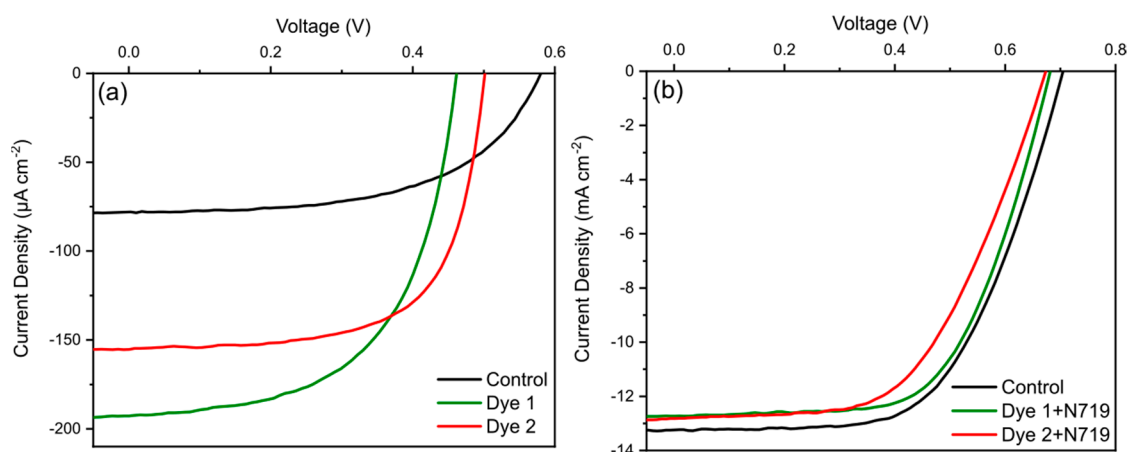


Figure 3. Photocurrent–voltage (J – V) characteristics of photoelectrochemical cells (PECs) sensitized only with (a) dye 1 and 2 including a control (unsensitized) together with (b) N719 co-sensitized. The control PEC in (b) was sensitized only with a dye N719.

Table 2. Summary of photovoltaic parameters for different PECs sensitized with bodipy dye 1 or 2 and co-sensitized with dye 1 + N719 or dye 2 + N719 including the corresponding control (unsensitized and N719 sensitized) PECs.

PEC	J_{SC} ($\mu A\ cm^{-2}$)	V_{oc} (mV)	FF (%)	PCE (%)
Control (unsensitized)	78.2	579.6	56.3	0.025
Dye 1	192.6	461.3	58.0	0.051
Dye 2	154.8	501.0	66.4	0.051
Control (N719 sensitized)	13.2	704.7	59.2	5.5
Dye 1 + N719	12.7	681.3	61.6	5.3
Dye 2 + N719	12.8	673.1	55.5	4.8

Previous reports have shown that the performance of DSSCs containing co-adsorbents, bodipy and N719 can be improved compared to a single sensitizer [35]. Therefore, in an attempt to improve PV parameters bodipy dyes in this study were used and co-sensitized with N719 to investigate if the same conclusions can also be extended to the other combinations of sensitizers. In comparison with the control (sensitized only with N719), both J_{SC} and V_{OC} diminished for bodipy (dye 1 and 2) co-sensitized (5 vol%) [35] PECs (Figure 3b and Table 2). A particularly noticeable decrease was observed for V_{OC} where the parameter is influenced by the recombination rate and adsorption mode of the sensitizer [41] that when compared to the control, negatively influenced the co-sensitized PECs. Therefore, the bodipy dyes used in this study were shown to have a negative effect when implemented together with a N719 dye. We postulate that such an outcome was as a result of an increase in recombination centers which can be attributed to either a mismatch in energy levels or unsuitable molar absorption coefficient. Despite this, the bodipy dyes were shown to successfully sensitize TiO_2 photoelectrodes, and further work into modifying the functional groups could lead to improved single sensitized, and co-sensitized PV performance. Specifically, efforts should be made into replacing electronegative elements, for example fluorine, with other functional groups that do not have such tendency to attract a bonding pair of electrons since this characteristic negatively affects the PV performance. In addition, other methods that aim to extend the absorption onset include attachments of an electron donor or acceptor to the C2 and C6 positions [29].

5. Conclusions

Two bodipy dyes with different carboxylic acids on the *meso*-position of the bodipy core have been synthesized. The bodipy dyes were used to sensitize TiO_2 photoelectrodes which were characterized using spectroscopic techniques (UV/Vis absorption, FTIR and XPS). On the basis of these results, the TiO_2 photoelectrodes were used to fabricate PECs. Their PV parameters were analyzed, and the results showed superior light harvesting and thus higher power conversion efficiencies compared to the control (unsensitized) PECs. Furthermore, the bodipy dyes were co-sensitized (5 vol%) with a N719 dye to investigate their interactions in a PEC. The results showed a decrease in efficiencies indicating co-sensitization had a negative effect on the photovoltaic performance parameters of co-sensitized PECs. Further improvements in efficiencies are possible by designing/modifying bodipy dyes with different light absorbing groups within the organic framework to tune the absorption spectral range with high molar extinction coefficients and use them as co-sensitizers for solar cell devices.

Supplementary Materials: The following are available online at <http://www.mdpi.com/2079-4991/9/10/1346/s1>, Figure S1: 1H -NMR of bodipy dye 1, Figure S2: 1H -NMR of bodipy dye 2, Figure S3: Tauc plots for solutions of bodipy (a) dye 1 and (b) dye 2, Figure S4: XRD patterns for TiO_2 photoelectrodes, Figure S5: FTIR spectra of untreated and sensitized TiO_2 photoelectrodes, Figure S6: The high-resolution (a) N 1s and (b) F 1s XPS spectra for control (unsensitized) TiO_2 photoelectrode, Figure S7: Average (a) J_{SC} , (b) V_{OC} , (c) FF and (d) power conversion efficiency (PCE) of the fabricated PECs sensitized only with bodipy dye 1 or 2 including a control (unsensitized), Table S1: FTIR peak wavenumbers and assignments for bodipy dye 1 and 2.

Author Contributions: Experiments were designed by T.J.M and I.P.P with contribution from J.D.W. All dyes were synthesized by J.L.D. Materials characterization and PECs fabrication was performed by F.A. The manuscript was written by F.A. with contributions of J.L.D, T.J.M and I.P.P. All authors have given approval to the final version of the manuscript.

Funding: The authors acknowledge financial support from Surface Measurement Systems Ltd. T.J.M would like to thank the Ramsay Memorial Trust for their financial assistance. T.J.M and I.P.P would like to acknowledge the EPSRC for financial support (EP/M015157/1).

Conflicts of Interest: The authors declare no conflict of interest.

References

- Nayak, P.K.; Mahesh, S.; Snaith, H.J.; Cahen, D. Photovoltaic solar cell technologies: Analysing the state of the art. *Nat. Rev. Mater.* **2019**, *4*, 269. [\[CrossRef\]](#)
- Khatri, I.; Shudo, K.; Matsuura, J.; Sugiyama, M.; Nakada, T. Impact of heat-light soaking on potassium fluoride treated CIGS solar cells with CdS buffer layer. *Prog. Photovolt. Res. Appl.* **2018**, *26*, 171–178. [\[CrossRef\]](#)
- Munkhbayar, B.; Nine Md, J.; Jeoun, J.; Ji, M.; Jeong, H.; Chung, H. Synthesis of a graphene–tungsten composite with improved dispersibility of graphene in an ethanol solution and its use as a counter electrode for dye-sensitized solar cells. *J. Power Sources* **2013**, *230*, 207–217. [\[CrossRef\]](#)
- Batmunkh, M.; Shrestha, A.; Bat-Erdene, M.; Nine, M.J.; Shearer, C.J.; Gibson, C.T.; Slattery, A.D.; Tawfik, S.A.; Ford, M.J.; Dai, S.; et al. Electrocatalytic activity of a 2D phosphorene-based heteroelectrocatalyst for photoelectrochemical cells. *Angew. Chem. Int. Ed.* **2018**, *57*, 2644–2647. [\[CrossRef\]](#) [\[PubMed\]](#)
- Stroyuk, O.; Raevskaya, A.; Gaponik, N. Solar light harvesting with multinary metal chalcogenide nanocrystals. *Chem. Soc. Rev.* **2018**, *47*, 5354–5422. [\[CrossRef\]](#) [\[PubMed\]](#)
- Shrestha, A.; Batmunkh, M.; Tricoli, A.; Qiao, S.Z.; Dai, S. Near-infrared active lead chalcogenide quantum dots: Preparation, post-synthesis ligand exchange, and applications in solar cells. *Angew. Chem. Int. Ed.* **2019**, *58*, 5202–5224. [\[CrossRef\]](#) [\[PubMed\]](#)
- Ye, L.; Xiong, Y.; Chen, Z.; Zhang, Q.; Fei, Z.; Henry, R.; Heeney, M.; O'Connor, B.T.; You, W.; Ade, H. Sequential deposition of organic films with eco-compatible solvents improves performance and enables over 12%-efficiency nonfullerene solar cells. *Adv. Mater.* **2019**, *31*, 1808153. [\[CrossRef\]](#) [\[PubMed\]](#)
- Zhang, J.; Tan, H.S.; Guo, X.; Facchetti, A.; Yan, H. Material insights and challenges for non-fullerene organic solar cells based on small molecular acceptors. *Nat. Energy* **2018**, *3*, 720–731. [\[CrossRef\]](#)
- Ye, L.; Hu, H.; Ghasemi, M.; Wang, T.; Collins, B.A.; Kim, J.-H.; Jiang, K.; Carpenter, J.H.; Li, H.; Li, Z.; et al. Quantitative relations between interaction parameter, miscibility and function in organic solar cells. *Nat. Mater.* **2018**, *17*, 253–260. [\[CrossRef\]](#)
- Jeon, N.J.; Na, H.; Jung, E.H.; Yang, T.-Y.; Lee, Y.G.; Kim, G.; Shin, H.-W.; Seok, S.I.; Lee, J.; Seo, J. A fluorene-terminated hole-transporting material for highly efficient and stable perovskite solar cells. *Nat. Energy* **2018**, *3*, 682. [\[CrossRef\]](#)
- Macdonald, T.J.; Batmunkh, M.; Lin, C.-T.; Kim, J.; Tune, D.D.; Ambroz, F.; Li, X.; Xu, S.; Sol, C.; Papakonstantinou, I.; et al. Origin of performance enhancement in TiO₂-carbon nanotube composite perovskite solar cells. *Small Methods* **2019**, 1900164. [\[CrossRef\]](#)
- Rong, Y.; Hu, Y.; Mei, A.; Tan, H.; Saidaminov, M.I.; Seok, S.I.; McGehee, M.D.; Sargent, E.H.; Han, H. Challenges for commercializing perovskite solar cells. *Science* **2018**, *361*, eaat8235. [\[CrossRef\]](#) [\[PubMed\]](#)
- Ren, Y.; Sun, D.; Cao, Y.; Tsao, H.N.; Yuan, Y.; Zakeeruddin, S.M.; Wang, P.; Grätzel, M. A stable blue photosensitizer for color palette of dye-sensitized solar cells reaching 12.6% efficiency. *J. Am. Chem. Soc.* **2018**, *140*, 2405–2408. [\[CrossRef\]](#) [\[PubMed\]](#)
- Ambroz, F.; Sathasivam, S.; Lee, R.; Gadipelli, S.; Lin, C.-T.; Xu, S.; Poduval, R.K.; Mclachlan, M.A.; Papakonstantinou, I.; Parkin, I.P.; et al. Influence of lithium and lanthanum treatment on TiO₂ nanofibers and their application in n-i-p solar cells. *ChemElectroChem* **2019**, *6*, 3590–3598. [\[CrossRef\]](#)
- Macdonald, T.J.; Ambroz, F.; Batmunkh, M.; Li, Y.; Kim, D.; Contini, C.; Poduval, R.; Liu, H.; Shapter, J.G.; Papakonstantinou, I.; et al. TiO₂ nanofiber photoelectrochemical cells loaded with sub-12 nm AuNPs: Size dependent performance evaluation. *Mater. Today Energy* **2018**, *9*, 254–263. [\[CrossRef\]](#)
- Nazeeruddin, M.K.; Klein, C.; Liska, P.; Grätzel, M. Synthesis of novel ruthenium sensitizers and their application in dye-sensitized solar cells. *Coord. Chem. Rev.* **2005**, *249*, 1460–1467. [\[CrossRef\]](#)
- Nazeeruddin, M.K.; Kay, A.; Rodicio, I.; Humphry-Baker, R.; Mueller, E.; Liska, P.; Vlachopoulos, N.; Graetzel, M. Conversion of light to electricity by cis-X₂bis(2,2'-bipyridyl-4,4'-dicarboxylate)ruthenium(II) charge-transfer sensitizers (X = Cl-, Br-, I-, CN-, and SCN-) on nanocrystalline titanium dioxide electrodes. *J. Am. Chem. Soc.* **1993**, *115*, 6382–6390. [\[CrossRef\]](#)
- Kolemen, S.; Bozdemir, O.A.; Cakmak, Y.; Barin, G.; Erten-Ela, S.; Marszalek, M.; Yum, J.-H.; Zakeeruddin, S.M.; Nazeeruddin, M.K.; Grätzel, M.; et al. Optimization of distyryl-Bodipy chromophores for efficient panchromatic sensitization in dye sensitized solar cells. *Chem. Sci.* **2011**, *2*, 949–954. [\[CrossRef\]](#)

19. Ji, J.-M.; Zhou, H.; Kim, H.K. Rational design criteria for D- π -A structured organic and porphyrin sensitizers for highly efficient dye-sensitized solar cells. *J. Mater. Chem. A* **2018**, *6*, 14518–14545. [[CrossRef](#)]
20. Song, H.; Liu, Q.; Xie, Y. Porphyrin-sensitized solar cells: systematic molecular optimization, coadsorption and cosensitization. *Chem. Commun.* **2018**, *54*, 1811–1824. [[CrossRef](#)]
21. Kuang, D.; Walter, P.; Nüesch, F.; Kim, S.; Ko, J.; Comte, P.; Zakeeruddin, S.M.; Nazeeruddin, M.K.; Grätzel, M. Co-sensitization of organic dyes for efficient ionic liquid electrolyte-based dye-sensitized solar cells. *Langmuir* **2007**, *23*, 10906–10909. [[CrossRef](#)] [[PubMed](#)]
22. Chen, Y.; Yang, L.; Wu, J.; Wang, G.; Huang, W.; Melkonyan, F.S.; Lu, Z.; Huang, Y.; Marks, T.J.; Facchetti, A. Performance, morphology, and charge recombination correlations in ternary squaraine solar cells. *Chem. Mater.* **2018**, *30*, 6810–6820. [[CrossRef](#)]
23. Erten-Ela, S.; Ueno, Y.; Asaba, T.; Kubo, Y. Synthesis of a dibenzo-Bodipy-incorporating phenothiazine dye as a panchromatic sensitizer for dye-sensitized solar cells. *New J. Chem.* **2017**, *41*, 10367–10375. [[CrossRef](#)]
24. Singh, S.P.; Gayathri, T. Evolution of BODIPY dyes as potential sensitizers for dye-sensitized solar cells. *Eur. J. Org. Chem.* **2014**, *2014*, 4689–4707. [[CrossRef](#)]
25. He, H.; Ji, S.; He, Y.; Zhu, A.; Zou, Y.; Deng, Y.; Ke, H.; Yang, H.; Zhao, Y.; Guo, Z.; et al. Photoconversion-tunable fluorophore vesicles for wavelength-dependent photoinduced cancer therapy. *Adv. Mater.* **2017**, *29*, 1606690. [[CrossRef](#)]
26. Turksoy, A.; Yildiz, D.; Akkaya, E.U. Photosensitization and controlled photosensitization with bodipy dyes. *Coord. Chem. Rev.* **2019**, *379*, 47–64. [[CrossRef](#)]
27. Lee, C.Y.; Hupp, J.T. Dye sensitized solar cells: TiO₂ sensitization with a bodipy-porphyrin antenna system. *Langmuir* **2010**, *26*, 3760–3765. [[CrossRef](#)]
28. Urbani, M.; Grätzel, M.; Nazeeruddin, M.K.; Torres, T. Meso-substituted porphyrins for dye-sensitized solar cells. *Chem. Rev.* **2014**, *114*, 12330–12396. [[CrossRef](#)]
29. Klifout, H.; Stewart, A.; Elkhaila, M.; He, H. BODIPYs for dye-sensitized solar cells. *ACS Appl. Mater. Interfaces* **2017**, *9*, 39873–39889. [[CrossRef](#)]
30. Islam, A.; Chowdhury, T.H.; Qin, C.; Han, L.; Lee, J.-J.; Bedja, I.M.; Akhtaruzzaman, M.; Sopian, K.; Mirloup, A.; Leclerc, N. Panchromatic absorption of dye sensitized solar cells by co-Sensitization of triple organic dyes. *Sustain. Energy Fuels* **2017**, *2*, 209–214. [[CrossRef](#)]
31. Cheema, H.; Younts, R.; Gautam, B.; Gundogdu, K.; El-Shafei, A. Design and synthesis of BODIPY sensitizers with long alkyl chains tethered to N-carbazole and their application for dye sensitized solar cells. *Mater. Chem. Phys.* **2016**, *184*, 57–63. [[CrossRef](#)]
32. Qin, C.; Mirloup, A.; Leclerc, N.; Islam, A.; El-Shafei, A.; Han, L.; Ziessel, R. Molecular engineering of new thienyl-bodipy dyes for highly efficient panchromatic sensitized solar cells. *Adv. Energy Mater.* **2014**, *4*, 1400085. [[CrossRef](#)]
33. Li, Z.; Mintzer, E.; Bittman, R. First synthesis of free cholesterol-BODIPY conjugates. *J. Org. Chem.* **2006**, *71*, 1718–1721. [[CrossRef](#)] [[PubMed](#)]
34. Pakhomov, A.A.; Kononevich, Y.N.; Stukalova, M.V.; Svidchenko, E.A.; Surin, N.M.; Cherkaev, G.V.; Shchegolikhina, O.I.; Martynov, V.I.; Muzafarov, A.M. Synthesis and photophysical properties of a new BODIPY-based siloxane dye. *Tetrahedron Lett.* **2016**, *57*, 979–982. [[CrossRef](#)]
35. Wanwong, S.; Sangkhun, W.; Wootthikanokkhan, J. The effect of co-sensitization methods between N719 and boron dipyrromethene triads on dye-sensitized solar cell performance. *RSC Adv.* **2018**, *8*, 9202–9210. [[CrossRef](#)]
36. Krauss, T.N.; Barrena, E.; Zhang, X.N.; de Oteyza, D.G.; Major, J.; Dehm, V.; Würthner, F.; Cavalcanti, L.P.; Dosch, H. Three-dimensional molecular packing of thin organic films of PTCDI-C₈ determined by surface X-Ray diffraction. *Langmuir* **2008**, *24*, 12742–12744. [[CrossRef](#)] [[PubMed](#)]
37. Dharma, J.; Pital, A. *Simple Method of Measuring the Band Gap Energy Value of TiO₂ in the Powder Form Using a UV/Vis/NIR Spectrometer*; Perkin Elmer: Shelton, CT, USA, 2012.
38. Jiang, X.; Li, S.; Xiang, G.; Li, Q.; Fan, L.; He, L.; Gu, K. Determination of the acid values of edible oils via FTIR spectroscopy based on the OH stretching band. *Food Chem.* **2016**, *212*, 585–589. [[CrossRef](#)]
39. Mao, M.; Song, Q.-H. The structure-property relationships of D- π -A BODIPY dyes for dye-sensitized solar cells. *Chem. Rec.* **2016**, *16*, 719–733. [[CrossRef](#)]

40. Mishra, A.; Fischer, M.K.R.; Bäuerle, P. Metal-free organic dyes for dye-sensitized solar cells: From structure: Property relationships to design rules. *Angew. Chem. Int. Ed.* **2009**, *48*, 2474–2499. [[CrossRef](#)]
41. Fan, K.; Yu, J.; Ho, W. Improving photoanodes to obtain highly efficient dye-sensitized solar cells: A brief review. *Mater. Horiz.* **2017**, *4*, 319–344. [[CrossRef](#)]



© 2019 by the authors. Licensee MDPI, Basel, Switzerland. This article is an open access article distributed under the terms and conditions of the Creative Commons Attribution (CC BY) license (<http://creativecommons.org/licenses/by/4.0/>).